METAMORPHIC AND GEOCHRONOLOGICAL STUDY OF

ANATECTIC ALUMINOUS GNEISSES:

INSIGHTS ON EVOLUTION OF THE HINTERLAND IN THE

CENTRAL GRENVILLE PROVINCE

by

Stéphanie Lasalle

A Thesis submitted to the School of Graduate Studies

in partial fulfillment of the requirements for the degree of

Doctor of Philosophy

Department of Earth Sciences

Memorial University of Newfoundland

St. John's, Newfoundland and Labrador

May 2014

ABSTRACT

This thesis is an integrated petrographic, metamorphic, and geochronological investigation of granulite-facies aluminous gneisses from the central Grenville Province in Québec, Canada. The project aimed at characterizing the gneiss protoliths and reconstructing the metamorphic history of the region. The results provide insight into the evolution of the Laurentian margin upon which the Grenville orogen is built, and contribute to our understanding of the Grenvillian orogeny. The rocks come from a metasedimentary sequence and a volcanogenic bimodal (felsic-mafic) sequence, both exposed in the orogenic hinterland. They consist of garnet–biotite–quartz–K-feldspar–plagioclase with kyanite in the north (high-pressure segment) and sillimanite in the south (mid-pressure segment), and display microstructural evidence of anatexis.

The nature of the protoliths was constrained by zircon textures and *in situ* U–Pb ages obtained via laser ablation–inductively coupled plasma mass spectrometry (LA–ICPMS). Detrital zircon grains from the metasedimentary samples show Laurentian affinities, with ages between 2700 and 1500 Ma. In contrast, well-preserved igneous zircon grains from a sample of the bimodal sequence suggest a deposition age of 1238 ± 13 Ma, coeval with an episode of crustal extension in the central Grenville orogen.

The metamorphic evolution of the aluminous rocks is inferred by interpretation of microstructures and mineral chemistry within the framework of isochemical pressure–temperature (*P–T*) diagrams (*i.e.,* pseudosections), and *in situ* (LA–ICPMS) U–Pb dating of monazite. Data from a kyanite-bearing rock record a steep *P–T* path peaking at ~ 14.5 kbar and 860–900 °C, as in other parts of the high-*P* segment. In contrast, sillimanite-

bearing rocks record large variations in T relative to P with a peak at ~ 9.5 kbar and 850 °C.

Monazite mainly occurs in the rock matrix, where it commonly shows complex internal textures. Areas dark on backscattered electron (BSE) images record ages of 1070–1020 Ma with a main cluster at 1060 Ma. The large spread of ages in individual samples is consistent with a protracted residence of the host rocks under high-T conditions. In contrast, BSE-bright rims within matrix grains recorded ages of 1010–990 Ma, attributed to (re)crystallization that was promoted by fluid infiltration of the host rocks. This late event is coeval with ultra-potassic magmatism in this area and may record the orogenic collapse.

ACKNOWLEDGMENTS

I would like to thank *John Hanchar*, our Department Head, to whom I owe my 'arrival' on the island where I was only supposed to do a short internship under his supervision. Dr. Hanchar was the one introducing me to Dr. Indares and the rest is now history. Dr. Hanchar became a member of my Thesis committee, alongside with *Dr. Greg Dunning*, *Dr. Toby Rivers*, and *Dr. Charles Hurich*, and I really wish to acknowledge the role of these professors in my research and thank them for their constructive comments and corrections, mainly made during my Comprehensive exam and Thesis Proposal. I would like to especially thank Greg for all the 'U–Pb' discussions we had over the past 2 years while I was working on my zircon and monazite projects. Greg had the gift to give me back my confidence and my energy, in moments where I would struggle with my U-Pb LA–ICPMS data, and after each meeting with him, I was usually boosted for a week! *Toby* was also instrumental near the end of my PhD, both morally and financially, and I cannot thank him (and *his wife Pat*) enough for the kindness over the last few months of hardship.

I also wish to especially acknowledge my fellow student *Chris (now Dr. Christopher M. Fisher)* for everything he did for and with me during all these years at MUN, from all the 'everyday-life stuffs' we shared, to the 'secrets' of collecting and reducing the best possible zircon and monazite U–Pb LA–ICPMS data. He is, by far, one of the greatest students I have ever met and a great person, and I am just truly grateful to know him and hopefully, will never forget and always apply what he taught me.

Now, I want to thank 'my precious girls', without you, I have no clue how I would have managed not to jump in the snow from my office window at days where everything went completely wrong: *Kate* (or should I say Dr. Kate Souders), you have been such an inspiration and support, I can't thank you enough and wish we could share 'mute hugs' for the next 40 years; *Renita*, you're the younger sister I never had, and at the same time

TABLE OF CONTENTS

ᥱ----------------ᥫ

ᥱ----------------ᥫ

<div align="center">

ᑳ---------------ᑰ

</div>

                        CR----------------ЄO

4. CHAPTER 4 - *IN SITU* **LASER ABLATION–ICPMS DATING OF MONAZITE FROM ALUMINOUS GNEISSES: INSIGHTS ON THE TECTONO-METAMORPHIC HISTORY OF A GRANULITE-FACIES DOMAIN IN THE CENTRAL GRENVILLE PROVINCE**..**143**

$\mathcal{CR}$----------------$\wp$

x

                          ɢ----------------ꙅ

LIST OF TABLES

ભ----------------ৡ

ભ----------------ৡ

ભ----------------ৡ

LIST OF FIGURES

૭----------------ஒ

LIST OF APPENDICES

CO-AUTHORSHIP STATEMENT

The manuscript presented as **Chapter 2** entitled 'Contrasting types of Grenvillian granulite-facies aluminous gneisses: Insights on protoliths and metamorphic events from zircon morphologies and ages' was published in *Precambrian Research* in May 2013 (volume 228, pages 117-130). The paper is co-authored by Dr. Christopher M. Fisher (Memorial University at the time of the work, now at Washington State University), Dr. Aphrodite Indares (Memorial University), and Dr. Greg Dunning (Memorial University). As the first author, I was responsible for most aspects of the project including reviewing the literature, imaging the zircon grains, collecting and processing the U-Pb data. For the latter, the help and guidance of Dr. Christopher Fisher was significant. Mike Tubrett, Wilfredo Diegor and Rebecca Lam also assisted with the operation of the ICPMS. Co-authors gave guidance for interpretation of the data and drawing conclusions. They also edited/corrected the written manuscript before submission. The manuscript was written and submitted by me.

The manuscript presented as **Chapter 3** entitled 'Anatectic record and contrasting *P–T* paths of aluminous gneisses from the central Grenville Province' was published in the *Journal of Metamorphic Geology* (online March 28th, 2014; DOI: 10.1111/jmg.12083). The paper is co-authored by Dr. Aphrodite Indares (Memorial University). As the first author, I was responsible for most aspects of the project with a significant focus on the imaging work. The color code chosen for the SEM-MLA maps of thin-sections is now commonly used by our research team as well as other collaborators. Dr. Indares gave me invaluable guidance, especially for interpretating the *P–T* data. She

also edited/corrected the written manuscript before submission, and helped to revise it properly. The manuscript was written and submitted by me.

The manuscript presented as **Chapter 4** entitled '*In situ* laser ablation–ICPMS dating of monazite from aluminous gneisses: Insights on the tectono-metamorphic history of a granulite-facies domain in the central Grenville Province' is now *in press* at *Canadian Journal of Earth Sciences* (CJES). This Chapter corresponds to the revised version, awaiting final proofs, published online on April 8th, 2014 (DOI:10.1139/cjes-2013-0170).The paper is co-authored by Dr. Aphrodite Indares and Dr. Greg Dunning (Memorial University). As the first author, I was responsible for most aspects of the project including reviewing the literature, imaging the monazite grains, and collecting the U–Pb data. Mike Tubrett, Wifredo Diegor and Rebecca Lam assisted with the operation of the ICPMS. Co-authors gave guidance for interpretation of the data and drawing conclusions. They also edited/corrected the written manuscript before submission. The manuscript was written and submitted by me.

CHAPTER 1

1. INTRODUCTION AND OVERVIEW

1.1.   LARGER CONTEXT AND AIM OF THE THESIS

This thesis is an investigation of granulite-facies anatectic aluminous gneisses from the central portion of the Mesoproterozoic Grenville Province in Québec, Canada. This is an integrated petrographic, metamorphic and isotopic study, with the intent to improve our understanding of the crustal evolution of the Grenville Province.

Granulite-facies gneisses, including anatectic rocks, represent the final product of crustal recycling in continental collisional settings (Brown, 2004; 2007; 2010). Such rocks are common in the middle to lower crust of large hot orogens (LHOs), in which temperatures remain above ~ 750 °C for several tens of million years, leading to substantial anatexis, viscosity reduction, and crustal flow (Rosenberg and Handy, 2005; Beaumont *et al.,* 2006; Godin *et al.*, 2006; Grujic, 2006; Jones *et al.,* 2006).

Vestiges of middle to lower orogenic crust are presently exposed as gneiss complexes at the exhumed cores of ancient LHOs and provide insights on deep crustal processes. Gneiss complexes consist of pervasively deformed, high-grade metamorphic rocks that often are poorly understood due to difficulties in assessing their original field relationships, and because original rock microstructures tend to be obliterated by metamorphic recrystallization. Among the different types of gneisses, aluminous rocks (*e.g.*, metapelite, metagreywacke, or products of hydrothermally altered felsic volcanic rocks; Bonnet *et al.,* 2005; Bonnet and Corriveau, 2007) have mineralogies that are particularly sensitive to changes in pressure and temperature (*P–T)* and undergo extensive anatexis at granulite-facies conditions (Spear *et al.,* 1999). Therefore, their mineral assemblages and microstructures provide a record of *P–T* changes and of the anatectic

history that are important for understanding the geodynamic evolution of orogenic crust. In addition, aluminous rocks commonly contain zircon and monazite that can offer insight on the timing of metamorphism, but also, in the case of zircon, insight on the age and setting of the protoliths; thus on the type of crust present before the final orogeny.

The Grenville Province, the result of the collision between Laurentia and (probably) Amazonia (Tohver *et al.,* 2006), is a prime example of an ancient LHO, perhaps the oldest in Earth's history (Beaumont *et al.,* 2006). It constitutes the youngest portion of the Canadian Shield, in area over 2000 km long with a minimum width of 600 km in eastern Canada and the United States (Rivers *et al.*, 2012). Its final architecture is inferred to be the result of deformation and metamorphism due to crustal thickening, crustal flow (Jamieson *et al.,* 2007) and subsequent orogenic collapse (Rivers, 2012).

The main objective of this thesis is to investigate the origin and metamorphic evolution of anatectic aluminous gneisses in the Manicouagan area (Québec, hinterland of the central Grenville Province; Fig. 1.1) with special focus on those from the Canyon domain. Types and ages of protoliths are inferred based on zircon morphologies, internal textures, and U–Pb LA–ICPMS geochronology. The *P–T(–t)* and anatectic history is assessed using integrated microstructural data, mineral chemistry, and phase equilibria modelling, as well as *in situ* U–Pb LA–ICPMS dating of monazite. The findings of this thesis contribute to a better understanding of the Laurentian crust in the Grenville Province and of the tectono-thermal history of the Grenvillian orogeny in general and of the hinterland in particular. The remaining part of this introductory chapter outlines the geological background of the study, the approaches used and the organization of the thesis.

1.2. GEOLOGICAL BACKGROUND

1.2.1. Grenville Province: general characteristics

The majority of units exposed in the Grenville Province belong to the southeast Laurentian margin. This long-lived margin grew by formation and/or accretion of arcs for over 500 my (1700–1200 Ma; Rivers and Corrigan, 2000; Gower and Krogh, 2002). Major crust-forming events are known as Labradorian (1710–1600 Ma), Pinwarian (1520–1460 Ma), and Elzevirian (1250–1190 Ma) (Gower and Krogh, 2002), and there are also remnants of a 1.4 Ga island arc (Montauban arc; Corrigan and van Breemen, 1997).

The southeast Laurentian margin was reworked and metamorphosed during the Grenvillian orogeny (*ca.* 1080–980 Ma), leading to the first order tectonic divisions summarized below (*cf.,* inset map Fig. 1.1). The Parautochthonous belt is composed of rock units that were deformed and metamorphosed during the Grenvillian orogeny but which can be traced across the Grenville Front into the foreland. Metamorphism is late Grenvillian in age (*ca.* 995–985 Ma), progressively increasing in intensity from greenschist facies to high-*P* granulite and locally eclogite-facies conditions to the southeast (Indares and Dunning, 2001; Jordan *et al.,* 2006; Indares *et al.,* 2008; Rivers, 2008). In contrast, the Allochthonous belts (or hinterland) are an assemblage of terranes which are part of the Laurentian margin but not directly linked with the foreland, and are interpreted as the root of a collapsed plateau, juxtaposed against remnants of the old and strong upper crust, the 'orogenic lid'(Rivers, 2008). Separating this hinterland from the Parautochthonous belt is the Allochton Boundary (AB; inset map Fig. 1.1) which first

worked as a thrust and then as a normal-sense detachment (Rivers, 2008). Metamorphism in the hinterland is mainly mid-*P* (upper amphibolite to granulite) with high-*P* rocks (granulites and eclogites) locally exposed to the northwest, and is coeval with the culmination of the Grenvillian orogeny (1080–1050 Ma; Ottawan phase of Rivers, 1997; Rivers *et al.,* 2012).

Geodynamical models for the Grenvillian Orogen involve syn- to post-convergence crustal flow (model of hot fold nappes; Jamieson *et al.,* 2010; Jamieson and Beaumont, 2011) and a late stage orogenic collapse (Rivers, 2008). Crustal flow models were successful at explaining the architecture of the hinterland in the southwest Grenville, before collapse of the plateau, but less so in the central Grenville, in part due to inadequate geological constraints at that time (Jamieson *et al.,* 2010, Jamieson and Beaumont, 2011).

1.2.2. Regional geology: the Manicouagan area and the Canyon domain

This study focuses on the Manicouagan area of the central Grenville Province (Québec) where the hinterland consists of three contrasting *P*-segments (Dunning and Indares, 2010; and refs. therein): a coherent high-*P* segment (Manicouagan Imbricate Zone; MIZ), a mid-*P* segment (Island and Canyon domains; Banded complex) and the orogenic lid (Hart Jaune terrane; HJT). This hinterland lies structurally above the Parautochthonous Gagnon terrane (Archean and Paleoproterozoic ages; van Gool *et al.,* 2008), and is made of Mesoproterozoic lithologic associations, mainly Labradorian (1.7–1.6 Ga; anorthosite and gabbroic suites in MIZ and in the Island domain) and Pinwarian

(1.5–1.4 Ga; units in the Canyon domain and Hart Jaune terrane). In addition, the Banded complex, a 1.2 Ga felsic-mafic supracrustal sequence is intercalated within the previous associations and is attributed to a crustal extension episode (Dunning and Indares, 2010).

The Canyon domain (Hynes *et al.,* 2000) is exposed south of the Manicouagan reservoir and dominantly consists of layered rocks (Dunning and Indares, 2010), which were grouped by Indares and Moukhsil (2013) into two principal lithologic associations (Fig. 1.1). These are: (a) a metasedimentary sequence to the south (Complexe de la Plus Value; PLV) of metagreywacke, anatectic metapelite, quartzite and minor calcsilicate, deposited between *ca.* 1700 and 1500 Ma (Moukhsil *et al.,* 2013); and (b) a number of associations in the center and north of the domain, including a *ca.* 1410 Ma suite of layered mafic to intermediate rocks (LMS; Dunning and Indares, 2010) locally associated with a quartzofeldspathic unit (QFU) of unknown age, and a layered bimodal sequence (LBS) in which felsic layers locally grade to garnetites and aluminous ± nodular gneisses. The LBS is inferred to represent metamorphosed remnants of a volcanic belt, the age of which was unknown prior to this study. In addition, late tectonic 990–980 Ma ultrapotassic and granite-pegmatite dykes are abundant in the central-southern part of the Canyon domain. Lithologic associations similar to that of the LBS and the Banded complex were also identified in the high-*P* segment of the hinterland, north of the Manicouagan reservoir (*i.e.,* southern tip of the MIZ; Indares and Moukhsil, 2013).

Metamorphism in the Canyon domain is inferred to be of mid-*P* granulite-facies, based on the absence of muscovite and the presence of garnet–sillimanite–biotite–K-feldspar in aluminous rocks and orthopyroxene–clinopyroxene–garnet+/-hornblende in mafic rocks. The age is constrained at *ca.* 1080–1040 Ma based on U–Pb monazite dating

(isotopic dilution–thermal ionisation mass spectrometry; ID–TIMS; Dunning and Indares, 2010). In some cases, monazite ages from a single sample showed a scatter of data over several 10s of million years, the significance of which is unclear. In contrast, metamorphism of the rocks inferred to be related to that of the LBS and Banded complex, north of the reservoir, is of high-P granulite-facies (with kyanite instead of sillimanite in aluminous gneisses) with ages at *ca.* 1040–1030 Ma (*e.g.,* Baie du Nord segment, BNS; Indares and Dunning, 2001).

The aluminous rocks of this study come from the PLV and the LBS (including an exposure of the LBS north of the reservoir), and provide a record of the deposition of the PLV in the Canyon domain, an age for the LBS, and a record of the *P–T–t* evolution of the Canyon domain.

1.3. APPROACHES TO THE STUDY OF ALUMINOUS GNEISSES

The thesis research has three main components: evaluating the anatectic record and *P–T* paths, zircon dating and monazite dating. This section outlines the different approaches used. Because documentation of the microstructures at the hand sample and micro-scale is of crucial importance for each one of the research components, the imaging approach is described first.

1.3.1. Imaging of rock microstructures

A range of imaging techniques was used in addition to optical microscopy. One strength of the present study is the production of false-color thin-section maps using a

secondary electron microscope (SEM; model FEI Quanta 600), equipped with an energy dispersive X-ray (EDX) analytical system (Roentec XFlash 3001 SDD; silicon drift detector) and mineral liberation analysis software (MLA; designed by JKTech; Gu, 2003). Once carefully colored, these maps give an overview of the rock microstructures that is rather unique and essential when dealing with minerals that are colorless under the microscope. This method also provides the modal mineral proportions needed for the phase equilibria modelling.

Finer-scale microstructures were imaged using cathodoluminescence (CL) to help identify former melt domains. This successfully highlighted the presence of cuspate mono- or poly-crystalline domains of quartz and/or feldspars interpreted as the product of melt crystallization (Guilmette *et al.,* 2011; Mitchell *et al.,* 2014).

In addition, zircon and monazite were imaged by back-scattered electron (BSE) and cathodoluminescence (CL) and, in the case of monazite, by chemical elemental maps (for U, Th, Pb, Y) produced by electron probe microanalysis (EPMA). Imaging allows identification of distinctive textural and chemical domains within grains, thus providing a guide for the location of the spots to be analyzed for geochronology as well as a framework for the interpretation of the data (Hanchar and Miller, 1993; Williams *et al.,* 1999; Corfu *et al.,* 2003).

1.3.2. Anatectic record and *P–T* path determination

A record of the *P–T* evolution of metamorphic rocks is preserved in their mineral assemblages, microstructures and mineral compositions. The relatively new and

8

increasingly popular approach of modelling phase equilibria allows the interpretation of microstructures and mineral chemistry in terms of *P–T* paths within the context of isochemical *P–T* diagrams, also called 'equilibrium phase diagrams' or 'pseudosections'. Available software, such as Perplex (Connolly and Kerrick, 1987; Connolly, 1990), THERMOCALC (Powell *et al.,* 1998), and Theriak-Domino (de Capitani and Petrakakis, 2010) rely on an internally consistent thermodynamic data base (Powell and Holland, 1988). The most poweful software is THERMOCALC, which is the most time-consuming but has the advantage of giving more control to the user.

   P–T pseudosections display the stability fields of mineral assemblages for a specific bulk-rock composition, placing first-order *P–T* constraints on the observed mineral assemblage. On these stability fields, one may superimpose isopleths of phase proportions and of mineral composition parameters. Comparison of the phase proportion isopleths with observed textural data, and of the mineral composition isopleths with the measured mineral compositions of the rock in question, allows researchers to infer the conditions of the metamorphic peak and (parts of) the *P–T* path. Finally, because during dynamic metamorphism anatectic rocks commonly experience melt loss (White and Powell, 2002), pseudosections built for the measured bulk rock composition can only predict the *P–T* evolution subsequent to the melt loss. Evaluating the prograde history requires calculation of *P–T* pseudosections in which melt is reintegrated back into the bulk composition (*e.g.,* Indares *et al.,* 2008).

1.3.3. *In situ* U–Pb dating of zircon in epoxy mounts

Zircon, a nesosilicate with the formula $ZrSiO_4$, is the most widely used accessory mineral for U–Pb dating of geological events, owing to its slow diffusion of Pb (Cherniak, 2010). Zircon morphology, internal texture, and chemical composition can provide information on its growth history, thus on rock protoliths, and on subsequent thermal- or fluid-related disturbances during orogenic events. Imaging of zircon (see section 1.3.1.) permits distinction betweeen igneous and metamorphic grains and detection of multiple growth episodes; therefore it is critical for the interpretation of zircon data (*e.g.,* Hanchar and Miller, 1993; Hanchar and Rudnick, 1995; Vavra *et al.,* 1996, 1999; Möller *et al.,* 2002; Tikhomirova, 2002; Aleinikoff *et al.,* 2006; Corfu, 2003, 2007). However, in high-grade rocks such as those present in orogenic crust, zircon morphologies and internal textures commonly show great complexity, and distinguishing between igneous and metamorphic traits may be difficult in some cases (*e.g.,* is this a metamorphic zircon with a smoothed 'soccer-ball' shape, or an igneous grain which originally grew with a stubby morphology and then was significantly rounded ?).

Various methods used for U–Pb zircon dating include isotopic dilution–thermal ionization mass spectrometry (ID–TIMS; Parrish and Noble, 2003), and *in situ* methods such as secondary ion mass spectrometry (SIMS; Ireland and Williams, 2003) and laser ablation–inductively coupled plasma mass spectrometry (LA–ICPMS; *e.g.,* Feng, *et al.,* 1993; Fryer *et al.,* 1993; Košler and Sylvester, 2003), which is used in the present study. The *in situ* LA–ICPMS dating method combines high spatial resolution (spot sizes of 20–30 µm are common) with a precision of 1–2% r.s.d. which although lower than the high

analytical resolution of ID–TIMS (*e.g.,* 0.1% r.s.d. or better), is able to resolve ages of discrete domains in complex crystals (*e.g.,* Gibson *et al.*, 2004). However, in order to maximise analytical precision, numerous issues need to be monitored when proceeding with U–Pb dating of zircon by LA–ICPMS.

First, detailed CL imaging of zircon internal textures does not assure that one will be able to link the resulting U–Pb ages of specific domains of grains to specific events. This problem is minimized if compositional data are also collected for those same zircon domains, but for logistical reasons this was not done in the context of the present study. Second, in metamorphic rocks, zircon commonly produces discordant U–Pb data that can be attributed to one or more of the following: Pb loss and/or diffusion, common Pb contamination, physical mixing of different zones of different composition and/or age (Corfu, 2013), and zircon recrystallization which is also a problem at granulite-facies conditions (*e.g.,* Nasdala *et al.,* 2005).

U–Pb data processing, or data reduction, remains a subject of great debate as interpretations may depend on the method and software used. Many laser ablation laboratories have unique methods for data collection and reduction, which in turn, leads to difficulties when comparing results. In this thesis, the software Iolite (Paton *et al.,* 2010) running in IgorPro (WaveMetrics Inc., www.wavemetrics.com) is used for the U–Pb data reduction. However, because this work is not focused on analytical development or data reduction procedures, these issues are not discussed in depth.

1.3.4.   *In situ* U–Pb dating of monazite in thin sections

Monazite, a light rare earth element (LREE)-bearing orthophosphate (*i.e.,* LREE PO$_4$), is a common accessory mineral in metamorphosed pelitic rocks from greenschist to amphibolites-facies and above (Kingsbury *et al.*, 1993). Owing to its high thorium and uranium concentrations (*i.e.,* up to tens of wt % of Th and a few wt % of U) but very low amount of non-radiogenic lead (*i.e.,* often less than 1 ppm of ^{204}Pb), as well as very slow volume diffusion of Pb (Cherniak, 2010), monazite is a key tool for dating metamorphism in high-grade rocks (Parrish, 1990; Montel *et al.,* 1996; Foster *et al.,* 2002; Pyle and Spear, 2003; Gibson *et al.,* 2004; Kohn and Malloy, 2004; Williams *et al.,* 1999, 2007).

Common preservation of growth zoning can be imaged using several techniques (see section 1.3.1.) and allows, in principle, dating of complex metamorphic histories by using *in situ* methods (*e.g.,* McFarlane and Harrison, 2006; Kelsey *et al.,* 2008; Williams *et al.,* 1999, 2007). In addition, dating of monazite grains in thin-section permits linking ages to specific microstructural settings and potentially to distinct metamorphic reactions (*e.g.,* Simonetti *et al.,* 2006; Kelsey *et al.,* 2007, 2008; Cutts *et al.,* 2010; Langone *et al.,* 2011; Kelly *et al.,* 2012; Gervais and Hynes, 2012). However, owing to complexities of natural systems, assigning U–Pb ages of distinct overgrowths within a grain to specific metamorphic reactions or parts of a metamorphic *P–T* path(s) remain problematic (*e.g.,* Spear and Pyle, 2002; Harrison *et al.*, 2002; Williams *et al.*, 2007; Kelsey *et al.*, 2008). In the case of LHOs which have incubation periods of several tens of millions of years, with potentially several 'pulses' of monazite growth, separated only by 10 or 20 millions of

years, the precision of the U–Pb data obtained by *in situ* methods such as LA–ICPMS may limit the ability to distinguish specific growth events.

1.4. STRUCTURE OF THE THESIS

After this introduction (Chapter 1), the thesis consists of three main chapters followed by a summary and conclusions (Chapter 5), and by the appendices (see text and accompanying CD). Each chapter has its own list of references, with a complete list in Chapter 6.

A note about the samples used: the aluminous gneisses investigated in this thesis belong to two contrasting lithological associations of the Canyon domain (Manicouagan area, hinterland of the central Grenville Province, Fig. 1.1.): two samples are from the PLV metasedimentary sequence (samples HJ60b and M1b) whereas the three others are from the bimodal (felsic-mafic) sequence LBS, inferred to be of dominantly volcanic origin (samples 244, 216, and 333x). Sample locations are from the mid-*P* segment, except for 244, which was collected in a lithologic association similar to the LBS in the high-*P* segment.

Chapter 2 is the manuscript of a paper published in *Precambrian Research* (Lasalle *et al.,* 2013). This chapter presents zircon data from four of the five aluminous gneisses (the sample from location 216 did not yield enough zircon grains to be properly analyzed). The morphology of the zircon grains, their internal texture, and the distributions of their U–Pb ages (obtained via LA–ICPMS) and Th/U ratios provide constraints on the age and nature of the protoliths as well as on subsequent thermal

events. In addition, when integrated with previously published data, the new results refine relationships between different crustal units and suggest a possible order of geological events for the Canyon domain of the central Grenville Province.

Chapter 3 is the final version of a manuscript published in the *Journal of Metamorphic Geology* (Lasalle and Indares, 2014). This chapter documents the effect of granulite-facies metamorphism and partial melting using four samples of aluminous gneisses. The microstructures and mineral chemistries of these rocks were interpreted in terms of *P*–*T* paths within the framework of *P*–*T* pseudosections calculated with THERMOCALC for both measured and melt-reintegrated rock compositions. This manuscript provides the first comprehensive assessment of the metamorphic record of mid-*P* rocks in the Grenvillian hinterland, as well as a comparison between the *P*–*T* evolution of two juxtaposed high-*P* and mid-*P* portions of the orogen. The results are discussed in light of recent thermo-mechanical models for the evolution of the Grenvillian Province.

Chapter 4 is the revised manuscript, awaiting the final proofs, submitted to *Canadian Journal of Earth Sciences* (Lasalle *et al., in press*). This chapter focuses on *in situ* LA–ICPMS U–Pb dating of monazite, undertaken to reassess the spread of monazite ages previously identified by ID–TIMS (Dunning and Indares, 2010) in the same rocks, and to evaluate a potential contribution from a late Grenvillian thermal event in this area. To that end, the LA–ICPMS ages are interpreted in the context of the general microstructure of the rocks, as well as in the context of specific zones in single grains.

Chapters 2 to 4 are reformatted, and in some instances slightly reworded relative to the published versions in order to use a consistent terminology.

REFERENCES

Aleinikoff, J. N., Schenck, W. S., Plank, M. O., Srogi, L. A., Fanning, C. M., Kamo, S. L. and Bosbyshell, H., 2006. Deciphering igneous and metamorphic events in high-grade rocks of the Wilmington Complex, Delaware: Morphology, cathodoluminescence and backscattered electron zoning, and SHRIMP U–Pb geochronology of zircon and monazite. *Geological Society of America Bulletin*, **118**: 39–64.

Beaumont, C., Nguyen, M. H., Jamieson, R. A. and Ellis, S., 2006. Crustal flow modes in large hot orogens. *In:* Law, R. D., Searle, M. P., and Godin, L. *(Eds).* Channel Flow, Ductile Extrusion and exhumation in Continental Collision Zones. *Geological Society, London*, Special Publications, **268**: 91–145.

Bonnet, A. and Corriveau, L., 2007. Alteration vectors to metamorphic hydrothermal systems in gneissic terranes. *In:* Goodfellow, W.D. *(Eds.).* Mineral Deposits of Canada: A Synthesis of Major Deposit-Types, District Metallogeny, the Evolution of Geological Provinces, and Exploration Methods. *Geological Association of Canada, Mineral Deposits Division, Special Publication,* **5**: 1035–1049.

Bonnet, A., Corriveau, L. and La Flèche, M. R., 2005. Chemical imprint of highly metamorphosed volcanic-hosted hydrothermal alterations in the Romaine Supracrustal Belt, eastern Grenville Province, Quebec. *Canadian Journal of Earth Sciences,* **42(10)**: 1783–1814.

Brown, M., 2010. Melting of the continental crust during orogenesis: the thermal, rheological, and compositional consequences of melt transport from lower to upper continental crust. *Canadian Journal of Earth Sciences*, **47**: 655–694.

Brown, M., 2007. Crustal melting and melt extraction, ascent and emplacement in orogens: mechanisms and consequences. *Journal of the Geological Society, London,* **164**: 709–730.

Brown, M., 2004. The mechanism of melt extraction from lower continental crust of orogens. *Transactions of the Royal Society of Edinburgh, Earth Sciences*, **95**: 35–48.

Cherniak, D. J., 2010. Diffusion in Accessory Minerals: Zircon, Titanite, Apatite, Monazite and Xenotime. *Reviews in Mineralogy and Geochemistry*, **72**: 827–869.

Connolly, J. A. D., 1990. Multivariable phase diagrams: an algorithm based on generalized thermodynamics. *American Journal of Science*, **290**: 666–718.

Connolly, J. A. D. and Kerrick, D. M., 1987. An algorithm and computer program for calculating composition phase diagrams. *CALPHAD*, **11**:1–55.

Corfu, F., 2007. Multistage metamorphic evolution and nature of the amphibolite-granulite-facies transition in Lofoten-Vesterålen, Norway, revealed by U–Pb in accessory minerals. *Chemical Geology*, **214**: 108–128.

Corfu, F., 2013. A century of U-Pb geochronology: The long quest towards concordance. *GSA Bulletin*, **125 (1/2)**: 33–47.

Corfu, F., Hanchar, J. M., Hoskin, P. W. O. and Kinny, P. D., 2003. Atlas of zircon textures. *In:* Hanchar, J. M., Hoskin, P. W. O. *(Eds.).* Zircon. *Reviews in Mineralogy and Geochemistry,* **53**: 469–500.

Corrigan, D and van Breemen, O., 1997. U–Pb age constraints for the lithotectonic evolution of the Grenville Province along the Mauricie transect, Quebec. *Canadian Journal of Earth Sciences*, **34**: 299–316.

Cutts, K. A., Kinny, P. D., Strachan, R. A., Hand, M., Kelsey, D. E., Emery, M., Friend, C. R. L. and Leslie, A. G., 2010. Three metamorphic events recorded in a single garnet: Integrated phase modelling, *in situ* LA-ICPMS and SIMS geochronology from the Moine Supergroup, NW Scotland. *Journal of Metamorphic Geology*, **28**: 249–267.

de Capitani C. and Petrakakis K., 2010. The computation of equilibrium assemblage diagrams with Theriak/Domino software. *American Mineralogist,* **95**:1006–1016.

Dunning, G. and Indares, A., 2010. New insights on the 1.7-1.0 Ga crustal evolution of the central Grenville Province from the Manicouagan – Baie Comeau transect. *Precambrian Research*, **180**: 204–226.

Feng, R., Machado, N. and Ludden, J., 1993. Lead geochronology of zircon by LaserProbe-inductively coupled plasma mass spectrometer (LP–ICPMS). *Geochimica et Cosmochimica Acta*, **57**: 3479–3486.

Foster, G., Gibson, H. D., Parrish, R., Horstwood, M., Fraser, J. and Tindle, A., 2002. Textural, chemical and isotopic insights into the nature and behavior of metamorphic monazite. *Chemical Geology*, **19**: 183–207.

Fryer, B. J, Jackson, S. E. and Longerich, H. P., 1993. The application of laser ablation microprobe-inductively coupled plasma mass spectrometer (LAM–ICPMS) to *in situ* (U)-Pb geochronology. *Chemical Geology*, **109**: 1–8.

Gervais, F. and Hynes, A., 2012. Linking metamorphic textures to U–Pb monazite *in situ* geochronology to determine the age and nature of aluminosilicate-forming reactions in the Northern Monashee Mountains, British-Columbia. *Lithos*, **160–161**: 250–267.

Gibson, H. D. T, Carr, S. D., Hamilton, M. A. and Brown, R. L., 2004. Correlating yttrium zones and age domains in monazite with metamorphic reactions involving major pelitic phases: an integration of ID–TIMS and SHRIMP geochronology with Y-Th-U X-ray mapping. *Chemical Geology*, **211**: 237–260.

Godin, L., Grujic, D, Law, R. D. and Searle, M. P., 2006. Channel flow, ductile extrusion and exhumation in continental collision zones: an introduction. *In:* Law, R. D., Searle, M. P., and Godin, L. *(Eds).* Channel Flow, Ductile Extrusion and exhumation in Continental Collision Zones. *Geological Society, London*, Special Publications, **268**: 1–23.

Gower, C. F. and Krogh, T. E., 2002. A U–Pb geochronological review of the Proterozoic history of the eastern Grenville Province. *Canadian Journal of Earth Sciences,* **39**: 795–829.

Grujic, D., 2006. Channel flow and continental collision tectonics: an overview. *In:* Law, R. D., Searle, M. P., and Godin, L. *(Eds).* Channel Flow, Ductile Extrusion and exhumation in Continental Collision Zones. *Geological Society, London*, Special Publications, **268**: 25–37.

Gu, Y., 2003. Automated scanning electron microscopy based mineral liberation analysis. An introduction to JKMRC/FEI Mineral Liberation Analyser. *Journal of Minerals and Materials, Characterization and Engineering,* **2**: 33–41.

Guilmette, C., Indares, A. D. and Hébert, R., 2011. High-pressure anatectic paragneisses from the Namche Barwa, eastern Himalayan Syntaxis; textural evidence for partial melting, phase equilibria modelling and tectonic implications. *In:* Schulman, K., O'Brien, P., White, R., Brown, M., Lexa, Ondrej *(Eds.)*. Granulite-facies metamorphism and the rheology of the lower crust, Granulites and Granulites 2009. *Lithos*, **124**: 66–81.

Hanchar, J. M. and Miller, C. F., 1993. Zircon zonation patterns as revealed by cathodoluminescence and backscattered electron images: Implications for interpretation of complex crustal histories. *Chemical Geology*, **110**: 1–13.

Hanchar, J. M. and Rudnick, R. L., 1995. Revealing hidden structures: the application of cathodoluminescence and back-scattered electron imaging to dating zircons from lower crustal xenoliths. *Lithos,* **36**: 289–303.

Harrison, T. M., Catlos, E. J., and Montel, J.-M., 2002. U–Th–Pb dating of phosphate minerals. *In:* Kohn, M. J., Rakovan, J., Hughes, J. M. *(Eds.)*. Phosphates: geochemical, geobiological, and materials importance. *Reviews in Mineralogy and Geochemistry, Mineralogical Society of America,* **48 (14)**: 523–558.

Hynes, A., Indares, A., Rivers, T. and Gobeil, A., 2000. Lithoprobe line 55: integration of out-of-plane seismic results with surface structure, metamorphism, and geochronology, and the tectonic evolution of the eastern Grenville Province. *Canadian Journal of Earth Sciences*, **37**: 341–358.

Indares, A. and Moukhsil, A., 2013. Geon 12 crustal extension in the central Grenville Province, implications for the orogenic architecture, and potential influence on the emplacement of anorthosites. *Canadian Journal of Earth Sciences*, **50**: 955–966.

Indares, A., White, R. W. and Powell, R., 2008. Phase equilibria modelling of kyanite-bearing anatectic paragneisses from the central Grenville Province. *Journal of Metamorphic Geology*, **26**: 815–836.

Ireland, T. R. and Williams, I. S., 2003. Considerations in zircon geochronology by SIMS. *In:* Hanchar, J. M., Hoskin, P. W. O. *(Eds.).* Zircon. *Reviews in Mineralogy and Geochemistry,* **53**: 215–241.

Jamieson, R. A. and Beaumont, C., 2011. Coeval thrusting and extension during post-convergent ductile flow - implications for exhumation of high-grade metamorphic rocks. *Journal of Metamorphic Geology*, **29**: 33–51.

Jamieson, R. A., Beaumont, C., Nguyen, M. H. and Culshaw, N. G., 2007. Synconvergent ductile flow in variable-strength continental crust: Numerical models with application to the western Grenville orogen. *Tectonics*, **26**: 1–23.

Jamieson, R. A., Beaumont, C., Warren, C. J. and Nguyen, M. H., 2010. The Grenville Orogen explained? Applications and limitations of integrating numerical models with geological and geophysical data. *In:* Lithoprobe - parameters, processes and the evolution of a continent (Lithoprobe Synthesis Volume II, *(Eds.)* Clowes, R M., and Skulski, T.). *Canadian Journal of Earth Sciences*, **47**: 517–539.

Jones, R. R., Holdsworth, R. E., Hand, M. and Goscombe, B., 2006. Ductile extrusion in continental collision zones: ambiguities in the definition of channel flow and its identification in ancient orogens. *In:* Law, R. D., Searle, M. P., and Godin, L. *(Eds).* Channel Flow, Ductile Extrusion and exhumation in Continental Collision Zones. *Geological Society, London*, Special Publications, **268**: 201–219.

Kelly, N. M., Harley, S. L. and Möller, A., 2012. Complexity in the behavior and recrystallization of monazite during high-T metamorphism and fluid infiltration. *Chemical geology*, **322-323**: 192–208.

Kelsey, D. E., Clark, C. and Hand, M., 2008. Thermobarometric modelling of zircon and monazite growth in melt-bearing systems: examples using model metapelitic and metapsammitic granulites. *Journal of Metamorphic Geology*, **26**: 199–212.

Kelsey, D. E., Hand, M., Clark, C. and Wilson, C. J. L., 2007. On the application of *in situ* monazite chemical geochronology to constraining P-T-t histories in high-temperature (>850 °C) polymetamorphic granulites from Prydz Bay, East Antarctica. *Journal of the Geological Society*, **164**: 667–683.

Kingsbury, J. A., Miller, C. F., Wooden, J. L. and Harrison, T.M., 1993. Monazite paragenesis and U-Pb systematics in rocks of the eastern Mojave Desert, California, U.S.A.: implications for thermochronometry. *Chemical Geology*, **110**: 147–168.

Kohn, M. J. and Malloy, M. A., 2004. Formation of monazite via prograde metamorphic reactions among common silicates: Implications for age determinations. *Geochimica et Cosmochimica Acta*, **68**: 101–113.

Košler J. and Sylvester P., 2003. Present trends and the future of zircon in geochronology: laser ablation ICPMS. *In:* Hanchar, J. M., Hoskin, P. W. O. *(Eds.).* Zircon. *Reviews in Mineralogy and Geochemistry,* **53**: 243–275.

Langone, A., Braga, R., Massonne, H. J. and Tiepolo, M., 2011. Preservation of old (prograde metamorphic) U–Th–Pb ages in unshielded monazite from the high-pressure paragneisses of the Variscan Ulten Zone (Italy). *Lithos*, **127**: 68–85.

Lasalle, S. and Indares, A., 2014. Anatectic and *P–T* record of aluminous gneisses from diverse protoliths and contrasting-pressure crustal belts in the central Grenville Province. *Journal of Metamorphic Geology*, *in press*, DOI: 10.1111/jmg.12083.

Lasalle, S., Dunning, G. and Indares, A., 2014. *In situ* laser ablation–ICPMS dating of monazite from aluminous gneisses: Insights on the tectono-metamorphic history of a granulite-facies domain in the central Grenville Province. *Canadian Journal of Earth Sciences, in press,* DOI:10.1139/cjes-2013-0170.

Lasalle, S., Fisher, C. M., Indares, A. and Dunning, G., 2013. Contrasting types of Grenvillian granulite-facies aluminous gneisses: Insights on protoliths and metamorphic events from zircon morphologies and ages. *Precambrian Research*, **228**: 117–130.

McFarlane, C. R. M. and Harrison, T. M., 2006. Pb-diffusion in monazite: constraints from a high-*T* contact aureole setting. *Earth and Planetary Science Letters,* **250**: 376–384.

Mitchell, R., Indares, A. and Ryan, B., 2014. High to ultrahigh temperature contact metamorphism and dry partial melting of the Tasiuyak Paragneiss, Northern Labrador. *Journal of Metamorphic Geology, in press,* DOI:10.1111/jmg.12086.

Möller, A., O'Brien, P. J., Kennedy, A. and Kröner, A., 2002. Polyphase zircon in ultrahigh-temperature granulites (Rogaland, SW Norway): constraints for Pb diffusion in zircon. *Journal of Metamorphic Geology,* **20**: 727–740.

Montel, J.-M., Foret, S., Veschambre, M., Nicollet, C. and Provost, A., 1996. Electron microprobe dating of monazite. *Chemical Geology,* **131**: 37–53.

Moukhsil, A., Solgadi, F., Clark, T., Indares, A. and Blouin, S., 2013. Geology of the Daniel-Johnson Dam (Manic 5) area, Côte-Nord region (NTS 22K14, 22K15, 22K16, 22N03 and 22N02). Ministère des Ressources naturelles et de la Faune, RG-2013.

Nasdala, L., Hanchar, J. M., Kronz, A., and Whitehouse, M. J., 2005. Long-term stability of alpha particle damage in natural zircon. *Chemical Geology*, **220**: 83−103.

Parrish, R. R., 1990. U−Pb dating of monazite and its application to geological problems. *Canadian Journal of Earth Sciences,* **27**: 1431–1450.

Parrish, R. R. and Noble, S. R., 2003. Zircon U-Th-Pb Geochronology by Isotope Dilution –Thermal Ionization Mass Spectrometry (ID-TIMS). *In:* Hanchar, J. M., Hoskin, P. W. O. *(Eds.).* Zircon. *Reviews in Mineralogy and Geochemistry,* **53**: 183–213.

Paton, C., Woodhead, J., Hellstrom, J., Hergt, J., Greig, A. and Maas, R., 2010. Improved laser ablation U–Pb zircon geochronology through robust downhole fractionation correction. *Geochemistry Geophysics Geosystems*, **11**: 1–36.

Powell, R. and Holland, T. J. B., 1988. An internally consistent thermodynamic dataset with uncertainties and correlations: application, methods worked examples and a computer program. *Journal of Metamorphic Geology*, **6**: 173–204.

Powell, R., Holland, T. J. B. and Worley, B., 1998. Calculating phase diagrams involving solid solutions via non-linear equations, with examples using THERMOCALC. *Journal of Metamorphic Geology*, **16**: 577–588.

Pyle, J. M. and Spear, F. S., 2003. Four generations of accessory-phase growth in low-pressure migmatites from SW New Hampshire. *American Mineralogist*, **88**: 338–351.

Rivers, T., 1997. Lithotectonic elements of the Grenville Province: review and tectonic implications. *Precambrian Research*, **86**: 117–154.

Rivers, T., 2008. Assembly and preservation of lower, mid, and upper orogenic crust in the Grenville Province-Implications for the evolution of large hot long-duration orogens. *Precambrian Research,* **167**: 237–259.

Rivers, T., 2012. Upper-crustal orogenic lid and mid-crustal core complexes: signature of a collapsed orogenic plateau in the hinterland of the Grenville Province. *Canadian Journal of Earth Sciences,* **49**: 1–42.

Rivers, T., Culshaw, N., Hynes, A., Indares, A., Jamieson, R. and Martignole, J., 2012. The Grenville Orogen - A post-LITHOPROBE perspective. Chapter 3 *In* Tectonic Styles in Canada: The LITHOPROBE Perspective. Edited by J.A. Percival, F.A. Cook, and R.M. Clowes. Geological Association of Canada, Special Paper 49, pp. 97–236.

Rosenberg, C. L. and Handy, M. R., 2005. Experimental deformation of partially melted granite revisited: implications for the continental crust. *Journal of metamorphic Geology*, **23**: 19–28.

Simonetti, A., Heaman, L. M., Chacko, T. and Banerjee, N. R., 2006. *In situ* petrographic thin-section U–Pb dating of zircon, monazite and titanite using laser ablation-MC-ICP-MS. *International Journal of Mass Spectrometry*, **253**: 87–97.

Spear, F. S. and Pyle, J. M., 2002. Apatite, monazite, and xenotine in metamorphic rocks. *In:* Kohn, M. J., Rakovan, J., Hughes, J. M. *(Eds.).* Phosphates: geochemical, geobiological, and materials importance. *Reviews in Mineralogy and Geochemistry, Mineralogical Society of America*, **48**: 293–336.

Spear, F. S., Kohn, M. J. and Cheney, J. T., 1999. P–T paths from anatectic pelites. *Contributions to Mineralogy and Petrology*, **134**: 17–32.

Tichomirowa, M., 2003. Recrystallisation of zircons during granulite-facies metamorphism (Germany, Central Erzgebirge). *Journal of the Czech Geological Society*, **48**: 124.

Tohver, E., Teixeira, W., van der Pluijm, B., Geraldes, M. C., Bettencourt, J. S. and Rizzotto, G ., 2006. Restored transect across the exhumed Grenville orogen of Laurentia and Amazonia, with implications for crustal architecture. *Geology*, **34**: 669–672.

van Gool, J. A. M., Rivers, T. and Calon, T., 2008. Grenville Front zone, Gagnon terrane, south-western Labrador: configuration of a midcrustal foreland fold-thrust belt. *Tectonics*, **27**: 1–35.

Vavra, G., Schmidt, R. and Gebauer, D., 1999. Internal morphology, habit and U–Th–Pb microanalysis of amphibolite to granulite-facies zircons: geochronology of the Ivrea zone (southern Alps). *Contributions to Mineralogy and Petrology*, **134**: 380–404.

Vavra, G., Gebauer, D., Schmid, R. and Compston, W., 1996. Multiple zircon growth and recrystallization during polyphase Late Carboniferous to Triassic metamorphism

in granulites of the Ivrea Zone Southern Alps: an ion microprobe SHRIMP study. *Contributions to Mineralogy and Petrology*, **122**: 337–358.

WaveMetrics, Inc. IGOR Pro 6.3 manual, Lake Oswego, OR, www.wavemetrics.com.

White, R. W. and Powell, R., 2002. Melt loss and the preservation of granulite-facies mineral assemblages. *Journal of Metamorphic Geology*, **20**: 621–632.

Williams, M. L., Jercinovic, M. J. and Hetherington, C. J., 2007. Microprobe monazite geochronology: Understanding geologic processes by integrating composition and chronology. *Annual Review Earth Planetary Sciences*, **35**: 137–175.

Williams, M. L., Jercinovic, M. J. and Terry, M. P., 1999. Age mapping and dating of monazite on the electron microprobe: Deconvoluting multistage tectonic histories. *Geology*, **27**: 1023–1026.
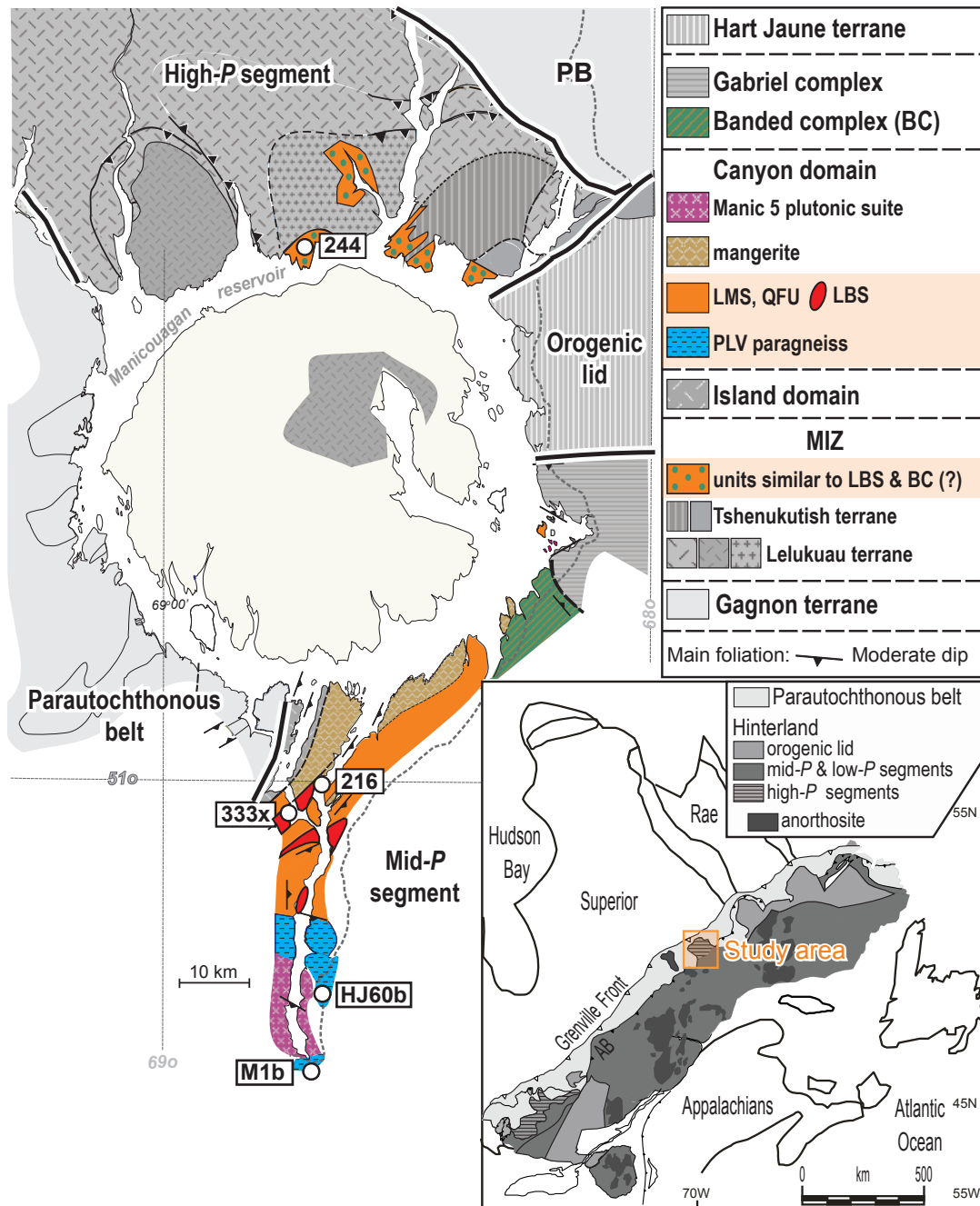
Figure 1.1: Simplified geological map of the Manicouagan area with location of the five samples of interest and inset map showing the general framework and location of the Grenville Province (updated from Dunning and Indares, 2010). AB – Allochton Boundary; LMS – layered mafic suite; QFU – layered quartzofeldspathic unit; LBS – layered bimodal sequence, including zones of hydrothermal alteration; PLV – Complexe de la Plus Value; MIZ – Manicouagan Imbricate Zone.

27

CHAPTER 2

2. CONTRASTING TYPES OF GRENVILLIAN GRANULITE-FACIES ALUMINOUS GNEISSES: INSIGHTS ON PROTOLITHS AND METAMORPHIC EVENTS FROM ZIRCON MORPHOLOGIES AND AGES

ABSTRACT

Zircon morphology, internal texture, U–Pb age distributions and Th/U ratios are used to characterize aluminous gneisses from two contrasting granulite-facies supracrustal sequences: a package of paragneisses and a dominantly bimodal felsic-mafic volcanic sequence, mostly exposed in the Canyon domain (Manicouagan area, central Grenville Province).

The aluminous paragneisses yielded zircon with fragmented igneous cores, overgrown by metamorphic rims. These cores show a spread in ages between 1500 Ma and 2700 Ma, consistent with a supply of detritus from the adjacent terranes of Laurentia. In contrast, a felsic gneiss with aluminous nodules inferred to represent a hydrothermally-altered felsic volcanic rock of the bimodal sequence yielded well-preserved igneous zircon dated at 1238 ± 13 Ma, an age that integrated with previously published data links this volcanic sequence to an episode of crustal extension in the central Grenville Province.

Metamorphic zircon grains and rims from the paragneisses gave two groups of pre-Grenvillian ages that demonstrate the effect of major magmatic events on the country rocks in the Canyon domain: (a) 1391–1408 Ma, coeval with the emplacement of an older layered mafic to intermediate volcanic suite, and (b) 1217–1260 Ma, coeval with the development of the 1238 Ma bimodal felsic-mafic volcanic sequence. In addition, metamorphic zircon rims from all the investigated aluminous gneisses records the high-grade Grenvillian metamorphism (*ca.* 1080–1040 Ma).

2.1.   INTRODUCTION

U–Pb dating of zircon is a key tool for unraveling complex successions of magmatic and metamorphic events in orogenic belts. In deeply exhumed orogens original rock units are largely transformed into gneisses as a result of high-grade metamorphism, anatexis and deformation, making interpretation of their original protolith and U–Pb ages challenging (Friend and Kinny, 1995; Roberts and Finger, 1997; Williams, 2001; Rubatto, 2002; Whitehouse and Kamber, 2005; Aleinikoff *et al.*, 2006; Whitehouse and Kemp, 2010). Even so, studies of internal morphologies combined with U–Pb analysis of zircon from specific rock associations provide insight into both the nature of protoliths and the sequence of subsequent geological events (Hanchar and Miller, 1993; Hanchar and Rudnick, 1995; Vavra *et al.*, 1996, 1999; Möller *et al.*, 2002; Aleinikoff *et al.*, 2006; Corfu, 2007). Given the complex zonation present in zircon with a multi-stage history of corrosion, recrystallization and growth typically present in high-grade rocks, *in situ* zircon dating by secondary ionization mass spectrometry (SIMS) or laser ablation–inductively coupled plasma mass spectrometry (LA–ICPMS), in conjunction with cathodoluminescence (CL) or back-scattered electron (BSE) imaging is often the most appropriate way to resolve the nature and age of diverse geological events (Black *et al.*, 1986; Hanchar and Miller, 1993; Corfu *et al.*, 2003; Košler and Sylvester, 2003).

An additional difficulty in identifying protoliths in high-grade metamorphic terranes is that rocks of different origins but similar bulk compositions may end up having similar metamorphic mineral assemblages. For instance, aluminous gneisses from upper amphibolite to granulite-facies portions of the hinterland of the Grenville Province are

traditionally inferred to have originated in sedimentary environments as mudstone and graywacke. In several cases this is supported by the lithologic associations of the host sequence. However, aluminous gneisses may also be derived from hydrothermally altered felsic volcanic rocks (Bonnet and Corriveau, 2007), or sedimentary layers in volcanogenic settings. Distinguishing between metasedimentary and dominantly volcanogenic supracrustal sequences is important for understanding the tectonic evolution of the Laurentian margin upon which the Grenville orogen was built. As shown by Bonnet *et al*. (2005) in the southeast of the Grenville Province, metamorphosed volcanic belts can be identified by detailed field, petrological and geochemical studies; however such environments are generally underexplored in the hinterland of the province.

Further insights on the origin of aluminous gneisses in high-grade terranes can be potentially provided by the morphologies, compositions and distribution of ages of pre-metamorphic zircon. In the simplest scenario, magmatic zircon in those derived from felsic volcanic rocks is expected to have a pristine igneous morphology displaying oscillatory zoning, variably overgrown by metamorphic rims (Corfu *et al*., 2003), and yield a clustered distribution of U–Pb ages around the crystallization age of the protolith. Alternatively, in aluminous paragneisses, zircon is expected to be fragmental or with resorbed cores truncated by metamorphic rims (Corfu *et al*., 2003) and to likely yield a range of ages corresponding to the ages of the eroded material that fed the sedimentary basin. This distinction may not be that straightforward; for instance felsic volcanic rocks commonly contain inherited as well as magmatic zircon (Dunning *et al*., 1990, 2002) and in some sedimentary basins (*e.g.*, restricted) a unimodal distribution of zircon may be

31

dominant, depending on the tectonic setting (Cawood *et al*., 2012). Therefore zircon data can be best interpreted in the context of specific lithologic associations.

In the hinterland of the central Grenville Province, a complex assemblage of layered supracrustal rock units including a (meta) pelite–graywake–quartzite–marble sequence and dominantly bimodal felsic-mafic volcanic sequences is exposed in the Manicouagan area, with aluminous gneisses interlayered in both. Previous work in this area has revealed magmatic events, spanning ages from 1.7 to 1.0 Ga, and granulite-facies Grenvillian metamorphism between 1.08 and 1.0 Ga (Indares *et al*., 2000; Indares and Dunning, 2004; Dunning and Indares, 2010). Therefore, the (1.7–1.2 Ga) rock units in the Manicouagan area collectively provide a window on both the protracted evolution of the Laurentian margin upon which the Grenville orogen was built, and the subsequent Grenvillian orogeny (*ca.* 1.1–0.98 Ga). However, the ages of key supracrustal sequences, and how such sequences fit into the puzzle remain unclear.

In this contribution, we document the zircon U–Pb age distributions, morphologies, and Th/U from four aluminous gneisses belonging to two contrasting lithological associations of the Manicouagan area (hinterland of the central Grenville Province), mostly exposed in the Canyon domain: a sequence of paragneiss and a layered bimodal sequence which is inferred to represent remnants of a volcanic belt. The objectives are to: (a) examine the zircon record of aluminous gneisses formed in different environments; (b) provide insights on the age and nature of protoliths, and on subsequent thermal events; and (c) explore the tectonic implications of the results for the evolution of the hinterland of the central Grenville Province.

2.2. GEOLOGICAL SETTING

2.2.1. General setting of the Canyon domain

The Grenville Province (Fig. 2.1) contains lithotectonic packages that were formed at the southeast margin of Laurentia prior to *ca.* 1.2 Ga and were subsequently involved in continental collision at *ca.* 1.1–1.0 Ga, during the Grenvillian orogeny (Rivers, 2008). In the central Grenville Province, the structurally lowest units exposed along the shores of the Manicouagan reservoir belong to the Gagnon terrane, which is part of the Parautochthonous belt (Rivers *et al*., 1989). These units range in age from Archean to Paleoproterozoic and were deformed and metamorphosed during late stages of the Grenvillian orogeny (*ca.* 1.0 Ga; Jordan *et al*., 2006; van Gool *et al*., 2008). In contrast, the structurally higher hinterland mainly consists of Mesoproterozoic lithotectonic units that formed between 1.7 Ga and 1.2 Ga and were metamorphosed during the culmination of the Grenvillian orogeny (*ca.* 1.08–1.04 Ga; Indares *et al*., 2000; Dunning and Indares, 2010).

The Canyon domain, located in the hinterland, is exposed on the southern shore of the Manicouagan reservoir, structurally above plutonic units of Labradorian age (Fig. 2.1; *ca.* 1.69–1.65 Ga, Lelukuau terrane and Island domain; Indares *et al*., 2000; Dunning and Indares, 2010). The predominant constituent of the Canyon domain is an assortment of mafic to quartzofeldspathic layered rock units (Dunning and Indares, 2010). Based on lithologic associations, these authors were the first to suggest an extrusive origin for some components. They also obtained a crystallization age of 1410 ± 16 Ma (U–Pb zircon; ID–

TIMS) for a layered mafic to intermediate suite, which they tentatively correlated with the Montauban arc, exposed ~450 km to the SSW (Nadeau and van Breemen, 1994).

In addition, a distinctive lithologic association dominated by heterogeneous mafic sheets and bleached felsic layers, but also comprising garnetites, felsic gneisses with garnet and sillimanite-rich nodules, and calcsilicate rocks, is discontinuously exposed in the central and northern part of the Canyon domain, and is referred to herein as the layered bimodal sequence (LBS). In this type of association, garnetites and felsic nodular gneisses are typically thought to be derived from hydrothermally altered volcanic rocks (Bonnet and Corriveau, 2007) and the LBS is inferred to represent a metamorphosed volcanic belt. No direct age data are available for the LBS. However, along strike, to the NE of the Canyon domain, another bimodal felsic-mafic sequence, identified as the Banded complex (Fig. 2.1), was dated at 1202 +40/−25 Ma 1238 +16/−13 Ma (Indares and Dunning, 2004) and inferred to represent metavolcanic rocks deposited during a period of crustal extension (Dunning and Indares, 2010). Therefore it is possible that part of the LBS is correlative in age with the Banded complex.

Conversely, a metasedimentary sequence of metagraywacke, metapelite, quartzite and minor calcsilicate was recently identified in the southern part of the Canyon domain by Moukhsil *et al.* (2013). Based on lithologic associations and continuity, this sequence is correlated with the Complexe de la Plus Value (PLV), defined farther east, and inferred to have been deposited at *ca.* 1.5 Ga (Moukhsil *et al.*, 2012). The extension of the PLV into the southern Canyon domain is referred to as PLV-CD.

Units of the Canyon domain were metamorphosed under mid-pressure granulite-facies conditions during the Grenvillian orogeny. Monazite from several aluminous gneisses in this region yielded ages attributed to the metamorphism between *ca.* 1000–1030 Ma and *ca.* 1080 Ma (U–Pb ID–TIMS; Dunning and Indares, 2010). In addition, units similar to the LBS are also exposed along the north shore of the reservoir and were metamorphosed under high-*P* granulite-facies conditions at *ca.* 1040 Ma (Indares *et al.,* 2000; Indares and Dunning, 2001).

Aluminous paragneisses from the PLV-CD and felsic gneiss with garnet-sillimanite nodules and aluminous layers from the LBS were the subject of a detailed petrographic and zircon study. In this contribution we focus on the zircon morphologies and ages as outlined earlier, whereas the detailed petrography and metamorphic interpretation of these rocks will be presented in a separate contribution.

2.2.2.   Sample location, petrography, and previous monazite geochronology

The four aluminous rocks studied were collected from the PLV-CD (samples HJ60b and M1b) and from the LBS (sample 333x from the LBS in the Canyon domain, and 244 in the extension of the LBS north of the Manicouagan reservoir; Fig. 2.1). These samples consist of quartz–K-feldspar–plagioclase–garnet–Al-silicate–biotite and leucosome. However, samples collected south of the reservoir (333x, HJ60b and M1b) have sillimanite as the Al-silicate phase, while sample 244 is kyanite-bearing.

The samples from the PLV-CD were collected in outcrops dominated by variably migmatized garnet–sillimanite–biotite-bearing paragneiss (Fig. 2.2a and b). In addition,

the outcrop in location M1 contains transposed veins of felsic pegmatite (Fig. 2.2b). Sample 333x from the LBS comes from a ~ 2 m thick felsic gneiss with aluminous nodules (Fig. 2.2c) interlayered with fine-grained felsic rocks and heterogeneous mafic sheets. This rock sample consists of sillimanite-bearing garnet-rich nodules and elongated quartz lenses in a finer grained K-feldspar-dominated matrix. Finally sample 244 was collected in a several cm-thick aluminous sheet interlayered with massive felsic rocks (Fig. 2.2d).

Monazite from the same samples has been previously used to constrain the age of Grenvillian metamorphism in this area in the range of *ca.* 1080–1060 Ma for the PLV-CD samples in the south, and *ca.* 1036–1044 Ma for the LBS samples, farther north, with two monazite grains at 1001 Ma in sample 333x. In addition, an inherited monazite age at 1219 +60/−65 Ma was found in sample 244 (Dunning and Indares, 2010).

2.3. ANALYTICAL METHOD AND PROCEDURE

Zircon grains were extracted using conventional heavy mineral separation methods. Rock samples were washed and crushed. Zircon was concentrated using a Wilfley table, heavy liquids and a Frantz magnetic separator. Zircon fractions were collected at increasing field strength up to 1.7A. Four 1 inch mounts were made, with one size of zircon grains per mount to facilitate polishing to the approximate grain centers.

The morphology and internal texture of zircon were examined prior to U–Pb age determination. About 100 grains per sample were imaged, and about half of those were analyzed. The overall morphology of zircon was characterized by transmitted light (TL)

using a standard petrographic microscope. The internal texture was revealed using a (FEI Quanta 400) Scanning Electron Microscope (SEM) and a cathodoluminescence (CL) detector at Memorial University. These images were then used to guide spot analyses in selected zones of individual grains by LA–ICPMS to determine U–Pb ages. The Energy Dispersive X-ray (EDX) system installed on the SEM was used to identify the mineralogy of inclusions in zircon. Most inclusions were characterized by collecting elemental spectra that were then compared to a mineral database. In addition, elemental false-color maps were acquired for the most complex inclusions.

2.3.1. Instrumentation and operating conditions

U–Pb analyses on single zircon crystals were done using the laser ablation–inductively coupled plasma mass spectrometry (LA–ICPMS) technique at Memorial University of Newfoundland employing a Finnigan Element XR2 single collector ICPMS and a GEOLAS 193nm ArF Excimer laser. Instrumentation and analytical parameters are summarized in Table 2.1. The diameter of the laser spot was fixed at 30µm for all analyses. Three zircon standards 91500 (ID–TIMS age of 1065 Ma; Wiedenbeck *et al*., 1995), Plešovice (ID–TIMS age of 337.1 ± 0.3 Ma; Sláma *et al*., 2008) and 02123 (ID–TIMS age of 295 ± 1 Ma; Ketchum *et al.,* 2001) were used for both calibration and quality control (*i.e.,* secondary standards). Tuning parameters of the instrument were kept constant during a run but in some cases they were modified between runs depending on the U content of samples. The relative U content of zircon zones was visually estimated based on the CL intensity. Two sets of laser parameters were used, with a constant laser

fluence of 3 J/cm2 but varying the repetition rate between a lower setting at 4–5 Hz to analyze high-U zones (CL dark) and a higher setting at 8 Hz to analyze low-U zones (CL bright). This was done in order to achieve adequate Pb count rates, while keeping ^{238}U in counting mode (thereby avoiding cross-calibration between counting and analog mode). When using the 4–5 Hz setting, the zircon standard 91500 had low ^{207}Pb counts, and thus the Plešovice zircon was the reference material for the run. When using a higher setting, Plešovice zircon was a secondary standard and 91500 was the reference material. Zircon 02123 was analyzed as a secondary standard using both conditions.

2.3.2. Data collection, processing, and graphic representation

Analyses were carried out over 4 days, divided into 12 runs of analyses; 9 runs were done using the 8 Hz setting and the zircon standard 91500 as a calibration material, while 3 runs used the 4–5 Hz setting and the Plešovice zircon as a calibration material (Table 2.1). A single analysis was ~ 2 minutes long, beginning with 35 s of gas blank followed by a 60 s ablation period (Table 2.1). The remaining 25 s facilitated complete sample wash-out. Data were processed using the freeware Iolite (Paton *et al.,* 2010) running in IgorPro (WaveMetrics Inc., www.wavemetrics.com). The down-hole fractionation was corrected using the 'smoothed cubic spline' model while the instrumental drift was corrected using the 'automatic spline'. Analyses within each run were organized as follows, using a standard bracketing technique: each run began with 3–4 analyses of the reference material and thereafter it was analyzed once every 3 analyses of unknowns or secondary standards. Concentrations in U and Th were determined based on the 91500

zircon standard using concentrations of 80 ppm and 30 ppm, respectively (Wiedenbeck *et al.,* 2004).

Among the 266 analyses of zircon standard 91500 collected during the 9 runs, 19 analyses (~ 7 %) with outlying U–Pb ratios (≥ 2 %) were discarded. When the zircon standard Plešovice was used for the calibration of the other 3 runs, 3 analyses from a total of 73 (~ 4 %) were discarded using the same criteria. In contrast, for the purpose of 'transparency', rather than showing only the perfectly concordant data, all analyses of unknowns are presented with different types of ellipses on each concordia diagrams for all four samples. Concordant analyses include analyses with 0−5 % discordance (most of the analyses are ≤ 2 % discordant). The per cent discordance was calculated as % disc = $(1–(Age\ ^{206}Pb/^{238}U\ /\ Age\ ^{206}Pb/^{207}Pb)) \times 100$. Discordant analyses with ≥ 6 % discordance may in some cases still overlap the concordia curve, at the 2σ level of uncertainties.

The discordant data were not corrected for common Pb. Due to the significant proportion of discordant data, and the fact that the major cause for this discordance appears to be the physical mixing of different age domains during sampling, probability density plots, although common in provenance studies, were not used here. Mixing could not be completely avoided as CL images (2D) only show zoning at the surface of the grain, but as the laser pit deepens during an analysis, it could drill through the targeted zone and into a different one and this may not always be detectable. During the data reduction process, analyses were time integrated, and whenever an analysis showed significant changes in age with increasing pit depth, only the first segment was selected for further age calculation. Nevertheless, once carefully examined and sorted (*e.g.,* core

vs. rim) these discordant data appeared to support the interpretation of the concordant analyses.

2.3.3. Precision and accuracy from analyses of the reference material and the secondary standards

The precision and accuracy of the method was assessed using the two zircon standards, 02123 and Plešovice, treated as unknowns (Fig. 2.3). Zircon 02123 was analyzed 42 times over all 12 runs while zircon Plešovice was analyzed 33 times over 9 runs. The weighted average $^{206}Pb/^{238}U$ age for 40 analyses of zircon 02123 is 298.0 Ma ± 1.4 Ma (MSWD=4.2) compared to 295 ± 1 Ma (ID–TIMS data; Ketchum *et al.,* 2001). Thirty-three analyses of zircon Plešovice yielded a weighted average $^{206}Pb/^{238}U$ age of 342.3 Ma ± 1.6 Ma (MSWD=4.2) compared to 337.1 ± 0.3 Ma (ID–TIMS data; Sláma *et al.,* 2008). These 2 average ages show a 1–1.5 % offset compared to the ID–TIMS ages, and relatively high MSWD values. However such values are commonly observed in large sets of LA−ICPMS data from secondary standards, and can be attributed to the analyses being done on several pieces of zircon, over several runs on different days (*e.g.,* Gerdes and Zeh, 2006; Gehrels *et al*., 2008; Frei and Gerdes, 2009).

In this paper, reported ages are $^{207}Pb/^{206}Pb$ ages unless stated otherwise. These ages are calculated from the measured $^{207}Pb/^{206}Pb$ using ISOPLOT (Ludwig, 2003). The uncertainty on single data points is reported at 2σ. When a weighted average age is calculated, it is reported at the 95 % confidence level.

2.4. RESULTS

Figures 2.4 to 2.7 show the different characteristics of the zircon population for each sample: the general morphology as seen in transmitted light (TL) under the microscope (Figs. 2.4a, 2.5a, 2.6a, 2.7a), internal textures imaged by cathodoluminescence (CL) (Figs. 2.4b, 2.5b, 2.6b, 2.7b) with white dots representing the location of the U–Pb laser spots, and finally, the concordia diagrams with the U–Pb data (Figs. 2.4c, 2.5c, 2.6c, 2.7c). The Th/U ratio is plotted against the $^{207}Pb/^{206}Pb$ age (Fig. 2.8) to highlight possible differences between zircon populations (*cf.,* Gehrels *et al.,* 2009) and Fig. 2.9 presents representative mineral inclusions found in zircon from sample 333x.

2.4.1. Samples HJ60b and M1b from the PLV-CD

2.4.1.1. Zircon morphology and internal textures

Zircon in samples HJ60b (Fig. 2.4) and M1b (Fig. 2.5) has similar morphologies and internal textures, and it is mainly colorless, with rare to no inclusions. Grains are generally sub-rounded to round with a length to width ratio of about 1–1.5. They range in size from ~ 100 μm to ~ 200 μm and commonly show distinct cores of various sizes (Figs. 2.4a, 2.5a). In some cases (mostly in HJ60b) zircon appears slightly darkened by the presence of a dense web of fine cracks which are dominant in the core and radiate towards the outside of the rim. Finally, aside from rare grains with well terminated

prisms, zircon shows intense rounding with resorbed contours and a few composite grains where one zircon is welded to another (Figs. 2.4a, 2.5a).

In terms of internal textures identified in CL, the dominant type of zircon, referred to as Type I, mainly consists of a bright core, a dark mantle, and a lighter outer rim (Figs. 2.4b, 2.5b). Commonly fragment-like, with acicular shape in the most elongate grains, cores display regular oscillatory and/or concentric zoning, whereas the mantles and rims are either homogeneous or zoned. In addition, a few cores of M1b zircon, with bright and zoned rims, seem to contain a nucleus of different shape (grains I-4, 5, 18, 19). In some instances, convoluted features affect the core and its regular oscillatory zoning whereas mantle and rim seem undisturbed. Finally, in some cases the CL brightness is reversed (*i.e.,* dark cores, bright rims). The second type of zircon, Type II, consists of well-rounded grains, relatively dark in CL, with faint sector zoning, and a discontinuous bright outline. In sample HJ60b, some of these grains have a small rounded core (grain II-1; Fig. 2.4b) and in sample M1b, they have a dark rim with fine oscillatory zoning (grain II-29; Fig. 2.5b).

2.4.1.2. *Zircon U–Pb ages and Th/U ratios*

In each sample HJ60b and M1b, 56 zircon grains (mostly of Type I) have been analyzed with 85 and 82 analyses respectively (Tables 2.2–2.3; Figs. 2.4c, 2.5c). About 30–40% of the data are concordant (filled ellipses) and show a similar bimodal distribution with a larger set mainly between 1.8 and 1.5 Ga (with one or two data points older than 2 Ga), and a smaller set between 1.4 and 1.0 Ga. As highlighted in the inset,

which excludes Archean ages (insets in Figs. 2.4c, 2.5c), the older dataset mainly corresponds to core analyses of Type I zircons while most rims and Type II grains yielded ages younger than 1.4 Ga. This pattern is also observed in the discordant data (empty ellipses on concordia diagram; Figs. 2.4c, 2.5c). About 50 analyses are discordant for each sample, and spread along a line between *ca.* 1.9 and 1.0 Ga (1.2 Ga for zircon in M1b), showing again older ages for the cores and younger ages for the rims (insets in Figs. 2.4c, 2.5c). Such a pattern of discordance is mainly attributed to the physical mixing between core and rim areas of the zircon during analyses, as this could not be completely avoided. Pb loss could also account for part of the discordance within the oldest core data but is considered unlikely for the youngest data from rims, as there is little time between when the zircon crystallized and when it experienced metamorphism. Contamination by common Pb is considered the main cause for discordance of a few data points shifted to the upper right far away from the concordia curve. The final potential cause for discordant analyses is elemental fractionation occurring during ablation, but it is only when the data points show reverse discordance (above the concordia curve) that this can be distinguished from other possible causes.

In zircon from HJ60b, two of the five oldest data points are concordant at 2555 ± 39 Ma and 2746 ± 16 Ma (from bright cores of Type I zircon; Fig. 2.4b, grains 57 and 9). The remaining cores yielded ages in the range of 1.5–1.95 Ga, with the majority between 1.6 and 1.85 Ga. An exception is the core of grain 13 which yielded an age of 1217 ± 54 Ma. Concordant ages from rims range between 1022 and 1344 Ma and a weighted average age of 1044 ± 15 Ma (MSWD=0.026, prob. 0.97) was calculated for the three youngest data points. Grain 1 from Type I zircon gave the best example of the age

difference between core and rim (bright zoned fragmental core: 1881 ± 16 Ma; darker homogeneous rim: 1180 ± 30 Ma). This rim age overlaps within error with the 1217 ± 54 Ma core age of grain 13a.

In M1b, four data points are Archean, the concordant one at 2470 ± 19 Ma was collected from the bright fragmental core of Type I grain 14 (Fig. 2.5b and c). The rim of this grain was dated at 1230 ± 21 Ma, which agrees within error with the age of 1260 ± 43 Ma of the metamorphic rim of grain 6. Several other Type I grains gave concordant core and rim data supporting the bimodal distribution of old cores vs. young rims. We note that, in contrast to sample HJ60b, most rim ages in M1b are pre-Grenvillian, except of that of grain 27 (1062 Ma). In addition, two zircon cores in M1b yielded ages younger than 1500 Ma: (a) a rounded Type II grain with dark gray sector zoning (grain 9: 1391 ± 33 Ma), and (b) a Type I zircon fragment (grain 8: 1257 ± 43 Ma).

The Th/U ratios for zircon from the two samples reveal the same bimodal distribution and are significantly lower in the young rims than in the older cores (Table 2.3; Fig. 2.8a and b). Th/U ratios of the six concordant rim analyses of HJ60b zircon are in the range of 0.01–0.04 while those of 23 of 26 core analyses are between 0.25 and 0.97. Similarly, in M1b, eight of the ten rim data have a Th/U ratio ≤ 0.08 while among the 25 core data, 21 have Th/U ratios in the range of ≥ 0.31–1.32.

2.4.2. Samples 333x and 244 from the LBS

2.4.2.1. Zircon morphology and internal textures

In 333x, zircon is yellowish-brown, consists of elongate prisms (mostly 180–250 µm long, with some up to ~ 300 µm) with short pyramidal terminations and multiple polymineralic inclusions (Fig. 2.6a). The length to width ratio is ~ 2–2.5 for most prisms and reaches up to ~ 4.5 in a few acicular grains. Zircon cores are commonly large and very distinct (Fig. 2.6a). In several grains, these cores are fractured, perpendicular to the elongation c-axis or randomly, whereas the rim is not. A few grains show smoothed outlines consistent with resorption (Fig. 2.6a).

In CL most grains show a large bright core with fine oscillatory zoning surrounded by a darker rim (Fig. 2.6b). Some cores overgrow a pre-existing nucleus of different brightness and/or texture (grains 2, 20). The rims range from barely visible to a 10–20 µm thick isomorphic gray layer (grain 18) and either replace the core or are separated from it by a discontinuous black mantle (grain 19). In a few grains the bright core has a light gray convolute or skeletal structure, in some cases overgrown by an oscillatory structure of the same gray luminescence (grain 23). These cores are also enveloped by a thin black mantle and a thin gray isomorphic rim.

Mineral inclusions are exclusively present in the cores of zircon and range in shape and size from beads of a few microns in diameter to 'football-like', over 50 µm long (Fig. 2.9). The smallest inclusions are commonly monomineralic while the large ones contain several phases. The most common phases are quartz, albite, K-feldspar and monazite. In

addition biotite (locally chloritized), rutile, clay, muscovite, allanite, magnetite, ilmenite, and pyrrhotite are locally present. When quartz, albitic plagioclase and K-feldspar are together, they are separated by distinct straight boundaries (Fig. 2.9a-b).

In sample 244, zircon is colorless with rare small monomineralic inclusions and a strongly bimodal morphology. Two thirds of the grains are elongate, 150–200µm long prisms, with a length to width ratio of 2 –2.5 and rounded to well terminated outlines. In contrast, one third of the grains are rounded, ~ 100 µm in diameter (Fig. 2.7a). When distinct, cores are relatively small and in rare cases, zircon grains have irregular resorbed silhouettes (Fig. 2.7a).

Two main types of zircon have been identified in terms of internal structure (Fig. 2.7b). Type I zircon consists of elongate and stubby grains commonly having a small fragment-like bright to light gray core. This core either displays oscillatory zoning (grains I-5, 6) or is homogeneous in color with a round or convolute structure (grains I-6, 8, 19). A CL-dark mantle of various widths surrounds the core and is rimmed by one or two lighter gray layers. These overgrowths also are of various widths and homogeneous (grains I-2, 3, 5, 6, 8, 9, 19) or display oscillatory zoning (grain I-6) or sector zoning (grains I-12, 14, 21). Type II zircon grains are nearly spherical grains, and show three varieties of internal textures: a pervasive dark sector zoning through most of the grain and a fine bright outermost rim (grains II-17, 33); a large bright core faintly zoned, in a thin dark mantle, rimmed by one or two thin dull layers (grains II-18, 31); or a small fragment-like and concentrically zoned bright core enveloped in a thin, discontinuous dark layer, and a thick dull rim with sector zoning (grains II-1, 9). Examples of other

zircon grains that cannot be classified into Type I or Type II but display distinctive morphologies and internal textures were grouped together (grains 2, 4, 7, 10, 14).

2.4.2.2. Zircon U–Pb ages and Th/U ratios

51 zircon grains were analyzed from 333x (72 analyses; Table 2.4; Fig. 2.6c) and 53 grains from 244 (84 analyses; Table 2.5; Fig. 2.7c). In contrast with the large spread of ages observed for the two PLV-CD samples, the distribution of U–Pb data in the LBS samples is relatively 'clustered'. Indeed, no Archean ages are found, the oldest U–Pb ages are *ca.* 1.5–1.7 Ga, and while most concordant and discordant data for 333x are between *ca.* 1.1 and 1.3 Ga, all concordant data in 244 (except one) cluster between *ca.* 1.0 and 1.1 Ga. In this sample, the proportion of concordant *vs.* discordant analyses is clear in the data table but not on the corresponding concordia diagram as the filled ellipses almost all overlap. Despite this overlap, the link between age and morphological domain in the zircon grain remains, and is visible in the inset of Fig. 2.7c. In contrast, in the case of sample 333x, all but 23 analyses are discordant and the distribution of U–Pb data did not correlate with the targeted area in the grains; $^{207}Pb/^{206}Pb$ ages from cores and rims all overlap on concordia (Fig. 2.6c). For these two LBS samples, the major cause for discordance is the presence of various amounts of common Pb, especially in 333x. As other zircon grains from the PLV-CD samples analyzed in the same mounts did not show such discordance it is assumed that this common Pb did not come from surface contamination. Ancient Pb loss, elemental fractionation and mixing of different age domains are also considered as potential causes for discordance. Aside from one clear

reversely discordant data point at 1.2 Ga (Fig. 2.7c) that indicates elemental fractionation, it is nearly impossible to distinguish between each phenomenon.

Zircon data in sample 333x, including all concordant and discordant analyses of rims and cores, overlap and show a spread in ages from *ca.* 1.0 to 1.5 Ga with a tighter cluster between 1.2 and 1.3 Ga. The most meaningful data were provided by zircon cores undisturbed by convolute features. Indeed, grain 2 (Fig. 2.6b) was analyzed in three spots with all three ellipses concordant and overlapping; the bright core yielded an age of 1248 ± 45 Ma, and the darker area around it, still showing oscillatory zoning, yielded ages of 1256 ± 40 Ma and 1265 ± 54 Ma. Another well preserved grain, zircon 5 (Fig. 2.6b) yielded an age of 1297 ± 95 Ma (the large uncertainty is here due to the analysis being shorter than 15 s) for the inner core and 1265 ± 50 Ma for the outer core. Based on the location of the spot and the quality of the analysis, 16 data points from the set of 23 most concordant ones in the range of 1.3–1.2 Ga, were selected to calculate a weighted average $^{207}Pb/^{206}Pb$ age of 1238 ± 13 Ma (MSWD=1.4) which represents the dominant age of zircon growth in this sample. An alternative possibility is that the oldest data points near 1300 Ma represent the age of the zircon and, points at younger ages would reflect Pb loss from 1300 Ma. However, all $^{207}Pb/^{206}Pb$ ages overlap within the 2σ error with the calculated average of 1238 ± 13 Ma, thus this age is preferred. The distribution of points would then be partly due to elemental fractionation of Pb from U, which does not affect the $^{207}Pb/^{206}Pb$ age. The youngest age reported for this sample at 1002 ± 42 Ma was from a wide dark homogeneous rim of grain 18 (Fig. 2.6b).

In 244, both concordant and discordant zircon rim ages are relatively young, between 1.0 and 1.1 Ga (inset in Fig. 2.7c). Concordant core data (filled ellipses) roughly

overlap with this cluster of rim ages, spreading between 1030 and 1130 Ma, but more than 50 % of core analyses are actually discordant and suggest ages in the range of 1.7–1.4 Ga (Fig. 2.7c). The analysis with the oldest concordant age of 1603 ± 28 Ma corresponds to the relict core of grain 5 (Fig. 2.7b, Type I). The weighted average $^{207}Pb/^{206}Pb$ age of 17 concordant analyses of the relatively young zircon was calculated at 1040 ± 6.7 Ma (MSWD=0.44, prob. 0.97), including 8 analyses of 8 'soccer ball' grains and 9 analyses of the mantles of 8 zircon grains with a more prismatic shape. The 8 data from the 'soccer balls' alone yield a weighted average age of 1043 ± 11 Ma (MSWD=0.74, prob. 0.64), and those of the mantles alone yield a weighted average age of 1037 ± 8.7 Ma (MSWD=0.16, prob. 0.996).

Th/U ratios calculated with the concordant data of 333x zircon cores range between 0.30 and 1.00, and the single rim analysis that yielded the age of 1002 Ma has a lower Th/U ratio of 0.16 (Table 2.4, Fig. 2.8c). In contrast, Th/U ratios of the most concordant data of the 244 zircon cluster between 0.02 and 0.28 , with little to no difference between zircon cores, mantle, rims and the 'soccer balls' grains (Table 2.5; Fig. 2.8d). On the Th/U *vs.* $^{207}Pb/^{206}Pb$ age diagram (Fig. 2.8d) most of the older discordant core data have low Th/U ratios, with only a few up to 0.9.

2.5.   DISCUSSION

2.5.1.   Summary and interpretation of the data

The great majority of zircon in HJ60b and M1b (Type I) is inferred to be detrital, with fragments of igneous cores showing a large spread of older ages (between *ca.* 2746

and *ca.* 1500 Ma) overgrown by younger metamorphic rims (between *ca.* 1450 and *ca.* 1000 Ma). This is consistent with the Th/U ratios that are high for the cores and low for the rims, generally characteristic of igneous and metamorphic zircon respectively (*cf.,* Gehrels *et al.,* 2009). The detrital character of zircon cores is consistent with the sedimentary origin of the host rocks.

In both samples, the Type II zircon including pristine examples of 'soccer-ball' grains, with distinct to well-rounded faces and sector zoning or no zoning, is inferred to be of metamorphic origin (Corfu *et al.,* 2003). This zircon yielded younger ages, in the same range as the rims of Type I grains, and its lower Th/U ratios are in agreement with crystallization in the presence of a hydrous melt during a metamorphic event (Gehrels *et al.,* 2009). In the case of HJ60b, thick rims of Type I zircon with textures similar to the Type II grains yield mostly Grenvillian ages of *ca.* 1045 Ma, while in contrast, in M1b, metamorphic grains (Type II) and rims of Type I yielded mostly pre-Grenvillian ages at *ca.* 1360–1400 Ma and *ca.* 1230–1260 Ma and only one Grenvillian age at 1076 ± 37 Ma.

The morphology, internal texture, and high Th/U ratios of zircon in 333x are consistent with igneous crystallization. In addition, the higher length to width ratio of zircon in this sample, and the presence of acicular cores is suggestive of a volcanic origin for this rock (Corfu *et al.,* 2003). This is further supported by the mineralogy and the microstructural arrangement of phases in the polymineral inclusions commonly present in the zircon cores which is attributed to (a) trapping of a rhyolitic liquid by zircon during growth, (b) quenching of this liquid into a glass, and (c) recrystallization into distinct phases during metamorphism. The only grain older than 1300 Ma is inferred to be exotic, incorporated into the magma at the source or during its ascent through the crust.

Metamorphic zircon in this sample is only represented by thin rims, the largest of which gave a late Grenvillian age at *ca.* 1000 Ma.

In contrast, zircon in sample 244 is to a large extent metamorphic, as suggested by the large rims overgrowing older cores with igneous texture, and the common 'soccer-ball' morphologies. This is supported by most of the concordant U–Pb data clustering around Grenvillian ages (*ca.* 1040 Ma) and having low Th/U ratios. However, the discordant data from the relict cores in zircon (together with one concordant age at 1603 ± 28 Ma) display a wider spread of older ages, between 1.7 and 1.4 Ga, with higher Th/U ratios. Thus, zircon cores in 244 are most likely detrital, strongly corroded and overgrown during subsequent metamorphism, suggesting that some aluminous layers of the LBS are of sedimentary (tuffaceous?) origin.

2.5.2.   Implications of the protolith ages

The ages of fragmental igneous cores of zircon from the PLV-CD samples HJ60b and M1b spread between 1500 and 1900 Ma with fewer data between 2400 and 2700 Ma. This is broadly similar to the spread in ages obtained in a provenance study of zircon from a quartzite collected in the type location of the PLV farther east (Lac du Milieu area; Moukhsil *et al.,* 2012).   The age distribution of zircon from the quartzite shows peaks at *ca.* 2.5–2.7 Ga, *ca.* 1.7–1.9 Ga and *ca.* 1.0 Ga, the later representing the age of Grenvillian metamorphism. This age distribution is consistent with provenance from units of the Laurentian margin and more specifically it correlates with ages of units identified farther north in the Manicouagan area, including the Archean basement and the

Paleoproterozoic supracrustal sequence of the Parautochthonous Gagnon terrane (Jordan *et al.,* 2006; van Gool *et al.,* 2008) and the Labradorian-age units of the Lelukuau terrane and the Island domain (Fig. 2.1, Indares *et al.,* 2000; Dunning and Indares, 2010). In the Lac du Milieu area, the deposition age for the PLV is further constrained by a 1482 ± 21 Ma granite, which intrudes the sequence. In the PLV-CD samples (HJ60b and M1b), the age break defined by concordant zircon data, between fragmental igneous cores older than *ca.* 1.5 Ga and rims younger than *ca.* 1.45 Ga is consistent with this age limit and suggests deposition at *ca.* 1.5 Ga. However, the two samples also yielded younger igneous zircon (one grain each: 1257 ± 43 Ma in M1b and 1217 ± 54 Ma in HJ60b) raising the possibility that the metasedimentary sequence at the extension of the PLV in the southern Canyon domain (PLV-CD) was deposited after *ca.* 1.2 Ga, or that in this area the PLV was partly reworked (eroded and redeposited) at *ca.* 1.2 Ga. A key characteristic of the PLV-CD is the presence of transposed and dismembered felsic pegmatite, most prominent in location M1b. Therefore an alternative possibility is that the 1.2 Ga-zircon crystallized from the pegmatitic liquid and dates the age of the pegmatite injection into the sedimentary package. This is also consistent with the presence of well-preserved zircon rims of that age in the PLV-CD rocks (notably in the M1b sample).

Ages in the range of 1700–1400 Ma (without Archean and/or Paleoproterozoic components) are also provided by relict zircon cores in sample 244, although these are less well constrained due to discordance. This age range is consistent with a more local provenance of zircon, and we note that the only concordant data point in that range is at 1603 ± 28 Ma which overlaps with the age range of neighboring plutonic units of the Lelukuau terrane. These ages indicate that (a) the sampled layer in location 244 of the

LBS represents a metasedimentary layer with zircon of local provenance; and (b) the LBS is younger than *ca.* 1.6 Ga.

The age of the LBS is best constrained by zircon from sample 333x, at *ca.* 1.24 Ga. In addition, the dominance of 1238 ± 13 Ma igneous zircon with volcanic attributes in 333x is consistent with the inferred extrusive origin of this unit, and supports the interpretation that the aluminous composition and nodular character of the rock is the result of hydrothermal alteration. The age determined for the LBS is similar to that of the Banded complex, recognized to the NE (Fig. 2.1) and the emplacement of which was attributed to crustal extension (Dunning and Indares, 2010). The new data suggest that the 1.2 Ga magmatism is more widespread in the central Grenville Province than originally thought.

2.5.3. Implications of the pre-Grenvillian metamorphic events

Pre-Grenvillian metamorphic events were mostly recorded by zircon rims from samples HJ60b and M1b in the PLV-CD, and correspond to two main groups of ages. The older one, between 1391 ± 33 Ma and 1408 ± 24 Ma, suggests a metamorphic pulse M1 at *ca.* 1.4 Ga (Fig. 2.8a and b). This event is also recorded in some cores and mantles of zircon from sample 244, and is correlative with the emplacement of the layered mafic to intermediate suite of the Canyon domain at 1410 ± 16 Ma (Dunning and Indares, 2010).

The younger group of ages, between 1217 ± 5 Ma and 1260 ± 43 Ma, was typically provided by homogeneous zircon rims suggesting a second metamorphic pulse M2 at *ca.* 1.2 Ga. These ages are similar to the crystallization age of scarce igneous zircon in the

same samples (1217 ± 54 Ma in HJ60b and 1257 ± 43 Ma in M1b) and which has been attributed to felsic pegmatite injections in these rocks (see previous section). This age interval also overlaps with the age of LBS as determined by 333x zircon and indicates that the magmatic event that led to the formation of the LBS had a thermal effect on older rocks in the area.

The zircon data from sample 244 do not provide a record of the M2 pulse. Since this layer is part of the LBS, this is consistent with deposition broadly coeval with the formation of the extrusive layers. However, a 1219 +60/−56 Ma monazite was recovered in the same layer (Dunning and Indares, 2010), possibly suggesting metamorphism (hydrothermal alteration?) shortly after deposition.

2.5.4.   Age of Grenvillian metamorphism

Zircon from all samples records Grenvillian age metamorphism, but to variable extent. The best developed metamorphic zircon ('soccer-ball' grains and wide rims around relict igneous cores) were extracted from sample 244 and show overlapping ages with a weighted average at *ca.* 1040 ± 6.7 Ma (metamorphic pulse M3; Fig. 2.8d). This represents the age of the main metamorphic event that affected this rock and overlaps with the ID–TIMS monazite age at 1044 ± 1.5 Ma for the same sample (Dunning and Indares, 2010). This sample is kyanite-bearing and comes from the northern tip of the LBS north of the reservoir (Fig. 2.1), which reached high-*P* granulite-facies conditions.

In contrast, the remaining samples are sillimanite-bearing and come from the Canyon domain, south of the reservoir (Fig. 2.1), which records mid-*P* granulite-facies

conditions. Three metamorphic rims of zircon in sample HJ60b from the PLV-CD also yielded a weighted average age of 1044 ± 15 Ma, in agreement with the monazite ID–TIMS age previously published for the same sample at 1059 ± 1.2 Ma (Dunning and Indares, 2010). However, the older monazite age of 1081 ± 5 Ma reported by Dunning and Indares (2010) was not reproduced in zircon in this study. In sample M1b only one rim of a sub-rounded zircon grain gave a Grenvillian metamorphic age at 1076 ± 37 Ma, which agrees within uncertainty with the ID–TIMS monazite age of 1065 ± 2.4 Ma (Dunning and Indares, 2010). Finally, the widest homogeneous gray rim of zircon extracted from sample 333x was dated at 1002 ± 42 Ma. This age agrees with both ID–TIMS monazite ages from this sample at 1001 ± 3 Ma and 1036 ± 6 Ma (Dunning and Indares, 2010). This younger age may indicate that parts of the Canyon domain were also affected by metamorphism during the waning stages of the Grenvillian orogeny.

2.6.   CONCLUSIONS

The combination of detailed study of the zircon morphology and internal textures, with careful U–Pb dating of specific zones in the zircon grains using LA–ICPMS technique, allowed constraints to be placed on the nature of protoliths of granulite-facies rocks that have similar mineral assemblages but contrasting origins: aluminous paragneisses from a metasedimentary sequence (PLV-CD) and aluminous sheets within a layered, dominantly bimodal (felsic–mafic) volcanic sequence (LBS).

The fragmental igneous cores of zircon from the metasedimentary package mainly yielded ages that spread between 1500 and 2700 Ma, consistent with a well-mixed

sedimentary origin and with data obtained from a quartzite in the type area of the PLV (Moukhsil *et al.,* 2012). In contrast, zircon extracted from an aluminous gneiss located in a zone of the LBS inferred to be a hydrothermally altered volcanic rock, yielded a clustered distribution of ages centered around 1238 ± 13 Ma. The age distribution, combined with the general morphology, the internal texture, and the mineral inclusion suite of the analyzed zircon confirm an igneous origin for this component in the LBS. Finally, relict igneous cores in a second aluminous layer from the LBS gave ages in the range of 1.7–1.4 Ga, consistent with a sedimentary origin of this layer and with zircon of local provenance.

These new results, integrated with previously published data, refine relationships between different crustal units and establish the following order of events in the Canyon domain of the central Grenville Province: (a) deposition of a sedimentary sequence of the southeast margin of Laurentia, at *ca.* 1.5 Ga with Archean to Labradorian age detritus from adjacent units (PLV; see also Moukhsil *et al.,* 2012); (b) formation of a layered suite of mafic to intermediate composition volcanic rocks (Dunning and Indares, 2010) whose thermal effects are recorded by new zircon growth in surrounding rocks (PLV-CD); (c) development of a *ca.* 1.24 Ga volcanic belt, preserved remnants of which are the Banded complex (Indares and Dunning, 2004; Dunning and Indares, 2010; Fig. 2.1), and the LBS which contains bimodal volcanic rocks, sedimentary sheets, and displays local evidence of hydrothermal alteration. This event is recorded in the country rocks (PLV-CD) by injections of felsic pegmatite and a thermal overprint leading to growth of metamorphic zircon; and (d) granulite-facies Grenvillian metamorphism with ages clustered at *ca.* 1.04 Ga and with a possible late overprint at 1.00 Ga in the Canyon Domain.

ACKNOWLEDGMENTS

REFERENCES

Aleinikoff, J. N., Schenck, W. S., Plank, M. O., Srogi, L. A., Fanning, C. M., Kamo, S. L. and Bosbyshell, H., 2006. Deciphering igneous and metamorphic events in high-grade rocks of the Wilmington Complex, Delaware: Morphology, cathodoluminescence and backscattered electron zoning, and SHRIMP U–Pb geochronology of zircon and monazite. *Geological Society of America Bulletin*, **118**: 39–64.

Black, L. P., Williams, I. S. and Compston, W., 1986. Four zircon ages from one rock: the history of a 3930 Ma-old granulite from Mount Sones, Enderby Land, Antarctica. *Contribution to Mineralogy and Petrology,* **94**: 427–437.

Bonnet, A. and Corriveau, L., 2007. Alteration vectors to metamorphic hydrothermal systems in gneissic terranes. *In:* Goodfellow, W.D. *(Eds.).* Mineral Deposits of Canada: A Synthesis of Major Deposit-Types, District Metallogeny, the Evolution of Geological Provinces, and Exploration Methods. *Geological Association of Canada, Mineral Deposits Division, Special Publication,* **5**: 1035–1049.

Bonnet, A., Corriveau, L. and La Flèche, M. R., 2005. Chemical imprint of highly metamorphosed volcanic-hosted hydrothermal alterations in the Romaine Supracrustal Belt, eastern Grenville Province, Quebec. *In:* Greenough, J. *(Eds.).* The Grenville Province: a geological and mineral resource perspective derived from government and academic research initiatives. *Canadian Journal of Earth Sciences,* **42**: 1783–1814.

Cawood, P. A., Hawkesworth, C. J., Dhuime, B., 2012. Detrital zircon record and tectonic setting. *Geology*, **40**: 875–878.

Corfu, F., 2007. Multistage metamorphic evolution and nature of the amphibolite-granulite-facies transition in Lofoten-Vesterålen, Norway, revealed by U–Pb in accessory minerals. *Chemical Geology*, **214**: 108–128.

Corfu, F., Hanchar, J. M., Hoskin, P. W. O. and Kinny, P. D., 2003. Atlas of zircon textures. *In:* Hanchar, J. M., Hoskin, P. W. O. *(Eds.).* Zircon. *Reviews in Mineralogy and Geochemistry,* **53**: 469–500.

Dunning, G. and Indares, A., 2010. New insights on the 1.7-1.0 Ga crustal evolution of the central Grenville Province from the Manicouagan – Baie Comeau transect. *Precambrian Research*, **180**: 204–226.

Dunning, G. R., O'Brien, S. J., Colman-Sadd, S. P., Blackwood, R. F., Dickson, W. L., O'neill, P. P. and Krogh, T. E., 1990. Silurian orogeny in the Newfoundland Appalachians. *Journal of Geology*, **98**: 895–913.

Dunning, G. R., Barr, S. M., Giles, P. S., McGregor, D. C., Pe-Piper, G. and Piper, D. J. W., 2002. Chronology of Devonian to early Carboniferous rifting and igneous activity in southern Magdalen Basin based on U–Pb (zircon) dating. *Canadian Journal of Earth Sciences*, **39**: 1219–1237.

Frei, D. and Gerdes, A., 2009. Precise and accurate in situ U–Pb dating of zircon with high sample throughput by automated LA-SF-ICP-MS. *Chemical geology*, **261**: 261–270.

Friend, C. R. and Kinny, P. D., 1995. New evidence for protolith ages of Lewisian granulites, northwest Scotland. *Geology*, **23**: 1027–1030.

Gehrels, G. E., Valencia, V. and Ruiz, J., 2008. Enhanced precision, accuracy, efficiency, and spatial resolution of U–Pb ages by laser ablation–multicollector–inductively coupled plasma–mass spectrometry. *Geochemistry Geophysics Geosystems*, **9 (3)**, Q03017, DOI:10.1029/2007GC001805.

Gehrels, G., Rusmore, M., Woodsworth, G., Crawford, M., Andronicos, C., Hollister, L., Patchett, J., Ducea, M., Butler, R., Klepeis, K., Davidson, C., Friedman, R., Haggart, J., Mahoney, B., Crawford, W., Pearson, D. and Girardi, J., 2009. U‑Th‑Pb geochronology of the Coast Mountains batholith in north‑coastal British Columbia: Constraints on age and tectonic evolution. Geological Society of America Bulletin, **121**: 1341–1361.

Gerdes, A. and Zeh, A., 2006. Combined U–Pb and Hf isotope LA-(MC-)ICP-MS analyses of detrital zircons: Comparison with SHRIMP and new constraints for the provenance and age of an Armorican metasediment in Central Germany. *Earth and Planetary Science Letters*, **249**: 47–61.

Hanchar, J. M. and Miller, C. F., 1993. Zircon zonation patterns as revealed by cathodoluminescence and backscattered electron images: Implications for interpretation of complex crustal histories. *Chemical Geology*, **110**: 1–13.

Hanchar, J. M. and Rudnick, R. L., 1995. Revealing hidden structures: the application of cathodoluminescence and back-scattered electron imaging to dating zircons from lower crustal xenoliths. *Lithos,* **36**: 289–303.

Indares, A. and Dunning, G., 2004. Crustal architecture above the high-pressure belt of the Grenville Province in the Manicouagan area: new structural, petrologic and U–Pb age constraints. *Precambrian Research*, **130**: 199–208.

Indares, A. and Dunning, G., 2001. Partial melting of high P–T metapelites from the Tshenukutish terrane (Grenville Province): petrography and U–Pb geochronology. *Journal of Petrology*, **42**: 1547–1565.

Indares, A., Dunning, G. and Cox, R., 2000. Tectono-thermal evolution of deep crust in a Mesoproterozoic continental collision setting: the Manicouagan example. *Canadian Journal of Earth Sciences*, **37**: 325–340.

Jordan, S. L., Indares, A. and Dunning, G., 2006. Partial melting of metapelites in the Gagnon terrane below the high-pressure belt in the Manicouagan area (Grenville Province): pressure temperature (P–T) and U–Pb age constraints and implications. *Canadian Journal of Earth Sciences*, **38**: 1309–1329.

Ketchum, J. W. F., Jackson, S. E., Culshaw, N. G. and Barr, S. M., 2001. Depositional and tectonic setting of the Paleoproterozoic Lower Aillik Group, Makkovik Province, Canada: evolution of a passive margin – foredeep sequence based on petrochemistry and U–Pb (ID-TIMS and LAM–ICP–MS) geochronology. *Precambrian Research*, **105**: 331–356.

Košler J. and Sylvester P., 2003. Present trends and the future of zircon in geochronology: laser ablation ICPMS. *In:* Hanchar, J. M., Hoskin, P. W. O. *(Eds.).* Zircon. *Reviews in Mineralogy and Geochemistry,* **53**: 243–275.

Ludwig, K. R., 2003. User's manual for Isoplot/Ex, Version 3.0. A geochronological toolkit for Microsoft Excel: Berkeley Geochronology Center Special Publication, **4**: 70 p.

Möller, A., O'Brien, P. J., Kennedy, A. and Kröner, A., 2002. Polyphase zircon in ultrahigh-temperature granulites (Rogaland, SW Norway): constraints for Pb diffusion in zircon. *Journal of Metamorphic Geology,* **20**: 727–740.

Moukhsil, A., Solgadi, F., Clark, T., Indares, A. and Blouin, S., 2013. Geology of the Daniel-Johnson Dam (Manic 5) area, Côte-Nord region (NTS 22K14, 22K15, 22K16, 22N03 and 22N02). Ministère des Ressources naturelles et de la Faune, RG-2013.

Moukhsil, A., Solgadi, F., Lacoste, P., Gagnon, M. and David, J., 2012. Géologie de la région du lac du Milieu (SNRC 22O03, 22O04, 22O06, 22J13 et 22J14). Ministère des Ressources naturelles et de la Faune, RG 2012–01.

Nadeau, L. and van Breemen, O., 1994. Do the 1.45–1.39 Ga Montauban group and the La Bostonnais complex constitute a Grenvillian accreted terrane? GAC–MAC, Program with Abstracts, 19, p. A81.

Paton, C., Woodhead, J., Hellstrom, J., Hergt, J., Greig, A. and Maas, R., 2010. Improved laser ablation U–Pb zircon geochronology through robust downhole fractionation correction. *Geochemistry Geophysics Geosystems*, **11**: 1–36.

Rivers, T., 2008. Assembly and preservation of lower, mid, and upper orogenic crust in the Grenville Province‐Implications for the evolution of large hot long‐duration orogens. *Precambrian Research,* **167**: 237–259.

Rivers, T., Martignole J., Gower, C. F. and Davidson, A., 1989. New tectonic divisions of the Grenville province, southeast Canadian Shield. *Tectonics*, **8**: 63–84.

Roberts, M. P. and Finger, F., 1997. Do U–Pb zircon ages from granulites reflect peak metamorphic conditions? *Geology*, **25**: 319–322.

Rubatto, D., 2002. Zircon trace element geochemistry: Partitioning with garnet and the link between U–Pb ages and metamorphism. *Chemical Geology,* **184**: 123–138.

Sláma, J., Košler, J., Condon, D. J., Crowley, J. L., Gerdes, A., Hanchar, J. M., Horstwood, M. S. A., Morris, G. A., Nasdala, L., Norberg, N., Schaltegger, U., Schoene, B., Tubrett, M. N. and Whitehouse, M. J., 2008. Plešovice zircon – a new natural reference material for U–Pb and Hf isotopic microanalysis. *Chemical Geology*, **249**: 11–35.

van Gool, J. A. M., Rivers, T. and Calon, T., 2008. Grenville Front zone, Gagnon terrane, south-western Labrador: configuration of a midcrustal foreland fold-thrust belt. *Tectonics*, **27**: 1–35.

Vavra, G., Schmidt, R. and Gebauer, D., 1999. Internal morphology, habit and U–Th–Pb microanalysis of amphibolite to granulite-facies zircons: geochronology of the Ivrea zone (southern Alps). *Contributions to Mineralogy and Petrology*, **134**: 380–404.

Vavra, G., Gebauer, D., Schmid, R. and Compston, W., 1996. Multiple zircon growth and recrystallization during polyphase Late Carboniferous to Triassic metamorphism in granulites of the Ivrea Zone Southern Alps: an ion microprobe SHRIMP study. 1T*Contributions to Mineralogy and Petrology*,**122**: 337–358.

Whitehouse, M. J. and Kamber, B. S., 2005. Assigning dates to thin gneissic veins in high-grade metamorphic terranes: A cautionary tale from Akilia, Southwest Greenland. Journal of Petrology, **46**: 291–318.

Whitehouse, M. J. and Kemp, A. I. S., 2010. On the difficulty of assigning crustal residence, magmatic protolith and metamorphic ages to Lewisian granulites:

constraints from combined in situ U–Pb and Lu-Hf isotopes. *In:* Law, R. D., Butler, R. W. H., Holdsworth, R. E., Krabbendam, M., Strachan, R. A. *(Eds.).* Continental Tectonics and Mountain Building: The Legacy of Peach and Horne. *Geological Society of London Special Publication*, **335**: 81–101.

Wiedenbeck, M., Allé, P., Corfu, F., Griffin, W. L., Meier, M., Oberli, F., von Quadt, A., Roddick, J. C. and Spiegel, W., 1995. Three natural zircon standards for U-Th-Pb, Lu-Hf, trace element and REE analyses. *Geostandards Newsletter*, **19**: 11–23.

Wiedenbeck, M., Hanchar, J.M., Peck, W.H., Sylvester, P., Valley, J., Whitehouse, M., Kronz, A., Morishita, Y., Nasdala, L., Fiebig, J., Franchi, I., Girard, J-P., Greenwood, R.C., Hinton, R., Kita, N., Mason, P.R.D., Norman, M., Ogasawara, M., Piccoli, P.M., Rhede, D., Satoh, H., Schulz-Dobrick, B., Skar, O., Spicuzza, M.J., Terada, K., Tindle, A., Togashi, S., Vennemann, T., Xie, Q. and Zheng, Y-F., 2004. Further characterization of the 91500 zircon crystal. *Geostandards and Geoanalytical Research,* **28**: 91–139.

Williams, I., 2001. Response of detrital zircon and monazite, and their U–Pb isotopic systems, to regional metamorphism and host-rock partial melting, Cooma complex, southeastern Australia. *Australian Journal of Earth Sciences*, **48**: 557–580.

Table 2.1: Operating conditions and instrument settings used for the U–Pb analyses using LA–ICPMS.

	for *bright* CL zone // for *dark* CL zone
ICPMS	
Type of ICPMS	high resolution double focusing magnetic
Brand and Model	ThermoFinnigan Element XR
forward power	1154-1172 W
GAS FLOWS	in L/min
Cool (Ar)	16
Auxiliary (Ar)	1.00-1.04
Sample (Ar)	0.698-0.702
Carrier (He)	0.600-0.836
LASER	
Type of laser	ArF Excimer
Brand and Model	GEOLAS 193 nm excimer
Laser wavelength	193 nm
Pulse duration	480s // 240-300s
Spot size	30 µm
Repetition rate	8 Hz / 4-5 Hz
Laser fluence	2-3 J/cm^2
DATA ACQUISITION PARAMETERS	
Resolution mode	low
Data acquisition protocol	time-resolved analysis
Scan mode	E-Scan
Scanned masses	204, 206, 207, 208, 232, 238
Settling time	0.001s, 0.030s (for 204)
Sample time	0.01, 0.02 (for 206), 0.03 (for 207)
Samples per peak	10
Number of scans (runs?)	975
Detector mode	Counting
Detector deadtime	19ns
Background collection	35 s
Ablation duration	60 s
Washout	25-30s
STANDARDISATION and DATA REDUCTION	
External standard used	Plešovice, 02123 // 91500, 02123
Reference standard used	91500// Plešovice
Data reduction software used	IOLITE

Table 2.2: Zircon (LA–ICPMS) U–Th–Pb data for sample HJ60b (PLV-CD).

HJ60b		Th (ppm)	U (ppm)	Th/U	RATIO ^{207}Pb/ ^{235}U	2SE	^{206}Pb/ ^{238}U	2SE	^{207}Pb/ ^{206}Pb	2SE	AGE ^{207}Pb/ ^{235}U	2SE	^{206}Pb/ ^{238}U	2SE	^{207}Pb/ ^{206}Pb	2SE	% disc
Concordant data																	
Zr17-R	f14	6	576	**0.01**	1.739	0.053	0.1716	0.0032	0.0732	0.0012	1022	20	1021	18	**1019**	**33**	**0**
Zr16-R*	g20	43	436	**0.10**	1.779	0.057	0.1729	0.0034	0.0740	0.0013	1037	21	1028	18	**1041**	**35**	**1**
Zr4-R*	b73	26	385	**0.07**	1.790	0.024	0.1745	0.0026	0.0741	0.00064	1041	9	1037	14	**1044**	**17**	**1**
Zr3-R*	e09	16	421	**0.04**	1.846	0.044	0.1796	0.0019	0.0742	0.0018	1062	16	1064	10	**1047**	**49**	**-2**
Zr1-R	f06	21	610	**0.03**	2.127	0.065	0.1952	0.0037	0.0793	0.0012	1157	21	1149	20	**1180**	**30**	**3**
Zr3-R	g02	18	621	**0.03**	2.759	0.084	0.2286	0.0043	0.0870	0.0013	1344	23	1327	23	**1360**	**29**	**2**
Zr13-c	e22	94	239	**0.39**	2.259	0.064	0.2035	0.0027	0.0808	0.0022	1200	20	1194	15	**1217**	**54**	**2**
Zr36-c	e45	40	124	**0.32**	3.322	0.092	0.2601	0.0036	0.0921	0.0025	1492	21	1491	18	**1469**	**52**	**-1**
Zr29-c	e51	153	393	**0.39**	3.557	0.086	0.2711	0.0029	0.0949	0.0023	1539	19	1548	14	**1527**	**46**	**-1**
Zr32-c	e39	76	144	**0.53**	3.668	0.093	0.2747	0.0031	0.0972	0.0024	1564	20	1564	16	**1571**	**46**	**0**
Zr41-c	e46	141	284	**0.49**	3.986	0.100	0.2854	0.0032	0.1009	0.0025	1631	21	1618	16	**1641**	**46**	**1**
Zr25-c	b61	343	482	**0.71**	3.993	0.062	0.2876	0.0048	0.1012	0.00087	1633	13	1632	24	**1645**	**16**	**1**
Zr19-c	e33	66	458	**0.14**	4.090	0.100	0.2936	0.0037	0.1012	0.0024	1652	20	1659	18	**1646**	**44**	**-1**
Zr7-c	g18	84	235	**0.36**	4.182	0.140	0.2950	0.0068	0.1018	0.0017	1668	28	1664	34	**1657**	**31**	**0**
Zr7-c	b76	182	283	**0.64**	4.171	0.055	0.2954	0.0044	0.1026	0.00077	1667	11	1669	22	**1671**	**14**	**0**
Zr10-c	b65	72	79	**0.91**	4.306	0.093	0.3029	0.0050	0.1027	0.0018	1693	18	1705	25	**1673**	**32**	**-2**
Zr17-c	e27	100	175	**0.57**	4.452	0.110	0.3058	0.0035	0.1047	0.0026	1721	20	1719	17	**1709**	**46**	**-1**
Zr53-c	e55	156	300	**0.52**	4.481	0.110	0.3087	0.0036	0.1050	0.0026	1726	21	1734	18	**1714**	**46**	**-1**
Zr10-c	e18	348	359	**0.97**	4.562	0.120	0.3086	0.0036	0.1069	0.0027	1742	21	1734	18	**1747**	**46**	**1**
Zr14-c	e24	112	236	**0.48**	4.561	0.110	0.3071	0.0034	0.1072	0.0026	1743	20	1726	17	**1752**	**44**	**2**
Zr14-c	b82	46	180	**0.25**	4.674	0.060	0.3157	0.0045	0.1077	0.00082	1762	11	1769	22	**1760**	**14**	**-1**
Zr14-c	b55	61	142	**0.43**	4.588	0.059	0.3077	0.0044	0.1083	0.00078	1747	11	1729	21	**1771**	**13**	**2**
Zr26-c	g36	329	399	**0.82**	4.768	0.140	0.3182	0.0060	0.1093	0.0017	1779	26	1780	30	**1787**	**28**	**0**
Zr34-c	g39	27	292	**0.09**	4.743	0.150	0.3181	0.0061	0.1099	0.0017	1774	26	1780	30	**1797**	**28**	**1**
Zr12-c	b66	77	105	**0.73**	4.943	0.066	0.3246	0.0046	0.1100	0.00089	1809	11	1813	22	**1800**	**15**	**-1**
Zr5-c	e12	239	271	**0.88**	4.998	0.120	0.3266	0.0037	0.1106	0.0026	1818	20	1821	18	**1809**	**43**	**-1**
Zr2-c	b72	209	231	**0.90**	4.895	0.065	0.3198	0.0046	0.1109	0.00088	1801	11	1788	23	**1814**	**14**	**1**
Zr13-c	b58	37	218	**0.17**	5.107	0.073	0.3327	0.0049	0.1112	0.0011	1837	12	1851	24	**1819**	**18**	**-2**
Zr1-c^S	b56	133	458	**0.29**	5.174	0.071	0.3294	0.0053	0.1151	0.001	1850	12	1835	26	**1881**	**16**	**2**
Zr37-c	e42	134	148	**0.91**	5.831	0.160	0.3524	0.0040	0.1200	0.0032	1950	23	1947	19	**1956**	**48**	**0**

66

HJ60b		Th (ppm)	U (ppm)	Th/U	RATIO						AGE						% disc
					$^{207}Pb/$ ^{235}U	2SE	$^{206}Pb/$ ^{238}U	2SE	$^{207}Pb/$ ^{206}Pb	2SE	$^{207}Pb/$ ^{235}U	2SE	$^{206}Pb/$ ^{238}U	2SE	$^{207}Pb/$ ^{206}Pb	2SE	
Zr57-c	e54	139	255	0.55	11.300	0.270	0.4847	0.0056	0.1697	0.004	2547	22	2548	24	2555	39	0
Zr9-c	b59	26	53	0.49	13.920	0.190	0.5309	0.0081	0.1904	0.0018	2743	13	2746	34	2746	16	0
Discordant data																	
Zr6-R	g03	37	740	0.05	1.971	0.060	0.1830	0.0034	0.0772	0.0012	1106	21	1084	19	1127	31	4
Zr19-R	g07	32	619	0.05	2.013	0.063	0.1835	0.0036	0.0786	0.0013	1120	21	1086	19	1162	33	7
Zr27-R	g29	37	740	0.05	1.908	0.059	0.1739	0.0033	0.0789	0.0013	1083	20	1033	18	1169	33	12
Zr20-R	g14	27	605	0.04	2.075	0.067	0.1851	0.0038	0.0799	0.0015	1139	22	1095	21	1195	37	8
Zr2-R	g15	17	537	0.03	2.016	0.064	0.1782	0.0035	0.0813	0.0014	1122	22	1057	19	1229	34	14
Zr9-R	f09	20	725	0.03	2.169	0.068	0.1917	0.0038	0.0818	0.0014	1171	22	1130	21	1241	34	9
Zr10-R	f10	32	619	0.05	2.177	0.068	0.1911	0.0038	0.0820	0.0014	1173	22	1128	20	1246	33	9
Zr7-R	g19	17	757	0.02	2.330	0.075	0.2024	0.0041	0.0830	0.0015	1221	23	1188	22	1268	35	6
Zr8-R	f13	31	608	0.05	2.233	0.068	0.1929	0.0037	0.0832	0.0013	1191	21	1137	20	1275	30	11
Zr16-R	g23	17	811	0.02	2.541	0.079	0.2135	0.0041	0.0854	0.0014	1284	23	1248	22	1324	32	6
Zr6-R	b78	117	293	0.40	2.524	0.039	0.2107	0.0032	0.0871	0.00086	1277	11	1232	17	1362	19	10
Zr5-R	g01	96	660	0.15	2.596	0.080	0.2140	0.0041	0.0871	0.0014	1299	23	1251	22	1363	31	8
Zr12-R	f11	31	896	0.03	2.613	0.084	0.2156	0.0044	0.0871	0.0014	1303	24	1258	23	1363	31	8
Zr2-R	g16	48	697	0.07	2.543	0.080	0.2096	0.0041	0.0872	0.0015	1284	23	1227	22	1365	33	10
Zr26-R	g08	10	800	0.01	2.671	0.085	0.2186	0.0044	0.0874	0.0014	1322	23	1275	23	1369	31	7
Zr25-R	g41	24	707	0.03	2.684	0.083	0.2243	0.0043	0.0877	0.0014	1324	23	1305	22	1377	31	5
Zr14-R	g31	30	488	0.06	2.941	0.092	0.2326	0.0046	0.0913	0.0015	1392	24	1348	24	1453	31	7
Zr15-R[S]	g40	275	953	0.29	5.688	0.180	0.3024	0.0060	0.1375	0.0023	1930	28	1703	30	2196	29	22
Zr17-c	f15	371	801	0.46	2.086	0.066	0.1892	0.0037	0.0797	0.0014	1145	22	1117	20	1190	35	6
Zr9-c	e21	68	727	0.09	2.538	0.090	0.2149	0.0039	0.0849	0.0022	1277	26	1255	21	1313	50	4
Zr28-c	g33	73	832	0.09	2.328	0.085	0.1964	0.0047	0.0854	0.0017	1219	26	1157	25	1325	39	13
Zr8-c	b53	107	234	0.46	2.840	0.044	0.2262	0.0034	0.0908	0.0011	1368	12	1314	18	1442	23	9
Zr20-c	g12	188	1218	0.15	2.710	0.097	0.2088	0.0053	0.0926	0.0016	1329	27	1221	28	1479	33	17
Zr8-c	e14	344	773	0.45	3.052	0.072	0.2363	0.0023	0.0938	0.0022	1421	18	1367	12	1505	44	9
Zr7-c	e15	168	446	0.38	3.250	0.084	0.2504	0.0035	0.0941	0.0022	1469	20	1440	18	1509	44	5
Zr4-c	b75	46	237	0.19	3.245	0.044	0.2502	0.0036	0.0942	0.00075	1468	10	1439	19	1512	15	5
Zr5-c	b79	105	308	0.34	2.932	0.045	0.2242	0.0034	0.0943	0.0011	1389	12	1304	18	1514	22	14
Zr6-c	g32	634	469	1.35	3.143	0.099	0.2399	0.0046	0.0953	0.0016	1443	24	1386	24	1534	32	10
Zr54-c	e57	71	926	0.08	3.158	0.097	0.2400	0.0030	0.0953	0.0025	1446	23	1387	16	1534	49	10
Zr8-c	b81	112	287	0.39	3.445	0.057	0.2597	0.0040	0.0971	0.001	1515	13	1488	20	1569	19	5

HJ60b		Th (ppm)	U (ppm)	Th/U	RATIO $^{207}Pb/^{235}U$	2SE	$^{206}Pb/^{238}U$	2SE	$^{207}Pb/^{206}Pb$	2SE	AGE $^{207}Pb/^{235}U$	2SE	$^{206}Pb/^{238}U$	2SE	$^{207}Pb/^{206}Pb$	2SE	% disc
Zr50-c	e60	87	402	0.22	3.468	0.085	0.2582	0.0027	0.0974	0.0024	1520	19	1481	14	1575	46	6
Zr48-c	f01	145	126	1.15	3.402	0.089	0.2490	0.0029	0.0991	0.0026	1505	21	1433	15	1607	49	11
Zr23-c[S]	g25	277	537	0.52	3.587	0.120	0.2569	0.0059	0.1006	0.0019	1549	28	1473	30	1635	35	10
Zr27-c	g28	421	1313	0.32	3.401	0.110	0.2405	0.0049	0.1021	0.0016	1503	25	1389	26	1663	29	16
Zr28-c	e52	284	601	0.47	3.825	0.096	0.2726	0.0033	0.1023	0.0025	1597	20	1554	17	1666	45	7
Zr20-c	e32	84	257	0.33	4.320	0.110	0.3080	0.0041	0.1024	0.0025	1697	20	1730	20	1667	45	-4
Zr3-c	e08	75	352	0.21	4.229	0.100	0.2893	0.0032	0.1060	0.0026	1678	20	1638	16	1732	45	5
Zr19-c	g06	183	403	0.45	4.293	0.150	0.2843	0.0066	0.1072	0.002	1693	27	1612	33	1752	34	8
Zr21-c[S]	g24	222	434	0.51	4.383	0.150	0.2962	0.0064	0.1081	0.0021	1712	29	1672	32	1768	35	5
Zr3-c	b52	188	220	0.85	5.340	0.089	0.3539	0.0061	0.1084	0.001	1872	14	1952	29	1773	17	-10
Zr26-c	g35	1594	1064	1.50	4.519	0.140	0.3030	0.0058	0.1084	0.0016	1735	25	1705	29	1773	27	4
Zr34-c	e41	81	155	0.52	4.996	0.130	0.3324	0.0037	0.1089	0.0027	1818	22	1849	18	1781	45	-4
Zr4-c	e11	184	458	0.40	4.611	0.110	0.3061	0.0040	0.1089	0.0026	1752	21	1721	20	1782	44	3
Zr11-c	g27	55	146	0.38	4.748	0.150	0.3128	0.0060	0.1099	0.0019	1775	26	1756	30	1798	31	2
Zr49-c	e58	35	132	0.27	5.689	0.150	0.3638	0.0043	0.1139	0.0029	1930	23	2002	20	1863	46	-7
Zr30-c	e38	127	533	0.24	5.004	0.130	0.3178	0.0044	0.1145	0.0029	1819	23	1778	22	1872	46	5
Zr26-c	e36	124	434	0.28	6.155	0.160	0.3871	0.0048	0.1153	0.0028	2000	22	2109	22	1885	44	-12
Zr16-c	e25	70	168	0.42	5.738	0.140	0.3602	0.0041	0.1158	0.0028	1938	22	1982	20	1892	44	-5
Zr25-c	e35	69	197	0.35	5.322	0.150	0.3267	0.0044	0.1176	0.0031	1873	23	1822	21	1920	47	5
Zr18-c	e28	133	325	0.41	6.480	0.210	0.3168	0.0054	0.1467	0.0038	2035	28	1774	27	2308	44	23
Zr6-c	e17	46	428	0.11	9.704	0.230	0.4121	0.0042	0.1699	0.0039	2407	22	2225	19	2556	38	13
Zr15-c	b62	319	480	0.66	12.098	0.140	0.5122	0.0072	0.1708	0.00092	2611	11	2665	31	2565	9	-4
Zr9-c	g37	35	58	0.60	13.580	0.420	0.5170	0.0100	0.1912	0.0031	2719	30	2689	43	2753	27	2

-R: RIM analyses   -c: CORE analyses   [S] : analyses with shorter signal, < 15s   -R*: RIM analyses used in the calculation of the weighted average 7/6 age

Table 2.3: Zircon (LA–ICPMS) U–Th–Pb data for sample M1b (PLV-CD).

M1b		Th (ppm)	U (ppm)	Th/U	RATIO $^{207}Pb/^{235}U$	2SE	$^{206}Pb/^{238}U$	2SE	$^{207}Pb/^{206}Pb$	2SE	AGE $^{207}Pb/^{235}U$	2SE	$^{206}Pb/^{238}U$	2SE	$^{207}Pb/^{206}Pb$	2SE	% disc
Concordant data																	
Zr27-R	d05	8	354	**0.02**	1.862	0.041	0.1794	0.0033	0.0753	0.0014	1067	14	1064	18	**1076**	37	**1**
Zr14-R	j28	35	440	**0.08**	2.332	0.033	0.2078	0.0022	0.0814	0.0009	1222	10	1217	12	**1230**	21	**1**
Zr6-R	g12	46	249	**0.19**	2.350	0.054	0.2065	0.0033	0.0826	0.0018	1226	16	1211	17	**1260**	43	**4**
Zr66-R	g13	30	424	**0.07**	2.603	0.041	0.2237	0.0029	0.0843	0.0012	1300	12	1302	15	**1300**	28	**0**
Zr65-R	g25	31	425	**0.07**	2.558	0.050	0.2189	0.0032	0.0857	0.0016	1290	15	1276	17	**1331**	36	**4**
Zr29-R	c48	14	458	**0.03**	2.741	0.062	0.2293	0.0045	0.0869	0.0016	1338	17	1330	24	**1359**	35	**2**
Zr13-R	d21	15	531	**0.03**	2.886	0.057	0.2356	0.0040	0.0887	0.0015	1377	15	1364	21	**1397**	32	**2**
Zr19-R	g17	28	499	**0.06**	2.997	0.080	0.2436	0.0050	0.0888	0.0021	1406	20	1404	26	**1400**	45	**0**
Zr13-R	j17	31	455	**0.07**	2.979	0.050	0.2425	0.0036	0.0892	0.0011	1399	13	1396	17	**1408**	24	**1**
Zr24-R	j19	165	743	**0.22**	3.125	0.048	0.2489	0.0030	0.0909	0.0010	1439	12	1432	16	**1443**	20	**1**
Zr8-c[S]	j07	78	155	**0.50**	2.357	0.063	0.2094	0.0039	0.0825	0.0018	1228	19	1225	21	**1257**	43	**3**
Zr9-c	g15	35	599	**0.06**	2.953	0.051	0.2427	0.0036	0.0884	0.0015	1394	13	1400	19	**1391**	33	**-1**
Zr22-c	j08	575	613	**0.94**	3.451	0.056	0.2636	0.0034	0.0958	0.0011	1514	13	1508	17	**1544**	22	**2**
Zr13-c	ii03	117	179	**0.65**	3.545	0.065	0.2691	0.0033	0.0962	0.0014	1539	14	1538	16	**1552**	27	**1**
Zr7-c	g05	80	185	**0.43**	3.851	0.091	0.2838	0.0046	0.0981	0.0021	1603	19	1613	23	**1588**	40	**-2**
Zr10-c	f15	404	584	**0.69**	4.047	0.120	0.2917	0.0048	0.0993	0.0025	1642	23	1649	24	**1611**	47	**-2**
Zr4-c	g20	175	259	**0.68**	4.023	0.093	0.2893	0.0044	0.1012	0.0022	1637	19	1638	22	**1646**	40	**1**
Zr2-c	f09	73	237	**0.31**	4.137	0.110	0.2963	0.0041	0.1014	0.0026	1660	22	1673	20	**1650**	48	**-1**
Zr6-c	f12	445	647	**0.69**	4.300	0.110	0.3016	0.0039	0.1033	0.0025	1692	21	1699	19	**1684**	45	**-1**
Zr4-c	f11	129	190	**0.68**	4.420	0.120	0.3080	0.0039	0.1038	0.0027	1717	22	1732	20	**1693**	48	**-2**
Zr20-c	g16	37	103	**0.36**	4.299	0.120	0.2990	0.0063	0.1042	0.0027	1693	23	1685	31	**1700**	48	**1**
Zr30-c	d08	161	386	**0.42**	4.340	0.097	0.3007	0.0059	0.1047	0.0021	1698	18	1694	29	**1709**	37	**1**
Zr27-c	d04	271	657	**0.41**	4.383	0.086	0.3023	0.0052	0.1051	0.0018	1710	16	1703	26	**1716**	31	**1**
Zr19-c	j05	277	418	**0.66**	4.481	0.070	0.3086	0.0035	0.1054	0.0010	1725	13	1733	17	**1721**	17	**-1**
Zr14-c	f19	162	364	**0.44**	4.504	0.120	0.3101	0.0044	0.1060	0.0027	1733	22	1740	22	**1732**	47	**0**
Zr27-c	g20	183	259	**0.71**	4.765	0.090	0.3206	0.0050	0.1084	0.0019	1778	16	1794	24	**1773**	32	**-1**
Zr5-c	j31	82	287	**0.29**	4.741	0.062	0.3152	0.0031	0.1090	0.0009	1774	11	1765	15	**1782**	14	**1**
Zr17-c	g19	384	443	**0.87**	4.930	0.087	0.3272	0.0050	0.1098	0.0017	1808	15	1824	24	**1796**	28	**-2**
Zr1-c	g26	56	394	**0.14**	4.735	0.077	0.3141	0.0041	0.1099	0.0016	1774	13	1760	20	**1797**	27	**2**
Zr54-c	g09	243	185	**1.32**	4.958	0.092	0.3271	0.0049	0.1103	0.0020	1811	16	1824	24	**1804**	33	**-1**

69

M1b		Th (ppm)	U (ppm)	Th/U	RATIO 207Pb/235U	2SE	206Pb/238U	2SE	207Pb/206Pb	2SE	AGE 207Pb/235U	2SE	206Pb/238U	2SE	207Pb/206Pb	2SE	% disc
Zr29-c	g09	99	229	0.43	4.987	0.110	0.3261	0.0048	0.1103	0.0022	1814	17	1820	23	1805	36	-1
Zr51-c	g10	73	117	0.63	4.944	0.082	0.3238	0.0043	0.1109	0.0018	1810	14	1808	21	1814	29	0
Zr1-c	e14	62	248	0.25	5.235	0.110	0.3336	0.0045	0.1134	0.0023	1858	18	1856	22	1854	37	0
Zr29-c	g08	100	214	0.47	5.505	0.120	0.3437	0.0051	0.1158	0.0023	1898	18	1903	25	1892	36	-1
Zr14-c	j12	107	133	0.81	10.210	0.160	0.4596	0.0057	0.1614	0.0018	2450	14	2441	25	2470	19	1
Discordant data																	
Zr5-R	j30	77	453	0.17	2.122	0.036	0.1899	0.0026	0.0800	0.0012	1158	12	1120	14	1197	30	6
Zr31-R	d09	28	748	0.04	2.473	0.060	0.2116	0.0045	0.0838	0.0018	1267	18	1237	24	1288	42	4
Zr16-R	j26	35	537	0.06	2.398	0.039	0.2054	0.0026	0.0849	0.0011	1241	12	1205	13	1313	25	8
Zr4-R	j32	36	424	0.08	2.432	0.039	0.2076	0.0024	0.0851	0.0010	1251	11	1215	13	1318	22	8
Zr22-R	d12	8	1173	0.01	2.539	0.067	0.2113	0.0048	0.0858	0.0020	1284	19	1235	25	1334	45	7
Zr32-R	d11	35	728	0.05	2.506	0.051	0.2106	0.0037	0.0861	0.0015	1273	15	1232	19	1340	34	8
Zr28-R	d26	20	358	0.06	2.754	0.056	0.2267	0.0040	0.0886	0.0016	1343	15	1318	21	1395	35	6
Zrex2-R	d19	40	604	0.07	2.739	0.061	0.2203	0.0042	0.0896	0.0016	1338	17	1284	22	1417	34	9
Zr9-R	j16	35	515	0.07	2.831	0.048	0.2295	0.0030	0.0902	0.0011	1363	12	1333	16	1430	23	7
Zr26-R	d24	22	331	0.07	2.865	0.072	0.2305	0.0045	0.0906	0.0020	1370	19	1336	24	1438	42	7
Zr15-R	d34	53	757	0.07	2.625	0.061	0.2098	0.0040	0.0909	0.0017	1306	17	1227	21	1444	36	15
Zr2-R	j20	61	408	0.15	2.922	0.051	0.2335	0.0028	0.0912	0.0012	1387	13	1352	14	1451	25	7
Zr17-R	d23	58	544	0.11	2.833	0.065	0.2223	0.0043	0.0922	0.0018	1364	17	1295	23	1472	37	12
Zr18-R	j02	17	614	0.03	3.062	0.047	0.2418	0.0027	0.0926	0.0009	1422	12	1396	14	1479	19	6
Zr11-R	d36	152	357	0.43	2.982	0.062	0.2296	0.0040	0.0946	0.0017	1402	16	1332	21	1520	34	12
Zr21-R[S]	e15	37	632	0.06	3.251	0.074	0.2364	0.0038	0.0999	0.0021	1469	17	1368	20	1621	39	16
Zr7-R	j04	151	549	0.27	3.662	0.054	0.2639	0.0033	0.1014	0.0011	1563	12	1509	17	1650	20	9
Zr21-R[S]	d30	37	721	0.05	3.642	0.098	0.2554	0.0055	0.1028	0.0021	1559	21	1465	28	1675	38	13
Zr1-c	g19	99	233	0.42	2.871	0.072	0.2228	0.0037	0.0931	0.0022	1373	19	1296	20	1490	45	13
Zr6-c	j11	91	220	0.41	3.166	0.066	0.2470	0.0036	0.0938	0.0016	1447	17	1422	18	1504	32	5
Zr24-c	c49	1455	1923	0.76	3.180	0.071	0.2432	0.0048	0.0941	0.0018	1452	18	1403	25	1510	36	7
Zr13-c	f18	103	238	0.43	3.066	0.088	0.2374	0.0036	0.0941	0.0025	1425	21	1372	19	1510	50	9
Zr10-c	g13	81	218	0.37	3.289	0.098	0.2439	0.0047	0.0970	0.0022	1469	23	1405	24	1567	43	10
Zr5-c	f14	110	217	0.51	3.948	0.100	0.2925	0.0040	0.0979	0.0025	1622	21	1653	20	1585	48	-4
Zr11-c	d35	108	280	0.39	3.260	0.073	0.2394	0.0045	0.0987	0.0019	1470	17	1383	23	1600	36	14
Zr65-c	f32	309	458	0.68	3.744	0.110	0.2728	0.0040	0.0990	0.0025	1578	24	1554	20	1605	47	3
Zr1-c	f08	503	682	0.74	3.661	0.091	0.2666	0.0033	0.0994	0.0024	1563	20	1523	17	1612	45	6

70

M1b		Th (ppm)	U (ppm)	Th/U	RATIO $^{207}Pb/^{235}U$	2SE	$^{206}Pb/^{238}U$	2SE	$^{207}Pb/^{206}Pb$	2SE	AGE $^{207}Pb/^{235}U$	2SE	$^{206}Pb/^{238}U$	2SE	$^{207}Pb/^{206}Pb$	2SE	% disc
Zr2-c	c47	135	1456	0.09	3.636	0.074	0.2596	0.0047	0.1012	0.0017	1558	16	1487	24	1646	31	10
Zr3-c[S]	g04	42	346	0.12	3.965	0.110	0.2824	0.0057	0.1024	0.0024	1629	21	1603	29	1668	43	4
Zr63-c	f34	221	592	0.37	3.788	0.095	0.2657	0.0033	0.1029	0.0025	1589	20	1520	17	1677	45	9
Zr3-c[S]	f03	69	308	0.22	4.005	0.110	0.2771	0.0056	0.1048	0.0024	1634	22	1580	26	1711	42	8
Zr23-c	d27	469	599	0.78	4.057	0.110	0.2802	0.0067	0.1048	0.0022	1643	22	1591	34	1711	39	7
Zr61-c	f35	53	399	0.13	4.296	0.100	0.2954	0.0034	0.1058	0.0025	1692	20	1669	17	1729	43	3
Zr56-c	f28	270	314	0.86	4.188	0.120	0.2877	0.0048	0.1059	0.0027	1677	24	1629	24	1730	47	6
Zr23-c	d28	265	536	0.49	4.225	0.100	0.2897	0.0060	0.1060	0.0023	1678	19	1639	30	1732	40	5
Zr57-c	f25	57	108	0.53	4.157	0.120	0.2848	0.0041	0.1060	0.0028	1664	24	1616	20	1732	48	7
Zr3-c	d20	75	362	0.21	4.256	0.095	0.2886	0.0056	0.1065	0.0020	1686	18	1635	28	1740	34	6
Zr1-c	d32	453	580	0.78	4.173	0.090	0.2864	0.0056	0.1067	0.0020	1667	18	1623	28	1744	34	7
Zr28-c	d03	133	321	0.41	4.448	0.096	0.3008	0.0057	0.1068	0.0020	1721	18	1694	28	1746	34	3
Zr2-c	j21	93	188	0.49	4.483	0.070	0.3023	0.0033	0.1071	0.0011	1725	13	1702	17	1751	19	3
Zr15-c	ii04	291	164	1.78	4.222	0.090	0.2883	0.0048	0.1072	0.0017	1678	17	1632	24	1752	29	7
Zr18-c	j01	198	465	0.43	4.389	0.066	0.2968	0.0035	0.1077	0.0010	1710	12	1675	17	1760	17	5
Zr48-c	f24	88	103	0.85	4.569	0.120	0.3054	0.0039	0.1087	0.0027	1742	22	1717	19	1778	45	3
Zr50-c	g12	183	244	0.75	5.059	0.087	0.3387	0.0050	0.1088	0.0019	1828	14	1880	24	1779	32	-6
Zr16-c	j27	212	307	0.69	5.500	0.089	0.3601	0.0048	0.1110	0.0013	1899	14	1982	23	1816	21	-9
Zr9-c	j15	122	256	0.48	4.896	0.067	0.3150	0.0030	0.1119	0.0010	1800	12	1765	15	1830	16	4
Zrwex2-c	d16	70	261	0.27	4.825	0.097	0.3103	0.0055	0.1126	0.0020	1789	17	1742	27	1842	32	5
Zr62-c	f31	91	319	0.29	5.643	0.140	0.3570	0.0039	0.1139	0.0027	1921	21	1967	19	1862	43	-6
Zr19-c	g16	75	223	0.34	8.510	0.140	0.4080	0.0058	0.1522	0.0023	2288	15	2205	27	2371	26	7
Zr53-c[S]	f27	90	132	0.68	10.370	0.290	0.4752	0.0075	0.1582	0.0042	2470	25	2505	33	2437	45	-3
Zr21-c	d31	408	810	0.50	8.947	0.190	0.3872	0.0074	0.1676	0.0029	2332	19	2109	34	2534	29	17

-R: RIM analyses   -c: CORE analyses   [S]: analyses with shorter signal, < 15s

Table 2.4: Zircon (LA–ICPMS) U–Th–Pb data for sample 333x (LBS).

333x		Th (ppm)	U (ppm)	Th/U	RATIO $^{207}Pb/^{235}U$	2SE	$^{206}Pb/^{238}U$	2SE	$^{207}Pb/^{206}Pb$	2SE	AGE $^{207}Pb/^{235}U$	2SE	$^{206}Pb/^{238}U$	2SE	$^{207}Pb/^{206}Pb$	2SE	% disc
Concordant data																	
Zr18.1-R	e33	52	329	**0.16**	1.690	0.033	0.1695	0.0023	0.0726	0.0015	1005	13	1010	12	**1002**	42	**-1**
Zr27.1-R	ii13	346	506	**0.68**	2.250	0.058	0.2020	0.0036	0.0809	0.0013	1195	18	1187	19	**1218**	32	**3**
Zr1.2-oc	d10	50	94	**0.53**	2.104	0.048	0.1959	0.0028	0.0785	0.0019	1149	16	1153	15	**1160**	48	**1**
Zr19.2-oc	e30	167	191	**0.88**	2.302	0.055	0.2066	0.0031	0.0799	0.0019	1212	17	1210	17	**1195**	47	**-1**
Zr20.1-oc	e48	162	201	**0.81**	2.365	0.052	0.2133	0.0031	0.0808	0.0018	1230	16	1247	16	**1217**	44	**-2**
Zr6.1-oc	e20	112	184	**0.61**	2.303	0.050	0.2071	0.0029	0.0809	0.0018	1213	15	1214	15	**1218**	44	**0**
Zr22.2-oc	ii34	93	314	**0.30**	2.394	0.059	0.2130	0.0034	0.0814	0.0011	1241	18	1244	18	**1231**	27	**-1**
Zr7.1-oc	e71	117	232	**0.50**	2.341	0.049	0.2066	0.0029	0.0819	0.0017	1224	15	1211	15	**1243**	41	**3**
Zr2.2-oc	e06	167	226	**0.74**	2.353	0.056	0.2088	0.0031	0.0821	0.0019	1229	16	1222	17	**1248**	45	**2**
Zr2.3-oc	e07	178	273	**0.65**	2.457	0.050	0.2151	0.0029	0.0825	0.0017	1259	15	1256	15	**1256**	40	**0**
Zr5.1-oc	e67	66	113	**0.58**	2.483	0.059	0.2190	0.0032	0.0828	0.0021	1265	17	1276	17	**1265**	50	**-1**
Zr10.3-oc	g01	124	250	**0.50**	2.571	0.055	0.2239	0.0031	0.0831	0.0018	1292	16	1303	16	**1272**	42	**-2**
Zr11.1-oc	e77	249	383	**0.65**	2.674	0.060	0.2251	0.0035	0.0863	0.0020	1321	17	1308	19	**1345**	45	**3**
Zr17.1-oc	e45	165	412	**0.40**	2.931	0.062	0.2391	0.0036	0.0887	0.0019	1389	16	1383	19	**1398**	41	**1**
Zr1.1-c	c20	64	67	**0.96**	2.189	0.062	0.2003	0.0027	0.0794	0.0019	1174	19	1176	15	**1182**	47	**1**
Zr4.1-c	c35	45	45	**1.00**	2.282	0.062	0.2059	0.0026	0.0800	0.0020	1206	19	1206	14	**1197**	49	**-1**
Zr21.1-c	e10	53	79	**0.68**	2.352	0.057	0.2095	0.0030	0.0814	0.0020	1225	17	1226	16	**1231**	48	**0**
Zr2.1-c	e03	96	97	**0.98**	2.492	0.073	0.2161	0.0036	0.0828	0.0023	1265	21	1260	19	**1265**	54	**0**
Zr24.1-c	ii04	97	126	**0.77**	2.416	0.069	0.2139	0.0036	0.0828	0.0017	1251	21	1249	19	**1265**	40	**1**
Zr8.1-c	c13	36	36	**1.00**	2.416	0.070	0.2119	0.0029	0.0829	0.0021	1247	21	1238	15	**1267**	49	**2**
Zr5.2-c[S]	e68	42	44	**0.95**	2.540	0.120	0.2212	0.0051	0.0842	0.0041	1279	34	1287	27	**1297**	95	**1**
Zr9.1-c	c29	46	91	**0.50**	2.610	0.075	0.2219	0.0031	0.0862	0.0021	1302	21	1291	16	**1343**	47	**4**
Zr17.2-c	e46	83	130	**0.64**	3.545	0.094	0.2659	0.0042	0.0973	0.0025	1537	21	1519	21	**1573**	48	**3**
Discordant data																	
Zr14.1-R	ii05	41	1525	**0.03**	2.100	0.052	0.1900	0.0032	0.0796	0.0010	1149	17	1123	17	**1187**	25	**5**
Zr18.1-R	ii30	168	355	**0.47**	2.130	0.054	0.1880	0.0029	0.0813	0.0012	1157	17	1111	16	**1228**	29	**10**
Zr19.3-R[S]	e32	81	355	**0.23**	1.940	0.050	0.1597	0.0026	0.0886	0.0024	1095	17	955	15	**1396**	52	**32**
Zr17.2-R	c19	47	134	**0.35**	2.747	0.092	0.2053	0.0037	0.0951	0.0023	1333	25	1202	20	**1530**	46	**21**
Zr14.2-R	e58	30	231	**0.13**	2.842	0.062	0.1772	0.0025	0.1160	0.0025	1366	17	1051	14	**1895**	39	**45**

333x		Th (ppm)	U (ppm)	Th/U	RATIO $^{207}Pb/$ ^{235}U	2SE	$^{206}Pb/$ ^{238}U	2SE	$^{207}Pb/$ ^{206}Pb	2SE	AGE $^{207}Pb/$ ^{235}U	2SE	$^{206}Pb/$ ^{238}U	2SE	$^{207}Pb/$ ^{206}Pb	2SE	% disc
Zr15.2-oc	e65	86	406	0.21	1.861	0.041	0.1729	0.0026	0.0784	0.0017	1066	14	1028	14	1157	43	11
Zr1.3-oc	d13	75	137	0.55	2.353	0.052	0.2149	0.0030	0.0793	0.0017	1228	16	1254	16	1178	42	-6
Zr25.1-oc	ii08	38	326	0.12	2.086	0.052	0.1899	0.0029	0.0799	0.0012	1143	17	1121	16	1194	30	6
Zr1.2-oc[S]	c23	209	411	0.51	2.215	0.061	0.1946	0.0025	0.0825	0.0021	1186	20	1146	14	1257	50	9
Zr27.2-oc	ii14	144	330	0.44	2.268	0.060	0.1971	0.0033	0.0826	0.0013	1204	18	1160	18	1260	31	8
Zr26.2-oc	ii38	194	707	0.27	2.094	0.054	0.1742	0.0030	0.0855	0.0012	1146	18	1035	16	1328	27	22
Zr19.2-oc	ii03	118	175	0.67	2.404	0.067	0.1983	0.0032	0.0873	0.0016	1244	20	1166	17	1367	35	15
Zr21.3-oc[S]	e22	192	337	0.57	2.462	0.059	0.2035	0.0031	0.0877	0.0020	1259	17	1194	17	1376	44	13
Zr23.2-oc	ii29	138	219	0.63	2.580	0.066	0.2123	0.0033	0.0883	0.0013	1296	18	1241	18	1390	28	11
Zr10.1-oc	c28	180	348	0.52	2.372	0.058	0.1899	0.0025	0.0906	0.0020	1234	18	1121	14	1438	42	22
Zr20.2-oc	ii25	71	171	0.42	2.836	0.088	0.1980	0.0037	0.1032	0.0024	1367	23	1164	20	1682	43	31
Zr8.1-oc[S]	e26	159	242	0.66	2.525	0.091	0.1681	0.0033	0.1094	0.0041	1275	26	1001	18	1789	68	44
Zr5.3-oc	e70	67	86	0.78	3.665	0.082	0.2169	0.0035	0.1228	0.0029	1563	18	1265	18	1997	42	37
Zr3.1-oc	e09	92	301	0.30	7.419	0.160	0.2151	0.0033	0.2524	0.0055	2161	19	1256	17	3200	34	61
Zr15.1-c	e64	41	57	0.72	2.416	0.058	0.2184	0.0032	0.0812	0.0020	1249	17	1273	17	1226	48	-4
Zr33.1-c	ii07	546	1249	0.44	2.118	0.050	0.1859	0.0028	0.0824	0.0010	1154	16	1099	15	1256	23	12
Zr2.2-c	c26	92	130	0.71	2.370	0.058	0.2050	0.0024	0.0836	0.0018	1233	17	1202	13	1283	42	6
Zr11.2-c	e78	112	133	0.84	2.391	0.061	0.2013	0.0033	0.0855	0.0022	1239	18	1182	18	1327	50	11
Zr8.2-c	e27	50	74	0.67	2.477	0.076	0.2067	0.0036	0.0877	0.0028	1261	22	1211	19	1376	61	12
Zr19.1-c	h07	762	444	1.72	2.424	0.061	0.1999	0.0031	0.0883	0.0012	1249	18	1174	17	1389	26	15
Zr10.1-c	e83	87	240	0.36	2.775	0.063	0.2269	0.0033	0.0883	0.0020	1350	17	1318	17	1389	43	5
Zr20.2-c	e49	82	93	0.89	2.614	0.072	0.2088	0.0032	0.0911	0.0026	1301	20	1222	17	1449	54	16
Zr18.1-c[S]	ii26	268	211	1.27	2.547	0.080	0.1892	0.0034	0.0972	0.0023	1284	23	1117	19	1571	44	29
Zr14.1-c	e57	52	222	0.23	2.836	0.062	0.2119	0.0030	0.0973	0.0022	1365	16	1239	16	1573	42	21
Zr13.2-c	e52	86	67	1.28	2.768	0.100	0.2088	0.0039	0.0975	0.0038	1344	28	1222	21	1577	73	23
Zr6.2-c	e23	117	320	0.36	2.514	0.059	0.1801	0.0030	0.1011	0.0023	1277	18	1067	16	1644	42	35
Zr20.1-c[S]	ii24	261	354	0.74	2.651	0.084	0.1874	0.0033	0.1017	0.0024	1313	24	1107	18	1655	44	33
Zr1.4-c	e02	43	65	0.66	2.476	0.075	0.1716	0.0030	0.1040	0.0033	1267	22	1021	16	1697	58	40
Zr31.1-c	ii12	63	304	0.21	2.519	0.072	0.1736	0.0028	0.1052	0.0020	1280	20	1032	15	1718	35	40
Zr17.1-c	c16	112	53	2.11	3.076	0.088	0.2066	0.0030	0.1083	0.0028	1427	22	1210	16	1771	47	32
Zr11.1-c	c22	64	66	0.97	3.061	0.087	0.1966	0.0029	0.1125	0.0028	1421	21	1157	15	1840	45	37
Zr7.2-c[S]	e74	160	115	1.40	3.170	0.120	0.1915	0.0040	0.1200	0.0051	1444	29	1129	22	1956	76	42
Zr19.1-c	e29	84	74	1.12	3.546	0.110	0.2080	0.0037	0.1239	0.0038	1544	25	1219	20	2013	54	39

73

333x		Th (ppm)	U (ppm)	Th/U	RATIO $^{207}Pb/$ ^{235}U	2SE	$^{206}Pb/$ ^{238}U	2SE	$^{207}Pb/$ ^{206}Pb	2SE	AGE $^{207}Pb/$ ^{235}U	2SE	$^{206}Pb/$ ^{238}U	2SE	$^{207}Pb/$ ^{206}Pb	2SE	% disc
Zr3.1-c[S]	j03	196	104	1.88	2.980	0.140	0.1672	0.0050	0.1296	0.0064	1400	35	996	28	2093	87	52
Zr10.2-c	f01	67	57	1.17	3.921	0.120	0.2134	0.0040	0.1349	0.0047	1619	25	1246	21	2163	61	42
Zr18.2-c	e75	169	170	0.99	4.000	0.140	0.2153	0.0036	0.1355	0.0045	1629	27	1258	20	2170	58	42
Zr13.1-c	c36	39	114	0.34	4.150	0.150	0.2185	0.0027	0.1368	0.0046	1665	29	1273	14	2187	58	42
Zr28.1-c	c38	124	139	0.89	5.670	0.220	0.2186	0.0032	0.1863	0.0055	1923	33	1274	17	2710	49	53
Zr7.1-c[S]	c12	125	159	0.78	6.250	0.320	0.2226	0.0032	0.2059	0.0098	2005	47	1295	17	2874	77	55
Zr3.1-c[S]	c32	95	67	1.41	4.624	0.120	0.1632	0.0027	0.2062	0.0051	1751	23	974	15	2876	40	66
Zr5.1-ac[S]	ii17	134	202	0.66	2.257	0.076	0.1971	0.0038	0.0839	0.0025	1198	24	1159	21	1290	58	10
Zr6.1-ac	ii21	86	89	0.97	3.263	0.110	0.2266	0.0046	0.1031	0.0028	1476	26	1316	24	1681	50	22
Zr6.1-ac	c39	74	158	0.47	3.536	0.110	0.2120	0.0022	0.1196	0.0032	1523	24	1239	12	1950	48	36
Zr5.1-ac	c15	130	186	0.70	4.500	0.150	0.2089	0.0027	0.1536	0.0041	1718	24	1222	14	2386	45	49

-R: RIM analyses -c: CORE analyses -oc: analyses of the OUTER CORE -ac: analyses of ACICULAR CORE

[S] : analyses with shorter signal, < 15s

-*: analyses used in the calculation of the weighted average 7/6 age

Table 2.5: Zircon (LA–ICPMS) U–Th–Pb data for sample 244 (LBS).

					RATIO						AGE						
					$^{207}Pb/$		$^{206}Pb/$		$^{207}Pb/$		$^{207}Pb/$		$^{206}Pb/$		$^{207}Pb/$		
244		Th	U	Th/U	^{235}U	2SE	^{238}U	2SE	^{206}Pb	2SE	^{235}U	2SE	^{238}U	2SE	^{206}Pb	2SE	% disc
		(ppm)	(ppm)														
Concordant data																	
Zr16.1-sB	c36	41	483	**0.08**	1.764	0.033	0.1744	0.0024	0.0733	0.0012	1032	12	1038	13	**1023**	33	-1
Zr37.1-sB	c27	96	297	**0.41**	1.762	0.038	0.1743	0.0030	0.0733	0.0014	1030	14	1035	17	**1023**	39	-1
Zr17.1-sB	c11	121	341	**0.35**	1.726	0.038	0.1695	0.0026	0.0739	0.0015	1017	14	1009	14	**1039**	41	3
Zr32.1-sB	b47	38	448	**0.08**	1.741	0.029	0.1727	0.0033	0.0740	0.0007	1024	11	1027	18	**1041**	19	1
Zr34.1-sB	b33	36	188	**0.19**	1.736	0.033	0.1700	0.0033	0.0742	0.0010	1022	12	1013	18	**1047**	27	3
Zr35.1-sB[S]	b57	109	406	**0.27**	1.817	0.046	0.1765	0.0044	0.0746	0.0013	1051	17	1047	24	**1058**	35	1
Zr15.2-sB	b35	30	331	**0.09**	1.850	0.039	0.1801	0.0026	0.0746	0.0015	1064	14	1067	14	**1058**	40	-1
Zr33.1-sB	b26	44	277	**0.16**	1.772	0.038	0.1719	0.0036	0.0747	0.0012	1036	14	1022	20	**1060**	32	4
Zr11.1-R	b70	37	223	**0.17**	1.687	0.029	0.1687	0.0032	0.0726	0.0007	1004	11	1006	17	**1002**	21	0
Zr14.3-R	c03	49	279	**0.18**	1.696	0.035	0.1664	0.0023	0.0732	0.0014	1005	13	992	13	**1019**	39	3
Zr28.1-R	c44	28	294	**0.12**	1.671	0.045	0.1669	0.0035	0.0734	0.0018	1002	17	994	19	**1025**	50	3
Zr14.1-R	b37	41	207	**0.20**	1.798	0.035	0.1764	0.0024	0.0739	0.0013	1045	13	1047	13	**1038**	36	-1
Zr19.2-R	b29	35	288	**0.12**	1.716	0.030	0.1687	0.0033	0.0741	0.0009	1014	11	1005	19	**1043**	24	4
Zr14.2-R	b38	46	314	**0.15**	1.788	0.038	0.1747	0.0025	0.0742	0.0014	1040	14	1038	14	**1047**	38	1
Zr4.1-R	c15	43	459	**0.09**	1.810	0.035	0.1763	0.0024	0.0743	0.0013	1049	13	1047	13	**1049**	35	0
Zr2.4-R	b32	80	618	**0.13**	1.796	0.034	0.1742	0.0025	0.0745	0.0013	1044	13	1035	14	**1055**	35	2
Zr11.1-R	c34	54	334	**0.16**	1.854	0.035	0.1797	0.0024	0.0745	0.0013	1065	12	1065	13	**1055**	35	-1
Zr18.2-R	b59	24	529	**0.05**	1.773	0.028	0.1741	0.0032	0.0747	0.0006	1035	10	1035	18	**1061**	16	3
Zr2.3-R	b31	58	443	**0.13**	1.757	0.039	0.1724	0.0026	0.0748	0.0016	1028	14	1025	14	**1063**	43	4
Zr17.1-R	b60	47	506	**0.09**	1.794	0.029	0.1750	0.0033	0.0749	0.0006	1043	10	1039	18	**1067**	16	3
Zr13.1-R	c07	32	556	**0.06**	1.738	0.035	0.1687	0.0025	0.0752	0.0014	1023	13	1005	14	**1073**	37	6
Zr13.2-R	c08	33	676	**0.05**	1.862	0.037	0.1769	0.0025	0.0763	0.0013	1067	13	1050	13	**1103**	34	5
Zr9.1-m	c31	58	535	**0.11**	1.773	0.033	0.1743	0.0023	0.0737	0.0012	1036	12	1035	13	**1032**	33	0
Zr29.1-m	b64	24	341	**0.07**	1.713	0.027	0.1695	0.0032	0.0737	0.0006	1013	10	1009	18	**1033**	17	2
Zr21.1-m	b43	73	267	**0.28**	1.724	0.028	0.1703	0.0032	0.0738	0.0008	1018	11	1014	18	**1035**	21	2
Zr12.2-m	b50	26	343	**0.08**	1.644	0.034	0.1640	0.0033	0.0738	0.0011	989	13	979	18	**1036**	30	6
Zr8.1-m	b30	20	402	**0.05**	1.734	0.030	0.1693	0.0033	0.0740	0.0008	1020	11	1008	18	**1041**	22	3
Zr8.2-m	c36	14	551	**0.04**	1.762	0.038	0.1713	0.0031	0.0740	0.0014	1030	14	1019	17	**1042**	38	2
Zr6.2-m	c08	6	372	**0.02**	1.803	0.038	0.1758	0.0031	0.0741	0.0014	1046	14	1044	17	**1045**	38	0

244		Th (ppm)	U (ppm)	Th/U	RATIO ^{207}Pb/^{235}U	2SE	^{206}Pb/^{238}U	2SE	^{207}Pb/^{206}Pb	2SE	AGE ^{207}Pb/^{235}U	2SE	^{206}Pb/^{238}U	2SE	^{207}Pb/^{206}Pb	2SE	% disc
Zr3.2-m	c16	35	732	0.05	1.784	0.036	0.1746	0.0031	0.0742	0.0013	1038	13	1038	17	1046	35	1
Zr2.2-m	c35	21	609	0.05	1.740	0.036	0.1700	0.0031	0.0742	0.0013	1022	13	1011	17	1048	35	4
Zr2.2-c	b28	28	411	0.07	1.768	0.033	0.1745	0.0024	0.0736	0.0012	1034	12	1037	13	1031	33	-1
Zr2.1-c	b27	20	458	0.04	1.782	0.033	0.1755	0.0023	0.0740	0.0012	1038	12	1042	13	1040	33	0
Zr11.2-c	c46	27	459	0.06	1.827	0.034	0.1793	0.0024	0.0744	0.0012	1055	12	1063	13	1053	32	-1
Zr18.1-c	c17	4	30	0.13	1.859	0.075	0.1793	0.0032	0.0747	0.0028	1062	27	1063	17	1060	75	0
Zr31.1-c	b24	6	32	0.19	1.791	0.056	0.1730	0.0038	0.0752	0.0021	1039	20	1028	21	1074	56	4
Zr13.3-c	c40	25	640	0.04	1.897	0.036	0.1810	0.0025	0.0758	0.0013	1079	13	1073	14	1088	34	1
Zr38.1-c	b65	22	316	0.07	1.908	0.032	0.1817	0.0034	0.0761	0.0008	1082	11	1076	19	1098	21	2
Zr31.2-c	b25	10	44	0.23	1.974	0.068	0.1877	0.0044	0.0766	0.0026	1105	24	1108	24	1111	68	0
Zr8.1-c^S	c06	36	378	0.10	1.926	0.042	0.1826	0.0027	0.0769	0.0015	1089	15	1081	15	1119	39	3
Zr36.1-c	b56	30	324	0.09	1.898	0.031	0.1791	0.0034	0.0773	0.0008	1079	11	1062	19	1130	21	6
Zr5.1-c	b37	101	118	0.86	3.695	0.075	0.2733	0.0054	0.0989	0.0015	1569	16	1558	27	1603	28	3
Discordant data																	
Zr12.1-R^S	b48	28	342	0.08	1.652	0.036	0.1622	0.0040	0.0743	0.0013	989	14	969	22	1050	35	8
Zr3.2-R	c14	39	352	0.11	1.750	0.035	0.1689	0.0024	0.0749	0.0014	1027	13	1006	13	1066	38	6
Zr14.1-R	b46	30	359	0.08	1.734	0.039	0.1680	0.0038	0.0755	0.0012	1021	15	1000	21	1082	32	8
Zr22.1-R	b61	49	358	0.14	1.785	0.032	0.1717	0.0033	0.0759	0.0009	1040	11	1021	18	1091	23	6
Zr4.2-R	c41	13	451	0.04	1.782	0.035	0.1708	0.0029	0.0759	0.0013	1038	13	1017	16	1092	34	7
Zr13.1-R	b72	53	325	0.16	1.667	0.036	0.1599	0.0034	0.0760	0.0011	994	14	956	19	1095	29	13
Zr24.1-R	c17	22	216	0.09	1.726	0.048	0.1635	0.0032	0.0764	0.0018	1016	17	976	18	1106	47	12
Zr25.1-R	c11	35	345	0.13	1.819	0.039	0.1717	0.0031	0.0769	0.0014	1051	14	1022	17	1119	36	9
Zr3.1-R	c12	40	387	0.10	1.798	0.039	0.1672	0.0025	0.0780	0.0015	1044	14	997	14	1147	38	13
Zr23.1-R	c29	15	430	0.05	1.804	0.038	0.1662	0.0029	0.0785	0.0014	1047	14	991	16	1161	35	15
Zr30.1-R	b69	30	245	0.12	1.896	0.035	0.1745	0.0033	0.0786	0.0010	1078	12	1037	18	1162	25	11
Zr4.2-R	c33	60	368	0.16	1.916	0.036	0.1758	0.0024	0.0787	0.0013	1088	13	1044	13	1166	33	10
Zr26.1-R	c43	58	246	0.29	1.823	0.043	0.1660	0.0031	0.0793	0.0017	1051	15	989	17	1180	42	16
Zr7.1-R^S	b38	89	360	0.25	1.756	0.042	0.1529	0.0035	0.0835	0.0017	1029	15	919	20	1281	40	28
Zr27.2-m	c25	20	297	0.09	3.313	0.084	0.2213	0.0041	0.0758	0.0014	1035	13	1009	16	1089	37	7
Zr9.1-m	b73	19	556	0.03	2.146	0.048	0.1774	0.0033	0.0873	0.0015	1159	15	1052	18	1367	33	23
Zr7.2-m	b39	29	483	0.06	2.061	0.041	0.1712	0.0033	0.0875	0.0013	1136	13	1018	18	1372	29	26
Zr13.2-m	c21	6	1545	0.00	2.759	0.052	0.2259	0.0038	0.0884	0.0014	1344	14	1313	20	1392	30	6

244		Th (ppm)	U (ppm)	Th/U	RATIO $^{207}Pb/^{235}U$	2SE	$^{206}Pb/^{238}U$	2SE	$^{207}Pb/^{206}Pb$	2SE	AGE $^{207}Pb/^{235}U$	2SE	$^{206}Pb/^{238}U$	2SE	$^{207}Pb/^{206}Pb$	2SE	% disc
Zr7.3-m	c12	32	745	0.05	1.771	0.037	0.1695	0.0028	0.0891	0.0025	1137	20	1003	18	1406	54	29
Zr5.2-m[S]	c10	5	1764	0.00	2.848	0.063	0.2285	0.0046	0.0900	0.0017	1367	17	1326	24	1425	36	7
Zr10.2-m	c27	11	91	0.12	2.600	0.110	0.1824	0.0029	0.1022	0.0038	1287	32	1080	16	1664	69	35
Zr11.2-m	c20	21	1401	0.02	2.075	0.061	0.1682	0.0033	0.1076	0.0022	1480	20	1288	21	1759	37	27
Zr6.1-c	b68	8	104	0.08	2.227	0.060	0.2128	0.0047	0.0755	0.0018	1186	19	1244	25	1082	48	-15
Zr13.4-c	c41	22	503	0.04	2.122	0.044	0.1885	0.0028	0.0813	0.0015	1156	14	1113	15	1228	36	9
Zr34.2-c[S]	b34	99	632	0.16	2.232	0.049	0.1941	0.0043	0.0832	0.0012	1189	15	1143	23	1274	28	10
Zr19.1-c	b28	153	180	0.85	2.717	0.055	0.2229	0.0047	0.0881	0.0013	1330	15	1297	25	1385	28	6
Zr15.1-c	b34	26	879	0.03	2.878	0.055	0.2329	0.0034	0.0891	0.0014	1375	14	1349	18	1407	30	4
Zr3.1-c	c15	402	739	0.60	2.754	0.064	0.2201	0.0042	0.0903	0.0017	1343	17	1282	22	1432	36	10
Zr10.1-c	c25	10	32	0.32	2.290	0.120	0.1847	0.0040	0.0903	0.0047	1203	38	1092	21	1432	99	24
Zr17.2-c	c28	532	1797	0.35	2.758	0.055	0.2208	0.0040	0.0906	0.0015	1344	14	1286	21	1437	32	11
Zr18.1-c	b32	361	453	0.80	3.582	0.063	0.2651	0.0054	0.0984	0.0008	1546	14	1515	28	1594	14	5
Zr7.1-c	c04	270	620	0.44	3.485	0.078	0.2517	0.0038	0.0993	0.0016	1520	18	1449	20	1611	30	10
Zr2.1-c	c34	120	673	0.24	3.726	0.075	0.2701	0.0048	0.1002	0.0017	1576	16	1540	24	1628	32	5
Zr4.1-c	b51	111	576	0.19	3.311	0.070	0.2335	0.0046	0.1030	0.0014	1480	17	1352	24	1679	25	19
Zr24.2-c	c19	281	779	0.45	3.853	0.082	0.2519	0.0045	0.1097	0.0021	1602	17	1448	23	1794	35	19
Zr1.1-c	c40	39	1257	0.07	3.603	0.082	0.2311	0.0041	0.1128	0.0022	1546	18	1339	21	1845	35	27
Zr5.1-c[S]	c24	218	238	0.91	4.048	0.088	0.2569	0.0040	0.1148	0.0023	1642	18	1474	21	1877	36	21
Zr27.1-c	c24	49	898	0.07	3.500	0.110	0.2155	0.0048	0.1155	0.0033	1528	25	1259	25	1888	51	33
Zr6.1-c	c28	241	711	0.34	4.810	0.110	0.2982	0.0045	0.1155	0.0027	1782	20	1682	22	1888	42	11
Zr20.1-c	b74	84	592	0.14	3.614	0.080	0.2228	0.0045	0.1172	0.0022	1550	18	1298	24	1914	34	32
Zr16.1-c	b52	69	527	0.13	3.800	0.170	0.2309	0.0059	0.1197	0.0037	1576	36	1340	31	1952	55	31
Zr21.2-c	b44	215	282	0.76	5.271	0.110	0.3024	0.0070	0.1278	0.0015	1864	19	1703	35	2068	21	18

-R: RIM analyses   -c: CORE analyses   [S] : analyses with shorter signal, < 15s

-sB: 'soccer BALL' analyses and -m: 'MANTLE' analyses used in the calculation of the weighted average 7/6 ages
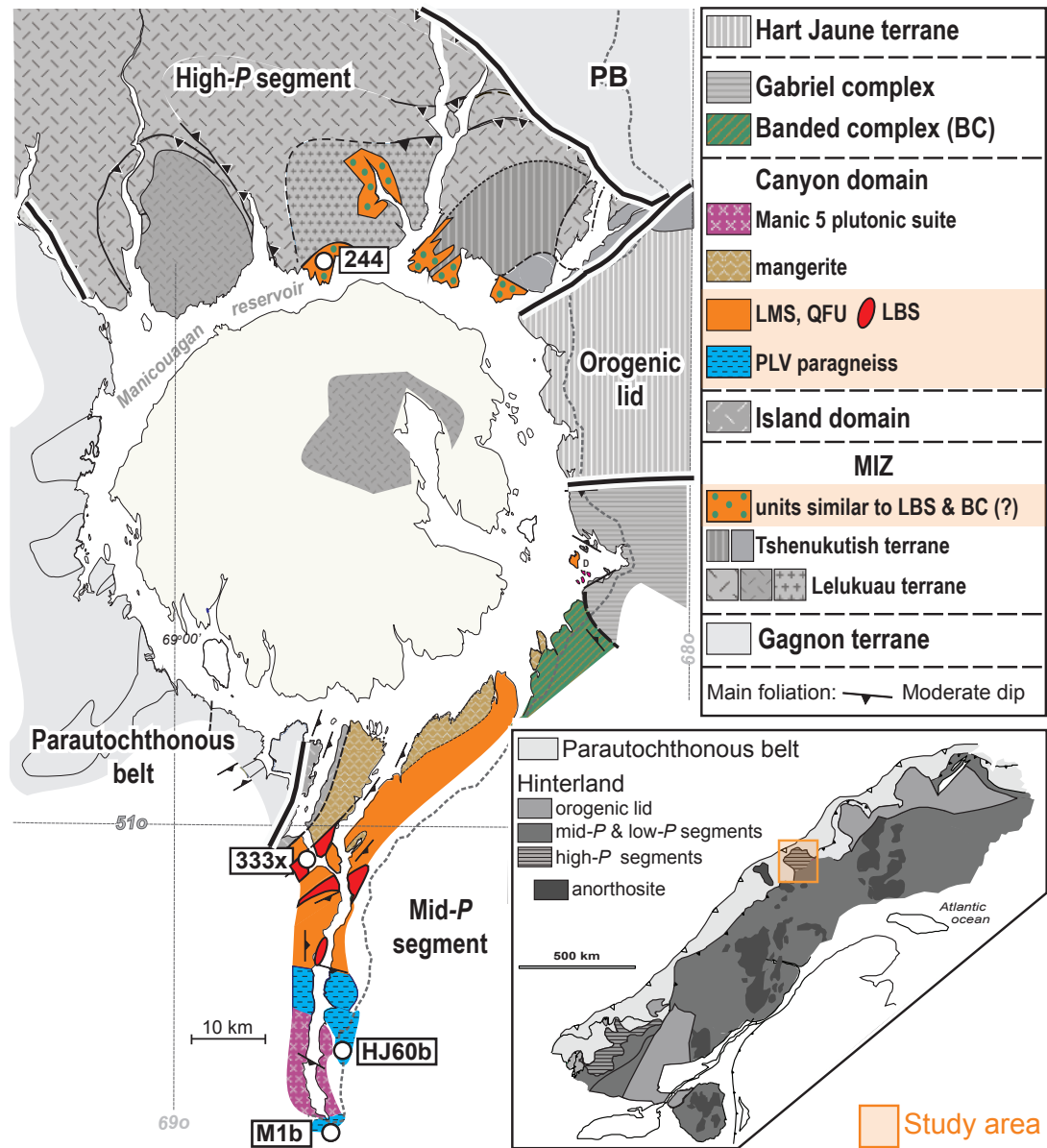
Figure 3.1: Simplified geological map of the Manicouagan area with location of the four samples of interest and inset map showing the general framework of the Grenville Province (updated from Dunning and Indares, 2010). LMS – layered mafic suite; QFU – layered quartzofeldspathic unit; LBS – layered bimodal sequence, including zones of hydrothermal alteration; PLV – Complexe de la Plus Value; MIZ – Manicouagan Imbricate Zone.
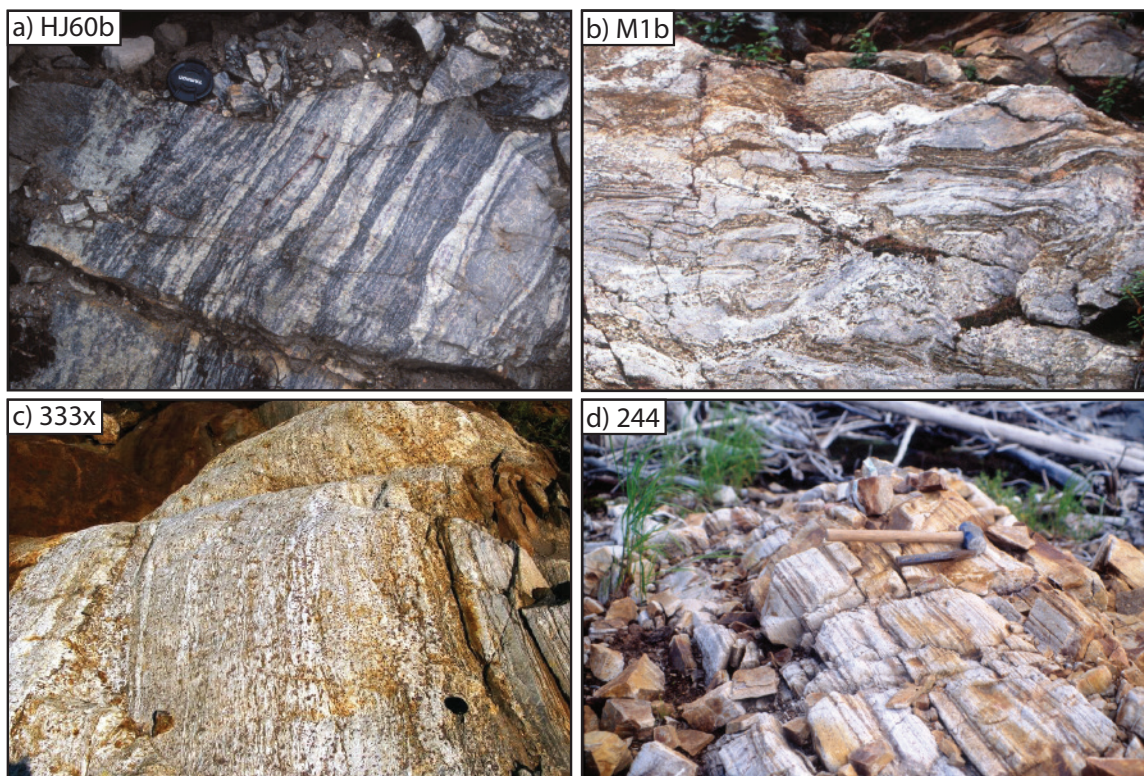
Figure 2.2: Outcrop photographs of the four rock samples discussed in this study: (a) HJ60b, (b) M1b, (c) 333x, and (d) 244.
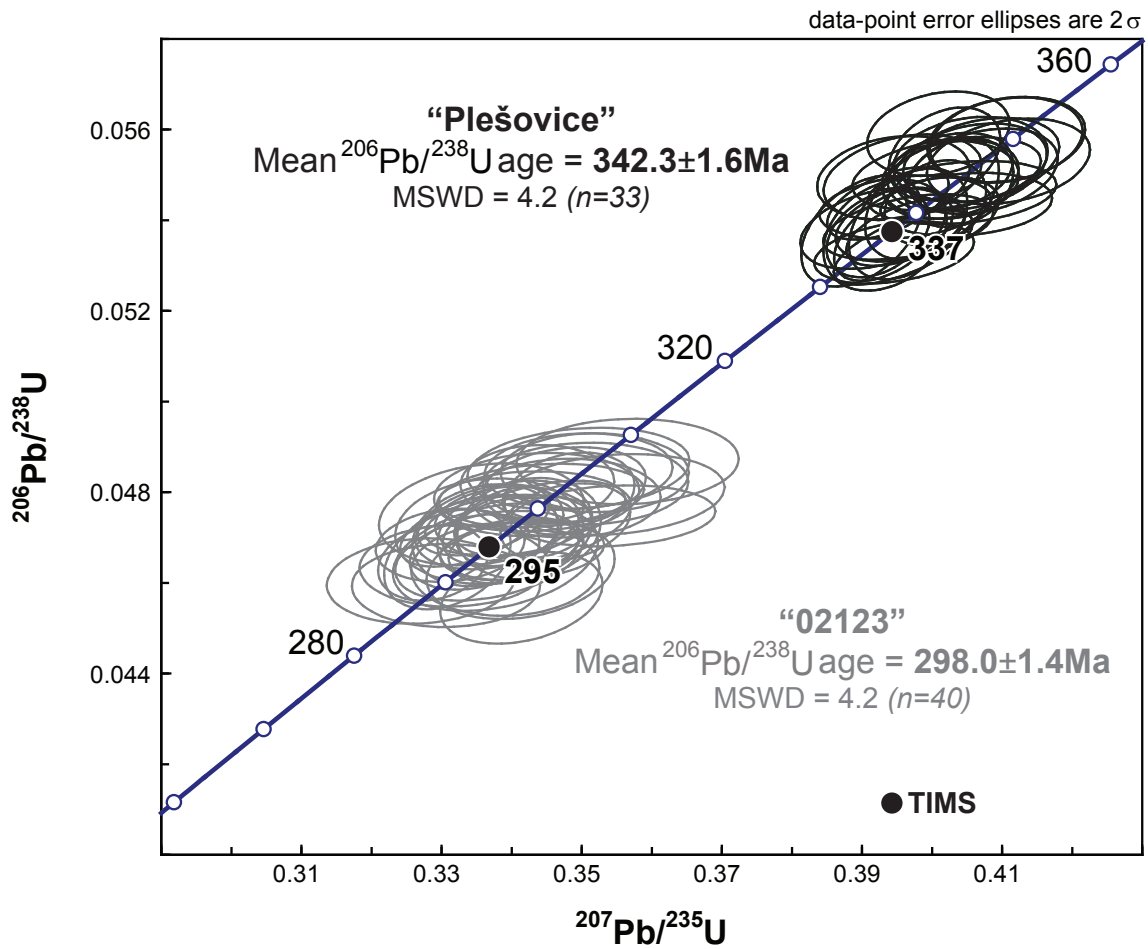
Figure 2.3: Concordia diagram highlighting the precision and accuracy of the U–Pb data. Both data sets obtained for the zircon standards 02123 and Plešovice are well clustered, and agree within error with the ID–TIMS ages previously determined at 295 ± 1 Ma for 02123 (Ketchum *et al.,* 2001) and at 337.1 ± 0.3 Ma for Plešovice (Sláma *et al.,* 2008).
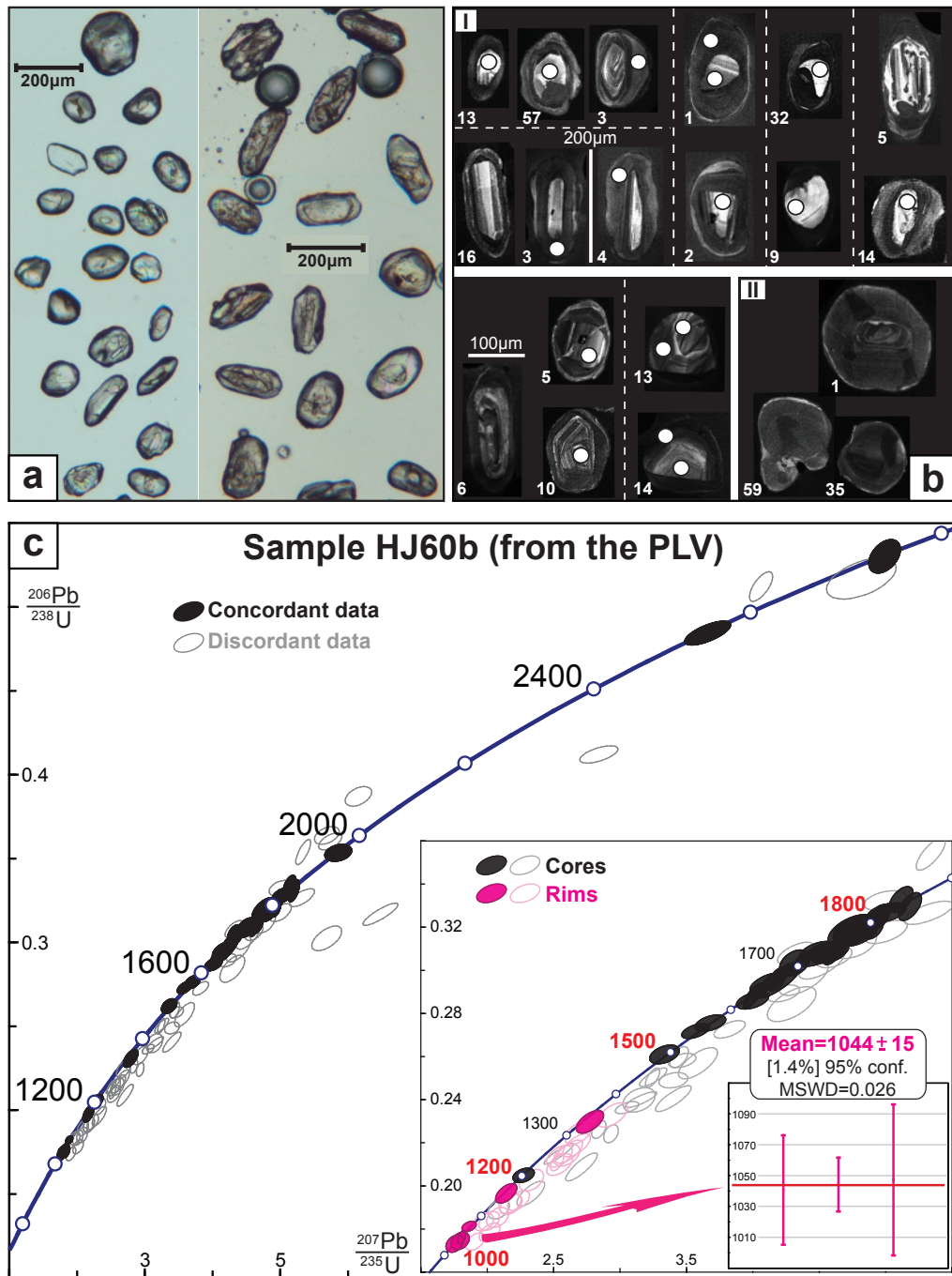
Figure 2.4: Zircon data of sample HJ60b: (a) transmitted light microphotographs, (b) CL images (the white dots correspond to the location of the U–Pb analyses and the numbers assigned to each grain correspond to the original numbering used during the imaging of all four mounts), and (c) concordia diagrams (n=85 U–Pb analyses on 56 grains) with in inset a close-up view of the main data set. For this sample, a plot showing the weighted average [207]Pb/[206]Pb age calculated for three rim analyses was added.
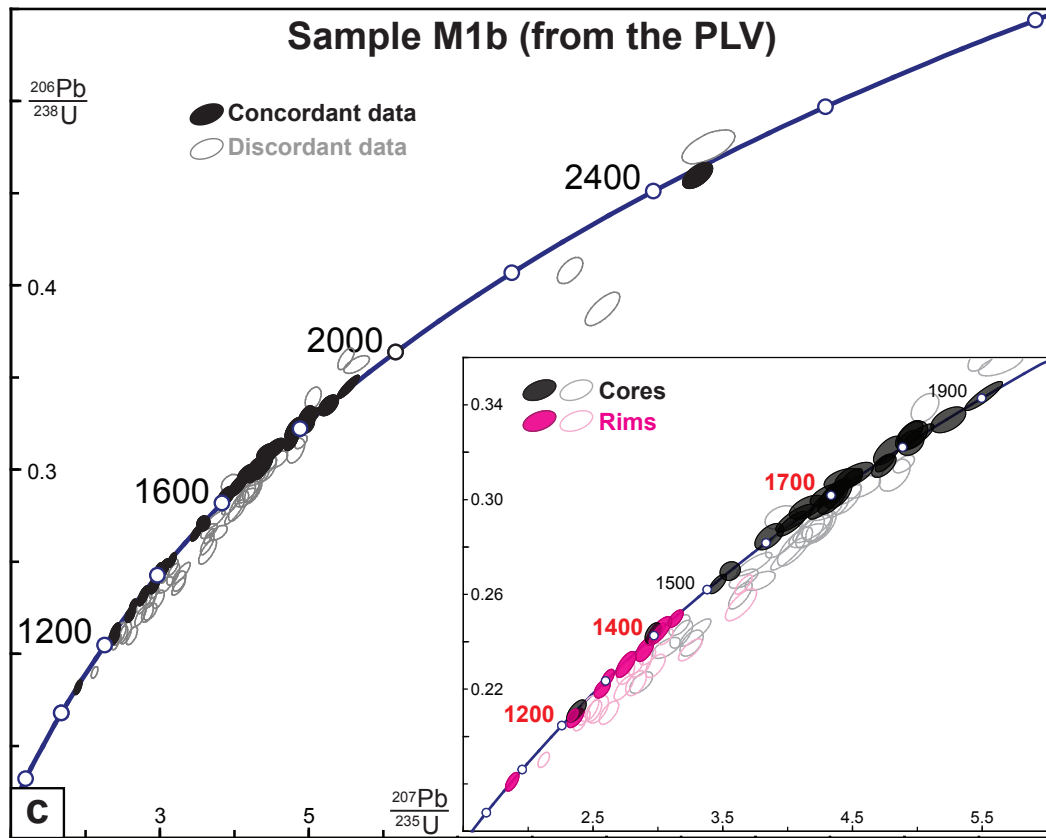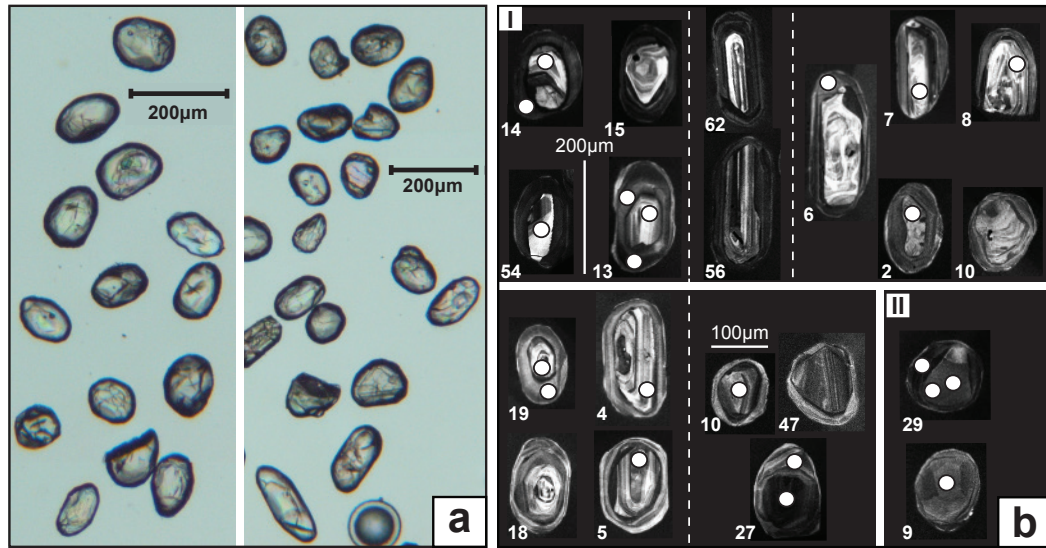
Figure 2.5: Zircon data of sample M1b: (a) transmitted light microphotographs, (b) CL images (the white dots correspond to the location of the U–Pb analyses and the numbers assigned to each grain correspond to the original numbering used during the imaging of all four mounts), and (c) concordia diagrams (n=82 U–Pb analyses on 56 grains) with in inset a close-up view of the main data set.
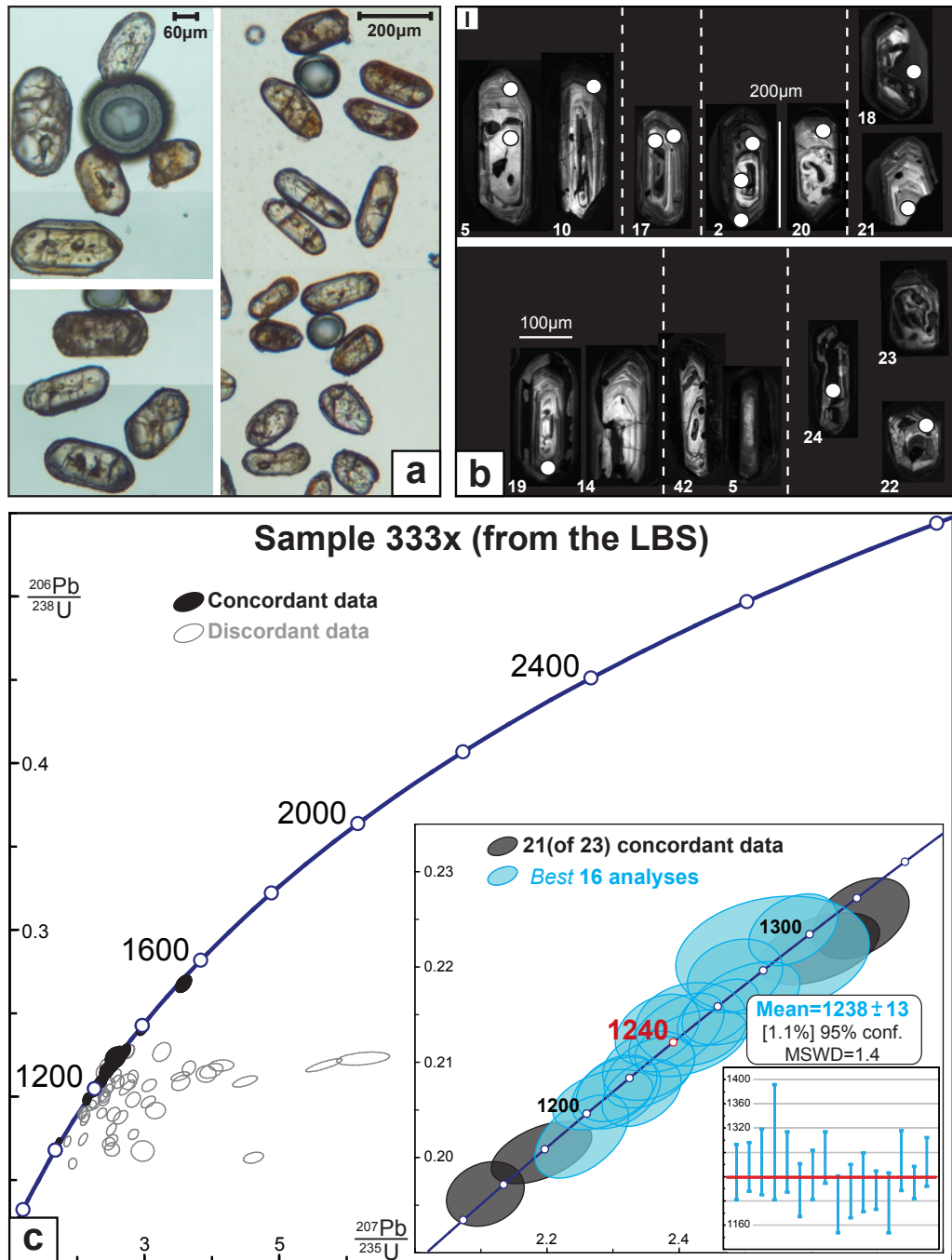
Figure 2.6: Zircon data of sample 333x: (a) transmitted light microphotographs, (b) CL images (the white dots correspond to the location of the U–Pb analyses and the numbers assigned to each grain correspond to the original numbering used during the imaging of all four mounts), and (c) concordia diagrams (n=72 U–Pb analyses on 51 grains) with in inset a close-up view of the main data set. For this sample, a plot showing the weighted average [207]Pb/[206]Pb age calculated for 16 (highest quality) analyses was added.
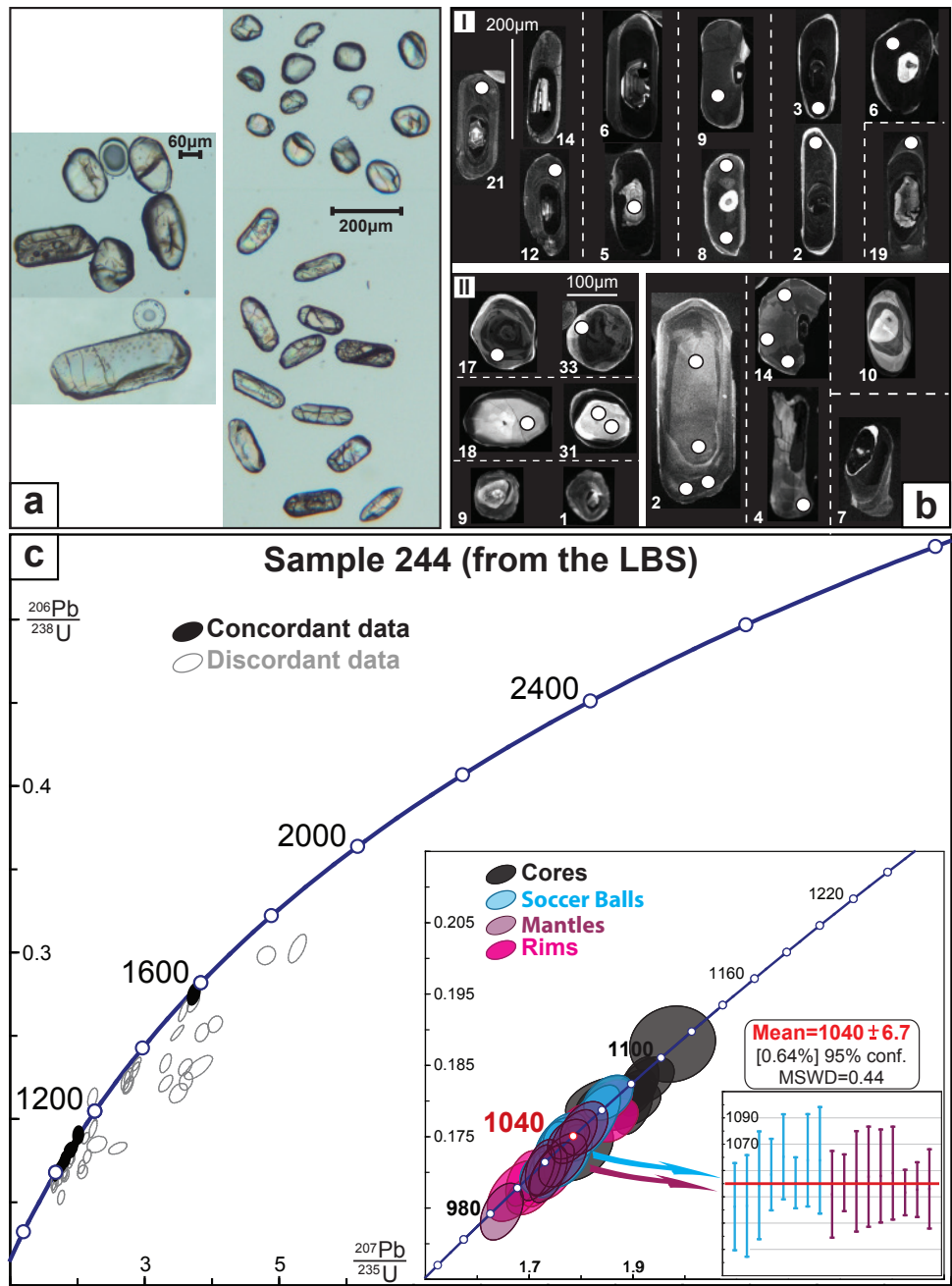
Figure 2.7: Zircon data of sample 244: (a) transmitted light microphotographs, (b) CL images (the white dots correspond to the location of the U–Pb analyses and the numbers assigned to each grain correspond to the original numbering used during the imaging of all four mounts), and (c) concordia diagrams (n=84 U–Pb analyses on 53 grains) with in inset a close-up view of the main data set. For this sample, a plot showing the weighted average ^{207}Pb/^{206}Pb age calculated for the 17 analyses including eight from 'soccer ball' zircon and seven from mantles was added.
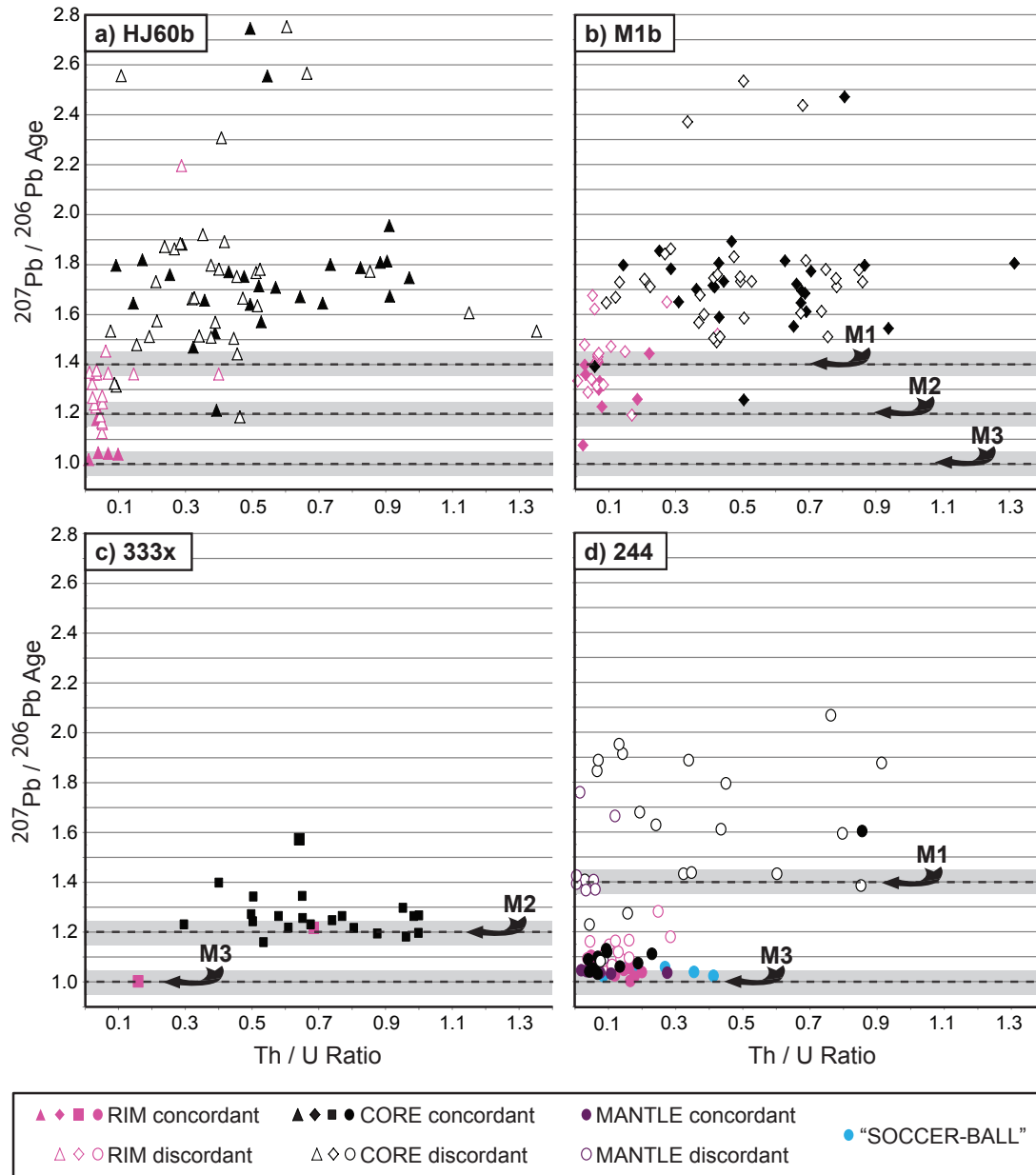
Figure 2.8: Plot after Gehrels *et al.* (2009) showing the Th/U ratios calculated for zircon of all four samples against the ^{207}Pb/^{206}Pb ages; (a) sample HJ60b, (b) sample M1b, (c) sample 333x, and (d) sample 244. Periods of time during which the occurrence/dominance of metamorphic events or 'pulses' (M1, M2, M3) is inferred are highlighted in dark grey, with a dotted line at the presumed age (1400 Ma, 1200 Ma, 1000 Ma).
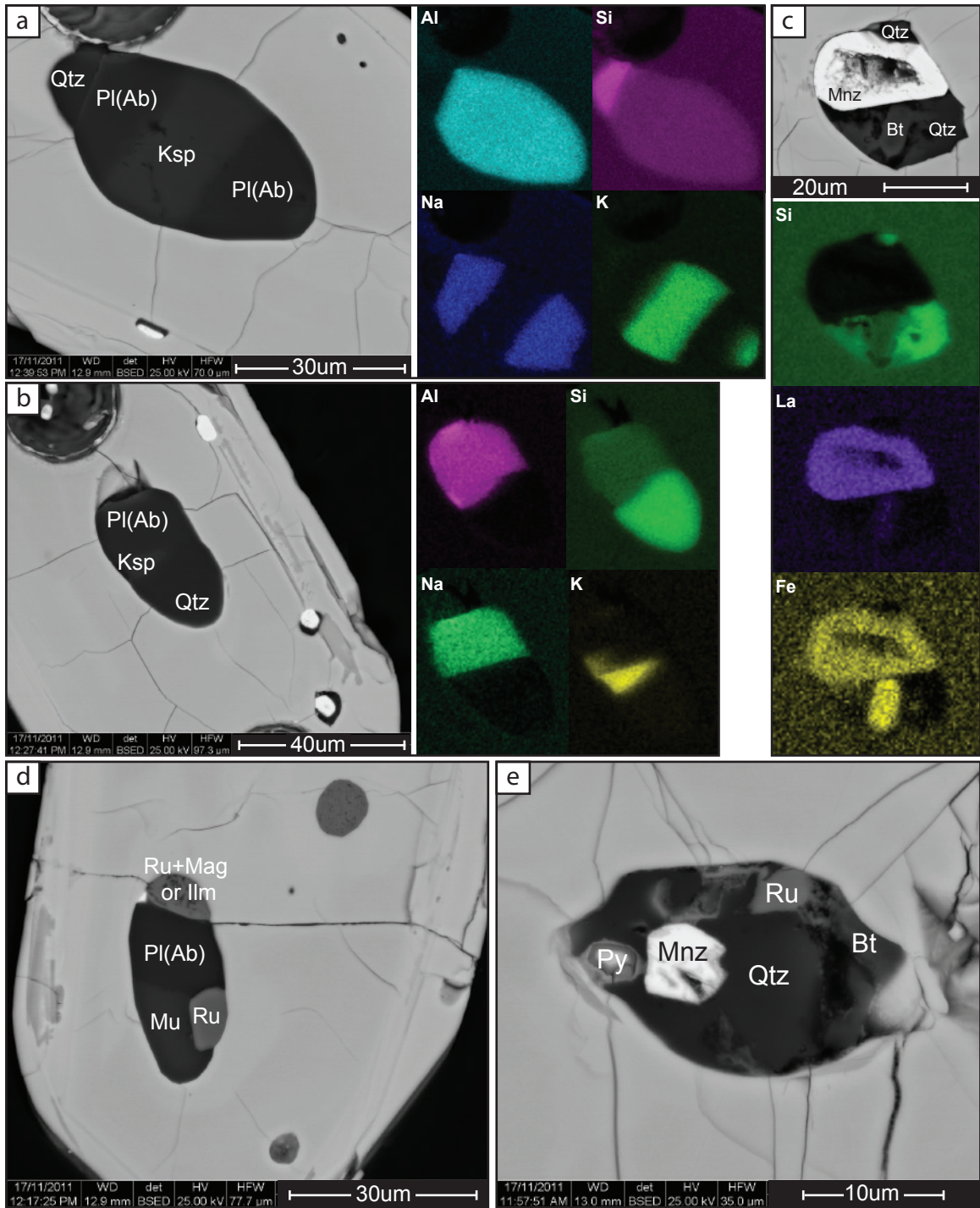
Figure 2.9: SEM images showing five polymineralic inclusions in zircon from sample 333x. For three of them, EDX false colors elemental maps are also shown to illustrate the characteristic 'banded' pattern of those inclusions.

APPENDICES OF CHAPTER 2 INCLUDED (AS EXCEL FILES) IN THE CD

APPENDIX 2.1: Zircon (LA-ICPMS) U–Pb data collected on zircon standard 91500.

Zircon standard 91500 was used as a calibration material in 9 runs, 19 analyses (~7%) with outlying U–Pb ratios (≥2%) were discarded among the 266 analyses.

APPENDIX 2.2: Zircon (LA-ICPMS) U–Pb data collected on zircon standard Plešovice

Zircon standard Plešovice was used as a calibration material in 3 runs (using the 4–5Hz setting), 3 analyses from a total of 73 (~4%) were discarded. This zircon was also treated as an unknown in 9 runs, to assess the precision and accuracy of the method. 33 analyses yielded a weighted mean $^{206}Pb/^{238}U$ age of 342.3 Ma ± 1.6 Ma (MSWD=4.2).

APPENDIX 2.3: Zircon (LA-ICPMS) U–Pb data collected on zircon standard 02123

Zircon 02123 was analyzed 42 times as an unknown over all 12 runs. The weighted average $^{206}Pb/^{238}U$ age for 40 analyses of zircon 02123 is 298.0 Ma ± 1.4 Ma (MSWD=4.2).

CHAPTER 3

3. ANATECTIC RECORD AND CONTRASTING *P–T* PATHS FROM ALUMINOUS GNEISSES FROM THE CENTRAL GRENVILLE PROVINCE

ABSTRACT

Anatectic aluminous gneisses, some derived from sedimentary rocks of broadly pelitic composition and others from hydrothermally altered felsic volcanic rocks, are exposed in the mid-P and high-P segments of the hinterland in the central Grenville Province. These gneisses consist dominantly of garnet, biotite, K-feldspar, plagioclase and quartz, with sillimanite or kyanite, and display microstructural evidence of anatexis by fluid-absent reactions consuming muscovite and/or biotite.

Melt-related microstructures, such as inter-granular films and/or interstitial quartz or feldspars enclosing relict phases, are most abundant in the metasedimentary samples. Despite anatexis at granulite-facies conditions, the hydrothermally altered rocks preserve earlier features attributed to the circulation of hydrothermal fluids, such as sillimanite seams, dismembered quartz veins, and garnet-rich aluminous nodules in a K-feldspar dominated matrix.

Microstructural and mineral chemical data, integrated with P–T pseudosections calculated with THERMOCALC for the metasedimentary rocks permit qualitative constraints on the P–T paths. Data from a high-P kyanite-bearing sample are consistent with a steep prograde P–T path up to ~14.5 kbar and 860–900 $^{\circ}$C, followed by decompression with minor cooling down to the solidus at ~11 kbar and 870 $^{\circ}$C. This pressure-dominated P–T path is similar to those inferred in other parts of the high-P segment in the central Grenville Province. In contrast, the P–T path predicted from a mid-P sillimanite-bearing paragneiss has a strong T gradient with P–T of ~9.5 kbar and 850 $^{\circ}$C at the thermal peak, and a retrograde portion down to ~8 kbar and 820 $^{\circ}$C. In a broad

sense, these two contrasting P–T patterns are consistent with predictions of thermo-mechanical modelling of large hot orogens in which P–T paths with strong P gradients exhume deeper rocks in the orogenic flanks, whereas P–T paths with strong T gradients in the orogenic core reflect protracted lateral transport of ductile crust beneath a plateau.

3.1. INTRODUCTION

Anatectic rocks commonly occur in the exposed internal zones (hinterland) of large hot orogens and their microstructures have the potential to preserve a record of high-temperature processes in orogenic environments at a range of scales, from localized partial melting to transport mechanisms in ductile crust (Brown, 2010). Identification of criteria for melt-related microstructures is sufficiently well established so that links can be made between the partial melting history and microstructural evolution of anatectic rocks (*cf.,* Vernon and Collins, 1988; Harte *et al.,* 1991; Sawyer, 1998; Holness *et al.,* 2011). Although in tectonically active metamorphic environments such microstructures are prone to obliteration by deformation and recrystallization, they can be preserved if protected by rigid porphyroblasts such as garnet, or if the melt crystallized late.

In the case of aluminous anatectic rocks, the availability of a felsic melt model (White *et al.,* 2002; 2007), allows for integrated interpretations of microstructures and mineral compositions in terms of P–T paths within the framework of P–T pseudosections (isochemical P–T phase diagrams). Studies of aluminous systems commonly refer to metasedimentary rocks such as metapelites and metagreywakes (Johnson *et al*., 2008; White *et al*., 2007). However, aluminous rocks may also be derived from hydrothermally

altered felsic volcanic precursors (Bonnet and Corriveau, 2007), in which case the overall aluminous bulk chemistry and the general microstructure at the onset of metamorphism may vary significantly from that of their metasedimentary counterparts.

Often compared to the Himalaya-Tibet system, the Mesoproterozoic Grenville Province is inferred to represent remnants of the oldest large hot orogen on Earth (*cf.,* in Rivers *et al.*, 2012).

The Grenvillian orogeny resulted in granulite-facies metamorphism and crustal anatexis in large portions of the exposed hinterland of the Province, which are further divided into high-*P* and mid-*P* segments, or belts. These are locally juxtaposed with crustal segments that experienced lower grade Grenvillian age metamorphism (low-*P* and orogenic lid; Rivers, 2008, 2012) and this overall configuration is attributed to the collapse of an orogenic plateau (Rivers, 2012).

Heterogeneous flow of middle to lower orogenic crust during high-grade metamorphism is inferred to have been instrumental in the overall tectonic evolution of the hinterland (Jamieson *et al.* 2007, 2010; Jamieson and Beaumont, 2011). Therefore, understanding the metamorphic record of the Grenville is critical for the assessment of the current tectonic models. However, rigorous investigation of the *P–T* conditions and paths as well as of the role of partial melting on the microstructural evolution of the anatectic rocks in the granulite-facies belts remains scarce.

Among the exceptions, a recent study has highlighted the metamorphic evolution of a high-*P* segment in the Manicouagan area of the central Grenville Province (Fig. 3.1; Indares *et al.,* 2008), where the recorded *P–T* paths are in the kyanite stability field (Cox and Indares, 1999a, b; Yang and Indares, 2005; Indares and Dunning, 2001). The high-*P*

segment in this area is tectonically overlain by mid-*P* granulite-facies rocks (Dunning and Indares, 2010) including sillimanite-bearing anatectic aluminous gneisses of diverse origins, such as metasediments of broadly pelitic composition and hydrothermally altered felsic volcanic rocks (Indares and Moukhsil, 2013; Lasalle *et al.,* 2013). These aluminous gneisses belong to lithologic associations of the Canyon domain (Hynes *et al.,* 2000; Dunning and Indares, 2010), and kyanite-bearing equivalents of some of them are also reported from the southern tip of the high-*P* segment. Exposure of both high-*P* and mid-*P* portions of the hinterland in the Manicouagan area (Fig. 3.1) provides a unique opportunity to gain insights on high-*T* metamorphic processes at a range of crustal depths.

The aim of this contribution is to investigate the effect of anatexis on the microstructural evolution of aluminous gneisses from the Canyon domain of the Manicouagan area and interpret this evolution in terms of *P–T* paths within the framework of *P–T* pseudosections. This study provides the first (to our knowledge) comprehensive assessment of the metamorphic record of mid-*P* rocks in the Grenvillian hinterland and a comparison between the *P–T* evolution of two juxtaposed high-*P* and mid-*P* segments. In addition, it discusses the results in the light of recent geodynamic models for the evolution of the Grenvillian orogen, and explores the effect of granulite-facies metamorphism and partial melting in a range of aluminous rock types.

3.2. REGIONAL GEOLOGY

The Manicouagan area straddles the boundary between the Parautochthonous belt and the structurally higher hinterland, in the central part of the Grenville Province (Fig. 3.1). In this area, the Parautochthonous belt is represented by Archean and Paleoproterozoic units of the Gagnon terrane (van Gool *et al.,* 2008), which were metamorphosed under amphibolite to granulite-facies conditions during the waning stages of the Grenvillian orogeny (*ca.* 990–980 Ma; Jordan *et al.,* 2006). In contrast, the hinterland consists of lithotectonic packages of Paleoproterozoic to Mesoproterozoic rocks (Dunning and Indares, 2010) with diverse metamorphic signatures acquired during the culmination of the Grenvillian orogeny (*ca.* 1080–1040 Ma), and which represent a stack of formerly deep (high-*P*), intermediate (mid-*P*) and relatively shallow Grenvillian crustal levels.

The structurally lowest component of the hinterland is the Manicouagan Imbricate zone (MIZ), exposed along the northern shores of the Manicouagan reservoir and consisting mainly of imbricated 1.65 Ga anorthosite-gabbro suite(s) to the east, 1.46 Ga augen gneiss, supracrustal rocks and 1.17 Ga gabbro sills to the west (Fig. 3.1; Cox *et al.,* 1998; Indares *et al.,* 2000). The MIZ was metamorphosed under high-*P* granulite- to eclogite-facies conditions (1500–1800 MPa and 800–900 $^{\circ}$C) at 1.05–1.02 Ga, followed by a retrograde *P–T* path dominated by decompression (Cox and Indares, 1999a, b; Indares and Dunning, 2001; Indares, 2003; Yang and Indares, 2005; Indares *et al.,* 2008).

In contrast, to the south, *ca.* 1.69 Ga mafic rocks of the Island domain and 1.5–1.2 Ga units of the Canyon domain were metamorphosed under mid-*P* granulite-facies

conditions at 1080–1040 Ma (Dunning and Indares, 2010; see below). Finally, the Hart Jaune terrane to the east (Fig. 3.1) is made of *ca.* 1.5 Ga rocks (Gobeil *et al.*, 1997a, b) that escaped any perceptible Grenvillian age deformation and metamorphism (Indares and Dunning, 2004). The boundary between the high-*P* and the mid-*P* portions of the hinterland is masked by the Triassic Manicouagan impact crater, but its eastern extension juxtaposes the MIZ with the Hart Jaune terrane (Fig. 3.1).

3.2.1.   The Canyon domain

The Canyon domain, first defined by Hynes *et al.,* (2000) in the southern part of the Manicouagan area, mainly consists of layered units, including a *ca.* 1.5 Ga supracrustal sequence which is part of the complex de la Plus Value (PLV; Moukhsil *et al.*, 2012), a *ca.* 1.4 Ga mafic suite, and a 1.24 Ga bimodal felsic–mafic sequence (LBS) with hydrothermally altered components (Hindemith and Indares, 2013; Indares and Moukhsil, 2013; Lasalle *et al.*, 2013; Dunning and Indares, 2010). In the Canyon domain, mineral assemblages of garnet, clinopyroxene, orthopyroxene, plagioclase and hornblende in mafic rocks, and garnet, sillimanite, K-feldspar±biotite in aluminous rocks, are reflective of mid-*P* granulite-facies metamorphism (Dunning and Indares, 2010). However, rocks typical of the LBS are also recognized north of the Manicouagan impact crater, in the southern tip of the high-*P* segment (Fig. 3.1), where, aluminous rocks have kyanite instead of sillimanite. Monazite ages from aluminous gneisses of the Canyon domain constrained the granulite-facies metamorphism at *ca.* 1080–1040 Ma (Dunning and Indares, 2010).

3.2.2. Sample localities

In the Canyon domain, aluminous gneisses occur in the metasedimentary sequence of the PLV and in the bimodal LBS (Fig. 3.1). In the latter, they are found as discrete layers, some of which are inferred to be of metasedimentary origin on the basis of zircon data (Lasalle *et al.,* 2013), and as diffuse layers, some of which have aluminous nodules, within felsic gneisses. On the basis of field relations, petrography and zircon data, the diffuse layers are inferred to be derived from hydrothermally altered felsic volcanic rocks (Indares and Moukhsil, 2013; Lasalle *et al.*, 2013; Hindemith and Indares, 2013). These will be referred to as HAF (hydrothermally altered felsic) rocks. The aluminous rocks investigated in this study come from various localities (Fig. 3.1) and include a metasedimentary rock from the PLV (location HJ60) and three gneisses from the LBS. Two of the latter, from the south, are HAF rocks, one grading into a felsic gneiss (location 216) and one with aluminous nodules (location 333), both from the LBS in the Canyon domain. The other (location 244), is an aluminous layer, several cm thick, inferred to be of sedimentary origin (Lasalle *et al.*, 2013) in sharp contact with massive felsic layers. Location 244 is from the LBS in the high-P segment (north of the Manicouagan reservoir; Fig. 3.1). In the following sections the symbol # is used to replace the word 'sample' in front of sample numbers.

3.3.   PETROGRAPHY

Figure 3.2 highlights the macroscopic characteristics of representative rock samples from each location. Samples from HJ60 and 244 consist of light-colored

quartzofeldspathic layers alternating with darker layers rich in garnet, Al-silicate, and biotite (Fig. 3.2a, b). In the two samples from location 216 the gneissosity is defined by thin layers rich in aluminous minerals and quartzofeldspathic lenses (Fig. 3.2c). In contrast, the sample from location 333 consists of garnet nodules (with biotite and sillimanite) unevenly distributed in a matrix rich in K-feldspar (Fig. 3.2d).

3.3.1. Microstructures

This study focuses on five samples with representative mineral assemblages and microstructures. The distribution of the minerals at the thin-section scale was imaged by false color maps (Fig. 3.3) generated using a Mineral Liberation Analysis (MLA) software (developed by JK Tech, University of Queensland, Australia; Gu, 2003) linked to a FEI Quanta 400 environmental scanning electron microscope (SEM) at the Bruneau Center of Memorial University. The SEM was setup with an accelerating voltage of 25 kV, a beam current of 10 nA, a 2 mm frame size (or horizontal field width), a dwell time of 10 ms, and a step size of 50 μm. The MLA software was used to generate a point-counted estimation of mineral proportions and a composition-sensitive false-color map of the mineral associations and textural relationships (Shaffer *et al.,* 2008; Shaffer, 2009). Smaller-scale microstructures were documented by optical microscopy and cathode-luminescence (CL) imaging (Figs. 3.4 and 3.5). SEM–MLA and CL imaging were of particular use in establishing the overall distribution of quartzofeldspathic phases and their mutual relations.

The main mineral assemblage of garnet, Al-silicate, biotite, K-feldspar, plagioclase and quartz is common to all samples (Fig. 3.3) with the Al-silicate being kyanite in #244 and sillimanite in every other case. Minor phases include rutile, ilmenite (in #HJ60b, #333x), apatite (in #244 and #216a, c), graphite (in #HJ60b), sulphides (all samples but #244), monazite and zircon. Mineral modal proportions estimated by SEM–MLA are shown in Table 3.1.

The metasedimentary samples (#244, #HJ60b) mainly consist of large garnet porphyroblasts in an Al-silicate and biotite-bearing quartzofeldspathic matrix (Fig. 3.3a, b; Table 3.1). In contrast, the HAF samples (#216a, c; #333x) have markedly lower proportions of garnet+biotite+Al-silicate (Fig. 3.3c–e; Table 3.1). A common feature in these samples is the concentration of sillimanite in thin seams that are locally mantled by plagioclase (#216a) or overgrown by variably elongated garnet. Sample 333x is distinct in that it has a K-feldspar dominated matrix with variably elongated domains of pure quartz and garnet that commonly forms grain aggregates, but that in one instance defines a large discontinuous lens (Fig. 3.3e).

3.3.1.1. Garnet

Garnet porphyroblasts are ~1.5 mm to 7 mm in size and are smallest and most evenly distributed in #216c. Generally they are sub-rounded (*cf.,* #HJ60b; Fig. 3.4a) to elongate along the foliation. The elongated type commonly overgrows Al-silicate and is mantled by plagioclase (*cf.,* #244, #216a and #333x; Figs. 3.3b, c, e and 3.4b). Garnet porphyroblasts generally contain inclusions of lobate quartz (*cf.,* #HJ60b and #216a; Fig.

3.3a, c), Al-silicate (Fig. 3.4b, c) and, in all samples but #333x, polymineralic inclusions and/or embayments that are especially abundant in #HJ60b. These inclusions consist of corroded quartz and/or biotite and/or sillimanite within cuspate pools or films of optically continuous quartz/feldspar, and delimited by straight to smoothened garnet faces (Fig. 3.4d–f). In contrast, garnet aggregates in #333x consist of small rounded grains that coalesce in patches and contain abundant 'drop-like' inclusions (Fig. 3.4g). In all samples, garnet rims are locally replaced by biotite (Fig. 3.4a) and, in #HI60b, by biotite–sillimanite clusters or feldspar pools enclosing small sillimanite prisms (Fig. 3.4h).

3.3.1.2. Al-silicates and biotite

Al-silicates occur both in the matrix and as small inclusions in garnet. They consist of kyanite in #244 and sillimanite in all other samples (with one exception, see below). In #244, matrix kyanite forms large blades with inclusions of apatite, quartz, and quartz rimmed by K-feldspar (Fig. 3.5a). These blades are corroded and locally mantled by plagioclase, from which they are variably separated by a thin film of quartz (Fig. 3.5b). In addition, in #216c, one small prism of kyanite, replaced by quartz or feldspar along cleavage planes, is included in garnet (Fig. 3.4c).

Sillimanite (in #HJ60b; #216a, c; #333x) is prismatic and generally associated with biotite. Matrix sillimanite in #216a, c, is mantled by plagioclase (Fig. 3.3d) from which it is locally separated by a thin rim of quartz, and contains scarce inclusions of corroded quartz rimmed by feldspar (Fig. 3.5c, d). Sillimanite in sites of garnet resorption occurs as

98

smaller prisms, which have in one instance coalesced in a large patch separated from garnet by a pool of K-feldspar (Fig. 3.5e).

Biotite forms large single laths or clusters, commonly with Al-silicate and variably replacing garnet (*cf.,* #HJ60b and #216c; Fig. 3.3e, c), and as smaller interstitial flakes. In the proximity of garnet, biotite rims form symplectites with quartz (*cf.,* #HJ60b; Fig. 3.5f, g).

3.3.1.3.   Quartzofeldspathic matrix

In the metasedimentary samples #244 and #HJ60b, quartz and feldspars show a relatively homogeneous distribution and grain size (Fig. 3.3a,b), except for a few larger grains. In contrast, the matrix in the HAF samples is heterogeneous (Fig. 3.3c–e). In #333x, quartz is restricted to large ribbons and the matrix mainly consists of coarse grained K-feldspar with plagioclase exsolution. In #216a and c, the matrix consists of alternating quartz±plagioclase-rich and K-feldspar-rich layers, with quartz commonly forming large, partly recrystallized ribbons whereas plagioclase is mostly concentrated in mantles around elongate garnet and sillimanite. Sample 216c contains one large plagioclase (~5 mm) with corroded rims and lobate inclusions of quartz. In addition, smaller-scale microstructures are observed in the matrix of #HJ60b and #216a including pools of feldspar engulfing corroded biotite and partly rimmed by garnet (#HJ60b only; Fig. 3.5h), and feldspar or quartz as interstitial pools between quartzofeldspathic minerals (Fig. 3.5i) or as thin films at grain boundaries (Fig. 3.5j–l).

3.3.2. Mineral chemistry

The mineral chemistry of garnet, biotite and plagioclase were determined using a 4 spectrometer Cameca Camebax MBX electron probe at Carleton University, and a collection of well characterized natural and synthetic standards. Analytical conditions were 15 kV accelerating potential and 20 nA beam current. Raw X-ray data were converted to elemental weight percent using the PAP model. Ranges of chemical composition parameters for analyzed garnet, plagioclase and biotite are shown in Table 3.2.

3.3.2.1. Garnet

Overall, garnet is almandine-rich with subordinate pyrope, minor grossular and negligible spessartine ($X_{sps}{\leq}0.02$) components. Figure 3.6 presents representative zoning profiles of the largest garnet grains in each sample. Generally, X_{alm} and X_{Fe} are lowest in the cores (X_{alm} 0.50–0.52 in #244, #216a, c, and 0.63 in #HJ60b, #333x) and variably increase at the rims, mostly adjacent to biotite. The zoning pattern of X_{prp} is antithetic to that of X_{alm} and both are consistent with diffusional homogenization of Fe and Mg in garnet at high-T conditions, followed by resetting of the rim composition by retrograde Fe–Mg exchange with biotite (Spear, 1991; Pattison and Bégin, 1994a, b).

X_{grs} is lowest in garnet from the sillimanite-bearing samples (Fig. 3.3d; X_{grs} =0.02–0.05; #331x; #HJ60; #216a,c), in which zoning patterns range from flat (garnet in #331x) to 'bell shaped', mostly in the small garnets of #216c (Fig. 3.6b). In the kyanite-bearing #244, X_{grs} in garnet varies between 0.03 and 0.15 (Fig. 3.6a) and shows a complex X_{grs}

profile with intermediate values (X_{grs} 0.09) in the core gradually increasing towards the rims (X_{grs} 0.14) then dropping sharply to minimum values at the outer rim (X_{grs} 0.03–0.04). X_{grs} variations in garnet core and inner rim are likely relics of growth zoning due to lower diffusion rates of Ca, even at high-T, relative to Fe and Mg (Florence and Spear, 1991). Profiles in X_{sps} are flat, to weakly increasing at the rims (#216c; Fig. 3.6b), consistent with partial replacement of garnet by biotite (Spear, 1991).

3.3.2.2. Biotite

Biotite laths adjacent to garnet and/or isolated in the matrix, as well as inclusions in garnet (in #216c and #331x only) were analyzed. X_{Fe} of biotite ranges from 0.30 to 0.45, Ti from 0.15 to 0.32 cations p.f.u. (based on 11 O), and Al^{VI} from 0.15 to 0.30 cations p.f.u., the latter being lowest in #216a,c (Fig. 3.7; Table 3.2). The correlation between the microstructural setting of biotite and the compositional parameters cited above (see also Spear and Parrish, 1996) is highlighted in Fig. 3.7. In #216c, #HJ60b, and #244, there is a trend of increasing X_{Fe} and Ti in biotite with increasing distance from garnet. In #216a, Ti follows this trend but X_{Fe} is uniform. In #333x there is a wide range of X_{Fe} without any clear trend, while Ti contents are relatively uniform. There is an inverse correlation between Al^{VI} and Ti, with the Al^{VI} varying most relative to Ti in #333x.

3.3.2.3. Plagioclase

X_{An} of analyzed plagioclase generally ranges between 0.02 (rarely in rims) and 0.26 and the least calcic plagioclase (X_{An} 0.03–0.10) is found in #333x (Table 3.2). In most

101

cases, plagioclase adjacent to garnet has the same composition as that isolated in the matrix. However in #216a, plagioclase mantling sillimanite and/or garnet has the highest X_{An} (0.24–0.25). The large plagioclase grain in #216c has a uniform composition with X_{An} 0.19, within the range of X_{An} of plagioclase in other microstructural domains of the same section.

3.3.3. Interpretation of microstructures

3.3.3.1. Peak assemblage and evidence for partial melting

The dominant mineral assemblage consists of garnet, Al-silicate, biotite, K-feldspar, plagioclase and quartz (with Al-silicate being kyanite in #244 and sillimanite in the rest) and in all samples but #333x there is also microstructural evidence for the presence of former melt. This evidence includes films and pools of optically continuous interstitial and/or xenomorphic feldspar and/or quartz enclosing corroded phases. Such microstructures, found both in the matrix and within garnet (Figs. 3.4d–f and 3.5i–l), are typically interpreted to represent melt pseudomorphs (Vernon and Collins, 1988; Harte *et al.,* 1991; Sawyer, 1998; Holness and Sawyer, 2008; Holness *et al.,* 2011, Johnson *et al.,* 2013).

This inferred peak mineral assemblage in the presence of former melt is consistent with the idealized biotite-consuming fluid-absent melting reaction,

biotite + Al-silicate + quartz ± plagioclase → garnet +K-feldspar + liquid, (R1)
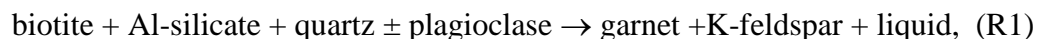
which occurs in aluminous rocks at T above the suprasolidus muscovite breakdown via reactions such as,

muscovite + quartz ± plagioclase → Al-silicate + K-feldspar + liquid, (R2)

(Spear *et al.,*1999).

3.3.3.2. *Microstructures consistent with fluid-absent melting consuming muscovite and biotite*

Evidence for melting involving muscovite in #216a, c and #244 is provided by the lobate inclusions of corroded quartz rimmed by feldspar within sillimanite and kyanite, respectively, (Fig. 3.5a, c) suggesting that these Al-silicates formed in the presence of melt. The biotite-consuming melting reaction R1 produces garnet, K-feldspar and liquid at the expense of biotite, Al-silicate, and quartz (±plagioclase). Microstructural evidence consistent with this reaction includes: (a) the presence of elongate garnet overgrowing Al-silicate in all samples (Figs. 3.3b, c, e and 3.4b); (b) the corroded aspect of most kyanite prisms in #244 (Fig. 3.5a, b); (c) the presence of feldspar pools (inferred to represent former melt) engulfing corroded biotite, sillimanite and/or quartz, as polymineralic inclusions or embayments in garnet (#HJ60b; #216a; Fig. 3.4d–f) and implying that garnet grew in the presence of melt; and (d) quartz or feldspar interstitial pools and films in the matrix (Fig. 3.5i–l), that are most common in #HJ60b. The preservation of former melt pools and films in the matrix is very rare in regionally metamorphosed terranes, but this is not the first time it has been reported (*cf.,* Hartel and Pattison, 1996; Sawyer 2001; Jordan *et al*., 2006; Guilmette *et al*., 2011).

3.3.3.3. *Microstructures consistent with retrograde reactions during melt crystallization*

In all samples (Figs. 3.4a and 3.5f, g) garnet rims replaced by biotite (± symplectitic with quartz), biotite+sillimanite and/or sillimanite+melt pseudomorphs, are consistent with crystallization of melt during cooling within the P–T field of reaction R1. These microstructures are best developed in the metasedimentary sample #HJ60b (Figs. 3.4h and 3.5e), perhaps suggesting that the other samples contained less melt during the metamorphic peak. The overall preservation of the peak assemblage in all samples and the lack of retrograde muscovite (despite evidence that partial melting initially occurred via muscovite breakdown in #216a, c and #244) implies that a large portion of melt was lost (White and Powell, 2002), a feature that is common when anatexis occurs in a tectonically active environment (Brown, 2002, 2004).

The microstructures described above provide a record of the anatectic history of the investigated samples that can be summarized as: (a) fluid-absent muscovite melting in the stability field of kyanite in the case of #244 (from the high-P segment; Fig. 3.1) and sillimanite in the case of the other samples; (b) fluid-absent melting consuming biotite, leading to garnet growth in the presence of melt at the expense of biotite and Al-silicate (all samples); (c) partial melt escape during prograde metamorphism; and (d) melt solidification at T above the stability field of muscovite (all samples). We note that the presence of one resorbed kyanite prism in garnet in #216a may be a prograde relic of an earlier metamorphic event.

3.3.3.4. *Inherited microstructures*

Despite anatexis at granulite-facies conditions, earlier features are recognized in the HAF samples and most particularly in #333x. Key microstructural elements in this rock are: (a) the atypical mineralogy of the matrix, which is composed almost exclusively of perthitic K-feldspar; (b) the elongate large quartz which may represent relict phenocrysts or folded and attenuated veins; (c) the distribution of sillimanite into thin seams that are reminiscent of fluid pathways; and (d) the general shape of the discontinuous garnet aggregate (highlighted by the dotted line in Fig. 3.3e), which is suggestive of a precursor Al and Fe-Mg-rich nodule that has been cracked, and infiltrated by the matrix. These characteristics are consistent with Al and K enrichment by hydrothermal alteration of a felsic precursor (Bonnet and Corriveau, 2007; Hindemith and Indares, 2013). In addition, an original volcanic protolith (rhyolite?) is supported by the zircon data published in Lasalle *et al.,* (2013). A distribution of sillimanite in seams is also clear in #216a, c (Fig. 3.3c, d). In addition, both #216a and c are characterized by coarse and flattened quartz aggregates that attest to the former presence of large quartz crystals and/or dismembered quartz veins within a finer grained rock.

3.4. MODELLING OF PHASE EQUILIBRIA

In this section, the microstructural evolution of the investigated rocks is evaluated within the framework of P–T pseudosections that are used in conjunction with mineral chemistry data to infer P–T paths. The calculations were performed in the Na_2O–CaO–K_2O–FeO–MgO–Al_2O_3–SiO_2–H_2O–TiO_2–Fe_2O_3 (NCKFMASHTO) system using the software THERMOCALC version 3.33 (updated from Powell and Holland, 1988) and the internally consistent dataset (file tc-ds55.txt) of Holland and Powell (1998) updated in November 2003. The a-x mixing models used were: garnet; biotite and silicate melt (White *et al.*, 2007); cordierite (Holland and Powell, 1998); orthopyroxene (White *et al.,* 2002); muscovite (Coggon and Holland, 2002); plagioclase and K-feldpsar (Holland and Powell, 2003); ilmenite (White *et al.,* 2000).

P–T pseudosections were calculated for #HJ60b, #244, #216c and #333x. The bulk composition of each sample was obtained by combining the mineral proportions estimated by SEM–MLA with the mineral chemistry. The bulk H_2O was calculated based on the proportion of biotite using the H–Ti substitution scheme of White *et al.,* (2007; see also Indares *et al.,* 2008; Guilmette *et al.,* 2011) and varies between 0.55 mol% (#333x) and 1.67 mol% (#HJ60b). The amount of oxygen (O), which is used to calculate the bulk Fe_2O_3 was set at a minimum: 0.01 mol% for #HJ60b and #333x, and 0.03 mol% for #244 and #216c to allow for the calculation, otherwise impossible, of certain phase boundaries. Finally, in the case of the apatite-bearing #244 and #216c, the CaO of apatite was excluded from the bulk composition to prevent overestimation of the Ca contents of Ca-bearing NCKFMASHTO model system phases.

The P–T pseudosections are shown in the P–T range of 5–15kbar (and 5–18 kbar for the kyanite-bearing #244) and 700–950 °C, and the stable phases were labeled using the following abbreviation scheme: garnet (g); biotite (bi); sillimanite (sill); kyanite (ky); rutile (ru); ilmenite (ilm); cordierite (cd); orthopyroxene (opx); muscovite (mu); quartz (q); silicate melt (liq). Isopleths of phase proportions were calculated and superimposed onto the pseudosections to illustrate the production/consumption of relevant phases (dotted lines; Figs. 3.8 and 3.10). In addition, the distribution of selected mineral composition isopleths ($z(g)$ = Ca/(Ca+Fe+Mg) and $x(g)$ = Fe/(Fe+Mg) in garnet; $x(bi)$ = Fe/(Fe+Mg) in biotite) is shown in Figs. 3.9 and 3.10.

3.4.1. P–T pseudosections using the estimated bulk compositions

A first set of P–T pseudosections (Figs. 3.8 and 3.9) was calculated using the estimated bulk compositions of the samples. As the microstructures suggest that some melt was removed during the prograde P–T evolution of the rocks, these bulk compositions are residual. Therefore these P–T pseudosections are only valid for assessing the peak and retrograde evolution of the rocks.

3.4.1.1.   *General topologies*

In Figs. 3.8a–d and 3.9a–d, quartz and K-feldspar are predicted in every field over the P–T range modelled. The topology of the observed mineral assemblage sill/ky+g+bi+pl+ksp+q+liq (±ru±ilm) (M1) is highlighted in Fig. 3.8. The M1 field is

limited by the solidus at low-*T* and the prograde disappearance of biotite at high-*T*, both of which have a steep d*P*/d*T*. The predicted overall *T*-range of the peak field is between 820 and 890 $^{\circ}$C; its width is largest for the bulk composition with the highest H_2O (#HJ60b; Fig. 3.8b) and the bi-out line is at the highest *T* in bulk compositions with relatively high X_{Fe} (#244 and #216c; Fig. 3.8c, d).

In terms of pressure, the M1-ky field, which represents the peak for the kyanite-bearing sample #244, is located between the sill/ky transition near 11kbar and the line marking the prograde appearance of muscovite near 18 kbar (Fig. 3.8a). In contrast, in the case of the sillimanite-bearing samples, the M1-sill field is bounded at low-*P* by the appearance of cordierite near 7 kbar and the sill/ky transition, within the *T* range of interest (Fig. 3.8b–d). The M1-sill field is transected by the ru-in and ilm-out lines with increasing *P*. However, these boundaries cannot be reliably used to further constrain the *P* of the peak assemblage because their locations are highly dependent upon the amount of oxygen used in the bulk rock composition, which is unconstrained.

Within the general M1-field (Fig. 3.8a–d) isopleths of phase proportions have a steep d*P*/d*T,* and with increasing *T*, garnet and melt proportions increase, while those of Al-silicate and biotite decrease. Most marked variations in phase proportions are predicted for the M1 field of #HJ60b (Fig. 3.8b), which is the widest; in this case the garnet proportion increases from ~18 to 30% and the liquid from 0 to 10%. In contrast only ~ 4% of garnet (from 19 to 23%) and ~3% of liquid are produced across the narrow M1-field of #333x (Fig. 3.8d). At *T*>T_{M1}, isopleths of phase proportions have a moderate positive d*P*/d*T* and are more widely spaced.

The distribution of $z(g)$, $x(g)$ and $x(bi)$ isopleths in the M1 field are shown in Fig. 3.9a–d. The $z(g)$ isopleths have a moderate to low dP/dT, and their spacing decreases in the kyanite-stability field. In contrast, the $x(g)$ and $x(bi)$ have steep dP/dT with values decreasing with increasing T.

3.4.1.2. *P–T constraints on the metamorphic peak and the retrograde evolution*

The *P–T* conditions of the metamorphic peak can be further constrained by comparing the modelled $z(g)$ and $x(g)$ isopleths of garnet with the measured values of these parameters. However, this approach should be used with caution. In terms of grossular, the analyzed garnets show relic growth zoning in the cores, variably smoothened by diffusion, and a steep decrease in some outer rims, which is consistent with retrograde zoning. Because the true grossular content of garnet at the metamorphic peak cannot be evaluated, a range of values was considered (excluding those of the outer rims). The analyzed garnets show homogeneous cores in terms of $x(g)$, implying diffusional homogenization at high-*T*. However, this process may have continued during early stages of cooling, therefore $x(g)$ can only be used as a minimum peak-*T* estimate.

The *P–T* conditions where the last melt crystallized, and which might be expected to record effective closure of the samples to diffusion can be constrained by the intersection of the isopleth $z(g)_{rim}$ with the solidus, and the phase proportions predicted by THERMOCALC at this intersection should be similar to those observed in the thin-sections.

Garnet from #244 shows the most prominent and irregular growth zoning (Fig. 3.6a). The range of X_{grs} for the inner rims is between 0.12 and 0.10 (with an exception of an anomalous peak at X_{grs} =0.14) which in terms of the modelled $z(g)$ values defines a *P*-range for the metamorphic peak between ~14 and 16 kbar (Fig. 3.9a). In terms of *T,* this field is bounded by the $x(g)$ of garnet cores, which falls close to the solidus, at ~ 870 ^{o}C, and the bi-out line at ~895 ^{o}C. The intersection of the $z(g)$ of the outer rims of garnet coincides with the kyanite–sillimanite transition line and intersects the solidus at ~11 kbar and 870 ^{o}C. This implies a decompression of at least 3 kbar and a maximum cooling of only 25 ^{o}C during melt crystallization.

The upper *P*-limit of the metamorphic peak for the sillimanite-bearing samples is set by the kyanite–sillimanite transition line. The tightest *P–T* constraints are provided by #HJ60b. Garnet X_{grs} profiles for this sample are the smoothest (except for the outer rims; Fig. 3.6d) defining a narrow range of $z(g)$ and the $x(g)$ of the garnet cores fall close to the bi-out line (Fig. 3.9b). The *P–T* range defined by the $z(g)$, $x(g)$ and the bi-out line is ~ 10 kbar and 840–850 ^{o}C. The intersection of the $z(g)$ of the outer rim of garnet with the solidus is at 8.2 kbar and 820 ^{o}C implying a decompression of ~2 kbar and cooling of 20–30 ^{o}C during melt crystallization.

The range of $z(g)$ in garnet cores in #216c falls within the kyanite field down to the sill-ky transition (Fig. 3.9c), which is at odds with microstructural evidence for sillimanite being present during the prograde evolution. In this sample, the intersection of $z(g)$ rims with the solidus is at 9.2 kbar and 870 ^{o}C. Finally, the predicted *P–T* conditions are lowest for #333x (Fig. 3.9d; 7.8 kbar and 840 ^{o}C) and close to those of melt solidification (6.8 kbar and 840 ^{o}C; in the vicinity of the cd-in line). However, these *P–T* conditions are

poorly constrained due to the low grossular content of this sample (~1%) and the wide spacing of $z(g)$ isopleths at that range.

Generally the proportions of phases predicted by THERMOCALC at the low-T end of the recorded P–T path (Fig. 3.8a–d) are similar to those observed (Table 3.1), except for the proportions of plagioclase and K-feldspar in #333x, the predicted amounts of which are largely lower and higher respectively. The matrix in this rock is mostly K-feldspar containing exsolution lamellae of plagioclase, which may have formed at T below the solidus.

Additional constraints on the retrograde P–T path may be placed by interpreting the observed retrograde microstructures in the framework of the calculated P–T pseudosections. For instance, the lack of Al-silicate overgrowing garnet rims in #244 is consistent with a steep P–T path, at low angle to the als isopleths (Fig. 3.8a). By contrast, partial or complete replacement of garnet by biotite+plagioclase±Al-silicate in #HJ60, for which the P–T pseudosections predict the widest M1 field, is consistent with a P–T path with moderate dP/dT crossing at high angle the bi, pl and sill isopleths (Fig. 3.8b). The absence of cordierite from the sillimanite-bearing samples is consistent with the intersection of the inferred P–T path with the solidus above the cd-in line (Fig. 3.8b–d). Finally, the isopleths reflecting the measured $x(g)$ at the garnet rims and $x(bi)$ of the biotite in matrix should reflect closure to diffusion of Fe and Mg between these two minerals at relatively low-T. In most cases these isopleths either overlap with the solidus or are located within the subsolidus fields.

3.4.2. Evidence for melt loss and melt reintegration

The overall good preservation of the peak assemblages, as well as the microstructural evidence for early melting involving muscovite, but for melt solidification outside the muscovite stability field, implies that some melt was lost during the prograde evolution. Indeed, the low-T subsolidus fields within the calculated P–T pseudosections are muscovite-free (except at high-P). Thus, in order to account for the possibility of melt loss and suggest a trajectory for the prograde evolution of the rocks (*cf.,* White and Powell, 2002), a second set of P–T pseudosections was calculated after reintegrating melt to the residual bulk compositions (Fig. 3.10).

Generally, the melt loss history of anatectic rocks cannot be known. However, as shown by White and Powell (2002) and Powell *et al.*, (2005) the main suprasolidus stability fields do not change significantly in different scenarios of melt loss. Therefore, by reintegrating a calculated melt proportion and composition into the measured rock composition (White *et al.,* 2004) useful insights can be gained on the prograde evolution. Here we considered the simplest scenario of melt loss in a single step, at the intersection of the solidus for the residual composition with a presumed prograde P–T path (Fig. 3.10). The composition of the melt stable at this P–T point was calculated by THERMOCALC, and an amount of that melt, sufficient to just saturate the solidus in H_2O at a reference P of 8 kbar, was added to the bulk composition (*cf.,* details of the approach in Indares *et al.,* 2008). This was done to maximize the amount of mica present before melting, and therefore the extent of the liquid-present fields. The amount of reintegrated melt ranges between 19.9 mol% in HJ60b and 26.5 mol% in 333x.

3.4.3.   Melt-reintegrated *P*–*T* pseudosections

3.4.3.1.   *General topologies*

The melt-reintegrated pseudosections are shown in Fig. 3.10a–d, along with isopleths of g, sill/ky, liq and *z(g)*, and with the position of the solidus as modelled with the residual bulk compositions (from Fig. 3.8). For reference, this residual solidus divides the *P*–*T* pseudosections in two parts. At higher *T* within the kyanite field, the topologies of the two sets of pseudosections are almost identical (compare Figs. 3.8 and 3.10), whereas within the sillimanite field, the topologies with the lowest variance fields in the melt-reintegrated pseudosections are truncated either by the pl-out line (in #HJ60b and #333x; Fig. 3.10b, d) or the sill-out line (#244; Fig. 3.10a). At lower *T*, across the full *P*-range, topologies of the two sets of pseudosections are different.

In all the melt-reintegrated *P*–*T* pseudosections, the M1 field(s) extend over a much larger *T*-interval and are terminated down-*T* by the disappearance of garnet between about 770 and 810 °C (Fig. 3.10a–d). In addition, muscovite is stable over a larger *P*-range. However, there are significant differences between the topologies in #244, #216c, #HJ60b and those in #333x. In the former case the mu-out line almost coincides with the ksp-in line and melt is produced mainly at *T* above the mu-out–ksp-in lines at *P* below 12 kbar (Fig. 3.10a–c). In contrast, in the case of #333x, K-feldspar is present throughout, the als-in line overlaps with the mu-out line across the whole *P*–*T* range and garnet is absent at low-*T* at any *P* (Fig. 3.10d). In this case, the g-free, mu-bearing field shows the lowest melt production with increasing *T*.

3.4.3.2.   Constraints on the prograde P–T evolution

Constraints on the prograde *P–T* evolution may be placed by interpreting the observed prograde microstructures and the measured zoning in the grossular content of garnet cores within the framework of the extended suprasolidus topologies. Garnet from #244 contains kyanite inclusions and shows a systematic increase in grossular towards a mantle zone, from ~0.08 to 0.12−0.15 (Fig. 3.6a). In terms of the modelled *z(g)* values this translates into increasing *P–T* conditions from the g-in line at ~10.5 kbar and 775 $^\circ$C to up to 15−16 kbar and 850−860 $^\circ$C (for *z(g)*=0.12 and 0.15, respectively) at the residual solidus (Fig. 3.10a). However, maximum grossular contents in the garnet rims are mostly around 0.12, with the peak value of 0.15 being exceptional and probably representing a site of apatite dissolution in the melt (*cf.,* Indares *et al.,* 2008).

In all other samples garnet overgrows sillimanite (except for one kyanite inclusion in #216a). For these samples the melt-reintegrated *P–T* pseudosections predict that garnet started growing at *T* conditions above the mu-out line, and that Al-silicate is not produced with increasing *P–T* conditions above the g-in line (Fig. 3.10b–d). It is therefore implied that all prograde Al-silicate predates garnet. The prograde *P–T* path most consistent with both the petrography and the melt reintegrated pseudosections is restricted at *P* below the sill-ky transition and has a strong *T* gradient. Such an evolution is also consistent with the measured and modelled grossular contents in garnet cores in #HJ60b (Fig. 3.10b), but not for those of #216c, in which the *z(g)* of the garnet cores fall in the kyanite field (Fig. 3.10c).

Sample #216c contains relict apatite and shows garnet distributed as numerous small grains in which Ca contents decrease markedly from core to rim (more than in larger garnets from other samples; *e.g.,* #216a, #HJ60c; Fig. 3.6). A potential interpretation is that nucleation of the small Ca-zoned garnet in #216c was favored in sites of apatite dissolution in the melt, within micro-domains enriched in Ca relative to the average bulk (see also Indares *et al.,* 2008). Since apatite cannot be modelled in THERMOCALC, it is not possible to interpret this high-Ca garnet in the context of *P–T* pseudosections. Finally, in #333x the grossular content of garnet is too low and homogeneous to place any additional constraint on the prograde *P–T* path.

3.5.   DISCUSSION AND CONCLUSIONS

3.5.1.   Anatectic record of aluminous rocks from the Grenvillian hinterland in the Manicouagan area

Aluminous gneisses of diverse origins, pelitic metasediments and metamorphosed hydrothermally altered felsic (HAF) volcanic rocks, from the mid-*P* segment of the hinterland in the central Grenville Province show garnet–sillimanite–biotite–quartz–K-feldspar–plagioclase assemblages and microstructural evidence of anatexis by fluid-absent melting reactions involving first muscovite, and then biotite, with increasing *T*. The same assemblage (with kyanite instead of sillimanite) and microstructural evidence of melting is also observed in aluminous metasedimentary layers on the southern boundary of the high-*P* segment, to the north.

Evidence of melting involving muscovite is best shown in HAF rocks of a broadly pelitic composition (#216a, c), whereas the most abundant evidence of former melt linked with biotite breakdown comes from the metasedimentary rocks (#HJ60b, #244). The only rock type that lacks evidence of former melt is a HAF quartz-poor and K-feldspar rich nodular gneiss (#333x). However, in all rocks, the presence of garnet overgrowing Al-silicate is consistent with the fluid absent melting reaction (R2). The peak assemblage is best preserved in HAF rocks, whereas the mid-P metasedimentary rock #HJ60b, which shows the most ample evidence of former melt, displays the most pronounced retrograde microstructures associated with melt crystallization.

3.5.2. P–T record

Microstructures and mineral chemistry data from the metasedimentary rocks (#244 and #HJ60b), were most suitable for P–T path predictions by phase equilibria modelling. Two types of P–T paths are predicted, depending on the Al-silicate present (Fig. 3.11). The data from the kyanite-bearing rock #244 are consistent with a steep prograde P–T path, reaching the metamorphic peak at ~14.5 kbar and 860–900 ^{o}C, followed by decompression with minor cooling down to the solidus at ~11 kbar and 870 ^{o}C, just above the sillimanite–kyanite transition line (Fig. 3.11, paths A-A'). In contrast, the P–T path predicted from the sillimanite-bearing rock #HJ60b (Fig. 3.11, path B) is characterized by a prograde portion with a strong T gradient below the sillimanite–kyanite transition line, up to ~ 9.5 kbar and 850 ^{o}C, and a retrograde portion down to the solidus at ~ 8 kbar and 820 ^{o}C, involving moderate decompression and cooling. Although P–T paths were not

established for the HAF rocks, and it is possible that different locations in the mid-*P* Canyon domain may have followed distinct *P–T* trajectories, microstructures constrain the *P–T* paths of all the sillimanite-bearing rocks below the sillimanite–kyanite transition and above the cordierite-in line. The two predicted *P–T* paths of the respective samples end at the solidus (point at which the microstructural evolution of the rocks ended) and they do not show any overlap, although it may be possible that the high-*P* path A-A' merges with the retrograde portion of path B at lower *P*.

3.5.3.   Regional patterns of metamorphism

The *P–T* path predicted for the kyanite-bearing rock #244 is broadly similar to those inferred in other parts of the high-*P* belt in the Manicouagan area (*cf.,* Indares *et al.,* 2008). These steep *P–T* loops have been attributed to rapid exhumation of the MIZ over a crustal-scale ramp on the underlying Parautochthonous belt (Indares *et al.,* 2000; Indares and Dunning, 2004) shortly after the peak of metamorphism, which was dated at *ca.* 1040–1030 Ma by Indares and Dunning (2001).

In contrast, the *P–T* path predicted for the sillimanite-bearing aluminous paragneiss #HJ60b is the first example ever inferred for the mid-*P* portion of the hinterland of the central Grenville Province, and maybe the first one determined using modern methodology in the Grenvillian hinterland in general. This path is characterized by larger *T* and lesser *P* variations relative to those of the high-*P* rocks. In addition, monazite from individual sillimanite-bearing aluminous samples shows a larger spread in Grenvillian metamorphic ages (*e.g., ca.* 1080–1050 Ma in #HJ60b; Dunning and Indares, 2010),

consistent with a longer residence under high-*T* conditions, and a tectonic transport dominated by lateral crustal flow during this time interval.

3.5.4. Comparison with predictions of tectonic models

In a broad sense, these two contrasting types of *P–T* paths discussed above can be compared with those predicted by recent numerical modelling of the Grenville orogeny (*e.g.,* Jamieson *et al.,* 2010; Jamieson and Beaumont, 2011). These models involve a laterally heterogeneous crust that develops ductile fold nappes during high-*T* metamorphism and have been most successful in explaining first order geological features in the western part of the Province, whereas in the case of the Manicouagan area, they were in part limited by the scarcity of geological constraints from the mid-*P* hinterland at the time (Jamieson *et al.,* 2010). However, despite the uncertainties involved (*cf.,* Jamieson *et al.,* 2010; Jamieson and Beaumont, 2011) and the fact that a given numerically modelled *P–T* path can be reproduced by a range of combinations of model parameters, there are some general trends that emerge. In regions near the orogenic flanks *P–T* paths are tight loops involving strong gradients in pressure whereas in the orogenic core they show large near isobaric heating segments reflecting protracted lateral transport of ductile crust beneath a plateau. These two contrasting patterns are well illustrated by our data from the Manicouagan area, which show steep *P–T* paths exhuming deeper rocks in the edge of the hinterland (MIZ) versus moderate-gradient *P–T* paths followed by intermediate-depth crustal levels farther in the orogenic core, within the Canyon domain.

ACKNOWLEDGMENTS

REFERENCES

Bonnet, A. and Corriveau, L., 2007. Alteration vectors to metamorphic hydrothermal systems in gneissic terranes. *In:* Goodfellow, W.D. *(Eds.).* Mineral Deposits of Canada: A Synthesis of Major Deposit-Types, District Metallogeny, the Evolution of Geological Provinces, and Exploration Methods. *Geological Association of Canada, Mineral Deposits Division, Special Publication,* **5**: 1035–1049.

Brown, M., 2010. Melting of the continental crust during orogenesis: the thermal, rheological, and compositional consequences of melt transport from lower to upper continental crust. *Canadian Journal of Earth Sciences*, **47**: 655–694.

Brown, M., 2004. The mechanism of melt extraction from lower continental crust of orogens. *Transactions of the Royal Society of Edinburgh, Earth Sciences*, **95**: 35–48.

Brown, M., 2002. Retrograde processes in migmatites and granulites revisited. *Journal of Metamorphic Geology*, **20**: 24–40.

Coggon, R. and Holland, T. J. B., 2002. Mixing properties of phengitic micas and revised garnet-phengite thermobarometers. *Journal of Metamorphic Geology*, **20**: 683–696.

Cox, R. A. and Indares, A., 1999a. Transformation of Fe-Ti gabbro to coronite, eclogite and amphibolite in the Baie du Nord segment, eastern Grenville Province. *Journal of Metamorphic Geology*, **17**: 537–555.

Cox, R. A. and Indares, A., 1999b. High pressure and temperature metamorphism of the mafic and ultramafic Lac Espadon suite, Manicouagan Imbricate Zone, eastern Grenville Province. *Canadian Mineralogist*, **37**: 335–357.

Cox, R. A., Dunning, G.R. and Indares, A., 1998. Petrology and U-Pb geochronology of mafic, high-pressure metamorphic coronites from the Tshenukutish domain, eastern Grenville Province. *Precambrian Research*, **90**: 59–83.

Dunning, G. and Indares, A., 2010. New insights on the 1.7-1.0 Ga crustal evolution of the central Grenville Province from the Manicouagan – Baie Comeau transect. *Precambrian Research*, **180**: 204–226.

Florence, F. P. and Spear, F., 1991. Effects of diffusional modification of garnet growth zoning on P–T path calculations. *Contributions to Mineralogy and Petrology*, **107**: 487–500.

Gobeil, A., 1997a. Géologie de la région du Lac Grand Mesnil. Ministère des Ressources naturelles, Québec; RG 96–04, p. 10.

Gobeil, A., 1997b. Géologie de la région du Lac Lacoursière. Ministère des Ressources naturelles, Québec; RG 96–03, p. 14.

Gu, Y., 2003. Automated scanning electron microscopy based mineral liberation analysis. An introduction to JKMRC/FEI Mineral Liberation Analyser. *J. Minerals and Materials, Characterization and Engineering,* **2**: 33–41.

Guilmette, C., Indares, A. D. and Hébert, R., 2011. High-pressure anatectic paragneisses from the Namche Barwa, Eastern Himalayan Syntaxis; textural evidence for partial melting, phase equilibria modelling and tectonic implications. *In:* Schulman, K., O'Brien, P., White, R., Brown, M., Lexa, Ondrej *(Eds.)*. Granulite-

facies metamorphism and the rheology of the lower crust, Granulites and Granulites 2009. *Lithos*, **124**: 66–81.

Harte, B., Pattison, D. R. M. and Linklater, C. M., 1991. Field relations and petrography of partially melted pelitic and semi-pelitic rocks. *In:* Voll, G., Töpel, J., Pattison, D. R. M. and Seifert, F. *(Eds.).* Equilibrium and kinetics in contact metamorphism: The Ballachulish Igneous Complex and its thermal aureole. Springer Verlag: Heidelberg, 181–210.

Hartel, T. H. D. and Pattison, D. R. M., 1996. Genesis of the Kapuskasing (Ontario) migmatitic mafic granulites by dehydration melting of amphibolite: the importance of quartz to reaction progress. *Journal of Metamorphic Geology,* **14:** 591–611.

Hindemith, M. and Indares, A., 2013. The petrographic and geochemical study of hydrothermally altered metavolcanics, metamorphosed at granulite-facies conditions from the Canyon domain in the central Grenville Province of Quebec, Canada. GAC-MAC annual meeting Winnipeg**,** Abstract vol. 36, p. 113.

Holland, T. J. B. and Powell, R., 2003. Activity-composition relations for phases in petrological calculations: an asymmetric multicomponent formulation. *Contributions to Mineralogy and Petrology*, **145**: 492–501.

Holland, T. J. B. and Powell, R., 1998. An internally-consistent thermodynamic data set for phases of petrological interest. *Journal of Metamorphic Geology*, **16**: 309–343.

Holness, M. B. and Sawyer, E. W., 2008. On the pseudomorphing of melt-filled pores in migmatites. *Journal of Petrology*, **49 (7)**: 1343–1363.

Holness, M. B., Cesare, B. and Sawyer, E. W., 2011. Melted Rocks under the Microscope: Microstructures and Their Interpretation. *Elements*, **7 (4)**: 247–252.

Hynes, A., Indares, A., Rivers, T. and Gobeil, A., 2000. Lithoprobe line 55: integration of out-of-plane seismic results with surface structure, metamorphism, and geochronology, and the tectonic evolution of the eastern Grenville Province. *Canadian Journal of Earth Sciences*, **37**: 341–358.

Indares, A., 2003. Metamorphic textures and P–T evolution of high-P granulites from the Lelukuau terrane, NE Grenville Province. *Journal of Metamorphic Geology*, **21**: 35–48.

Indares, A. and Dunning, G., 2004. Crustal architecture above the high-pressure belt of the Grenville Province in the Manicouagan area: new structural, petrologic and U–Pb age constraints. *Precambrian Research*, **130**: 199–208.

Indares, A. and Dunning, G., 2001. Partial melting of high P–T metapelites from the Tshenukutish terrane (Grenville Province): petrography and U–Pb geochronology. *Journal of Petrology*, **42**: 1547–1565.

Indares, A. and Moukhsil, A., 2013. Geon 12 crustal extension in the central Grenville Province, implications for the orogenic architecture, and potential influence on the emplacement of anorthosites. *Canadian Journal of Earth Sciences*, **50**: 955–966.

Indares, A., Dunning, G. and Cox, R., 2000. Tectono-thermal evolution of deep crust in a Mesoproterozoic continental collision setting: the Manicouagan example. *Canadian Journal of Earth Sciences*, **37**: 325–340.

Indares, A., White, R. W. and Powell, R., 2008. Phase equilibria modelling of kyanite-bearing anatectic paragneisses from the central Grenville Province. *Journal of Metamorphic Geology*, **26**: 815–836.

Jamieson, R. A. and Beaumont, C., 2011. Coeval thrusting and extension during post-convergent ductile flow - implications for exhumation of high-grade metamorphic rocks. *Journal of Metamorphic Geology*, **29**: 33–51.

Jamieson, R. A., Beaumont, C., Nguyen, M. H. and Culshaw, N. G., 2007. Synconvergent ductile flow in variable-strength continental crust: Numerical models with application to the western Grenville orogen. *Tectonics*, **26**: 1–23.

Jamieson, R. A., Beaumont, C., Warren, C. J. and Nguyen, M. H., 2010. The Grenville Orogen explained? Applications and limitations of integrating numerical models with geological and geophysical data. *In:* Lithoprobe - parameters, processes and the evolution of a continent (Lithoprobe Synthesis Volume II, *(Eds.)* Clowes, R M., and Skulski, T.). *Canadian Journal of Earth Sciences*, **47**: 517–539.

Johnson, T., Fischer, S. and White, R., 2013. Field and petrographic evidence for partial melting of TTG gneisses from the central region of the mainland Lewisian complex, NW Scotland. *Journal of the Geological Society*, **170**: 319–326.

Johnson, T., White, R. and Powell, R., 2008. Partial melting of metagreywacke: a calculated mineral equilibria study. Journal of Metamorphic Geology, **26**: 837 – 853.

Jordan, S. L., Indares, A. and Dunning, G., 2006. Partial melting of metapelites in the Gagnon terrane below the high-pressure belt in the Manicouagan area (Grenville

Province): pressure temperature (P–T) and U–Pb age constraints and implications. *Canadian Journal of Earth Sciences*, **38**: 1309–1329.

Lasalle, S., Fisher, C. M., Indares, A. and Dunning, G., 2013. Contrasting types of Grenvillian granulite-facies aluminous gneisses: Insights on protoliths and metamorphic events from zircon morphologies and ages. *Precambrian Research*, **228**: 117–130.

Moukhsil, A., Solgadi, F., Lacoste, P., Gagnon, M. and David, J., 2012. Géologie de la région du lac du Milieu (SNRC 22O03, 22O04, 22O06, 22J13 et 22J14). Ministère des Ressources naturelles et de la Faune, Quebec, RG 2012–01.

Pattison, D. R. M. and Begin, N. J., 1994a. Zoning patterns in orthopyroxene and garnet in granulites: implications for geothermometry. *Journal of Metamorphic Geology*, **12**: 387–410.

Pattison, D. R. M. and Bégin, N. J., 1994b. Hierarchy of closure temperatures in granulites and the importance of an intergranular exchange medium (melt?) in controlling maximum Fe-Mg exchange temperatures. *Mineralogical Magazine*, **58A**: 694–695.

Powell, R. and Holland, T. J. B., 1988. An internally consistent thermodynamic dataset with uncertainties and correlations: application, methods, worked examples and a computer program. *Journal of Metamorphic Geology*, **6**: 173–204.

Powell, R., Guiraud, M. and White, R. W., 2005. Truth and beauty in metamorphic phase-equilibria: conjugate variables and phase diagrams. *The Canadian Mineralogist*, **43**: 21–33.

Rivers, T., 2012. Upper-crustal orogenic lid and mid-crustal core complexes: signature of a collapsed orogenic plateau in the hinterland of the Grenville Province. *Canadian Journal of Earth Sciences,* **49**: 1–42.

Rivers, T., 2008. Assembly and preservation of lower, mid, and upper orogenic crust in the Grenville Province-Implications for the evolution of large hot long-duration orogens. *Precambrian Research,* **167**: 237–259.

Rivers, T., Culshaw, N., Hynes, A., Indares, A., Jamieson, R. and Martignole, J., 2012. The Grenville Orogen - A post-LITHOPROBE perspective. Chapter 3 *In* Tectonic Styles in Canada: The LITHOPROBE Perspective. Edited by J.A. Percival, F.A. Cook, and R.M. Clowes. Geological Association of Canada, Special Paper 49, pp. 97–236.

Sawyer, E.W., 2001. Melt segregation in the continental crust: distribution and movement of melt in anatctic rocks. *Journal of Metamorphic Geology*, **19**: 291–309.

Sawyer, E.W., 1998. Criteria for the recognition of partial melting. *Physics, Chemistry and Earth* (A), **24**: 269–279.

Shaffer, M., 2009. Discrimination of hematite and magnetite and quantifying their associations using the JKTECH Mineral Liberation AnalyzerTM. In The 48th Annual Conference of Metallurgists, Laurentian University, Sudbury, Ontario 73.

Shaffer, M., Gu, Y., and Rohde, M., 2008. Practical Applications for the Silicon Drift Xray Detector in SEM-Platformed Image Analysis: The Bruker-MLA in Practice. In SME Annual Meeting 2007 and CMS 109th National Western Conference 2007 The Power of Mining: Energy's Influence, Denver, CO, U.S.A., 25-28 February, 2007, 1(Preprint 07-029): 1-6.

Spear, F., 1991. On the interpretation of peak metamorphic temperatures in light of garnet diffusion during cooling. *Journal of Metamorphic Geology*, **9**: 379–388.

Spear, F. and Parrish, R., 1996. Petrology and cooling rates of the Valhalla Complex, British Columbia, Canada. *Journal of Petrology*, **37**: 733–765.

Spear, F. S., Kohn, M. J. and Cheney, J. T., 1999. P–T paths from anatectic pelites. *Contributions to Mineralogy and Petrology*, **134**: 17–32.

van Gool, J. A. M., Rivers, T. and Calon, T., 2008. Grenville Front zone, Gagnon terrane, south-western Labrador: configuration of a midcrustal foreland fold-thrust belt. *Tectonics*, **27**: 1–35.

Vernon, R. H. and Collins, W. J., 1988. Igneous microstructures in migmatites. *Geology,* **16**: 1126–1129.

White, R. W. and Powell, R., 2002. Melt loss and the preservation of granulite-facies mineral assemblages. *Journal of Metamorphic Geology*, **20**: 621–632.

White, R. W., Powell, R. and Clarke, G. L., 2002. The interpretation of reaction textures in Fe-rich metapelitic granulites of the Musgrave Block, central Australia: constraints from mineral equilibria calculations in the system $K_2O–FeO–MgO–Al_2O_3–SiO_2–H_2O–TiO_2–Fe_2O_3$. *Journal of Metamorphic Geology*, **20**: 621–632.

White, R. W., Powell, R. and Halpin, J. A., 2004. Spatially focused melt formation in aluminous metapelites from Broken Hill, Australia. *Journal of Metamorphic Geology*, **22**: 825–845.

White, R. W., Powell, R., and Holland, T. J. B., 2007. Progress relating to calculation of partial melting equilibria for metapelites. *Journal of Metamorphic Geology*, **25**: 511–527.

White, R. W., Powell, R., Holland, T. J. B. and Worley, B. A., 2000. The effect of TiO2 and Fe2O3 on metapelitic assemblages at greenschist and amphibolite facies conditions: mineral equilibria calculations in the system K2O–FeO–MgO–Al2O3–SiO2–H2O–TiO2–Fe2O3. *Journal of Metamorphic Geology*, **18**: 497–511.

Yang, P., and Indares, A., 2005. Mineral zoning, phase relations, and *P–T* evolution of high-pressure granulites from the Lelukuau terrane, northeastern Grenville Province, Quebec. *The Canadian Mineralogist*, **43**: 442–462.

Table 3.1: Mineral modal proportions (in %) as given by the SEM after MLA mapping (sill- sillimanite; g-garnet; bi- biotite; pl-plagioclase; ksp-K-feldspar; q-quartz; ru-rutile; ilm-ilmenite; ap-apatite, zr-zircon, mnz-monazite, gr-graphite, ser- sericite; sulph-sulphides).

	sill	g	bi[a]	pl	ksp	q	ru	ilm	ap	zr	mnz	gr.	sulph.	ser.[b]	SUM
HJ60b	9.5	14.3	14.3	8.5	23.0	25.1	0.10	0.15	0	0.03	0.02	0.48	0.9	1.8	**98.3**
244	3.7	19.3	12.7	18.8	21.6	23.4	0.12	0	0.36	0.03	0.03	0	0	0	**100.0**
216c	3.5	11.8	7.1	25.8	19.3	24.2	0.40	0	0.04	0.02	0.03	0.04	0.5	4.5	**97.2**
216a	0.5	12.0	4.0	18.6	29.2	31.0	0.35	0	0.14	0.03	0.01	0.01	0.4	2.5	**98.8**
333x	1.8	12.2	4.4	31.1	38.7	7.7	0.51	0.01	0	0.02	0.02	0	0.2	1.9	**98.5**

[a] including chlorite present as replacement phase after biotite
[b] sericite present as replacement after feldspar

Table 3.2: Chemical composition ranges of analyzed garnet, biotite, and plagioclase.

	Garnet					Biotite			Plagioclase
	Xalm	Xprp	Xgrs	Xsps	XFe	XFe	*Ti	*Al^{VI}	XCa (An)
HJ60b	0.62–0.72	0.24–0.33	0.02–0.04	0.01–0.02	0.66–0.75	0.36–0.44	0.16–0.28	0.21–0.30	0.20–0.26
244	0.48–0.55	0.34–0.41	0.02–0.14	0.01–0.02	0.55–0.60	0.20–0.33	0.17–0.30	0.16–0.30	0.21–0.25
216a	0.51–0.65	0.30–0.46	0.03–0.04	0–0.01	0.53–0.68	0.34–0.39	0.24–0.33	0.17–0.23	0.13–0.26 (0.02[a])
216c	0.48–0.72	0.24–0.47	0.02–0.05	0–0.02	0.51–0.75	0.17–0.37 (0.47[b])	0.18–0.28 (0.09[b])	0.18–0.25 (0.56[b])	0.11–0.21 (0.03[a])
331x	0.63–0.76	0.22–0.35	0.01	0.01	0.64–0.78	0.31–0.48	0.17–0.23	0.17-0.36	0.03–0.10

*Ti, Al^{VI} : cations on the basis of 11 oxygens
[a] Extreme values recorded by the rim of a plagioclase grain in the matrix (in #216c)
[b] Extreme values recorded by the rim of a biotite grain in the matrix (in #216c)
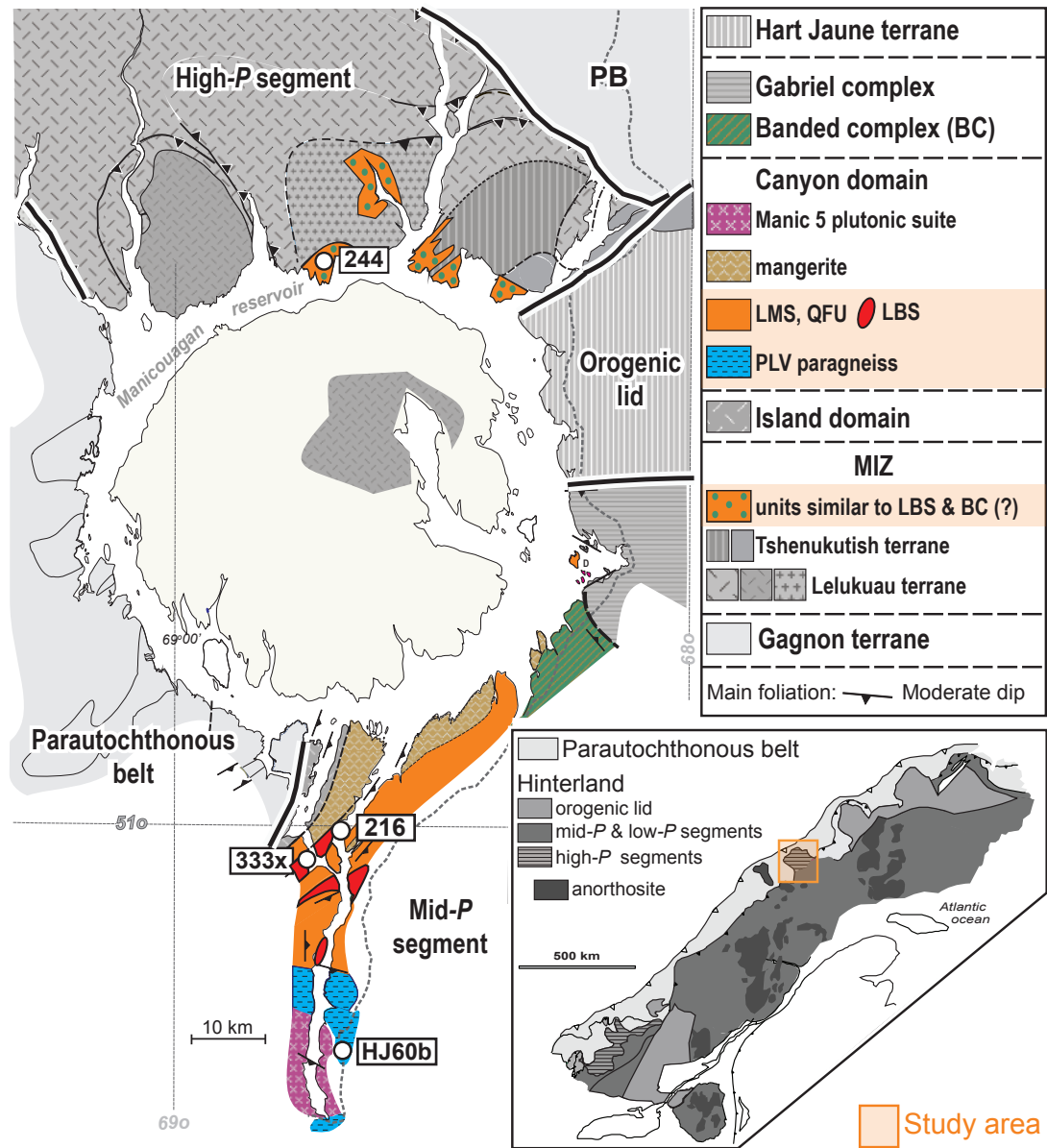
Figure 3.1: Simplified geological map of the Manicouagan area with location of the four samples of interest and inset map showing the general framework of the Grenville Province (updated from Dunning and Indares, 2010). LMS – layered mafic suite; QFU – layered quartzofeldspathic unit; LBS – layered bimodal sequence, including zones of hydrothermal alteration; PLV – Complexe de la Plus Value; MIZ – Manicouagan Imbricate Zone.
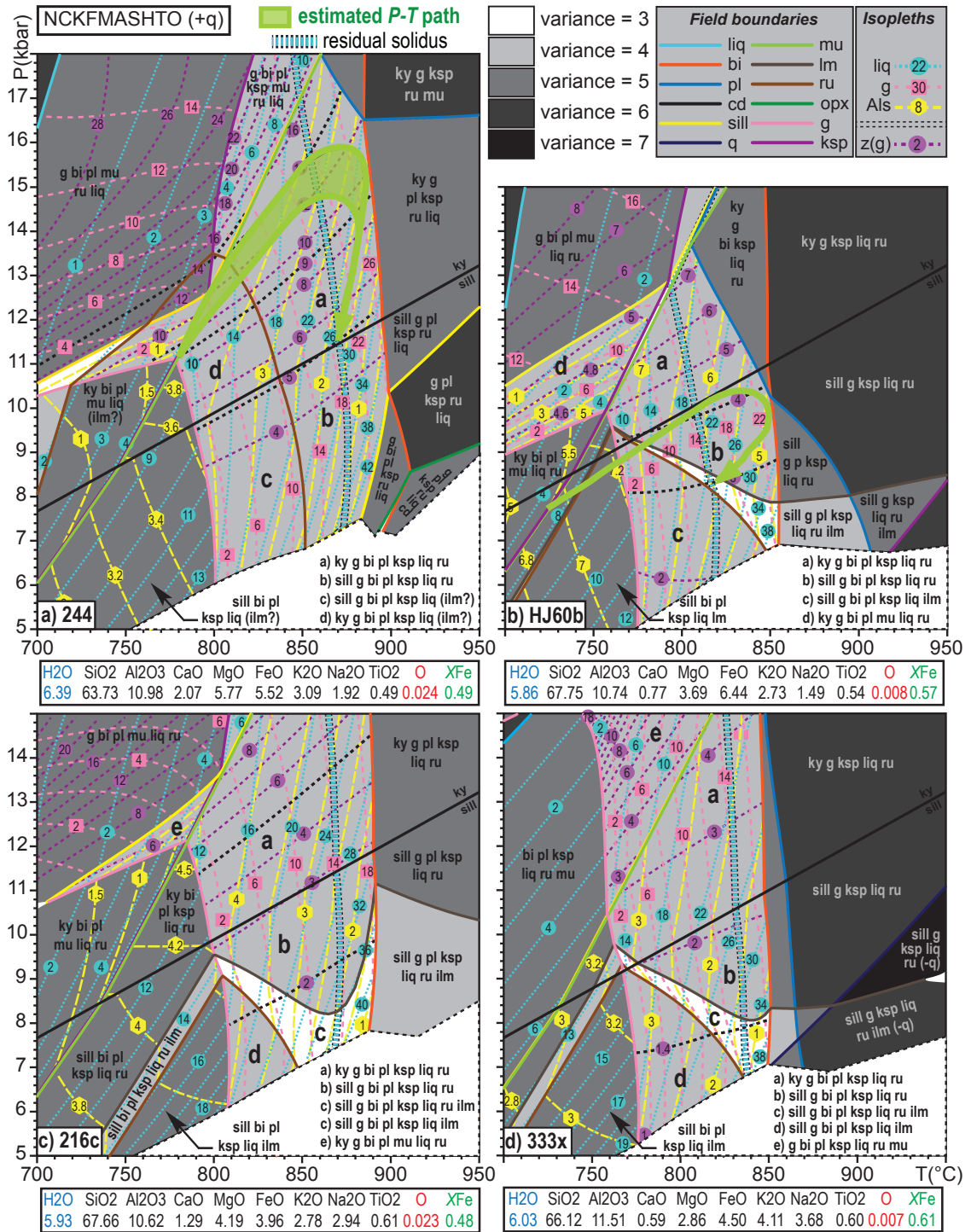
Figure 3.10: Melt-reintegrated *P–T* pseudosections showing the distribution of relevant isopleths, and the inferred overall *P–T* evolution (for #244 and #60b only; see explanation in text). The solidus calculated with the measured bulk compositions (from Figs. 3.8 and 3.9) is also shown for reference. Blank fields were not calculated. Notes on the melt reintegration:
(i) In #244, a proportion of 22% of liquid was added at the intersection of *z(g)*=11% with the solidus (at P=14.55 kbar–T=859.9 °C);
(ii) In HJ60b, a proportion of 20% of liquid was added at the intersection of *z(g)*=4% with the solidus (at P=8.83 kbar–T=808.5 °C);
(iii) In 216c, a proportion of 24% of liquid was added at the intersection of *z(g)*=4% with the solidus (at P=12.81 kbar–T=868.5 °C;
(iv) In 333x, a proportion of 26% of liquid was added at the intersection of *z(g)*=2% with the solidus (at *P*=10.20 kbar–*T*=832.2 °C).
For mineral abbreviations see caption of Fig. 3.8.

140
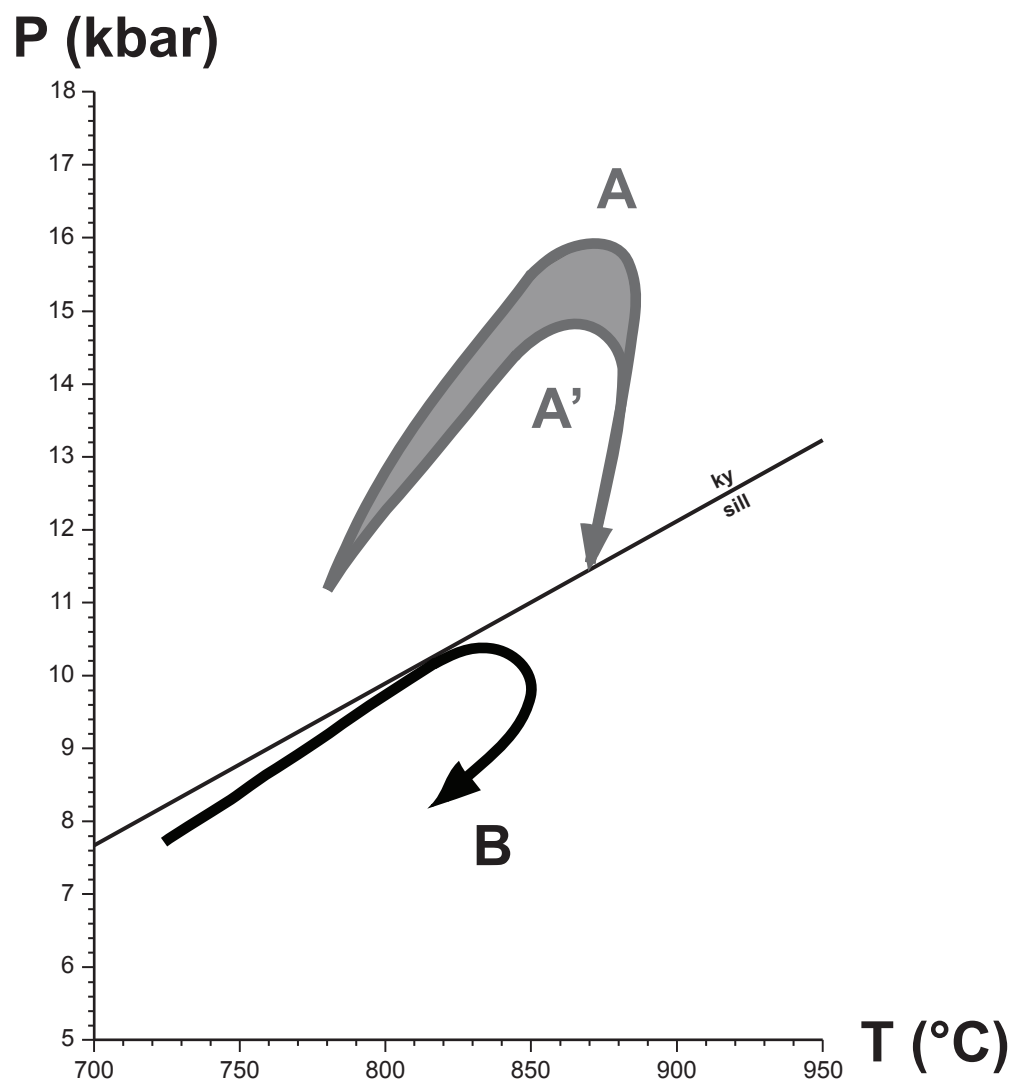
Figure 3.11: Schematic *P–T* paths from the high and mid-*P* portions of the hinterland in the Manicouagan area.
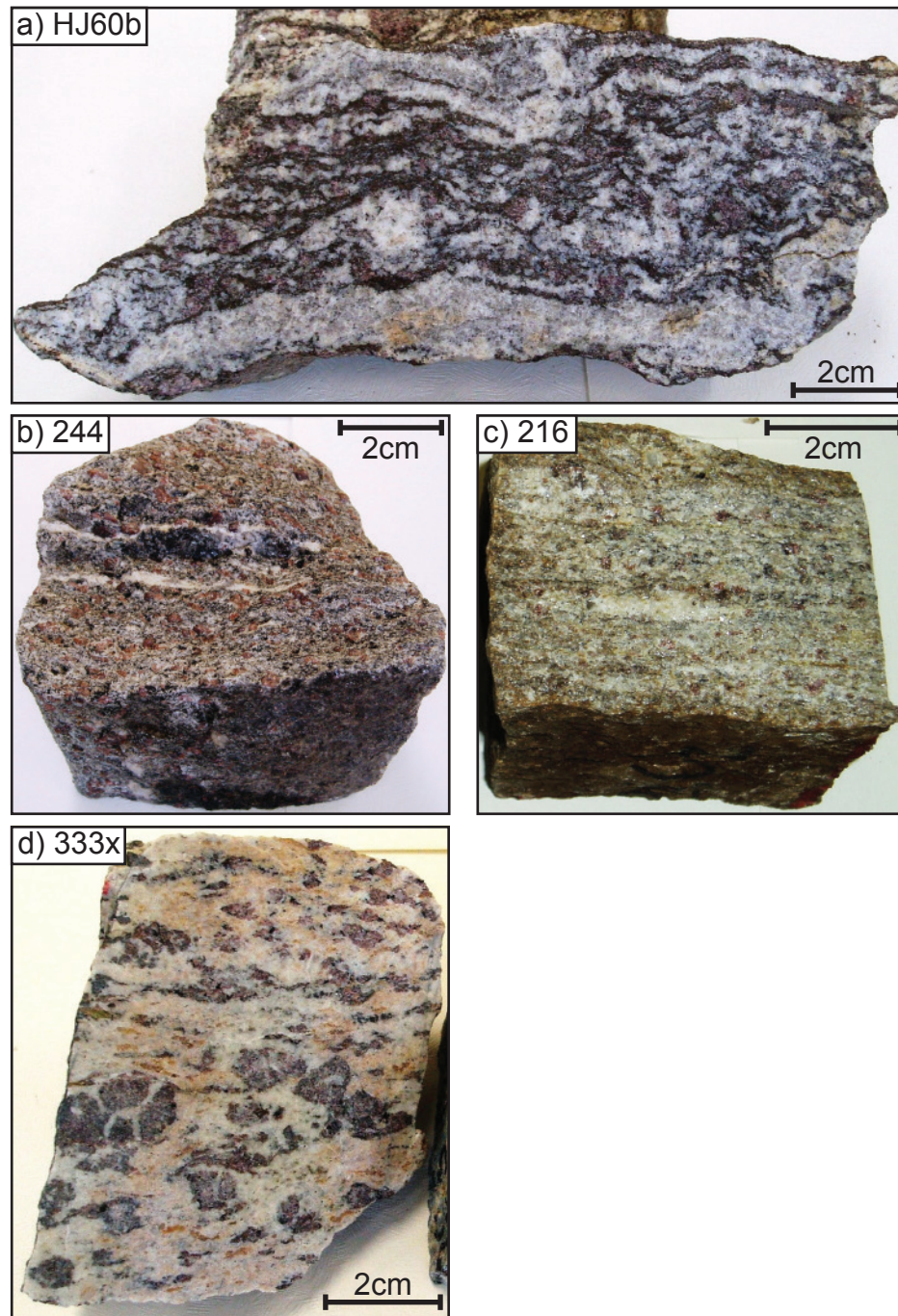
Figure 3.2: Photographs of the rock samples: (a) HJ60b: metasedimentary gneiss from the PLV, (b) 244: metasedimentary gneiss from the LBS, (c) 216 and (d) 333x: aluminous gneisses derived from hydrothermally altered felsic rocks of the LBS.
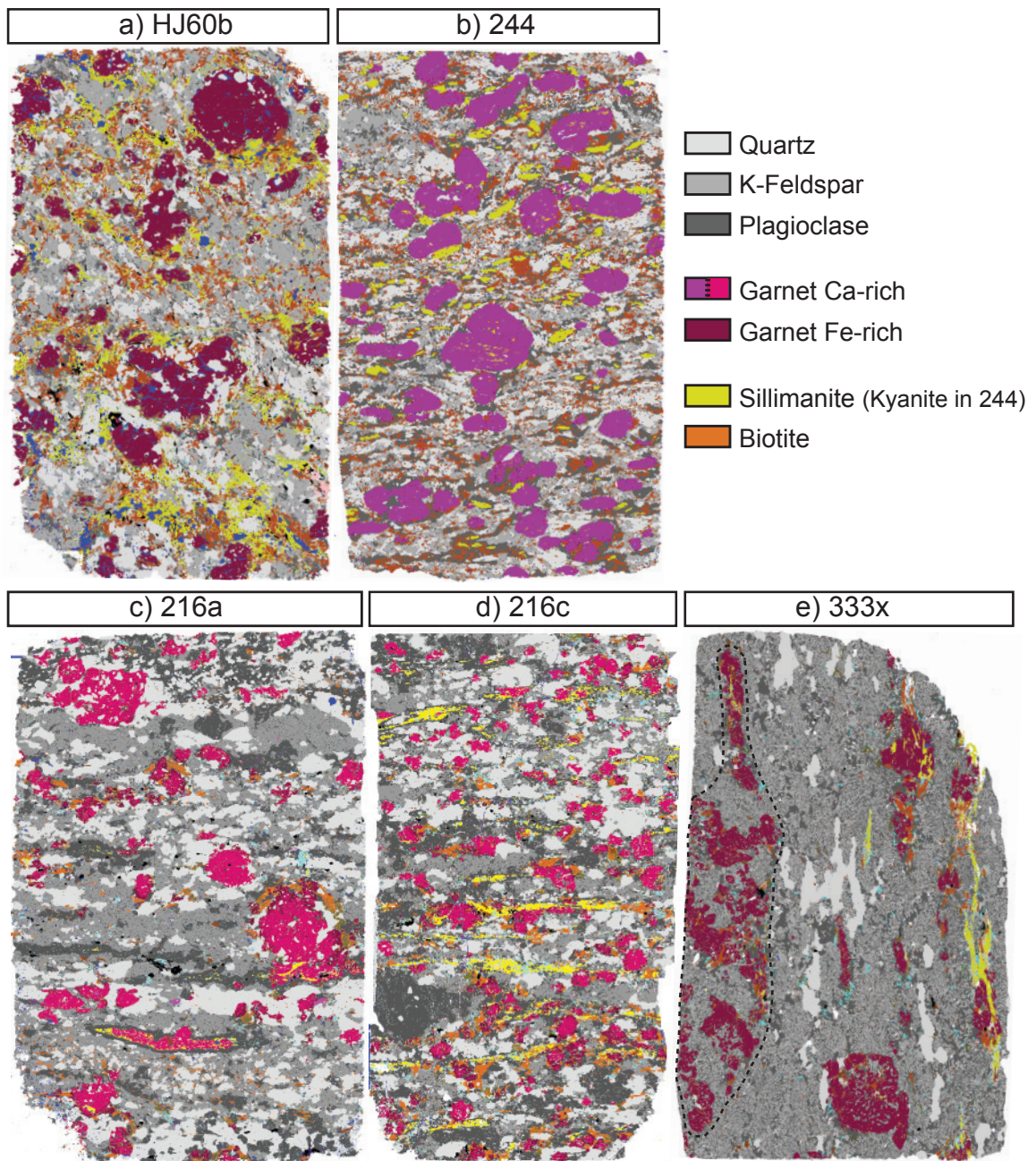
Figure 3.3: False-color maps of thin-sections generated by SEM-MLA: (a) #HJ60b, (b) #244, (c) #216a, (d) #216c, (e) #333x.
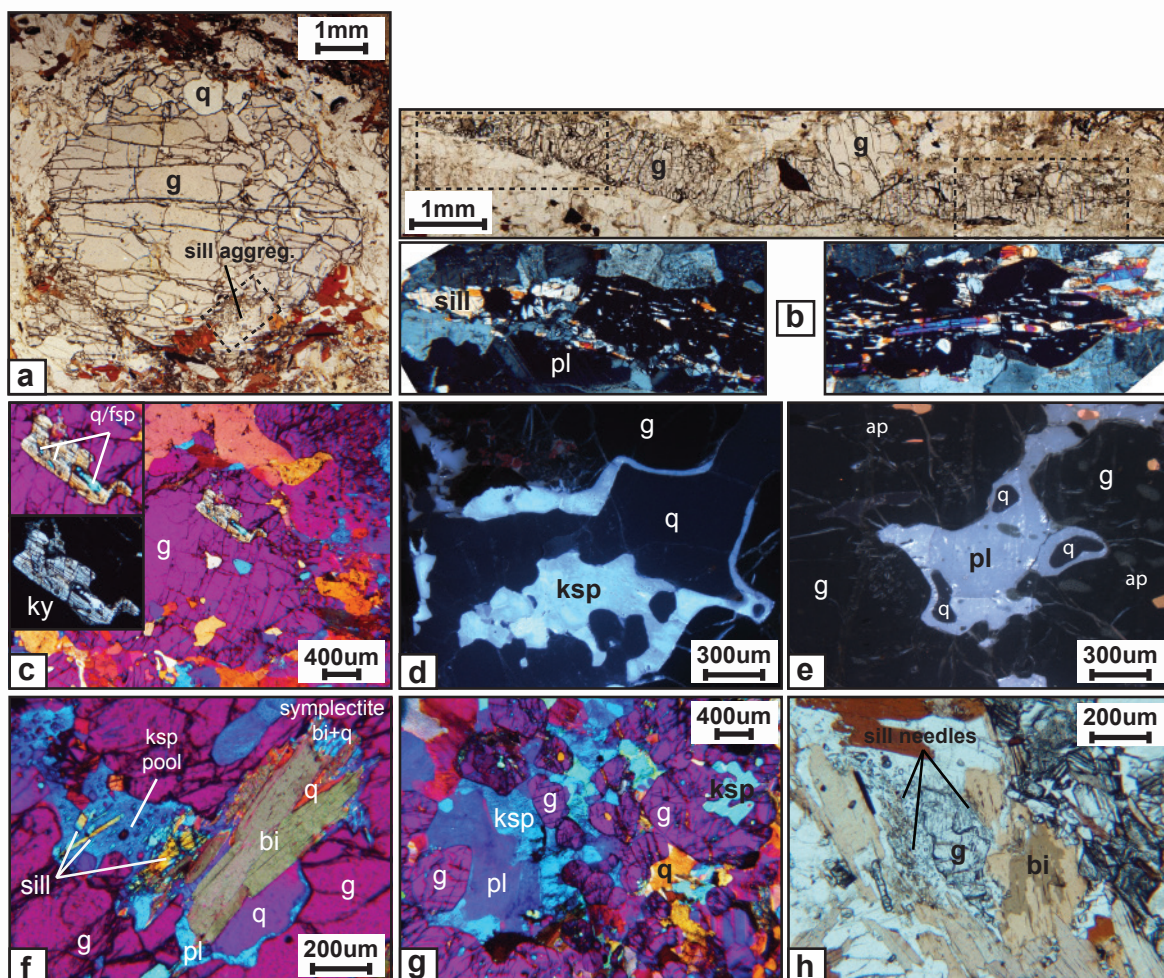
Figure 3.4: Photomicrographs of garnet microstructures viewed in: PPL, plane-polarized light; XPL, crossed-polarized light; XPLq: crossed-polarized light with accessory quartz plate; CL, cathodoluminescence. (a) Large garnet porphyroblast with rims corroded by biotite±sillimanite (#HJ60b; PPL). (b) Elongate garnet with inclusions and tails of sillimanite needles/prisms, mantled by plagioclase (#216a; PPL and XPL). (c) Garnet porphyroblast with rounded inclusions of quartz and one larger inclusion of kyanite; the latter is resorbed, and partly replaced by quartz or feldspar along cleavages (#216a; XPLq). (d) Embayment in garnet filled by a large squarish quartz grain thinly rimmed by K-feldspar (#HJ60b; CL). (e) Embayment in garnet filled with plagioclase (central part with a faint outline) and resorbed quartz, rimmed by a thin film of feldspar (#244; CL). (f) Embayment in garnet filled by resorbed biotite, sillimanite and quartz in a pool of K-feldspar; biotite rims are locally overgrown by biotite+ quartz symplectite and a newly grown sillimanite needle is also shown in the left (#HJ60b; XPLq). (g) Detail of a garnet aggregate (#333x; XPLq). (h) Resorbed garnet in a cloud of sillimanite needles, enclosed in a biotite cluster (#HJ60b; PPL).
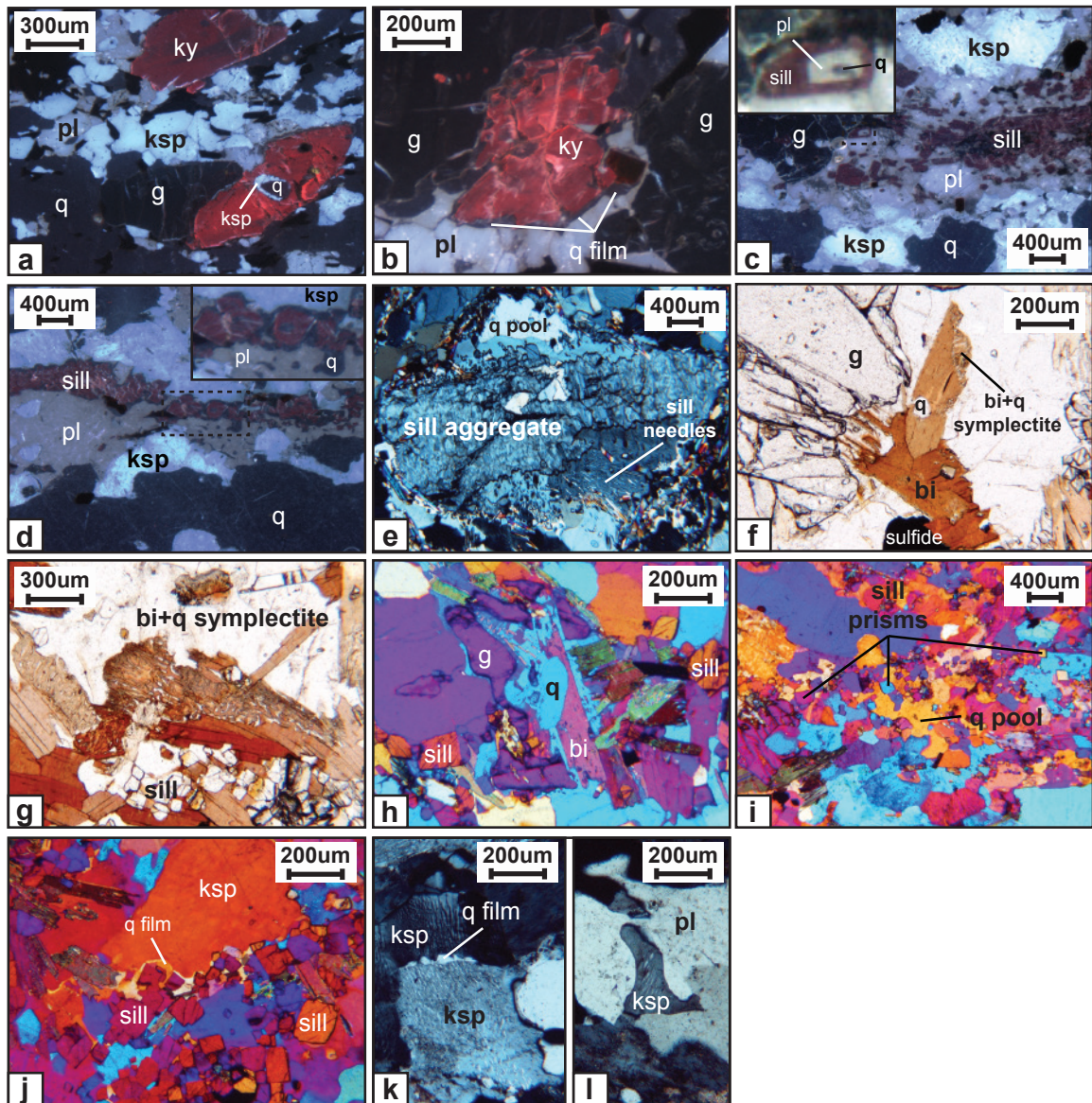
Figure 3.5: Photomicrographs of other microstructures viewed in; PPL, plane-polarized light; XPL, crossed-polarized light; XPLq, crossed-polarized light with accessory quartz plate; CL, cathodoluminescence. (a) Kyanite with a composite inclusion of rounded quartz partly rimmed by K-feldspar (#244; CL). (b) Resorbed kyanite, thinly coated by quartz, between two garnet grains (#244; CL). (c) Composite inclusion of resorbed quartz rimmed by feldspar, in sillimanite (#216; CL). (d) Thin coating of quartz around sillimanite seams mantled by plagioclase (#HJ60b; CL). (e) Largely coalesced aggregate of sillimanite needles in a pool of feldspar corroding garnet (#HJ60b; XPL), the location of this microtexture is shown as a box with a dotted outline in Fig. 3.4a. (f) Biotite lath rimmed by biotite+quartz symplectite against a corroded garnet rim (#HJ60b; PPL). (g) Biotite+quartz symplectite rimming a biotite+sillimanite cluster (#HJ60b; PPL). (h) Feldspar pool with resorbed biotite and garnet in the matrix of #HJ60b (XPLq). (i) Interstitial quartz pool in the matrix (#216c; XPLq). (j) Thin film of quartz around sillimanite prisms at the boundary of a coarse grain of K-feldspar (#HJ60b; XPLq). (k) 'String of beads' made of quartz between two K-feldpar grains (#216c; XPL). (l) Finger of K-feldpsar between two plagioclase grains (#216c; XPL).
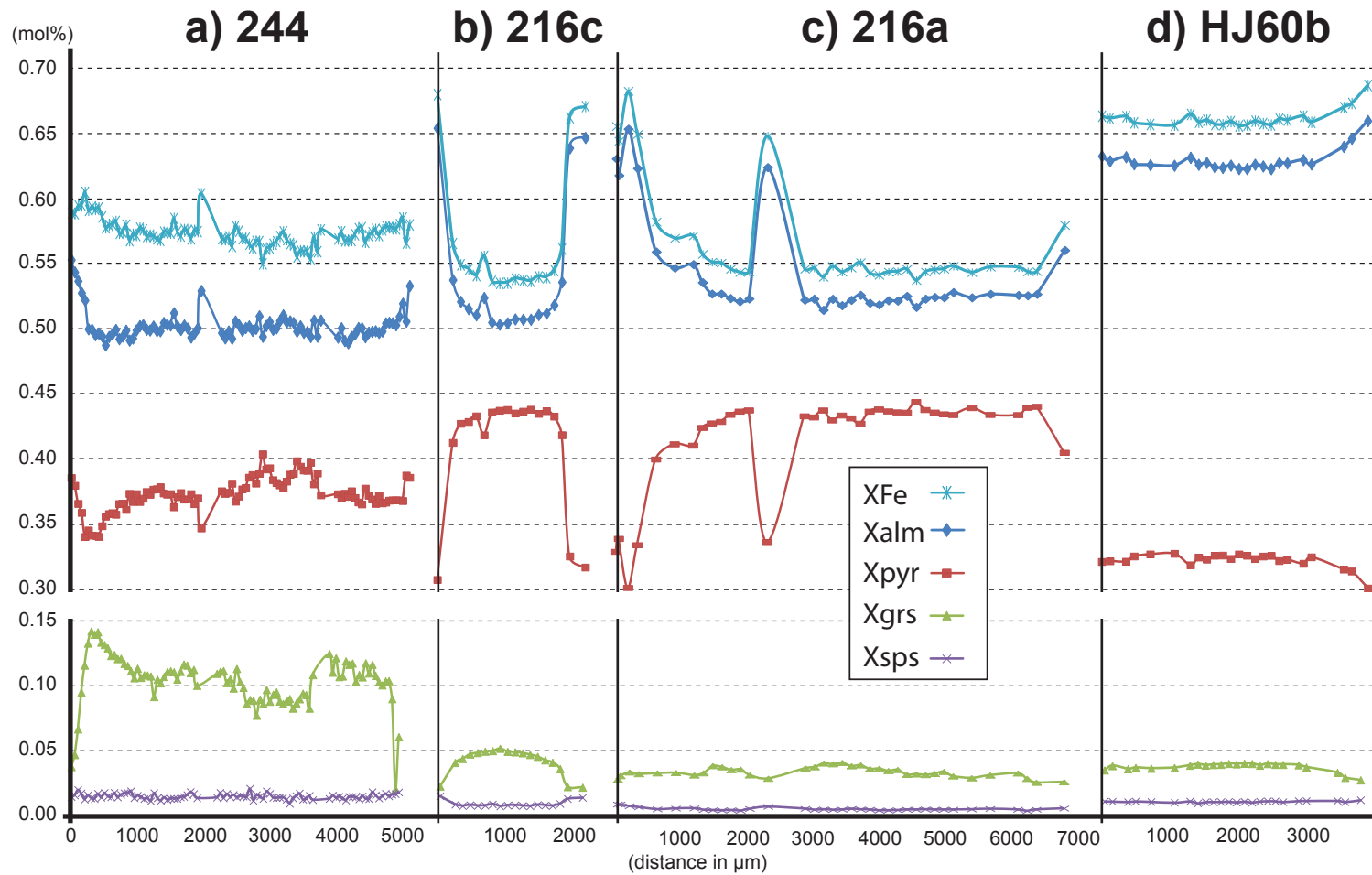
Figure 3.6: Zoning profiles of the largest garnet porphyroblasts analyzed in each sample (except for #333x in which garnet is unzoned).
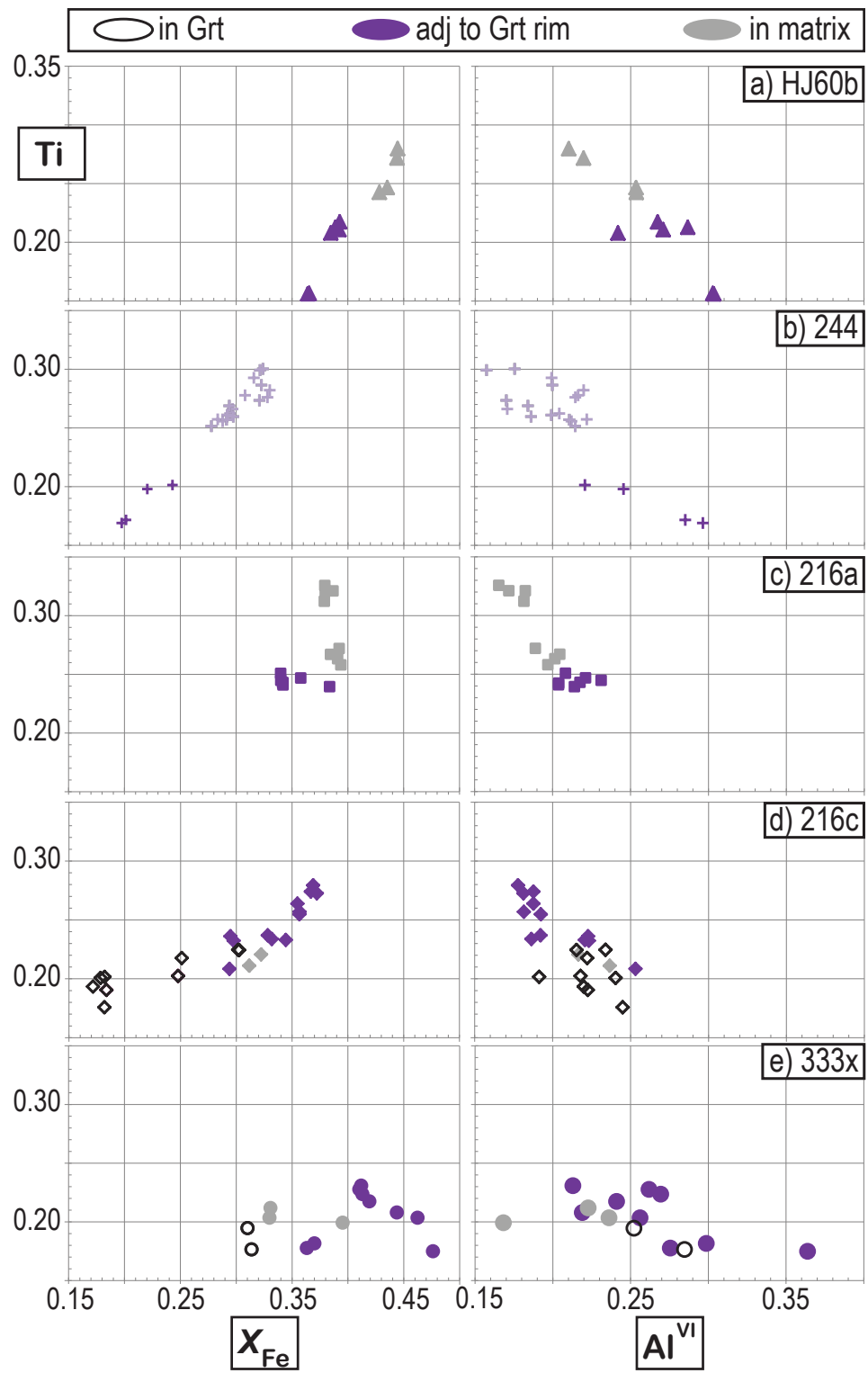
Figure 3.7: Biotite composition plots; Ti *vs.* X_{Fe} and Ti *vs.* Al^{IV}.
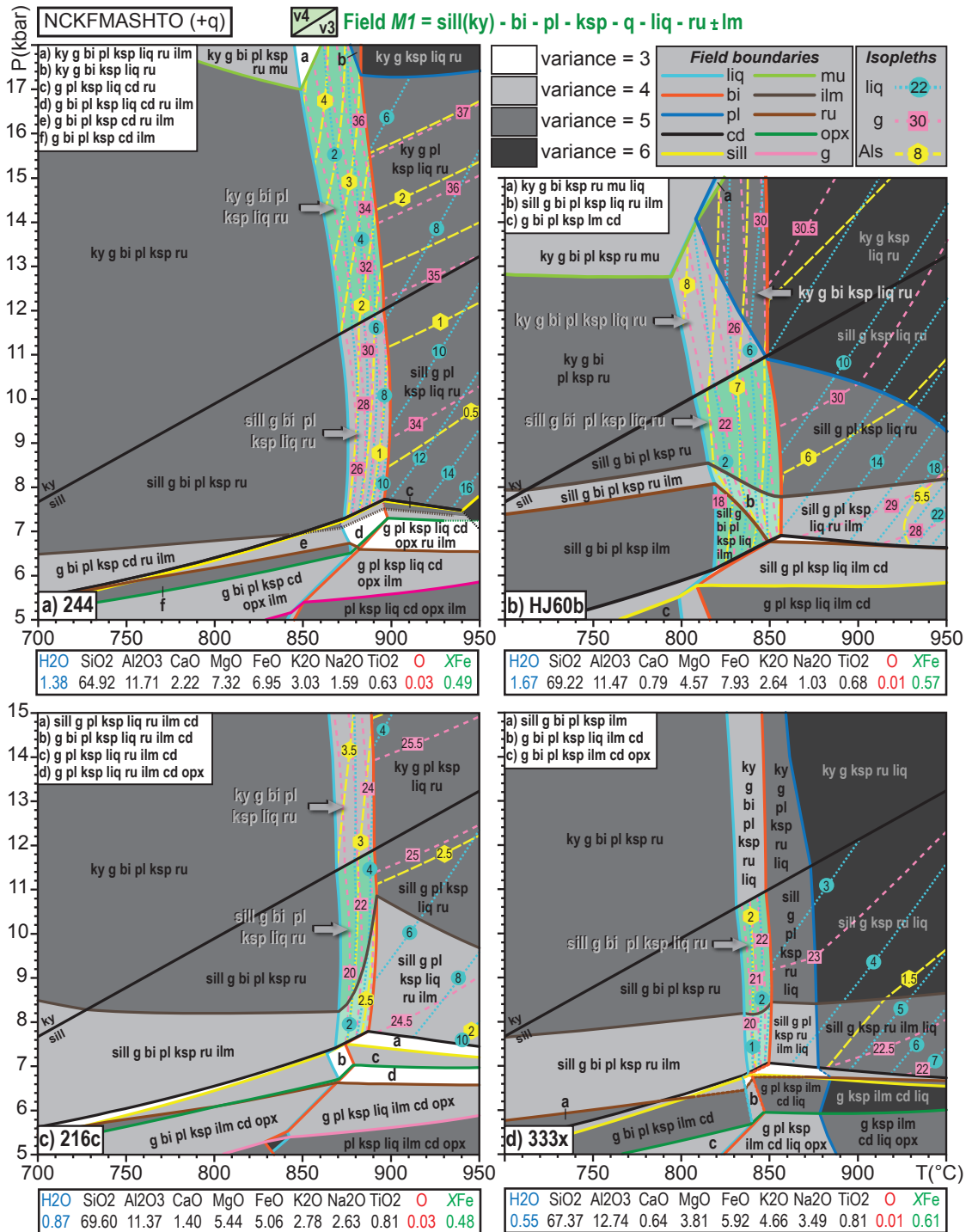
Figure 3.8: *P–T* pseudosections calculated with the estimated bulk rock composition specific to each sample #244, #HJ60b, #216c, #333x, showing the general topologies and the distribution of relevant phase proportion isopleths; the highlighted topology (field M1), corresponds to the mineral assemblage observed in the rocks. Mineral abbreviations: garnet (g); biotite (bi); sillimanite (sill); kyanite (ky); rutile (ru); ilmenite (ilm); cordierite (cd); orthopyroxene (opx); muscovite (mu); quartz (q); silicate melt (liq).
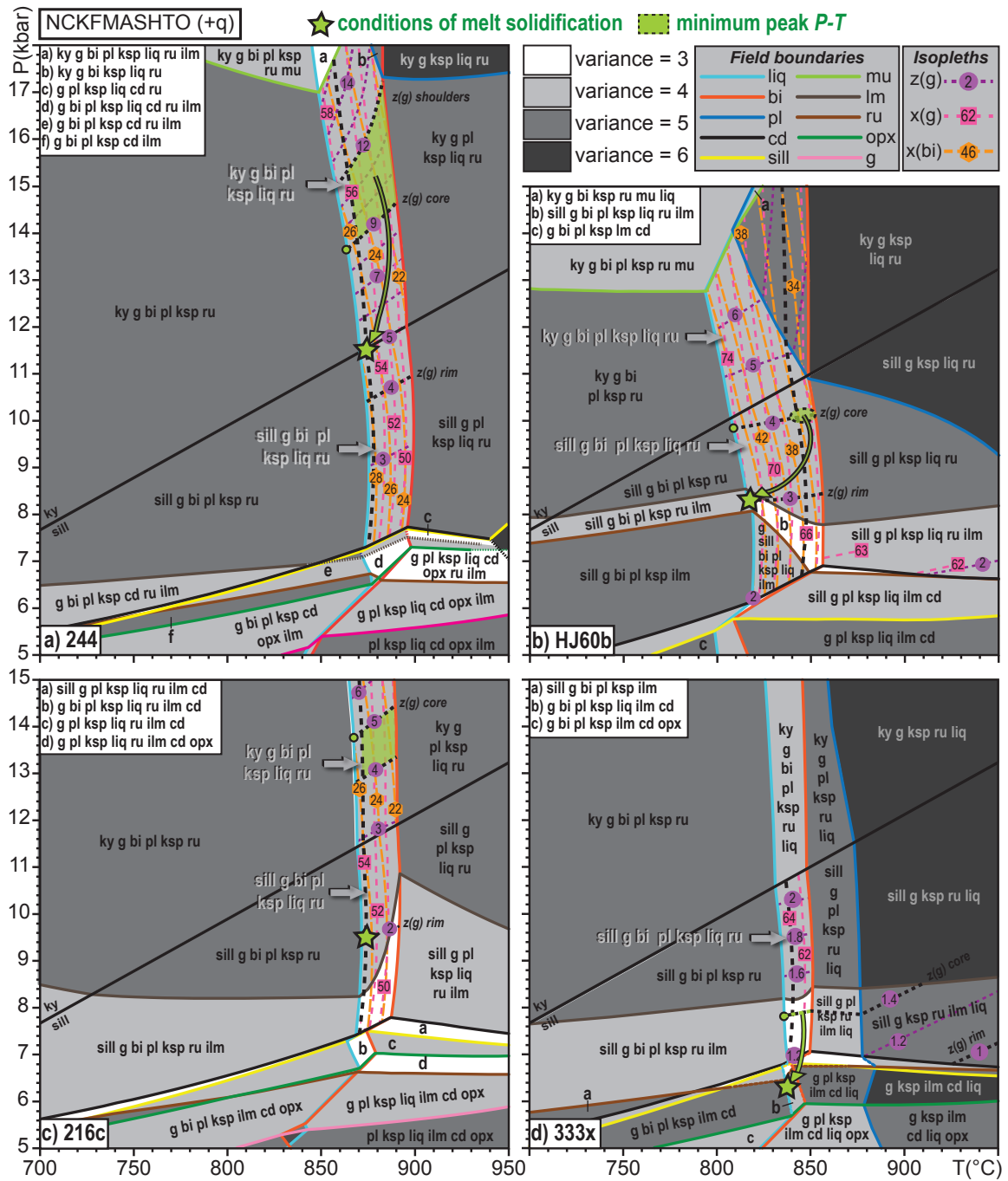
Figure 3.9: Same set of *P–T* pseudosections as in Fig. 3.8, showing the distribution of relevant mineral composition isopleths and inferred *P–T* paths. For mineral abbreviations see caption of Fig. 3.8.

APPENDICES OF CHAPTER 3 INCLUDED (AS JPEG FILES)

IN THE CD

APPENDIX 3.1: (BSE and/or false color MLA) maps showing the locations in thin-section of the microprobe analyses for all samples (JPEG files).

APPENDIX 3.2: Garnet microprobe data for all samples (EXCEL file)

This data table is a simplified version of the full table, after deletion of rows corresponding to easy and obvious calculation steps that would distract the reader from the main points.

APPENDIX 3.3: Plagioclase microprobe data for all samples (EXCEL file)

This data table is a simplified version of the full table, after deletion of rows corresponding to easy and obvious calculation steps that would distract the reader from the main points.

APPENDIX 3.4: Biotite microprobe data for all samples (EXCEL file)

This data table is a simplified version of the full table, after deletion of rows corresponding to easy and obvious calculation steps that would distract the reader from the main points.

CHAPTER 4

4. *IN SITU* LASER ABLATION–ICPMS DATING OF MONAZITE FROM ALUMINOUS GNEISSES: INSIGHTS ON THE TECTONO-METAMORPHIC HISTORY OF A GRANULITE-FACIES DOMAIN IN THE CENTRAL GRENVILLE PROVINCE

ABSTRACT

In situ U–Pb dating of monazite from granulite-facies anatectic aluminous gneisses of the hinterland of the Grenville Province (Manicouagan area) is used to constrain the age of metamorphic events. Matrix grains in these rocks show complex internal textures consistent with extensive corrosion and overgrowths which are attributed to partial dissolution of earlier monazite in anatectic melt followed by new growth during melt crystallization or subsequent fluid infiltration.

The new monazite data show: (a) inherited 'pre-Grevillian' ages up to *ca.* 1400 Ma in some rocks; (b) 'main Grenvillian' ages in the general range of *ca.* 1070–1020 Ma, with a variable spread in individual samples and a general cluster at 1070–1050 Ma; and (c) 'late Grenvillian' ages at *ca.* 1010–990 Ma, mostly restricted to BSE-bright rims of matrix grains. The wide age range of the main Grenvillian metamorphism suggests episodic growth of monazite over a wide time span, consistent with protracted residence of the host rocks under high-T conditions. The clusters in the age distribution likely represent major episodes of melt crystallization in the respective rocks, following the granulite-facies metamorphism. In contrast, the growth of the late Grenvillian monazite at *ca.* 1000 Ma is attributed to late fluid infiltration of the host rocks under greenschist-facies conditions, coeval with ultra-potassic magmatism. It is the first report of a late Grenvillian metamorphic overprint on granulite-facies mineral assemblages in the hinterland and is consistent with the model of extensional collapse of the orogen.

4.1. INTRODUCTION

In recent years, *in situ* dating of monazite has become a key tool for unravelling complex metamorphic histories of high-grade terranes. Although less precise than the isotopic dilution–thermal ionisation mass spectrometry (ID–TIMS) method, *in situ* techniques such as electron probe micro-analysis (EPMA) and laser ablation–inductively coupled plasma mass spectrometry (LA–ICPMS) have better spatial resolution, permitting dating of distinct zones in individual monazite grains as well as linking ages with specific microstructural settings (*e.g.,* Simonetti *et al.,* 2006; Kelsey *et al.,* 2007,2008; Cutts *et al.,* 2010; Langone *et al.,* 2011; Kelly *et al.,* 2012; Gervais and Hynes, 2012).

Recent studies have shown that the diffusivity of Pb in monazite is low, comparable to that in zircon (Cherniak *et al.,* 2004), and it is increasingly accepted that even in high-grade metamorphic rocks monazite ages most likely represent growth events rather than resetting (*e.g.,* Kelsey *et al.,* 2008; Dunning and Indares, 2010). During prograde metamorphism of aluminous rocks, monazite typically forms from upper greenschist throughout the amphibolite facies by reactions that involve other accessory phases but also rock forming silicates. However, during anatexis under granulite-facies conditions monazite is predicted to dissolve in the melt and to grow again only when melt crystallizes during cooling (Kelsey *et al.,* 2008; Spear and Pyle, 2010). In addition, monazite might also grow at sub-solidus conditions if there is fluid infiltration.

Interpretation of *in situ* monazite ages is a complicated enterprise for many reasons. For instance, low precision of the U–Pb data limits the ability to distinguish monazite

growth events occurring within a short period of time (*e.g.,* a few 10s of million years). Also, assigning monazite U–Pb ages to different parts of a metamorphic *P–T* path(s) remains difficult as internal elemental zoning, even if well documented (*e.g.,* EPMA) cannot always be related to specific metamorphic reactions (*e.g.,* Spear and Pyle, 2002; Harrison *et al.,* 2002; Williams *et al.,* 2007; Kelsey *et al.,* 2008). This is particularly challenging in the case of long duration orogens, in which the middle to lower crust remains under high metamorphic temperatures over several tens of my (large hot orogens; Beaumont *et al.,* 2006).

The Grenville Province is a prime example of an ancient, long-duration (*ca.* 1100–980 Ma) large hot orogen, often compared to the Himalaya-Tibet system (*e.g.,* Rivers, 2008). Geological research during the last few decades has provided a clear image of the general orogenic architecture and metamorphic styles of the Province (*cf.,* Rivers *et al.,* 2012) and resulted in compelling first order tectonic interpretations. For instance, it is established that during the culmination of the Grenvillian orogeny (*ca.* 1090–1050 Ma) large parts of the orogenic hinterland (high-*P* and mid-*P* segments or belts of Rivers *et al.,* 2012) were subjected to granulite-facies metamorphism, and heterogeneous flow of this middle to lower orogenic crust is inferred to have played a key role in the tectonic evolution of the Province (Jamieson *et al.,* 2007, 2010; Jamieson and Beaumont, 2011). In addition, the present juxtaposition of these high-grade metamorphic belts with crustal segments affected by a lower-grade (or imperceptible) Grenvillian overprint is attributed to orogenic collapse (*ca.* 1000–980 Ma; Rivers, 2012). In contrast, the structurally lower

Parautochthonous belt of the Province was metamorphosed during the presumed orogenic collapse, and final propagation of the orogen to the NW (Rivers, 2009).

Individual rocks from various parts of the granulite-facies segments show significant spread in metamorphic ages within the *ca.* 1090–1040 Ma interval (*e.g.,* Slagstad *et al.,* 2004; Dunning and Indares, 2010), raising the possibility of multiple metamorphic pulses, or protracted residence under high-*T* conditions. In addition, parts of the hinterland in the central and eastern Grenville Province record a late-Grenvillian thermal event (990–970 Ma), broadly coeval with the main metamorphism in the Parautochthonous belt. This event is manifested by pervasive intrusions of ultrapotassic dykes, inferred to have originated from metasomatized subcontinental lithosphere (Owens and Tomascak, 2002; Valverde-Cardenas *et al.,* 2012), felsic pegmatites and granite (Gower and Krogh, 2002; Dunning and Indares, 2010), but its effect on the country rocks has not been investigated.

The work presented here aims to reassess the spread of ID–TIMS monazite ages previously identified by Dunning and Indares (2010) in granulite-facies anatectic aluminous rocks from the Manicouagan area (central Grenville Province), and evaluate a potential contribution from the late-Grenvillian thermal event. To that end, *in situ* LA–ICPMS U–Pb dating of monazite was undertaken on the same samples as those of Dunning and Indares (2010), this time with the potential to place the age data in the context of the general microstructure of the rocks, as well as in the context of specific zones in single monazite grains. Metamorphic microstructures, and *P–T* paths inferred by phase equilibria modelling, are presented in another contribution (Lasalle and Indares,

147

2014). Here the focus is on the monazite populations, their microstructural setting in thin-section, and their U–Pb ages.

4.2. GEOLOGICAL BACKGROUND

4.2.1. Regional setting

This study focuses on the Manicouagan area in the central Grenville, enclosing the reservoir of the same name (Fig. 4.1; for a comprehensive geological overview see Dunning and Indares, 2010). In this area, the hinterland of the Province is located structurally above Archean to Paleoproterozoic rocks of the Parautochthonous Gagnon terrane (Rivers, 1989; Jordan *et al.,* 2006; van Gool *et al.,* 2008) and consists of lithotectonic domains made of 1.7 to 1.2 Ga Mesoproterozoic rocks, best exposed on the shoreline of the reservoir (Indares *et al.,* 2000; Indares and Dunning, 2004; Dunning and Indares, 2010). During the culmination of the Grenvillian orogeny, the northern (Manicouagan Imbricate Zone; MIZ; Fig. 4.1) and southern (Canyon and Island domains) portions of the hinterland were metamorphosed under high-*P* and mid-*P* granulite-facies conditions respectively (Indares and Dunning, 2001, 2004; Dunning and Indares, 2010) whereas to the east, between these two, the Hart Jaune terrane displays no record of Grenvillian age high-grade metamorphism and belongs to the 'orogenic lid' of Rivers (2008). In contrast, parautochthonous units on the western shore of the reservoir were metamorphosed under high-*P* granulite-facies conditions later, during the waning stages of the Grenvillian orogeny (Jordan *et al.,* 2006).

The samples of interest come mostly from the Canyon domain, which is exposed in

the southern part of the Manicouagan reservoir (Fig. 4.1). This domain is mainly composed of layered units, first documented by Dunning and Indares (2010) and further characterised by Indares and Moukhsil (2013). A *ca.* 1.5 Ga paragneissic sequence, known as the complex de la Plus Value (PLV; first defined farther east by Moukhsil *et al.*, 2012) is exposed in the southern part of the domain. In contrast, the central and northern parts are dominated by a complex lithologic association including a *ca.* 1.4 Ga old layered mafic suite (LMS), interleaved with a layered quartzofeldspathic unit (QFU) of unknown age, and a *ca.* 1.24 Ga layered bimodal mafic-felsic sequence (LBS*).* The LBS is inferred to represent remnants of a volcanic belt emplaced in an extensional setting, and locally contains aluminous layers some of which are attributed to pre-metamorphic hydrothermal alteration of felsic volcanic rocks (Hindemith 2014; Indares and Moukhsil, 2013; Lasalle *et al.,* 2013). Rocks typical of the LBS are also recognized 50 km to the north, in the southern tip of the Manicouagan Imbricate Zone, in the high-*P* segment (MIZ; Fig. 4.1). In addition, the southern part of the Canyon domain is pervasively injected by late to post-tectonic ultrapotassic dykes and felsic pegmatite that were dated at 980±3 Ma and 995±3.5 Ma, respectively (Dunning and Indares, 2010).

4.2.2. Summary of metamorphic ages in the Manicouagan area

Available age constraints for the Grenvillian metamorphism include monazite (Fig. 4.1), zircon and titanite data. In the Canyon domain, U–Pb monazite (ID–TIMS) ages of single grains from anatectic aluminous rocks range between *ca.* 1080 and 1020 Ma with a varied spread within individual samples, and the largest concentration at *ca.* 1062–1059

Ma (Dunning and Indares, 2010). In addition, recent metamorphic zircon U–Pb data (*in situ* LA–ICPMS; Lasalle *et al.,* 2013) for similar rocks yielded Grenvillian ages between *ca.* 1076 and 1044 Ma.

Grenvillian monazite ID–TIMS ages from other parts of the Manicouagan area (Fig. 4.1) include *ca.* 1050 Ma in the mid-*P* Gabriel complex (Indares and Dunning, 2004), *ca.* 1044 to 1033 Ma in the high-*P* Manicouagan Imbricate zone (Indares and Dunning, 2001; Dunning and Indares, 2010), with *ca.* 1020 Ma at the structural top, near the boundary with the Hart Jaune terrane, and 995–985 Ma in the Gagnon terrane (Jordan *et al.,* 2006). Finally, titanite ages from the Canyon domain and the Manicouagan Imbricate zone range between *ca.* 1000 and 985 Ma (Cox *et al.,* 1998; Dunning and Indares, 2010).

So far these data suggest that: (a) the monazite ages from individual samples are more clustered in the high-*P* segment relative to the mid-*P* segment; (b) that the latter also shows older ages (*e.g.,* at 1080 and 1060 Ma) which are absent from the high-*P* segment; and (c) high grade metamorphism in the Gagnon terrane is distinctly younger than in any part of the hinterland of the Manicouagan area.

The previous studies also revealed some pre-Grenvillian ages from inherited monazite (ID–TIMS; Fig.4.1): *ca.* 1740–1720 Ma in the Gagnon terrane (Jordan *et al.,* 2006); *ca.* 1478–1467 Ma in the Gabriel complex (Indares and Dunning, 2004) and the Canyon domain (Dunning and Indares, 2010); and *ca.* 1220 Ma from the high-*P* portion of the LBS (intercept age, Dunning and Indares, 2010). In addition, the zircon study by Lasalle *et al.,* (2013) identified pre-Grenvillian metamorphic events in the PLV in

Canyon domain at about 1.4 Ga and 1.2 Ga, which are probably linked to the emplacement of the LMS and LBS into their country rocks.

4.2.3. Sample locations

Five samples were selected for *in situ* monazite dating using LA–ICPMS: one from an aluminous paragneiss of the PLV (#HJ60b) and four from aluminous layers of the LBS (#244, #216a, #216c, and #333x; Fig. 4. 1). Among the latter, #244 is inferred to be of metasedimentary origin whereas the rest are inferred to be derived from hydrothermally altered felsic volcanic rocks (Lasalle *et al.,* 2013). The rocks are from the Canyon domain (mid-*P* portion of the hinterland) except for #244, which was collected on the extension of the LBS into the high-*P* segment. Sample #333x, is the same one used for the previous ID–TIMS study while #216a-c, #HJ60b and #244 are different samples from the same outcrops and rock types previously analyzed.

4.2.4. Summary of the petrography and *P–T* data

The detailed petrography of the rock samples is discussed in Lasalle and Indares (2014) therefore only a brief summary is presented here. All rocks are anatectic aluminous gneisses with the main mineral assemblage of quartz–K-feldspar–plagioclase–garnet–Al-silicate–biotite and leucosome, with trace amounts of rutile and/or ilmenite. Al-silicate is sillimanite in the mid-*P* samples (#HJ50b, #216a, c, #331x), and kyanite in the high-*P* #244.

151

The general distribution of phases in polished thin sections is shown in Fig. 4.2 by means of false-color maps (see also Lasalle and Indares, 2014). The metasedimentary samples #244, #HJ60b have the highest proportions of garnet+biotite+Al-silicate and mainly consist of large garnet porphyroblasts, variably overgrowing Al-silicate and domains rich in Al-silicate+biotite, enclosed in a quartzofeldspathic matrix (Fig. 4.2a, b). In the samples inferred to have acquired their aluminous character by hydrothermal alteration of felsic rocks (#216a-c and #333x), garnet+biotite+sillimanite is concentrated in thin seams, locally mantled by plagioclase (#216a) or overgrown by variably elongated garnet, and scarce biotite is mainly associated with garnet and sillimanite. Samples #216a-c display a layered quartzofeldspathic matrix with small and evenly distributed garnets (#216c; Fig. 4.2d), and a wider range of garnet sizes in #216a (Fig. 4.2c). Sample #333x is characterized by a K-feldspar dominated matrix enclosing elongated quartz domains and aggregates of framboidal garnet which define a large discontinuous lens (Fig. 4.2e).

At a finer scale, all samples display films and/or optically continuous pools of feldspar engulfing resorbed quartz, biotite, and/or Al-silicate. These microstructures are mostly observed as composite inclusions in garnet, but also, more rarely, in the matrix and are inferred to represent former melt pseudomorphs (Lasalle and Indares, 2014).

The peak metamorphic mineral assemblage in conjunction with microstructural evidence of garnet overgrowing Al-silicate and the presence of former anatectic melt, is consistent with P–T conditions within the field of the continuous biotite-consuming fluid-absent melting reaction Al-silicate+biotite+quartz+plagioclase→garnet+K-

feldspar+liquid. In all samples garnet is variably corroded by biotite (±sillimanite in the mid-*P* samples) consistent with back-reaction during the subsequent melt crystallization. However, overall good preservation of the peak assemblage suggests that part of the melt may have escaped from its source rocks, a feature commonly observed in rocks undergoing anatexis in orogenic environments (*e.g.*, Brown, 2004).

Metamorphic microstructures and mineral chemistry data integrated with phase equilibria modelling suggest: (a) a steep prograde *P*–*T* path up to ~ 14.5 kbar and 890 °C, followed by decompression with minor cooling to the solidus at ~ 11 kbar and 870 °C (just above the kyanite-sillimanite transition) in the high-*P* sample #244, similar to those inferred in other parts of the Manicouagan Imbricate zone; and (b) *P*–*T* paths with moderate d*P*/d*T* gradients, confined below the sillimanite-kyanite transition with maximum *P*–*T* at ~ 9.5 kbar and 850 °C, and a retrograde portion to ~ 8 kbar and 820 °C in the case of #HJ60b (Lasalle and Indares, 2014).

In addition, the mid-*P* aluminous rocks from both the PLV and the LBS display local subtle microstructures consistent with greenschist metamorphic overprint. These include fractured garnet with the cracks filled by chlorite (*e.g.*, #216, #HJ60; Fig. 4.3a-b), sillimanite pseudomorphed by a fine-grained mixture of an unidentified phase, probably sericite (#HJ60b; Fig. 4.3c), and graphite rimmed by sericite aggregates (Fig. 4.3d).

4.3.   DESCRIPTION OF THE MONAZITE POPULATIONS

4.3.1.   Imaging techniques

In each polished thin section, monazite (*cf.,* dark dots Fig. 4.2) was identified by SEM–MLA mineral mapping (Lasalle and Indares, 2014). The maps were produced by a Mineral Liberation Analysis (MLA) software (developed by JKTech, University of Queensland, Australia) linked to a FEI Quanta 400 environmental scanning electron microscope (SEM) at the Bruneau Center of Memorial University. The SEM was setup with an accelerating voltage of 25 kV, a beam current of 10 nA, a 2 mm frame size (or horizontal field width), a dwell time of 10 ms, and a step size of 50 μm. The MLA software was used to generate a point-counted estimation of mineral proportions and a composition-sensitive false-color map of the mineral associations and textural relationships (Shaffer *et al.,* 2008; Shaffer, 2009). In addition, a 1st order determination in terms of Th contents and zoning was done with the SEM. In order to map in more details, each monazite grain, the thin-sections had to be mapped a second time with the SEM coupled to the EDX and MLA software. Using the same SEM parameters (*e.g.,* contrast/brightness settings) than that used for the full-section mapping, we set up the scan to exclude all minerals being darker than the 8 bit brightness value of 130, which appeared to have excluded Fe oxides, but included minerals as bright or brighter than pyrrhotite, thus the presence of some grains of zircon and apatite with the monazite. Figure 4.4 presents each monazite grain in a unique way which highlights the general variations within and between samples. The largest grains that were selected for dating were also imaged in BSE (Fig. 4.5). In addition, some grains with the most complex

internal texture (grains 1 – 4 and 20 from # 216c) were mapped for Th, U, Pb and Y (Fig. 4.6) using a JEOL 8200 Electron microprobe, equipped with 5 wavelength spectrometers, at Dalhousie University. The voltage was set to 15 kV and the probe current between 0.10^{-7} and 0.10^{-8} A).

4.3.2.   Microstructural setting and main characteristics of monazite

All samples contain abundant monazite, mostly in the matrix (Fig. 4.2). Monazite is rare in garnet cores but it is commonly located at garnet rims, or in their vicinity (Fig. 4.2), and within biotite corroding garnet (*e.g.,* grains 12 and 13 in #216a; Fig. 4.2c). Matrix monazite is often found in a 500 µm radius around garnet and in #333x it is mainly concentrated in domains with seams of sillimanite overgrown by garnet and framboidal garnet aggregates. Monazite in the matrix occurs isolated, or more rarely in loose clusters (grains 13, 14 in #244; Fig. 4.2a; and grains 4, 8 in #216a; Fig. 4.2c), and a few grains, in all samples but #244 are attached to, or overgrow, zircon (Fig. 4.4b-e).

The number of monazite grains per thin-section ranges between 33 (#244) and 54 (#HJ60b). The largest grains (≥200 µm in length) occur in #244 and #216c, whereas maximum sizes are generally up to 150 µm elsewhere (Fig. 4.4), and the smallest grains are ≤50 µm in all samples. In addition, Figure 4.4 shows the first order zoning in Th. In the majority of cases individual grains are homogeneous with relatively low Th contents or show rims variably enriched in Th. In addition, a few grains (in all samples but #244) have patchy zones variably enriched in Th, and Th depleted rims. Most homogeneous are the monazite grains of #244, in which Th-enriched rims are ≤ 5 µm and discontinuous,

whereas those of #216c show the largest variety of patterns, hence the additional imaging of a few of the most representative grains with EPMA (Fig. 4.6).

Grain 1 is an example of monazite with a very thin (<5µm) and discontinuous Th-enriched rim around a large and homogeneous core depleted in Th and Pb, and a complex patchy zoning in Y which clearly stops before the rim outline (Fig. 4.6a). Monazite 2 displays the most complex zoning in EPMA (Fig. 4.6b). A 50 µm thick composite rim is defined by relatively higher Th content. In contrast, Th concentration is relatively lower in two places, matching areas of relatively higher Y concentration; the main core at the center of the grain of ~150 µm in diameter and a significantly smaller (30–40 µm) rounded domain first identified as rim. This feature could represent the relict core of a second monazite which was overgrown by the thick rim. In grains 4 and 20 (Fig. 4.6c, d) the Th-enriched overgrowth is also discontinuous but significantly thicker (up to ~20 µm). The core has relatively low U with some enriched distinct domains (mnz 20) or diffuse patches (mnz 4) in its center. In all four grains, zoning in Pb concentration matches that of Th with relative enrichment at the rim while small high Y patches are again limited to the core area (Fig. 4.6).

4.3.3. Monazite U–Pb dating by LA–ICPMS

4.3.3.1. Analytical method

The LA–ICPMS analyses were carried out directly on monazite grains in thin-sections, using the Finnigan Element XR2 instrument at Memorial University (Bruneau

Center, MAFIIC 2 lab). The 2.5x5 cm thin-sections were cut in half and analyzed over 3 days divided into 13 analytical runs. Each half thin-section was placed at the center of the cell, in a custom-made holder which also holds one small 5 mm epoxy mount containing the Trebilcock monazite standard (TIMS age 272 Ma, Tomascak, *et al.,* 1996) used as the reference material, and about a dozen grains of monazite KMO3-72 used as the secondary standard (TIMS age 1822±1.5 Ma, Dunning unpublished data). Reducing the thin-section size and centering it in the sample holder and ablation cell was done to minimize discrepancies between data collected on grains which would have been at the far corners of the section, and data from grains closer to the center. Such biases are noted in other studies and are suggested to be due to differences in flow circulation within the cell (Fisher *et al.,* 2011).

For each sample, up to 20 large monazite grains were analyzed (*cf.,* Fig. 4.4), using a spot diameter of 20 µm and following the standard bracketing technique. Each of the 13 analytical runs comprised between ~30 and 70 analyses (including these of the reference material and secondary standard). Trebilcock monazite was analyzed 3 or 4 times at the beginning and end of each run, and once after every 2 or 3 analyses of unknowns. The secondary standard KMO3-72 was analyzed regularly at least 4 times per run. A single analysis was <2 minutes long, including ~ 30s of gas blank, ~ 50s ablation, and ~ 20s of wash out. The instrument tuning parameters were slightly refined between the first and fifth run of day 1, varying between 2–3J and 2–4Hz. After that, the combination 2J–2Hz was kept constant during the remaining 8 runs. A list of the detailed instrument settings is presented Table 4.1. The freeware Iolite software (Paton *et al.,* 2010) running in IgorPro

(WaveMetrics, Inc; www.wavemetrics.com) was used for the data reduction; down-hole fractionation was corrected with a 'Smoothed cubic spline' model and the instrumental drift with the 'Automatic' type of spline. Once processed with Iolite, the data were exported in EXCEL and Isoplot (version 3.34; Ludwig, 2005) was used to calculate weighted average ages and make Tera-Wasserburg plots.

4.3.3.2. *Expected precision and accuracy based on standard data*

The monazite standard Trebilcock was analyzed 235 times in total and 39 outlier analyses (17%) were discarded (Fig. 4.7). The outliers were identified on the basis of their *measured* U/Pb ratios. If one or more ratios were ≥2% away from the mean calculated for the full run, the analysis was discarded. The weighted average $^{206}Pb/^{238}U$ age calculated for Trebilcock at 272.01 Ma ± 0.41 Ma (MSWD=0.63) agrees with the TIMS data at 272 ± 2 Ma (Tomascak *et al.,* 1996).

Monazite KMO3-72 was analyzed 97 times. After discarding 13 outlier analyses (13%) a weighted average $^{207}Pb/^{206}Pb$ age was calculated at 1820.3 Ma ± 2.2 Ma (MSWD=1.3) agreeing with the TIMS age at 1822±1.5 Ma (Dunning unpublished data). Due to the relatively young age of Trebilcock monazite, potential bias (*i.e.,* unreasonably large uncertainties) in the corrected $^{207}Pb/^{206}Pb$ ratios was expected for the unknown monazite samples. Analysing the secondary standard KMO3-72 helped to monitor this bias. No significant difference was found between the (final) corrected and (initial) measured $^{207}Pb/^{206}Pb$ ratios for that older monazite, meaning that the measured $^{207}Pb/^{206}Pb$ ratios were accurate and didn't need to be corrected when using Trebilcock.

Therefore, these measured ratios and corresponding ^{207}Pb/^{206}Pb ages with their initial (smaller) uncertainties are the ones reported in that paper. Only the two U/Pb ratios were corrected for, and carry their propagated error. Based on the standard data, ages are accurate, and a precision of ~2–3% (2SE) was expected for our ^{207}Pb/^{206}Pb data. Common Pb corrections were not applied here.

4.3.3.3. *Data rejection and presentation of the unknowns*

For Grenvillian age monazite (*i.e.,* broadly between *ca.* 1100 and 1000 Ma) a precision of ~ 2–3% translates in to ±20–30 Ma for a single analysis, therefore a significant overlap of the data is to be expected within this age range in the present study. Thus, only the highest quality analyses are considered here (Table 4.2; Fig. 4.8). The quality of an analysis was assessed by examining: (a) *the location of the U–Pb spot* as seen on a second set of BSE images acquired after analysis, on which we verified that our spots sampled the homogeneous area in the grain previously identified in BSE (these images are not shown here as pits representing failed analyses would have significantly alter the clarity of the photos); (b) *the precision on each isotopic age*, as data were eliminated if they showed large uncertainties that were clearly due to ablation anomalies; and (c) *discordance*, which was calculated using the formula ((1-(^{207}Pb/^{206}Pb age / ^{206}Pb/^{238}U age)) x 100). Data points more than 5% discordant were rejected.

After data assessment, 106 U–Pb analyses collected on 64 grains were kept (Table 4.2). Ages cited are ^{207}Pb/^{206}Pb unless stated otherwise. Grains that produced the most significant ages (*e.g.,* the oldest or youngest age in a sample, or distinct ages in core and

rim) and also served as examples of the various types of internal zoning are shown in Figure 4.5 with the location of the 20 µm laser ablation pits and corresponding $^{207}Pb/^{206}Pb$ ages.

4.4. RESULTS

Datasets vary in size from 16 U–Pb analyses carried out on 11 monazite grains in #333x to 37 analyses done on 26 grains in #216 (including grains in both #216a and c; Table 4.2). The main population of data points is between *ca.* 1100 Ma and 1000 Ma in all samples (Fig. 4.8) with a general trend of BSE-dark cores yielding older ages than BSE-light rims (Fig. 4.8). Older ages between 1500 Ma and 1150 Ma are only found in #HJ60b and #244 and are recorded in monazite grains included in garnet and /or cores of matrix grains (Table 4.2). The main data population falls within the range of the Grenvillian orogeny and will be referred to below as 'Grenvillian', while the older data points will be referred to as 'Pre-Grenvillian'.

4.4.1. Pre-Grenvillian ages

Six analyses in #244 and #HJ60b yielded distinctively pre-Grenvillian ages (Table 4.2; Fig. 4.8). In #244, these are 1421±21 Ma, 1180±27 Ma, and 1198±22 Ma and were retrieved in cores and/or rim of monazite grains 1 and 11 included in garnet (Fig. 4.5b). In contrast, in #HJ60b, the oldest ages, at 1445±27 Ma (core of grain 9), 1327±23 Ma (grain 4) and 1316±25 Ma (core of grain 8; Fig. 4.5b) are recorded by matrix monazite.

4.4.2. Grenvillian ages

The predominant monazite ages in all samples are Grenvillian (Table 4.2; Fig. 4.8), in the general range between 1119 and 960 Ma with the largest concentration within the interval 1069–1050 Ma.

In *#244* monazite ages are between 1106±42 Ma (core of matrix grain 10) and 1006±28 Ma (BSE-light rim of matrix grain 12) and cluster at 1050–1070 Ma with 14 analyses giving a weighted average ^{207}Pb/^{206}Pb age of 1061±9.6 Ma (MSWD = 0.081; Table 4.2; Figs. 4.5a, 4.8a). Most of the data in this interval come from matrix grains, except for rims of grains 11 and 24 which are included in garnet. In addition a few grains show clear age differences between core and rim; for instance 1092±34 Ma *vs.* 1006±28 Ma in grain 12 (Fig. 4.5a).

The majority of monazite ages in *#HJ60b* (Fig. 4.8b) are between 1055±35 Ma and 1082±37 Ma (cores of grains 4 and 11; Table 4.2; Fig. 4.5b). A few older ages (1100±25, 1098±32, and 1119±36) come from grains with pre-Grenvillian cores (*e.g.,* grain 8, Fig. 4.5b). In addition, a distinctively younger age at 988±28 Ma is recorded at the rim of grain 6, the core of which yielded an age at 1069±38 Ma (Fig. 4.5b). This grain is included in a thin quartz film around garnet.

In *#216* (Fig. 4.8c), monazite data mainly range between 1074±18 Ma and 994±28 Ma with two clusters for which weighted average ^{207}Pb/^{206}Pb ages were calculated at 1057.6±5.6 Ma (n=16, MSWD = 0.32) and 999.3±8.4 Ma (n=8, MSWD = 0.119). The oldest ages are recorded in BSE-dark cores of monazite, and the youngest ones in distinctive BSE-bright rims, common in matrix grains (Table 4.2). Several analyzed

grains show age differences of over 50 m.y. between the older core and the younger rim (Fig. 4.5c-d).

In *#333x* monazite the oldest age (1098±39 Ma) was recorded by the thick BSE-light rim of grain 1 included in garnet (Fig. 4.5e). Other ages mostly range between 1074±29 Ma and 1041±38 Ma (mostly BSE-dark cores of matrix grains or grains adjacent to garnet) without any particular cluster (Fig. 4.8d). In addition, a set of distinctly younger ages (1014±31 Ma to 980±31 Ma) is recorded in BSE-bright rims (*e.g.,* grain 2; Fig. 4.5e; and grain 20 included in texturally late biotite corroding garnet).

4.5.   DISCUSSION

4.5.1.   Monazite textures

In granulite-facies aluminous rocks, monazite included in garnet is expected to record ages of prograde metamorphism or previous metamorphic events (if any), whereas matrix monazite in addition may also record the age range of melt crystallization as well as later fluid infiltration, if applicable. Indeed for matrix monazite in #216c (Figs. 4.3 and 4.5), individual grains often show complex internal zoning where the distinction between a core and one or more rims is not clear. This is because the 2D images may not always properly reflect the 3D geometry in which the different monazite growth domains of different compositions and/or U–Pb ages may be actually organized (*cf.,* Spear and Pyle, 2002). However, even in 2D, the complex internal textures of several grains are clearly consistent with overgrowths on corroded earlier monazite (*e.g.,* grain 20 in #216c). Because of the anatectic nature of the host rocks such features might be explained by

162

partial dissolution of earlier monazite in the melt followed by new growth during melt crystallization or a later fluid infiltration event.

In situ LA–ICPMS dating of monazite revealed three distinct sets of ages in the aluminous gneisses of the PLV and the LBS. These data are complementary to the ID–TIMS data on monazite (Dunning and Indares, 2010), and LA–ICPMS data on metamorphic zircon from the same samples (Lasalle *et al.,* 2013) and place further constraints on the thermal evolution of these rocks.

4.5.2.   Age data

4.5.2.1.   Pre-Grenvillian ages

Pre-Grenvillian ages were exclusively found in rocks inferred to have originated as sedimentary layers: #HJ60b from the mid-*P* PLV, and #244 from the northern extension of the LBS into the high-*P* segment. The oldest age (*ca.* 1445 Ma) was recorded by #HJ60b from the PLV, and is close to the inferred deposition age of this sequence (Lasalle *et al.,* 2013; Moukhsil *et al.,* 2013). In #244, from the inferred extension of the LBS in the Manicouagan Imbricate zone, the oldest monazite, grain 11, (core dated at *ca.* 1421 Ma) is found included in garnet. This predates the *ca.* 1238 Ma age of formation of the LBS, as determined in the Canyon domain (Lasalle *et al.,* 2013) and implies the presence older crustal material in this northern part of the sequence.

4.5.2.2. *Grenvillian age metamorphism*

The data revealed two groups of Grenvillian ages. The oldest and predominant group, qualified as 'main' Grenvillian, was recorded in grains and portions of grains relatively dark in BSE, and the youngest, 'late' Grenvillian, in distinctive BSE-bright rims of matrix monazite.

Main Grenvillian ages cover a variably wide range in individual samples with a main concentration between *ca.* 1070 and 1050 Ma. In addition, #HJ60 and #244 show some older ages (*e.g.*, 1087 Ma, in #244 and 1081–1082 Ma, in #HJ60b) and #244, #331x and #216 a trail of younger ages down to *ca.* 1025 Ma (more evenly distributed in the case of #333x). The questions here are: (a) at which time within this range did the predominant granulite-facies mineral assemblage developed in these rocks ? ; and (b) what is the meaning of the age spread ? These can be addressed by considering a simplified scenario of monazite growth/consumption in anatectic rocks (Fig. 4.9; showing the *P–T* path of #HJ60). The rationale is that monazite can grow during prograde metamorphism, up to the onset of partial melting (M_{gr} (P) in Fig. 4.9). Once melting begins, prograde or earlier monazite would tend to dissolve in the melt, and then new monazite growth would occur during melt loss or subsequent melt crystallization (M*gr* (R) in Fig. 4.9) see Kelsey *et al.,* (2008). Therefore, ideally, the age of the peak can be bracketed between the last growth of prograde monazite and the 1st growth by melt crystallization (retrograde). Prograde monazite (or monazite formed during an earlier event) can be preserved anywhere in a rock (and preferentially as inclusions in garnet,

164

where it is best protected from later dissolution) whereas retrograde monazite would be restricted to the matrix.

Although some monazite grains in garnet record the oldest (or among the oldest) Grenvillian ages (*e.g.,* grain 1 #333x; grain 1 #HJ60), in other instances they show ages on the younger side of the main clusters (*e.g.,* 1050–1055 Ma: rims of grains 24 and 11 in #244; 1059 Ma: rim of grain 1 in #HJ60; and 1048 Ma: core of grain 17 in #216c). This may mean that the main cluster of data represents ages close to the granulite-facies metamorphic peak and differences between the last prograde monazite growth and that at early stages of melt crystallization are not resolvable with the resolution of data in this study (±20–40 Ma). However, the general trend of data trailing down to *ca.* 1025 Ma (#333x; #216, #244) would be consistent with protracted post thermal peak growth of monazite several tens of My.

Late Grenvillian ages between *ca.* 1014 and *ca.* 980 Ma were recorded in monazite from all 4 samples, most commonly in #216 (Table 4.2; Fig. 4.8). In contrast to the previous sets of ages, these come from distinctive textural zones, the BSE-bright and Th-enriched rims of various widths that are common in many matrix grains, and are inferred to represent a distinct monazite growth event.

In some instances the young BSE-bright domains clearly overgrow corroded earlier monazite as in the case of grain 20 in #216c (Fig. 4.7e) the internal texture of which shows a complex succession of at least 3 distinct episodes of growth-corrosion-new growth. The central part of the grain, as well as its thick rim, even displays a compositional gradation in Th content. We attribute the earlier episodes of corrosion/new

growth to dissolution of monazite in anatectic melt and regrowth during melt crystallization. In contrast, we interpret the late growth of the BSE-light rims to be related to an influx of fluids, which may be related to, the chlorite-filled cracks in garnet and pseudomorph of the sillimanite by very fine aggregates, possibly sericite, in #216 and #HJ60b (Fig. 4.3).

4.5.2.3. *Comparison with the ID–TIMS data*

Monazite ID–TIMS data from Dunning and Indares (2010) are shown as inset in Fig. 4.8. Due to the different scales of analytical precision between those (±2 My) and our LA–ICPMS data (±20–40 My; main plots Fig. 4.8), we cannot directly compare them. However, a few inferences can be drawn concerning the main Grenvillian ages: (a) in #244 and #331x the new data show a predominance of older ages relative to the TIMS data (*ca.* 1060 *vs.* 1040 Ma); and (b) for #HJ60b and #216 the age ranges are broadly similar. Most importantly, the late Grenvillian event which is clearly documented here was missed by the ID–TIMS study (except for a 1001±3 Ma age reported in 333x by Dunning and Indares 2010). A likely explanation is that the abrasion process (Krogh, 1982) used to clean-up grains before isotopic dilution TIMS analysis eliminated the thin monazite rims that were targeted in this LA–ICPMS study. However, as shown on the BSE images, rims with such a young age can, in rare cases, be relatively wide (*e.g.,* BSE-light rim in grain 2, #333x, Fig. 4.5e), and these wouldn't be completely removed by abrasion, which in turn would explain some mixed ages produced by TIMS.

4.5.2.4. Regional implications

The main Grenvillian age ranges reported here do not show any major difference between samples belonging to the high-*P* (#244) and mid-*P* segments of the hinterland (#HJ60, #216a-c and #331x). However, the wide age ranges reported here as well as in Dunning and Indares (2010), contrast with the very restricted ages reported from the eastern portion of the high-*P* segment in the same area (Fig. 4.1; Indares and Dunning, 2001) and imply that the duration of the main Grenvillian metamorphism in this segment was variable. We finally note that the main Grenvillian age ranges determined in this study are also similar to those reported from other granulite-facies portions of the Grenvillian hinterland (see in Rivers, 2008).

In contrast, this is the first report of late Grenvillian metamorphism in the hinterland. This event is attributed to infiltration of hot fluids under (sub-) greenschist facies conditions and is coeval with: (a) widespread intrusion of pegmatites and ultra-potassic dykes at 980–990 Ma in the Canyon domain (Dunning and Indares, 2010; Valverde Cardenas *et al.,* 2012); and (b) high-*P* granulite-facies metamorphism on the parautochthonous footwall of the hinterland (Jordan *et al.,* 2006). These features represent a major change in the orogenic evolution, which is attributed by Rivers (2012) to orogenic collapse.

4.6. CONCLUSIONS

In situ LA–ICPMS dating of monazite in granulite-facies anatectic aluminous gneisses provides new constraints on the thermal evolution of the central part of the Grenvillian hinterland. Monazite ages are linked to physical characteristics of the dated grains, with BSE-dark cores (or entire grains) giving consistently older ages that BSE-bright rims. The BSE-dark monazite gave a wide range of ages, some of which are inherited from earlier events and are only recorded in the metasedimentary samples (#HJ60 and #244). The range of the 'main' Grenvillian ages (~1070–1020 Ma) is comparable to that of the data of Dunning and Indares (2010), some of which were questioned as potentially representing mixed ages. However the present study shows that the spread is real. In the context of the granulite-facies anatectic host rocks, this spread of monazite ages may represent distinct monazite growth episodes linked to melt crystallization pulses in crustal rocks that remained under high-*T* conditions for a protracted period of time.

In contrast, the distinctly younger (*ca.* 1010–990 Ma) BSE-light rims are attributed to fluid infiltration, linked to the intrusion of ultra-potassic dykes and felsic pegmatite in the Canyon domain. This event is coeval with high-grade metamorphism in the underlying Parautochthonous belt, and the final propagation of the orogen to the NW, and therefore it likely records the response of the hinterland to orogenic collapse.

ACKNOWLEDGMENTS

REFERENCES

Beaumont, C., Nguyen, M.H., Jamieson, R.A., and Ellis, S. 2006. Crustal flow modes in large hot orogens. In Channel flow, ductile extrusion and exhumation in continental collision zones. Edited by R.D. Law, M.P. Searle, and L. Godin. Geological Society (of London), Special Publication 268. pp. 91–145.

Brown, M., 2004. The mechanism of melt extraction from lower continental crust of orogens. *Transactions of the Royal Society of Edinburgh, Earth Sciences*, **95:** 35–48.

Cherniak, D. J., Watson, E. B., Grove, M., Harrison, T. M., 2004. Pb diffusion in monazite: a combined RBS/SIMS study. *Geochimica et Cosmochimica Acta*, **68**: 829–840.

Cox, R. A., Dunning, G.R. and Indares, A., 1998. Petrology and U-Pb geochronology of mafic, high-pressure metamorphic coronites from the Tshenukutish domain, eastern Grenville Province. *Precambrian Research*, **90**: 59–83.

Cutts, K. A., Kinny, P. D., Strachan, R. A., Hand, M., Kelsey, D. E., Emery, M., Friend, C. R. L. and Leslie, A. G., 2010. Three metamorphic events recorded in a single garnet: Integrated phase modelling, *in situ* LA-ICPMS and SIMS geochronology from the Moine Supergroup, NW Scotland. *Journal of Metamorphic Geology*, **28**: 249–267.

Dunning, G. and Indares, A., 2010. New insights on the 1.7‑1.0 Ga crustal evolution of the central Grenville Province from the Manicouagan – Baie Comeau transect. *Precambrian Research*, **180**: 204–226.

Fisher, C. M., McFarlane, C. R. M., Hanchar, J. M., Schmitz, M. D., Sylvester, P. J., Lam, R., Longerich, H. P., 2011. Sm–Nd isotope systematics by laser ablation-multicollector-inductively coupled plasma mass spectrometry: Methods and potential natural and synthetic reference materials. *Chemical Geology*, **284:** 1–20.

Gervais, F. and Hynes, A., 2012. Linking metamorphic textures to U–Pb monazite *in situ* geochronology to determine the age and nature of aluminosilicate-forming reactions in the Northern Monashee Mountains, British-Columbia. *Lithos*, **160–161**: 250–267.

Gibson, H. D. T*,* Carr, S. D**.,** Hamilton, M. A. and Brown, R. L., 2004. Correlating yttrium zones and age domains in monazite with metamorphic reactions involving major pelitic phases: an integration of ID–TIMS and SHRIMP geochronology with Y-Th-U X-ray mapping. *Chemical Geology*, **211**: 237–260.

Gower, C. F. and Krogh, T. E., 2002. A U–Pb geochronological review of the Proterozoic history of the eastern Grenville Province. *Canadian Journal of Earth Sciences,* **39**: 795–829.

Harrison, T. M., Catlos, E. J., and Montel, J.-M., 2002. U–Th–Pb dating of phosphate minerals. *In:* Kohn, M. J., Rakovan, J., Hughes, J. M. *(Eds.).* Phosphates: geochemical, geobiological, and materials importance. *Reviews in Mineralogy and Geochemistry, Mineralogical Society of America,* **48 (14)**: 523–558.

Hindemith, M.A., 2014. Petrography and geochemistry of hydrothermally altered volcanic rocks metamorphosed at granulite-facies conditions: and example from the Central Grenville Province. Msc Thesis, Earth Sciences Department, Memorial University of Newfoundland, St John's.

Indares, A. and Dunning, G., 2004. Crustal architecture above the high-pressure belt of the Grenville Province in the Manicouagan area: new structural, petrologic and U–Pb age constraints. *Precambrian Research*, **130**: 199–208.

Indares, A. and Dunning, G., 2001. Partial melting of high P–T metapelites from the Tshenukutish terrane (Grenville Province): petrography and U–Pb geochronology. *Journal of Petrology*, **42**: 1547–1565.

Indares, A. and Moukhsil, A., 2013. Geon 12 crustal extension in the central Grenville Province, implications for the orogenic architecture, and potential influence on the emplacement of anorthosites. *Canadian Journal of Earth Sciences*, **50**: 955–966.

Indares, A., Dunning, G. and Cox, R., 2000. Tectono-thermal evolution of deep crust in a Mesoproterozoic continental collision setting: the Manicouagan example. *Canadian Journal of Earth Sciences*, **37**: 325–340.

Jamieson, R.A., Beaumont, C., Nguyen, M.H., Culshaw, N.G. 2007. Syn-convergent ductile flow in variable strength continental crust: Numerical models with applications to the western Grenville orogen. *Tectonics,* **26**: 1–23.

Jamieson, R.A., Beaumont, C.J., Warren, C.J., Nguyen, M.H. 2010. The Grenville orogen explained? Applications and limitations in integrating numerical models with geological and geophysical data. *Canadian Journal of Earth Sciences,* **47**: 517–539.

Jamieson, R.A., Beaumont, C. 2011. Coeval thrusting and extension during lower crustal ductile flow – implications for exhumation of high grade metamorphic rocks. *Journal of Metamorphic Geology,* **29**: 33–51.

Jordan, S. L., Indares, A. and Dunning, G., 2006. Partial melting of metapelites in the Gagnon terrane below the high-pressure belt in the Manicouagan area (Grenville Province): pressure temperature (P–T) and U–Pb age constraints and implications. *Canadian Journal of Earth Sciences*, **38**: 1309–1329.

Kelly, N. M., Harley, S. L. and Möller, A., 2012. Complexity in the behavior and recrystallization of monazite during high-*T* metamorphism and fluid infiltration. *Chemical geology*, **322-323**: 192–208.

Kelsey, D. E., Clark, C. and Hand, M., 2008. Thermobarometric modelling of zircon and monazite growth in melt-bearing systems: examples using model metapelitic and metapsammitic granulites. *Journal of Metamorphic Geology*, **26**: 199–212.

Kelsey, D. E., Hand, M., Clark, C. and Wilson, C. J. L., 2007. On the application of *in situ* monazite chemical geochronology to constraining *P–T*-t histories in high-temperature (>850 °C) polymetamorphic granulites from Prydz Bay, East Antarctica. *Journal of the Geological Society*, **164**: 667–683.

Krogh, T. E. 1982. Improved accuracy of U-Pb zircon ages by the creation of more concordant systems using an air abrasion technique. *Geochimica et Cosmochimica Acta*, **46**: 637–649.

Langone, A., Braga, R., Massonne, H. J. and Tiepolo, M., 2011. Preservation of old (prograde metamorphic) U–Th–Pb ages in unshielded monazite from the high-pressure paragneisses of the Variscan Ulten Zone (Italy). *Lithos*, **127**: 68–85

Lasalle, S. and Indares, A., 2014. Anatectic and P–T record of aluminous gneisses from diverse protoliths and contrasting-pressure crustal belts in the central Grenville Province. *Journal of Metamorphic Geology*, *in press*, DOI: 10.1111/jmg.12083.

Lasalle, S., Fisher, C. M., Indares, A. and Dunning, G., 2013. Contrasting types of Grenvillian granulite-facies aluminous gneisses: Insights on protoliths and metamorphic events from zircon morphologies and ages. *Precambrian Research*, **228**: 117–130.

Ludwig, K. R., 2003. User's manual for Isoplot/Ex, Version 3.0. A geochronological toolkit for Microsoft Excel: Berkeley Geochronology Center, Special Publication, **4**: 70 p.

Moukhsil, A., Solgadi, F., Clark, T., Indares, A. and Blouin, S., 2013. Geology of the Daniel-Johnson Dam (Manic 5) area, Côte-Nord region (NTS 22K14, 22K15, 22K16, 22N03 and 22N02). Ministère des Ressources naturelles et de la Faune, RG-2013.

Moukhsil, A., Solgadi, F., Lacoste, P., Gagnon, M. and David, J., 2012. Géologie de la région du lac du Milieu (SNRC 22O03, 22O04, 22O06, 22J13 et 22J14). Ministère des Ressources naturelles et de la Faune, RG 2012–01.

Owens, B.E., and Tomascak, P.B. 2002. Mesoproterozoic lamprophyres in the Labrieville Massif, Quebec: clues to the origin of alkalic anorthosites? Canadian Journal of Earth Sciences, **39(6):** 983–997. DOI:10.1139/e02-010.

Paton, C., Woodhead, J., Hellstrom, J., Hergt, J., Greig, A. and Maas, R., 2010. Improved laser ablation U–Pb zircon geochronology through robust downhole fractionation correction. *Geochemistry Geophysics Geosystems*, **11**: 1–36.

Pyle, J. M. and Spear, F. S., 2003. Four generations of accessory-phase growth in low-pressure migmatites from SW New Hampshire. *American Mineralogist*, **88**: 338–351.

Rivers, T., 2012. Upper-crustal orogenic lid and mid-crustal core complexes: signature of a collapsed orogenic plateau in the hinterland of the Grenville Province. *Canadian Journal of Earth Sciences,* **49**: 1–42.

Rivers, T. 2009. The Grenville Province as a large hot long-duration collisional orogen — insights from the spatial and thermal evolution of its orogenic fronts. In Ancient orogens and modern analogues. Edited by J.B. Murphy, J.D. Keppie, and A. Hynes. Geological Society (of London), Special Publication 327. pp. 405–444. doi:10.1144/SP327.17.

Rivers, T., 2008. Assembly and preservation of lower, mid, and upper orogenic crust in the Grenville Province‐Implications for the evolution of large hot long‐duration orogens. *Precambrian Research,* **167**: 237–259.

Rivers, T., Culshaw, N., Hynes, A., Indares, A., Jamieson, R. and Martignole, J., 2012. The Grenville Orogen - A post-LITHOPROBE perspective. Chapter 3 *In* Tectonic Styles in Canada: The LITHOPROBE Perspective. Edited by J.A. Percival, F.A. Cook, and R.M. Clowes. *Geological Association of Canada*, Special Paper 49, pp. 97–236.

Rivers, T., Martignole J., Gower, C. F. and Davidson, A., 1989. New tectonic divisions of the Grenville province, southeast Canadian Shield. *Tectonics*, **8**: 63–84.

Shaffer, M., 2009. Discrimination of hematite and magnetite and quantifying their associations using the JKTECH Mineral Liberation AnalyzerTM. In The 48th Annual Conference of Metallurgists, Laurentian University, Sudbury, Ontario 73.

Shaffer, M., Gu, Y., and Rohde, M., 2008. Practical Applications for the Silicon Drift Xray Detector in SEM-Platformed Image Analysis: The Bruker-MLA in Practice.

In SME Annual Meeting 2007 and CMS 109th National Western Conference 2007 The Power of Mining: Energy's Influence, Denver, CO, U.S.A., 25-28 February, 2007, 1(Preprint 07-029): 1-6.

Simonetti, A., Heaman, L. M., Chacko, T. and Banerjee, N. R., 2006. *In situ* petrographic thin-section U–Pb dating of zircon, monazite and titanite using laser ablation-MC-ICP-MS. *International Journal of Mass Spectrometry*, **253**: 87–97.

Slagstad, T., Hamilton, M.A., Jamieson, R.A., Culshaw, N.G., 2004. Timing and duration of melting in the mid orogenic crust: constraints from U-Pb (SHRIMP) data, Muskoka and Shawanaga domains, Grenville Province, Ontario. *Canadian Journal of Earth Sciences*, **41**: 1339–1365.

Spear, F. S. and Pyle, J. M., 2010 Theoretical modelling of monazite growth in a low-Ca metapelite. *Chemical Geology*, **273**: 111–119.

Spear, F. S. and Pyle, J. M., 2002. Apatite, Monazite, and Xenotine in Metamorphic Rocks. *In:* Kohn, M. J., Rakovan, J., Hughes, J. M. *(Eds.).* Phosphates: geochemical, geobiological, and materials importance. *Reviews in Mineralogy and Geochemistry, Mineralogical Society of America*, **48**: 293–336.

Spear, F. S., Pyle, J. M., Wark, D. A., 2002. Electron Microprobe Analysis of REE in Apatite, Monazite and Xenotime: Protocols and Pitfalls *In:* Kohn, M. J., Rakovan, J., Hughes, J. M. *(Eds.).* Phosphates: geochemical, geobiological, and materials importance. *Reviews in Mineralogy and Geochemistry, Mineralogical Society of America*, **48**: 337–362.

Tomascak, P. B., Krogstad, E. J., Walker, R. J., 1996. U–Pb monazite geochronology of granitic rocks from Maine: Implications for Late Paleozoic tectonics in the northern Appalachians, *Journal of Geology*, **104**: 185–195.

Valverde Cardenas, C., Indares, A. and Jenner, G., 2012 Mafic and ultrapotassic rocks from the Canyon domain (central Grenville Province): geochemistry and tectonic implications. *Canadian Journal of Earth Sciences*, **49(2)**: 412–433, DOI: 10.1139/e11-065.

van Gool, J. A. M., Rivers, T. and Calon, T., 2008. Grenville Front zone, Gagnon terrane, south-western Labrador: configuration of a midcrustal foreland fold-thrust belt. *Tectonics*, **27**: 1–35.

Whitney, D. L., and Evans, B. W., 2010. Abbreviations for names of rock-froming minerals. *American Mineralogist*, **95**: 185–187.

Williams, M. L., Jercinovic, M. J. and Hetherington, C. J., 2007. Microprobe monazite geochronology: Understanding geologic processes by integrating composition and chronology. *Annual Review Earth Planetary Sciences*, **35**: 137–175.

Table 4.1: Operating conditions and instrument settings used for the U–Pb LA–ICPMS analyses.

ICP-MS	
Type of ICPMS	high resolution double focusing
Brand and Model	ThermoFinnigan Element XR
forward power	1349 W
GAS FLOWS	in L/min
Cool (Ar)	16
Auxiliary (Ar)	1.01-1.02
Sample (Ar)	0.875
Carrier (He)	1.080
LASER	
Type of laser	ArF Excimer
Brand and Model	GEOLAS 193 nm excimer
Laser wavelength	193 nm
Pulse width	20 ns
Spot size	20 μm
Repetition rate	2-4 Hz
Laser fluence	2-3 J/cm^2
DATA ACQUISITION PARAMETERS	
Resolution mode	low
Data acquisition	time-resolved analysis
Scan mode	E-Scan
Scanned masses	204, 206, 207, 208, 232, 238
Settling time	0.001s, 0.030s (for 204)
Sample time	0.01, 0.02 (for 206), 0.03 (for
Samples per peak	10
Number of scans	975
Detector mode	Counting/ Analog for 238
Detector dead time	19ns
Background collection	30s
Ablation duration	50 s
Washout	20-40s
STANDARDISATION and DATA REDUCTION	
External standard used	KMO3-72
Reference standard	Trebilcock
Data reduction	IOLITE

Table 4.2: Monazite (LA–ICPMS) U–Pb data for sample 244 (UTM 522350 5724850).

an. #	Mnz.#	Spot.#	grain area	BSE	Occur.	RATIO $^{207}Pb/$ ^{235}U	2SE	$^{206}Pb/$ ^{238}U	2SE	$^{207}Pb/$ ^{206}Pb	2SE	AGES $^{207}Pb/$ ^{235}U	2SE	$^{206}Pb/$ ^{238}U	2SE	$^{207}Pb/$ ^{206}Pb	2SE	%disc
b28	12	4	R	\	M	1.723	0.068	0.1725	0.0041	0.0727	0.0010	1017	26	1025	22	**1006**	**28**	2
i39	13	1	R	\	M	1.843	0.087	0.1798	0.0042	0.0731	0.0013	1062	29	1065	23	**1017**	**36**	5
b43	3	2	R	\	M	1.760	0.072	0.1749	0.0043	0.0732	0.0012	1032	26	1038	24	**1019**	**33**	2
i24	16	2	R	\	M	1.703	0.078	0.1720	0.0038	0.0733	0.0013	1011	29	1023	21	**1022**	**36**	0
i12	8	2	R	\	ad_Grt	1.735	0.082	0.1728	0.0039	0.0734	0.0013	1026	30	1027	22	**1025**	**36**	0
k03	13	2	R	\	M	1.869	0.088	0.1792	0.0042	0.0736	0.0013	1068	31	1063	23	**1031**	**36**	3
i38	14	3	R	\	M	1.832	0.085	0.1770	0.0043	0.0739	0.0012	1056	31	1050	23	**1039**	**33**	1
b44	3	3	R	\	M	1.771	0.071	0.1726	0.0041	0.0742	0.0011	1037	25	1026	23	**1047**	**30**	-2
k07	11	2	R	\	Grt	1.816	0.082	0.1743	0.0039	0.0745	0.0011	1050	30	1035	21	**1055**	**30**	-2
b34	9	2	R	\	M	1.822	0.074	0.1776	0.0042	0.0747	0.0013	1057	26	1054	23	**1060**	**35**	-1
b67	2	4	R	\	M	1.810	0.074	0.1779	0.0044	0.0747	0.0012	1045	27	1056	24	**1060**	**32**	0
i21	15	2	R	\	emb_Grt	1.780	0.084	0.1753	0.0041	0.0747	0.0012	1037	30	1041	22	**1060**	**32**	-2
i08	7	1	R	\	M	1.750	0.082	0.1737	0.0039	0.0748	0.0014	1028	31	1032	22	**1063**	**38**	-3
b56	5	2	R	L	M	1.857	0.078	0.1785	0.0045	0.0750	0.0015	1066	27	1059	24	**1069**	**40**	-1
b40	4	2	R	\	M	1.805	0.073	0.1740	0.0042	0.0752	0.0011	1045	26	1033	23	**1074**	**29**	-4
b53	1	4	R	\	Grt	1.900	0.074	0.1813	0.0045	0.0757	0.0009	1080	25	1074	25	**1087**	**25**	-1
b62	2	1	R	\	M	1.872	0.079	0.1776	0.0047	0.0764	0.0014	1066	27	1054	25	**1106**	**37**	-5
k09	11	3	R	\	Grt	2.135	0.098	0.1929	0.0043	0.0793	0.0011	1157	32	1136	23	**1180**	**27**	-4

an. # – analysis number, **sect. #** – thin-section a or c, **Mnz. #** – monazite grain number, **Occur.** – Occurrence/textural context of the monazite grain, **R** – analyses of rim, **c** – analyses of core, **L** – zone of light BSE, **d** – zone of dark BSE, **M** – monazite grain in the matrix, **Grt** – monazite grain included in garnet, **ad_Grt** – monazite grain adjacent/touching garnet rim, **emb_Grt** – monazite grain included in a polymineralic embayment in garnet, **Grt incl** – monazite present as a single inclusion in garnet, **cor_Grt** – monazite grain included in an area with several mineral phases corroding garnet rim, **bi.cor_Grt** – monazite grain included in relatively large biotite corroding garnet rim.

The per cent discordance **(% disc.)** was calculated using the fomula $(1-(^{206}Pb/^{238}U$ age $/ ^{207}Pb/^{206}Pb$ age) x 100).

an. #	Mnz.#	Spot.#	grain area	BSE	Occur.	RATIO $^{207}Pb/^{235}U$	2SE	$^{206}Pb/^{238}U$	2SE	$^{207}Pb/^{206}Pb$	2SE	AGES $^{207}Pb/^{235}U$	2SE	$^{206}Pb/^{238}U$	2SE	$^{207}Pb/^{206}Pb$	2SE	%disc
	244																	
b38	4	1	c	\	M	1.764	0.073	0.1744	0.0042	0.0729	0.0013	1031	27	1036	23	**1011**	**36**	2
i20	15	1	c	\	emb_Grt	1.797	0.084	0.1794	0.0042	0.0734	0.0014	1043	31	1064	23	**1025**	**39**	4
b22	17	1	c	\	M	1.757	0.072	0.1730	0.0041	0.0739	0.0013	1027	27	1029	22	**1039**	**36**	-1
b35	9	3	c	L	M	1.822	0.074	0.1784	0.0042	0.0739	0.0012	1051	26	1058	23	**1039**	**33**	2
i09	7	2	c	\	M	1.793	0.084	0.1743	0.0041	0.0741	0.0014	1041	30	1035	23	**1044**	**38**	-1
b65	2	3	c	\	M	1.770	0.073	0.1742	0.0042	0.0741	0.0012	1031	26	1035	23	**1044**	**33**	-1
i36	14	2	c	\	M	1.877	0.088	0.1788	0.0040	0.0744	0.0015	1072	31	1060	22	**1052**	**41**	1
b41	3	1	c	\	M	1.833	0.075	0.1783	0.0043	0.0745	0.0014	1054	27	1058	24	**1055**	**38**	0
b58	6	1	c	\	M	1.734	0.073	0.1700	0.0042	0.0745	0.0014	1022	26	1012	23	**1055**	**38**	-4
i11	8	1	c	\	ad_Grt	1.825	0.087	0.1773	0.0041	0.0748	0.0015	1054	31	1051	22	**1063**	**40**	-1
i23	16	1	c	\	M	1.763	0.082	0.1747	0.0038	0.0748	0.0013	1032	30	1037	21	**1063**	**35**	-3
b32	9	1	c	L	M	1.809	0.075	0.1760	0.0042	0.0749	0.0015	1049	27	1045	23	**1066**	**40**	-2
b64	2	2	c	\	M	1.805	0.078	0.1764	0.0045	0.0750	0.0015	1046	27	1047	25	**1069**	**40**	-2
i26	21	2	c	\	M	1.783	0.085	0.1764	0.0043	0.0750	0.0015	1039	31	1046	24	**1069**	**40**	-2
b26	12	3	c	\	M	1.879	0.076	0.1801	0.0045	0.0759	0.0013	1071	27	1067	24	**1092**	**34**	-2
i14	10	1	c	\	M	1.857	0.089	0.1769	0.0046	0.0764	0.0016	1067	32	1048	25	**1106**	**42**	-5
b47	1	1	c	\	Grt	2.144	0.084	0.1948	0.0048	0.0800	0.0009	1160	27	1146	26	**1198**	**22**	-5
k06	11	1	c	\	Grt	2.954	0.130	0.2353	0.0050	0.0898	0.0010	1395	35	1362	26	**1421**	**21**	-4

an. # – analysis number, **sect. #** – thin-section a or c, **Mnz. #** – monazite grain number, **Occur.** – Occurrence/textural context of the monazite grain, **R** – analyses of rim, **c** – analyses of core, **L** – zone of light BSE, **d** – zone of dark BSE, **M** – monazite grain in the matrix, **Grt** – monazite grain included in garnet, **ad_Grt** – monazite grain adjacent/touching garnet rim, **emb_Grt** – monazite grain included in a polymineralic embayment in garnet, **Grt incl** – monazite present as a single inclusion in garnet, **cor_Grt** – monazite grain included in an area with several mineral phases corroding garnet rim, **bi.cor_Grt** – monazite grain included in relatively large biotite corroding garnet rim.

The per cent discordance **(% disc.)** was calculated using the fomula (1-($^{206}Pb/^{238}U$ age / $^{207}Pb/^{206}Pb$ age) x 100).

Table 4.3: Monazite (LA–ICPMS) U–Pb data for sample HJ60b (UTM 522750 5617620).

| HJ60b | | Spot.# | grain area | BSE | Occur. | RATIO $^{207}Pb/^{235}U$ | 2SE | $^{206}Pb/^{238}U$ | 2SE | $^{207}Pb/^{206}Pb$ | 2SE | AGES $^{207}Pb/^{235}U$ | 2SE | $^{206}Pb/^{238}U$ | 2SE | $^{207}Pb/^{206}Pb$ | 2SE | %disc |
an.#	Mnz.#																	
d42	6	2	R	\	M	1.730	0.066	0.1732	0.0049	0.0721	0.0010	1018	24	1029	27	**988**	**28**	4
f11	4	2	R	\	M	1.706	0.038	0.1676	0.0036	0.0738	0.0013	1009	14	999	20	**1036**	**36**	-4
f08	12	2	R	\	ad_Grt	1.830	0.040	0.1771	0.0039	0.0746	0.0013	1054	15	1051	21	**1058**	**35**	-1
d11	1	1	R	\	ad_Grt	1.872	0.067	0.1824	0.0050	0.0747	0.0009	1071	24	1081	27	**1059**	**24**	2
d33	8	3	R	\	M	1.866	0.068	0.1795	0.0049	0.0762	0.0010	1068	24	1064	27	**1100**	**25**	-3
d23	5	2	R	\	M	1.835	0.069	0.1794	0.0051	0.0761	0.0012	1057	25	1064	27	**1098**	**32**	-3
f09	4	1	c	\	M	1.863	0.041	0.1800	0.0042	0.0745	0.0013	1066	15	1065	23	**1055**	**35**	1
d22	5	1	c	\	M	1.929	0.077	0.1887	0.0057	0.0750	0.0014	1087	26	1114	31	**1069**	**38**	4
d40	6	1	c	\	M	1.862	0.073	0.1811	0.0053	0.0750	0.0014	1064	26	1072	29	**1069**	**38**	0
d12	1	2	c	\	ad_Grt	1.858	0.068	0.1796	0.0049	0.0753	0.0009	1067	24	1065	27	**1076**	**25**	-1
d39	11	2	c	\	ad_Grt	1.961	0.073	0.1876	0.0053	0.0755	0.0010	1101	25	1107	29	**1081**	**26**	2
d43	3	1	c	\	ad_Grt	1.912	0.070	0.1836	0.0051	0.0755	0.0009	1084	24	1087	28	**1081**	**24**	1
d34	11	1	c	\	ad_Grt	1.914	0.075	0.1852	0.0054	0.0755	0.0014	1085	25	1095	29	**1082**	**37**	1
d30	8	1	c	\	M	1.936	0.074	0.1852	0.0054	0.0769	0.0014	1090	26	1096	29	**1119**	**36**	-2
d31	8	2	c	\	M	2.494	0.092	0.2146	0.0058	0.0850	0.0011	1269	27	1252	31	**1316**	**25**	-5
f12	4	3	c	\	M	2.625	0.059	0.2230	0.0057	0.0855	0.0013	1302	17	1294	30	**1327**	**29**	-3
d26	9	1	c	\	M	3.297	0.120	0.2679	0.0080	0.0909	0.0013	1479	29	1527	40	**1445**	**27**	5

an. # – analysis number, **sect. #** – thin-section a or c, **Mnz. #** – monazite grain number, **Occur.** – Occurrence/textural context of the monazite grain, **R** – analyses of rim, **c** – analyses of core, **L** – zone of light BSE, **d** – zone of dark BSE, **M** – monazite grain in the matrix, **Grt** – monazite grain included in garnet, **ad_Grt** – monazite grain adjacent/touching garnet rim, **emb_Grt** – monazite grain included in a polymineralic embayment in garnet, **Grt incl** – monazite present as a single inclusion in garnet, **cor_Grt** – monazite grain included in an area with several mineral phases corroding garnet rim, **bi.cor_Grt** – monazite grain included in relatively large biotite corroding garnet rim.
The per cent discordance (**% disc.**) was calculated using the fomula (1-($^{206}Pb/^{238}U$ age / $^{207}Pb/^{206}Pb$ age) x 100).

333x an.#	Mnz.#	Spot.#	grain area	BSE	Occur.	RATIO ^{207}Pb/ ^{235}U	2SE	^{206}Pb/ ^{238}U	2SE	^{207}Pb/ ^{206}Pb	2SE	AGES ^{207}Pb/ ^{235}U	2SE	^{206}Pb/ ^{238}U	2SE	^{207}Pb/ ^{206}Pb	2SE	%disc
c33	2	4	R	L	M	1.667	0.039	0.1694	0.0032	0.0718	0.0011	997	15	1008	18	**980**	**31**	3
c31	2	3	R	L	M	1.681	0.040	0.1696	0.0032	0.0723	0.0011	1001	15	1010	18	**994**	**31**	2
c36	11	1	R	L	M	1.721	0.040	0.1712	0.0031	0.0730	0.0011	1017	15	1019	17	**1014**	**31**	0
c19	1	2	R	L	Grt	1.910	0.049	0.1836	0.0035	0.0761	0.0015	1084	17	1085	19	**1098**	**39**	-1
c14	20	1	\	\	bi.cor_Grt	1.650	0.042	0.1665	0.0032	0.0719	0.0011	987	16	993	18	**983**	**31**	1
h23	6	1	c	d	M	1.735	0.087	0.1718	0.0044	0.0731	0.0016	1016	31	1022	24	**1017**	**44**	1
c11	35	2	\	\	M	1.778	0.048	0.1772	0.0035	0.0732	0.0014	1038	18	1051	19	**1019**	**39**	3
h20	15	2	c	d	ad_Grt	1.760	0.086	0.1744	0.0040	0.0740	0.0015	1027	31	1036	22	**1041**	**41**	-1
h09	16	1	c	\	ad_Grt	1.724	0.084	0.1714	0.0044	0.0740	0.0014	1012	31	1023	23	**1041**	**38**	-2
c44	3	2	c	d	M	1.799	0.038	0.1750	0.0031	0.0742	0.0008	1044	14	1040	17	**1048**	**20**	-1
c43	3	1	c	d	M	1.814	0.041	0.1770	0.0034	0.0743	0.0009	1049	15	1050	18	**1051**	**25**	0
h19	15	1	c	d	ad_Grt	1.807	0.087	0.1750	0.0039	0.0746	0.0014	1044	32	1039	21	**1058**	**38**	-2
h30	9	1	c	d	M	1.804	0.083	0.1747	0.0037	0.0749	0.0010	1046	30	1038	21	**1064**	**26**	-3
c30	2	2	c	d	M	1.861	0.040	0.1795	0.0033	0.0752	0.0008	1068	14	1064	18	**1073**	**22**	-1
c34	21	1	c	d	M	1.824	0.038	0.1757	0.0032	0.0752	0.0007	1053	14	1044	17	**1073**	**20**	-3
c25	2	1	c	d	M	1.875	0.042	0.1803	0.0035	0.0752	0.0011	1071	15	1070	19	**1074**	**29**	0

an. # – analysis number, **sect. #** – thin-section a or c, **Mnz. #** – monazite grain number, **Occur.** – Occurrence/textural context of the monazite grain, **R** – analyses of rim, **c** – analyses of core, **L** – zone of light BSE, **d** – zone of dark BSE, **M** – monazite grain in the matrix, **Grt** – monazite grain included in garnet, **ad_Grt** – monazite grain adjacent/touching garnet rim, **emb_Grt** – monazite grain included in a polymineralic embayment in garnet, **Grt incl** – monazite present as a single inclusion in garnet, **cor_Grt** – monazite grain included in an area with several mineral phases corroding garnet rim, **bi.cor_Grt** – monazite grain included in relatively large biotite corroding garnet rim.

The per cent discordance **(% disc.)** was calculated using the fomula (1-(^{206}Pb/^{238}U age / ^{207}Pb/^{206}Pb age) x 100).

Table 4.5: Monazite (LA–ICPMS) U–Pb data for sample 216 (including sections a and c; UTM 521499 5647483).

216 an.#	s.#	Mnz.#	Spot.#	grain area	BSE	Occur.	RATIO $^{207}Pb/$ ^{235}U	2SE	$^{206}Pb/$ ^{238}U	2SE	$^{207}Pb/$ ^{206}Pb	2SE	AGES $^{207}Pb/$ ^{235}U	2SE	$^{206}Pb/$ ^{238}U	2SE	$^{207}Pb/$ ^{206}Pb	2SE	%disc
d32	c	20	1	R	L	M	1.642	0.051	0.1662	0.0039	0.0711	0.0010	985	20	992	21	**960**	**29**	3
g28	c	10	1	R	\	ad_Grt	1.636	0.056	0.1661	0.0042	0.0723	0.0010	983	21	991	23	**994**	**28**	0
d17	c	2	3	R	L	M	1.704	0.052	0.1708	0.0040	0.0723	0.0009	1011	20	1016	22	**995**	**24**	2
c29	a	11	1	R	L	M	1.691	0.069	0.1697	0.0043	0.0723	0.0008	1005	26	1011	24	**996**	**23**	2
g29	c	10	2	R	\	ad_Grt	1.643	0.056	0.1660	0.0041	0.0724	0.0010	987	21	992	23	**997**	**28**	-1
b62	a	4	1	R	L	M	1.690	0.029	0.1707	0.0035	0.0724	0.0009	1005	11	1016	19	**998**	**24**	2
b35	a	10	2	R	L	Grt incl.?	1.712	0.027	0.1706	0.0033	0.0726	0.0007	1014	10	1015	18	**1003**	**20**	1
g34	c	14	1	R	L	M	1.705	0.058	0.1711	0.0042	0.0726	0.0010	1011	22	1018	23	**1003**	**28**	1
b58	a	8	1	R	L	M	1.752	0.029	0.1749	0.0035	0.0727	0.0008	1027	11	1039	19	**1005**	**23**	3
b25	a	7	2	R	d	M	1.757	0.037	0.1749	0.0040	0.0734	0.0012	1031	13	1040	22	**1025**	**33**	1
g38	c	6	3	R	\	cor_Grt	1.775	0.061	0.1762	0.0042	0.0742	0.0012	1036	23	1045	23	**1047**	**33**	0
g11	c	15	1	R	L	ad_Grt	1.791	0.063	0.1740	0.0045	0.0747	0.0011	1040	23	1033	25	**1060**	**30**	-3
g44	c	1	2	R	\	M	1.761	0.059	0.1738	0.0043	0.0748	0.0010	1033	22	1032	24	**1063**	**27**	-3
g58	c	5	1	R	L	in Grt rim	1.769	0.061	0.1744	0.0046	0.0750	0.0011	1033	23	1035	25	**1069**	**29**	-3

an. # – analysis number, **sect. #** – thin-section a or c, **Mnz. #** – monazite grain number, **Occur.** – Occurrence/textural context of the monazite grain, **R** – analyses of rim, **c** – analyses of core, **L** – zone of light BSE, **d** – zone of dark BSE, **M** – monazite grain in the matrix, **Grt** – monazite grain included in garnet, **ad_Grt** – monazite grain adjacent/touching garnet rim, **emb_Grt** – monazite grain included in a polymineralic embayment in garnet, **Grt incl** – monazite present as a single inclusion in garnet, **cor_Grt** – monazite grain included in an area with several mineral phases corroding garnet rim, **bi.cor_Grt** – monazite grain included in relatively large biotite corroding garnet rim.

The per cent discordance **(% disc.)** was calculated using the fomula (1-($^{206}Pb/^{238}U$ age / $^{207}Pb/^{206}Pb$ age) x 100).

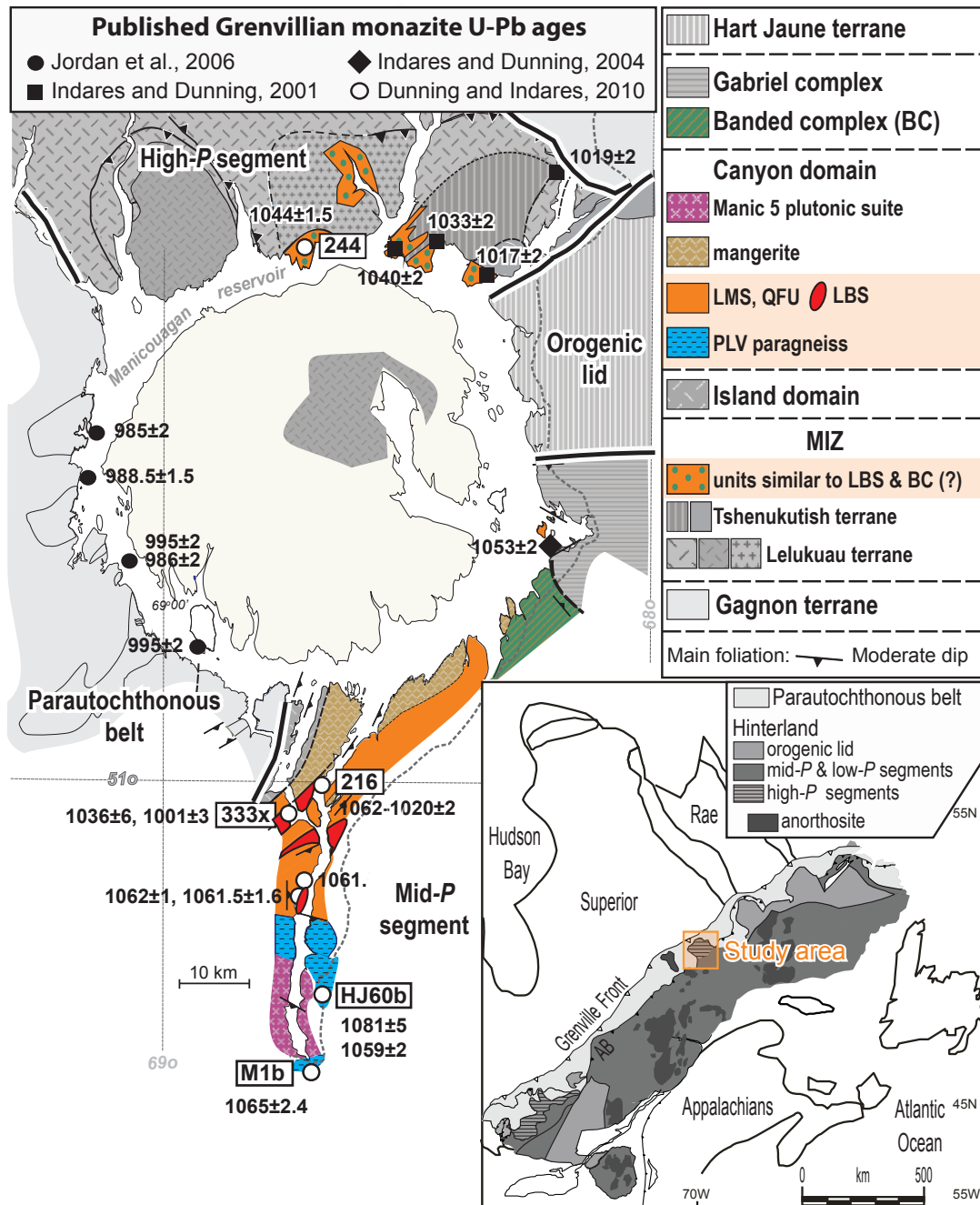| 216				grain			RATIO 207Pb/		206Pb/		207Pb/		AGES 207Pb/		206Pb/		207Pb/		
an.#	s.#	Mnz.#	Spot.#	area	BSE	Occur.	235U	2SE	238U	2SE	206Pb	2SE	235U	2SE	238U	2SE	206Pb	2SE	%disc
b47	a	6	1	c	\	M	1.750	0.029	0.1736	0.0035	0.0730	0.0008	1027	11	1031	19	**1014**	**23**	2
b46	a	21	2	c	d	M	1.795	0.027	0.1781	0.0034	0.0734	0.0007	1043	10	1057	19	**1025**	**18**	3
g14	c	16	1	c	d	M	1.765	0.062	0.1750	0.0043	0.0736	0.0011	1033	22	1041	24	**1031**	**30**	1
c31	a	11	2	c	d	M	1.767	0.071	0.1733	0.0043	0.0736	0.0007	1036	26	1031	24	**1031**	**20**	0
b52	a	12	1	c	\	bi.cor_Grt	1.833	0.029	0.1801	0.0036	0.0738	0.0007	1058	10	1067	19	**1036**	**20**	3
b26	a	2	1	c	\	ad_Grt	1.739	0.025	0.1702	0.0033	0.0739	0.0006	1024	9	1013	18	**1038**	**16**	-2
b55	a	13	1	c	\	bi.cor_Grt	1.818	0.028	0.1791	0.0036	0.0740	0.0008	1053	10	1063	19	**1042**	**22**	2
d35	c	20	3	c	d	M	1.776	0.052	0.1737	0.0040	0.0741	0.0007	1036	19	1033	22	**1045**	**20**	-1
d20	c	17	1	c	d	emb_Grt	1.818	0.054	0.1758	0.0042	0.0742	0.0007	1051	20	1044	23	**1048**	**20**	0
g12	c	15	2	c	\	ad_Grt	1.785	0.063	0.1744	0.0046	0.0743	0.0012	1042	23	1035	25	**1050**	**33**	-1
g61	c	5	3	c	d	ad_Grt	1.795	0.061	0.1782	0.0044	0.0743	0.0009	1043	22	1057	24	**1050**	**24**	1
b29	a	9	1	c	d	M	1.848	0.028	0.1798	0.0034	0.0743	0.0008	1062	10	1065	19	**1050**	**20**	1
d08	c	9	1	c	d	M	1.764	0.052	0.1712	0.0039	0.0744	0.0007	1032	19	1018	21	**1052**	**18**	-3
b63	a	4	2	c	d	M	1.876	0.030	0.1825	0.0036	0.0745	0.0008	1071	11	1082	20	**1054**	**22**	3
d12	c	21	2	c	d	M	1.817	0.053	0.1763	0.0040	0.0745	0.0008	1051	19	1048	22	**1055**	**21**	-1
g47	c	1	4	c	d	M	1.774	0.060	0.1757	0.0044	0.0745	0.0010	1036	22	1043	24	**1055**	**27**	-1
c22	a	25	1	c	d	emb_Grt	1.888	0.077	0.1830	0.0046	0.0745	0.0009	1077	27	1084	25	**1056**	**24**	3
d23	c	12	1	c	\	M	1.820	0.053	0.1756	0.0040	0.0745	0.0007	1052	19	1043	22	**1056**	**19**	-1
b34	a	10	1	c	d	Grt incl.?	1.843	0.027	0.1788	0.0035	0.0747	0.0007	1060	10	1061	19	**1059**	**18**	0
g26	c	6	2	c	d	cor_Grt	1.775	0.060	0.1733	0.0043	0.0749	0.0009	1036	22	1030	24	**1066**	**25**	-4
b59	a	8	2	c	d	M	1.912	0.032	0.1850	0.0037	0.0750	0.0008	1086	11	1094	20	**1068**	**22**	2
g62	c	4	3	c	d	M	1.800	0.061	0.1752	0.0043	0.0750	0.0010	1046	22	1041	23	**1069**	**25**	-3
d14	c	2	1	c	d	M	1.830	0.054	0.1776	0.0041	0.0752	0.0007	1056	19	1053	23	**1074**	**18**	-2

an. # – analysis number, **sect. #** – thin-section a or c, **Mnz. #** – monazite grain number, **Occur.** – Occurrence/textural context of the monazite grain, **R** – analyses of rim, **c** – analyses of core, **L** – zone of light BSE, **d** – zone of dark BSE, **M** – monazite grain in the matrix, **Grt** – monazite grain included in garnet, **ad_Grt** – monazite grain adjacent/touching garnet rim, **emb_Grt** – monazite grain included in a polymineralic embayment in garnet, **Grt incl** – monazite present as a single inclusion in garnet, **cor_Grt** – monazite grain included in an area with several mineral phases corroding garnet rim, **bi.cor_Grt** – monazite grain included in relatively large biotite corroding garnet rim.

The per cent discordance (**% disc.**) was calculated using the fomula (1-(^{206}Pb/^{238}U age / ^{207}Pb/^{206}Pb age) x 100).

184

Figure 4.1: Simplified geological map of the Manicouagan area (inspired by Indares and Moukhsil, 2013) showing previously published Grenvillian U–Pb monazite data (ID–TIMS; Dunning and Indares, 2010), and inset map showing the general framework and location of the Grenville Province. AB – Allochton Boundary; LMS – layered mafic suite; QFU – layered quartzofeldspathic unit; LBS – layered bimodal sequence, including zones of hydrothermal alteration; PLV – Complexe de la Plus Value; MIZ – Manicouagan Imbricate Zone.
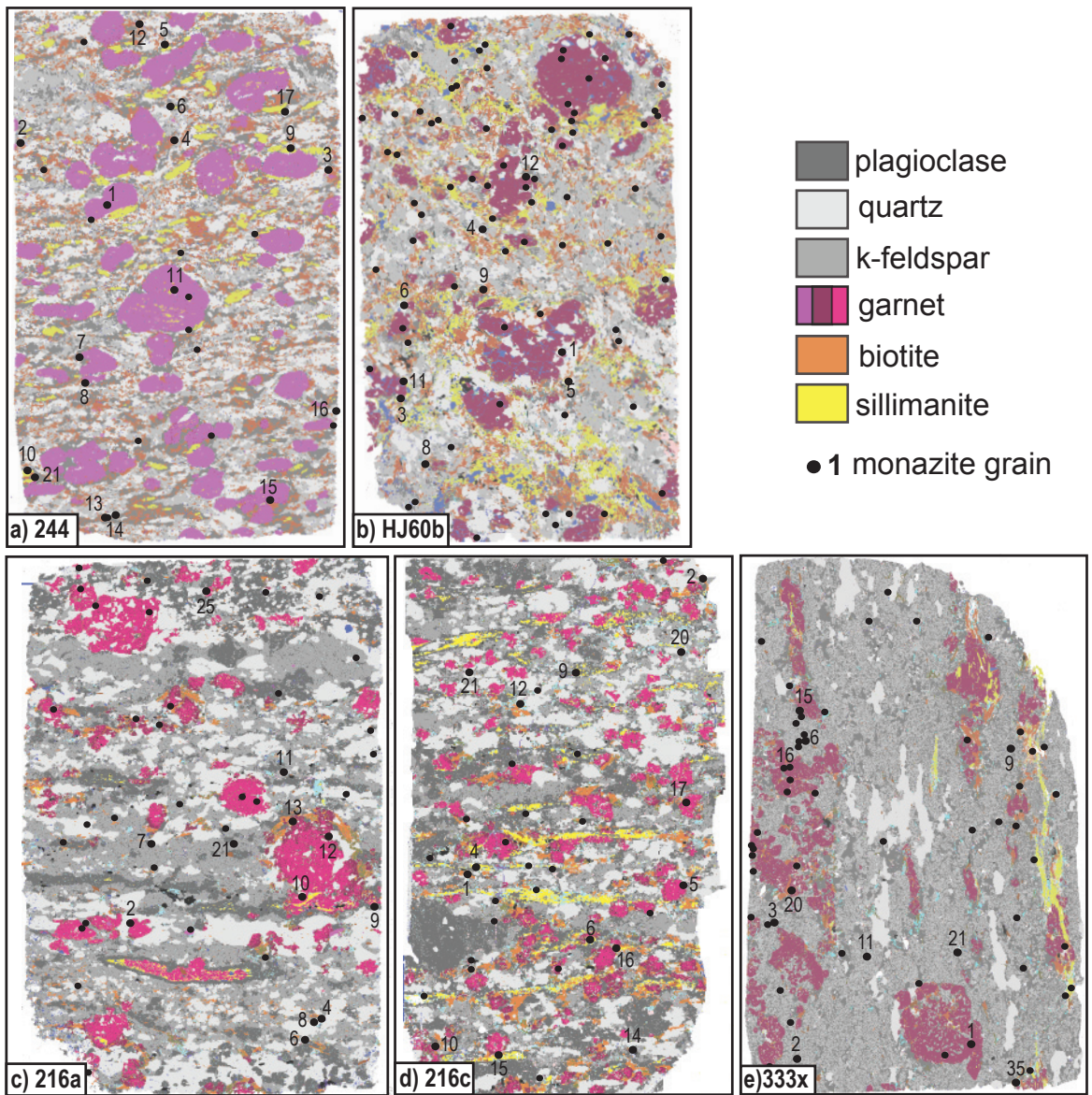
Figure 4.2: False color SEM-MLA maps of polished thin-sections, (a) #244, (b) #HJ60b, (c) #216a, (d) #216c, and (e) #333x, highlighting the main mineralogy, texture, and locations of monazite (black dots) for each sample (modified after Lasalle and Indares, 2014). Numbers were added for the monazite grains that are discussed in the text, tables, and other figures.
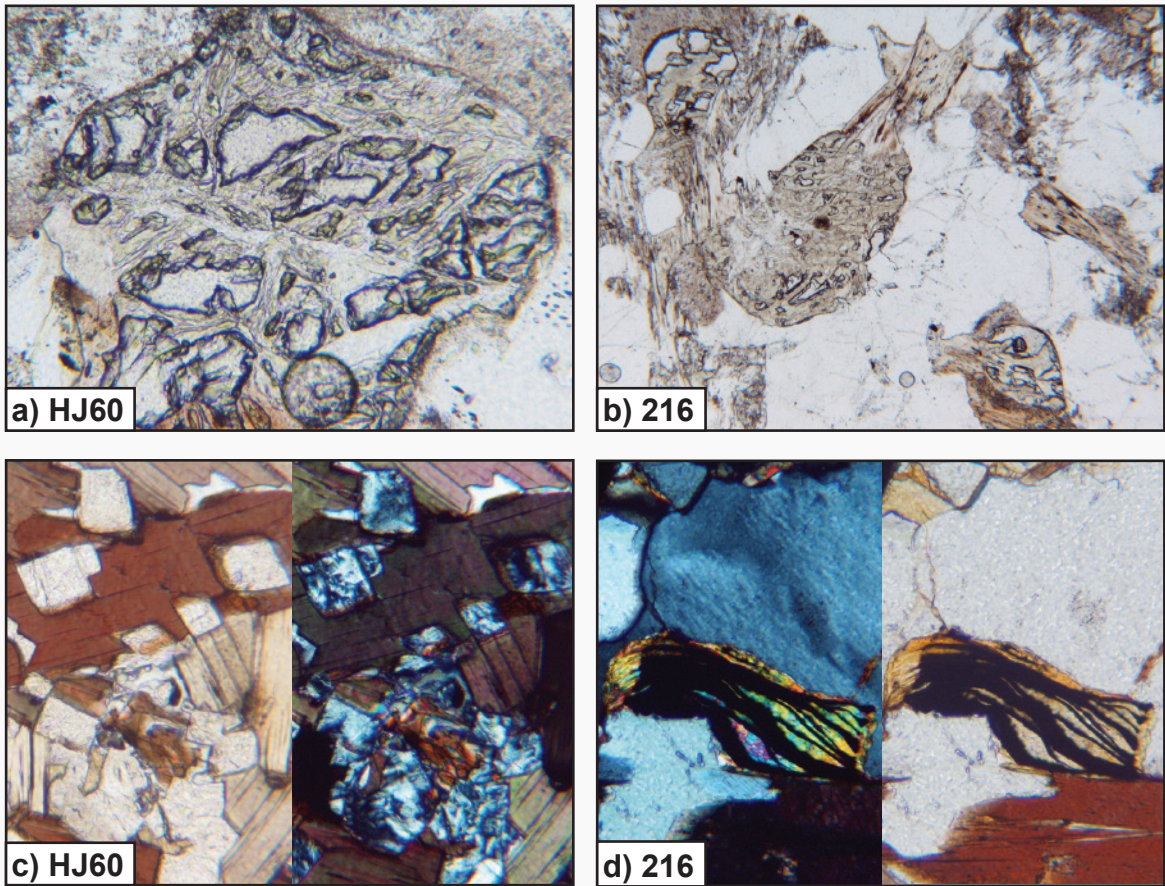
Figure 4.3: Photomicrographs illustrating the late greenschist (?) metamorphic features present in samples HJ60b and 216, viewed in: PPL, plane-polarized light and XPL: crossed-polarized light. (a) garnet porphyroblast replaced by chlorite (#HJ60; PPL). (b) 'cracked eggs' garnet, replaced by chlorite (#216a; PPL). (c) sillimanite pseudomorphed by fine aggregates of sericite (?) (#HJ60; PPL and XPL). (d) graphite rimmed by muscovite (#216; XPL and PPL).
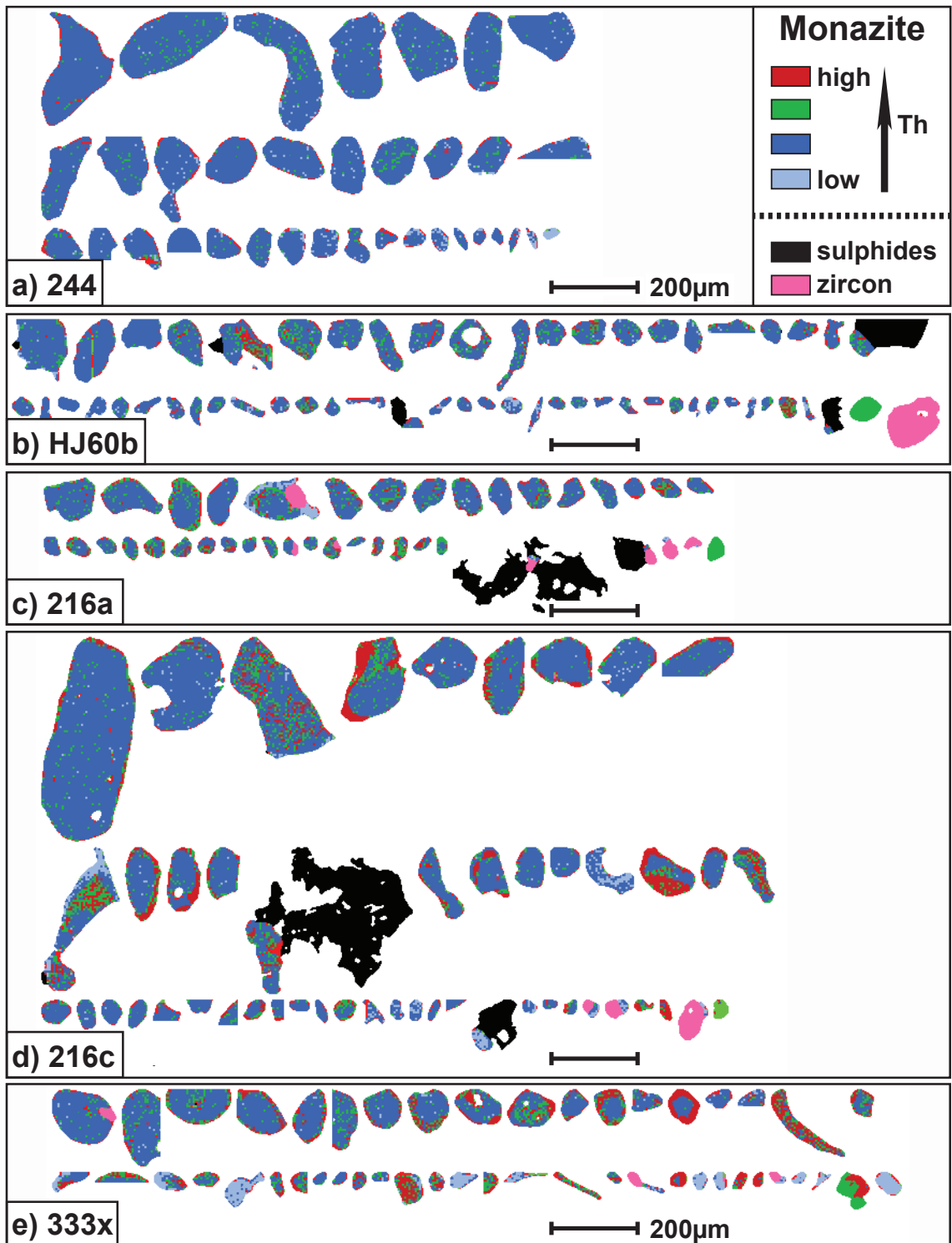
Figure 4.4: Silhouettes of monazite grains showing Th zoning and associated minerals, obtained by SEM mapping (a) #244, (b) #HJ60b, (c) #216a, (d) #216c, and (e) #333x.
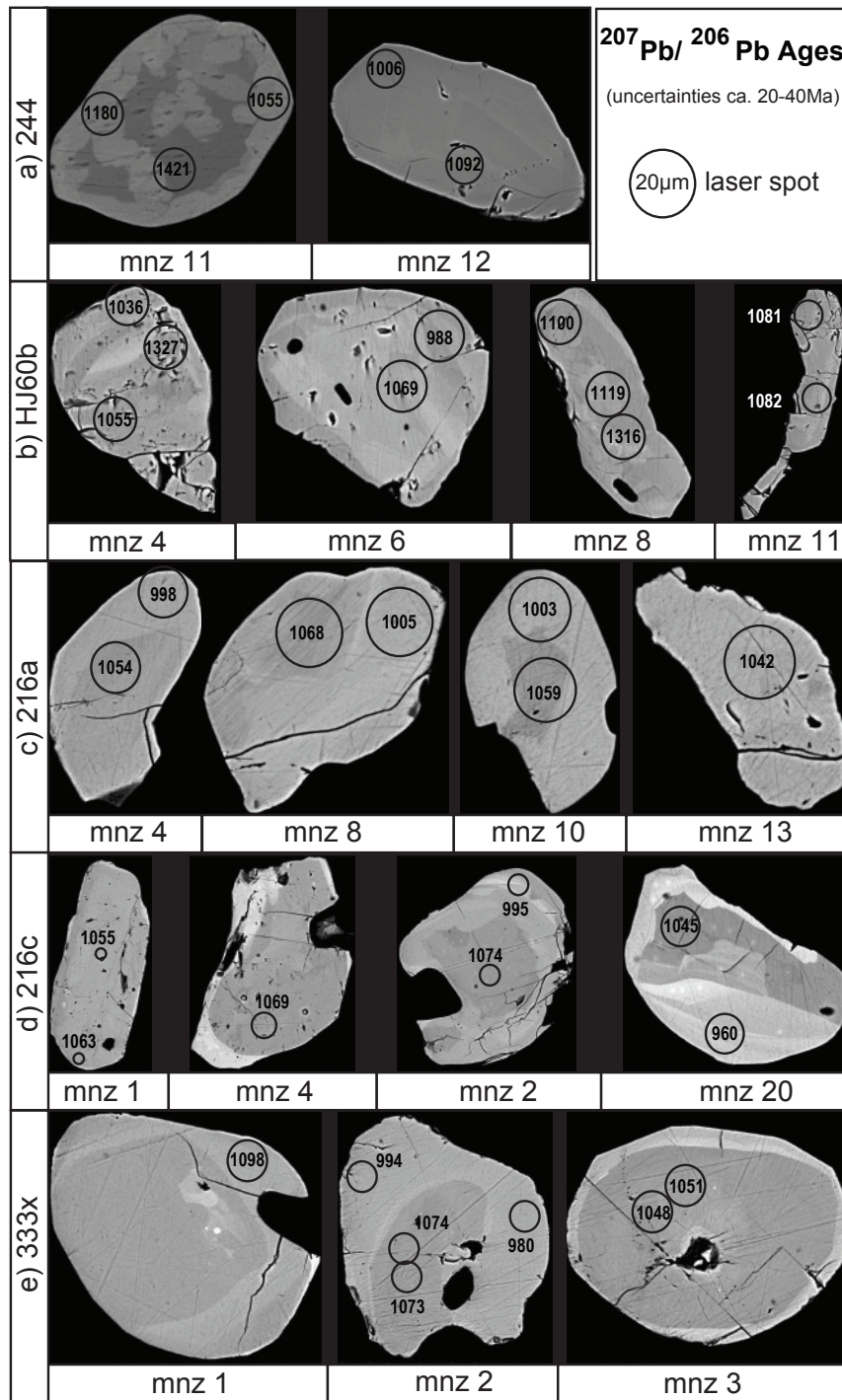
Figure 4.5: Monazite zoning as seen on BSE images, and location of the LA–ICPMS spot analyses (20 μm) labelled with the corresponding ^{207}Pb/^{206}Pb age; (a) #244, (b) #HJ60b, (c) #216a, (d) #216c, and (e) #333x. These grains are the most characteristic ones in terms of internal BSE zoning and/or U–Pb ages.
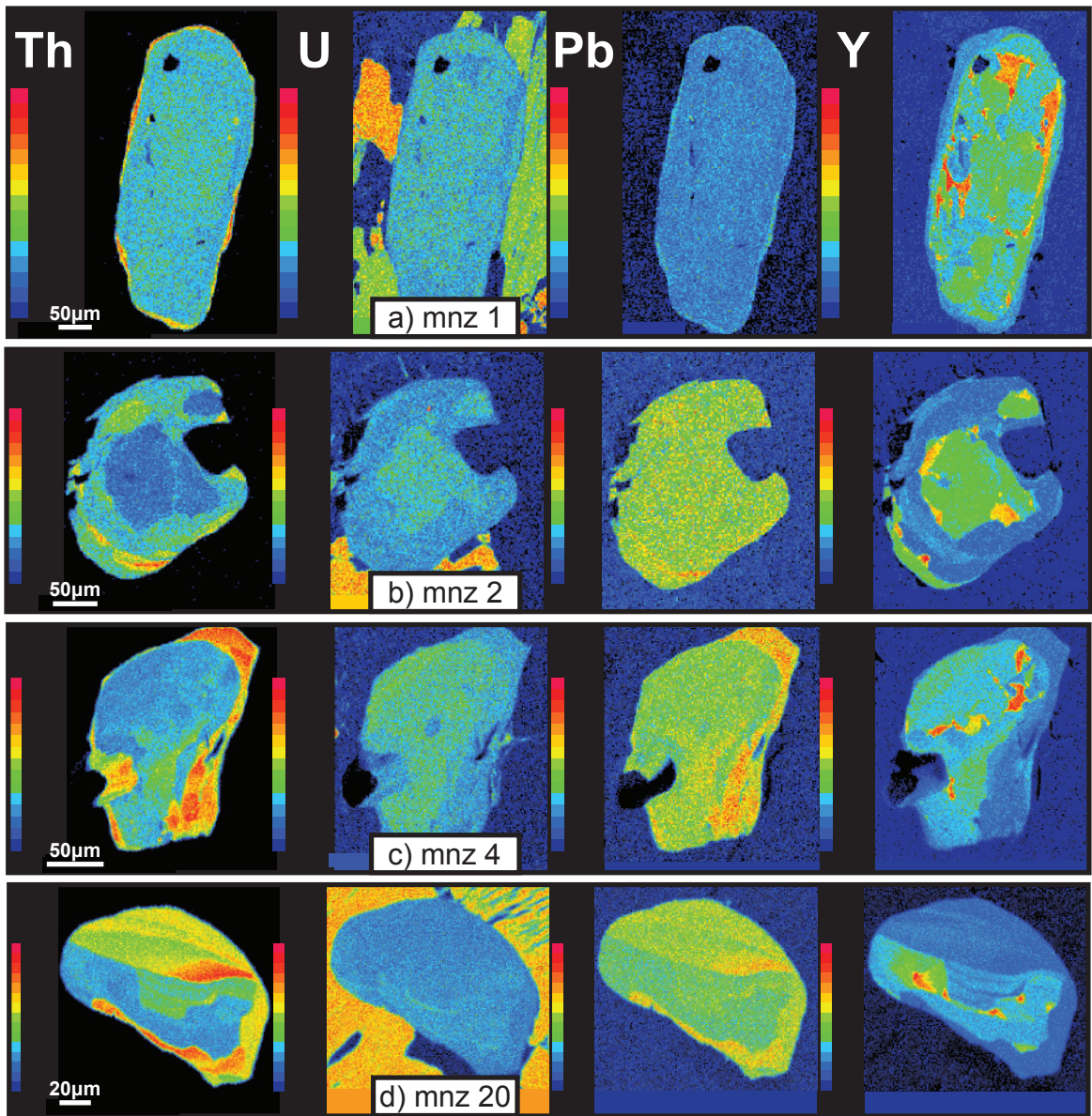
Figure 4.6: Examples of qualitative chemical maps acquired by EPMA, of 5 monazite grains from section 216c that display the most characteristic internal zoning in Th, U, Pb, and Y; (a) grain 1, (b) grain 2, (c) grain 4, (d) grain 20.
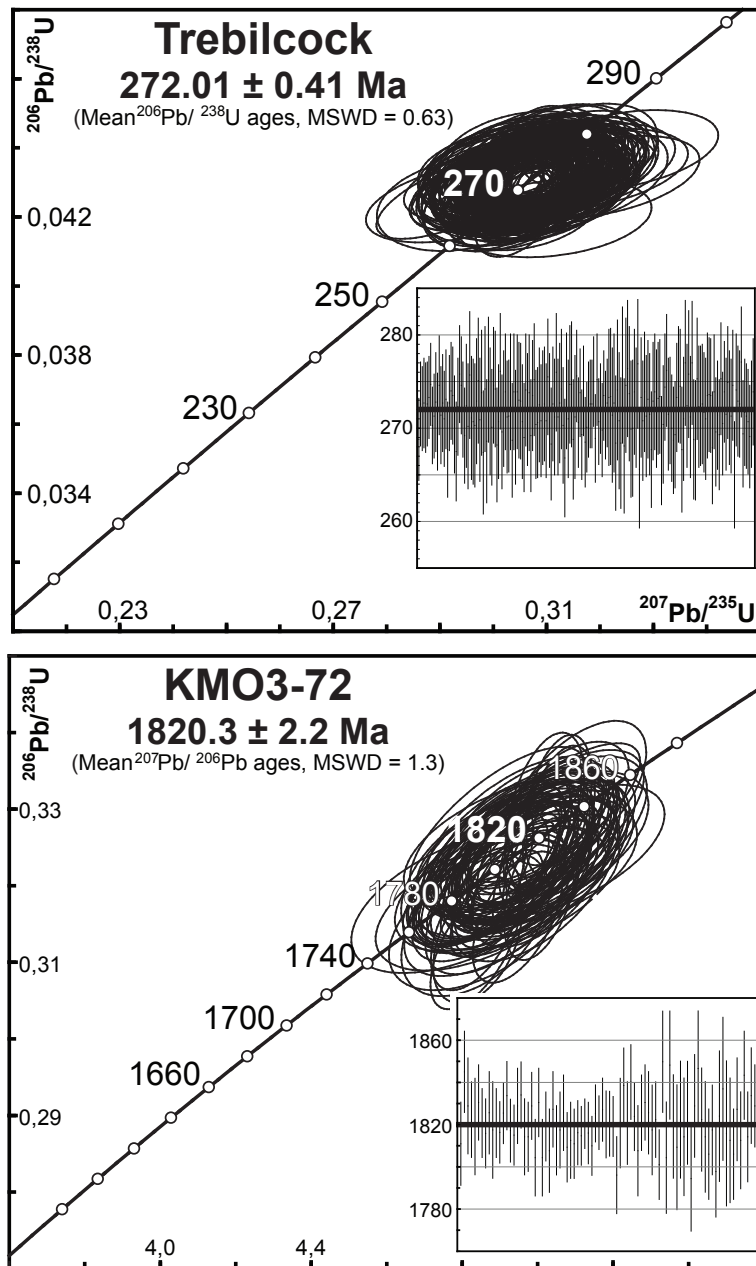
Figure 4.7: Precision and accuracy of the U–Pb data collected on the two monazite standards used in this study; (a) the Trebilcock monazite that was used as the reference material (n=196), (b) the monazite KMO3-72 that was used as secondary standard (n=84).
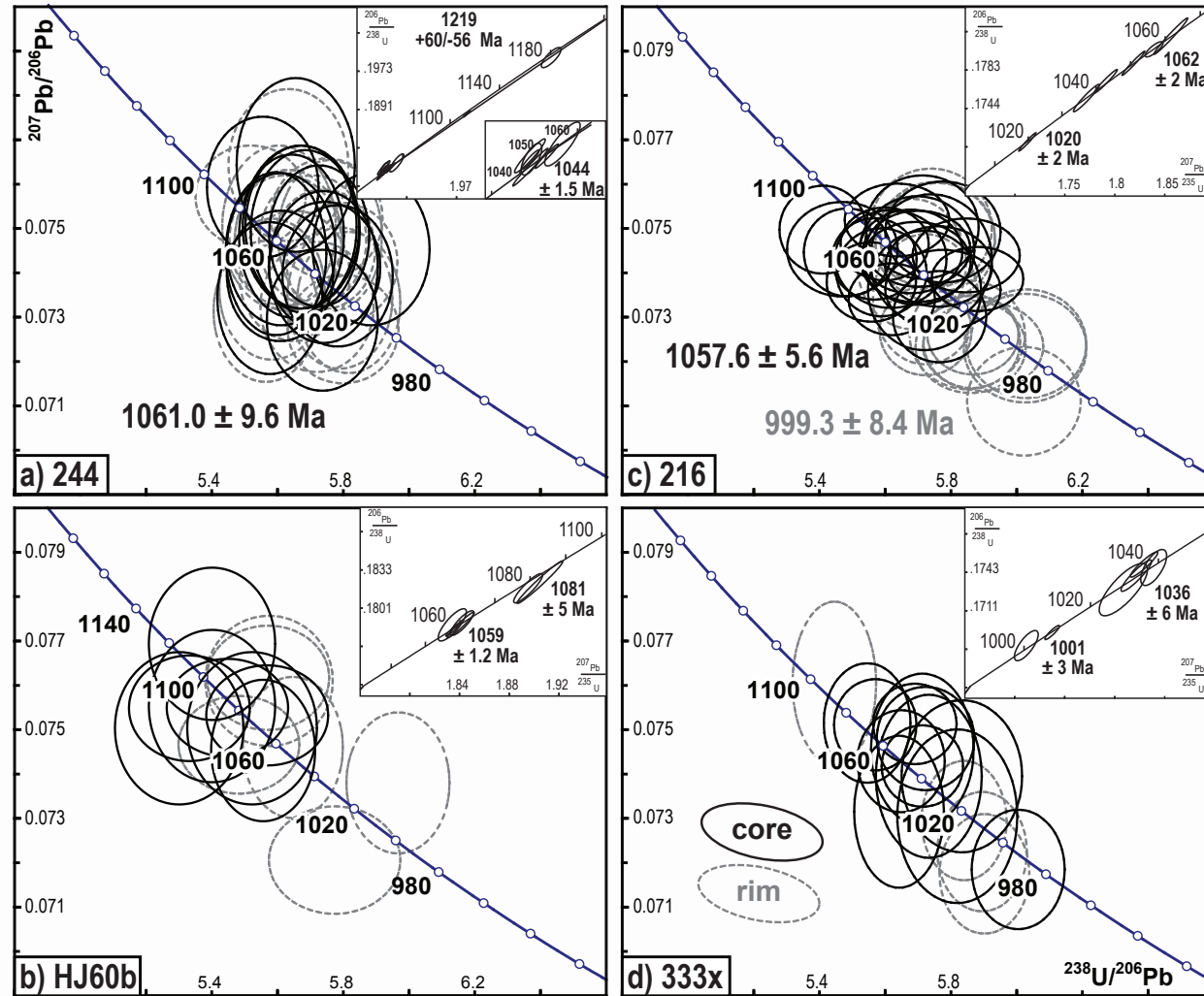
Figure 4.8: Tera-Wasserburg diagrams presenting the U–Pb data collected for each sample; with inset showing the corresponding ID–TIMS data modified after Dunning and Indares, (2010): (a) #244, (b) #HJ60b, (c) #216, (d) #333x.
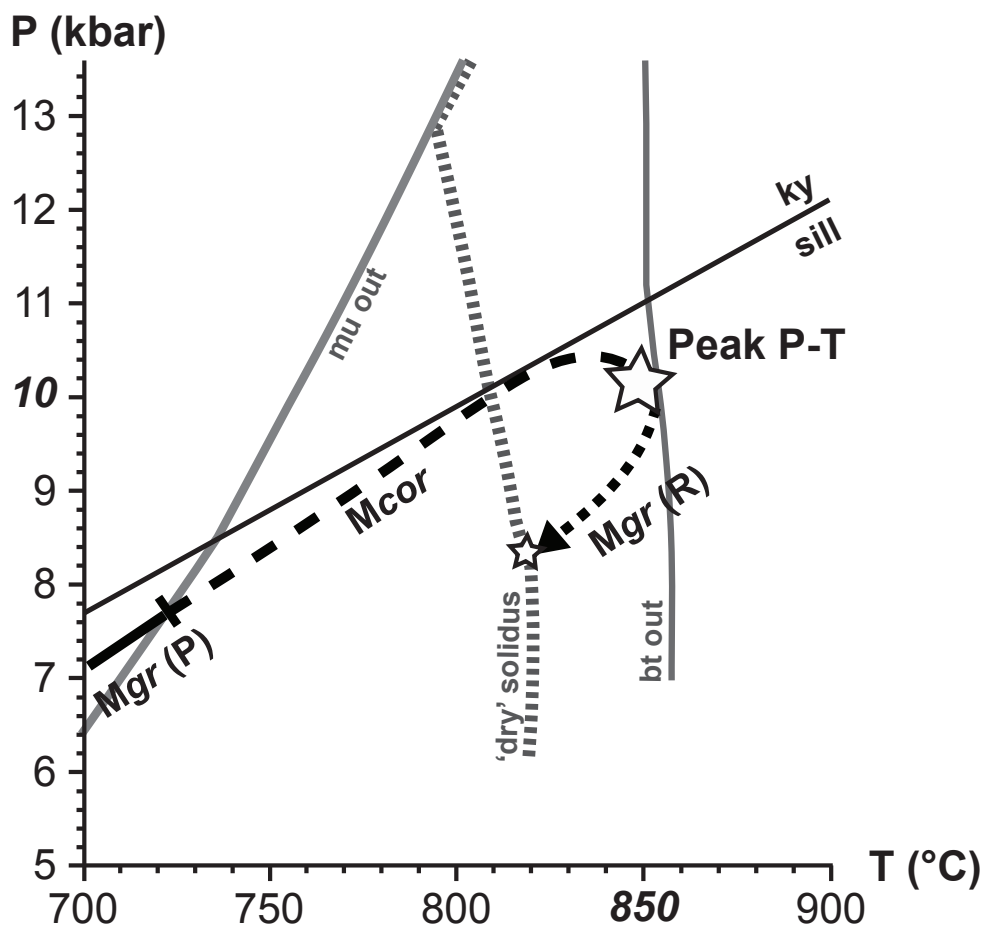
Figure 4.9: Schematic *P–T* path modelled for the mid-*P* sample HJ60b (inspired by Lasalle and Indares, 2014) showing presumed *P–T* ranges of monazite growth (M$_{gr}$), with a distinction between prograde (P) and retrograde (R), and the *P–T* range of monazite corrosion (M$_{cor}$). Important boundaries copied from the pseudosections (presented in Lasalle and Indares, 2014) are also reported. mu-out line: reaction muscovite+quartz±plagioclase→Al-silicate+K-feldspar+liquid; between the mu-out line and the bi-out line: continuous partial melting by reaction: biotite+Al-silicate+quartz±plagioclase→garnet+K-feldspar+liquid; 'dry' solidus: position of the solidus after melt loss.

APPENDICES OF CHAPTER 4 INCLUDED (AS EXCEL FILES)

IN THE CD

APPENDIX 4.1: Monazite (LA–ICPMS) U–Pb data collected on standard Trebilcock.

The monazite standard Trebilcock was analyzed 235 times in total and 39 outlier analyses (~17%) were discarded. A weighted average $^{206}Pb/^{238}U$ age was calculated at 272.01 Ma $\pm$ 0.41 Ma (MSWD=0.63).

APPENDIX 4.2: Monazite (LA–ICPMS) U–Pb data collected on standard KMO3-72

Monazite KMO3-72 was analyzed 97 times. After discarding 13 outlier analyses (13%) a weighted average $^{207}Pb/^{206}Pb$ age was calculated at 1820.3 Ma $\pm$ 2.2 Ma (MSWD=1.3).

CHAPTER 5

5. SUMMARY AND CONCLUSIONS

This study of granulite-facies aluminous rocks provides new insights into the makeup and tectono-metamorphic evolution of the hinterland in the central portion of the Grenville Province. The rocks investigated originate from the Canyon domain (first defined by Hynes *et al.,* 2000) and contrasting lithological sequences within that domain, which were redefined more recently (Dunning and Indares, 2010; Indares and Moukhsil, 2013; Moukhsil *et al.,* 2013); specifically the metasedimentary Complexe de la Plus Value (PLV), and the layered bimodal (felsic-mafic) sequence (LBS), as well as from contrasting pressure segments (high-*P vs.* mid-*P*) in the Grenville orogen. All samples consist of garnet–biotite–K-feldspar–plagioclase–quartz, with kyanite or sillimanite, and display microstructural evidence of anatexis. The main findings for each rock type and crustal segment are summarized below and in Table 5.1.

5.1. SUMMARY OF THE MAIN FINDINGS

5.1.1. High-*P* segment: northern extension of the LBS (sample 244)

The presence of relict detrital zircon with ages between 1.7 and 1.4 Ga in an aluminous gneiss intercalated with felsic layers in the northern extension of the LBS (sample 244) suggests that some aluminous components of the principally magmatic LBS are metasedimentary and of local provenance (Table 5.1). The only concordant age (at 1603 ± 28 Ma) within this interval overlaps with the age range of neighbouring plutonic units of the Lelukuau terrane, and suggests an upper age limit of *ca.* 1.6 Ga for the original deposition of the paragneiss. However, most zircon from sample 244 is

metamorphic, with large rims overgrowing older igneous cores, common 'soccer-ball' morphologies, and ages of *ca.* 1040 Ma (Table 5.1 and Fig. 5.1).

Sample 244 contains abundant evidence of former melt. Phase equilibria modelling predicts a steep prograde *P–T* path, up to ~ 14.5 kbar and 860–900 °C, followed by decompression down to the solidus at ~ 11 kbar and 870 °C (Table 5.1 and Fig. 5.1). Monazite from this sample records mainly Grenvillian ages, between *ca.* 1100 and 1000 Ma, with an apparent cluster at *ca.* 1060 Ma. In addition, there are a few older ages (up to *ca.* 1421 Ma) although these may not be reliable (Table 5.1).

5.1.2.   Mid-*P* segment: metasedimentary rocks of the PLV (samples HJ60b and M1b)

Zircon from aluminous gneisses of the PLV (samples HJ60b and M1b) is mostly detrital, consistent with the sedimentary origin of the host rocks, and is overgrown by metamorphic rims (Table 5.1). The age distribution of the detrital cores (*ca.* 2746 to 1500 Ma) is broadly comparable to that of zircon from a quartzite in the type locality of the PLV farther east (Lac du Milieu area; Moukhsil *et al.,* 2012). Most importantly, it is consistent with provenance from units of the Laurentian margin farther north, including the Archean basement and the Paleoproterozoic supracrustal sequence that were subsequently incorporated in the parautochthonous Gagnon terrane (Jordan *et al.,* 2006; van Gool *et al.,* 2008), and the Labradorian-age units of the Lelukuau terrane and the Island domain in the Grenville hinterland (Fig. 4.1; Indares *et al.,* 2000; Dunning and Indares, 2010).

197

In addition, samples HJ60b and M1b contain metamorphic zircon occurring as 'soccer-ball' grains and overgrowths on detrital grains. In sample M1b these metamorphic grains record pre-Grenvillian ages of *ca.* 1400–1360 Ma and *ca.* 1260–1230 Ma (Table 5.1), which overlap with the ages of crystallization of other major units within the Canyon domain, specifically the layered mafic sequence (LMS; Dunning and Indares, 2010; Indares and Moukhsil, 2013), and with the age of volcanic rocks in the LBS (see below), respectively. Therefore, these age ranges likely represent the thermal effect of these igneous events on the PLV. The latter age range listed above (*ca.* 1260–1230 Ma) is also represented by two imprecise zircon crystallization ages (1257 ± 43 Ma in sample M1b, 1217 ± 54 Ma in sample HJ60b), and is attributed to the crystallization of felsic pegmatite, which locally intrudes the PLV. In addition, Grenvillian metamorphic ages are recorded in these samples (*ca.* 1076 ± 37 Ma in sample M1b, *ca.* 1045 Ma in sample HJ60b; Table 5.1).

The majority of diagnostic metamorphic microstructures noted were found in sample HJ60b, which also displays the most widespread evidence of former melt. The predicted *P–T* path for this sample has a prograde portion with a moderate d*P*/d*T* gradient, constrained to pressures below the sillimanite-kyanite boundary and attaining peak conditions of up to ~ 9.5 kbar and 850 °C, and a retrograde portion down to the solidus at ~ 8 kbar and 820 °C (Fig. 5.1). Sample HJ60b yielded a few pre-Grenvillian monazite grains hosting ages up to *ca.* 1445 Ma, with a dominant Grenvillian age population (*ca.* 1080 Ma to 1050 Ma) including a cluster at *ca.* 1060 Ma (HJ60b; Table 5.1 and Fig. 5.1).

5.1.3. Mid-*P* segment: aluminous layers of the LBS (samples 333x and 216)

Samples 216 and 333x come from a homogeneous aluminous gneiss and nodular aluminous gneiss respectively, both of which grade into 'bleached' felsic gneiss. Of the two, only sample 333x yielded abundant zircon. These zircon grains have prismatic morphologies and oscillatory zoning suggestive of a magmatic origin supporting the interpretation that aluminous nodular gneisses in the LBS were derived from hydrothermally altered volcanic rocks. The 1238 ± 13 Ma age of igneous crystallization constrains the age of volcanism in the LBS, and is similar to that of the Banded complex, recognized to the northeast of the study area (Fig. 4.1). The emplacement of these two lithologic associations has been attributed to crustal extension (Dunning and Indares, 2010; Indares and Moukhsil, 2013), and the new data from this study suggest that magmatism at 1.2 Ga was more widespread in the central Grenville Province than previously recognized. In contrast, metamorphic zircon in sample 333x is limited to thin rims on igneous grains, the largest of which yielded a late Grenvillian age of *ca.* 1000 Ma.

Microstructures indicative of partial melting are more diverse in sample 216. The suggested *P–T* paths are of the same type as in sample HJ60b (*i.e.,* they are characterized by moderate d*P*/d*T* gradients and are constrained within the *P–T* window between the sillimanite-kyanite transition and the cordierite-in line) but the thermal peak is less well constrained.

Monazite grains in both 216 and 333x yielded Grenvillian ages from *ca.* 1070 Ma trailing down to *ca.* 1025 Ma (BSE dark grains), as well as late Grenvillian ages of *ca.*

1010–980 Ma in BSE-bright overgrowths (more common in sample 216). The BSE-bright

overgrowths, as well as chlorite-filled cracks in garnet and very fine aggregates of sericite

(?) pseudomorphing sillimanite are attributed to late-stage fluids.

5.2. CONCLUSIONS

These new results, integrated with existing data for the mid-*P* Canyon domain and

the northern extension of the LBS into the high-*P* segment of the hinterland, constrain the

relationships between the different crustal units of the Laurentian margin within the

central Grenville Province, and their subsequent tectono-thermal evolution during the

Grenvillian orogeny.

5.2.1. Pre-Grenvillian evolution of the Laurentian margin

The new zircon data from this study (see inherited ages for zircon cores and some

rims; Table 5.1) confirm the succession of pre-Grenvillian events in the Canyon domain

determined by Indares and Dunning (2004), Dunning and Indares (2010), Moukhsil *et al*.

(2012, 2013), and Indares and Moukhsil (2013) that can be summarized in chronological

order as follows: (a) deposition of a clastic sedimentary sequence at the southeast margin

of Laurentia at *ca.* 1.50 Ga, containing Archean- to Paleoproterozoic (Labradorian-aged)

detritus (PLV; see also Moukhsill *et al.,* 2012); (b) formation of a suite of layered igneous

rocks with mafic to intermediate composition at *ca.* 1.41 Ga (LMS; Dunning and Indares,

2010) whose thermal effects are recorded by zircon overgrowths in adjacent units (*i.e.,*

PLV; this study); (c) development of a *ca.* 1.24 Ga volcanic belt, including the Banded

complex (Indares and Dunning, 2004; Dunning and Indares, 2010) and the LBS, which contains bimodal volcanic rocks and interbedded sedimentary strata, and displays local evidence of hydrothermal alteration. This event is recorded in the country rocks (PLV) by injections of felsic pegmatite and a thermal overprint leading to growth of metamorphic zircon.

5.2.2. Grenvillian tectono-thermal evolution

Data presented here highlight two contrasting Grenvillian metamorphic signatures in the hinterland of the central Grenville Province (Fig. 5.1). The kyanite‑bearing high-P segment is characterized by steep 'hair pin' P–T paths (northern LBS: this study), which is similar to that determined for the eastern MIZ (sample BNS3; Indares, *et al.,* 2008; Fig. 5.1). Age data from Grenvillian monazite in the northern LBS (sample 244; this study) range between *ca.* 1100 and 1000 Ma but most are clustered at *ca.* 1060 Ma, which agrees with the ID–TIMS data of Dunning and Indares (2010). Farther east, ages were constrained at *ca.* 1040 and 1030 Ma (BNS3; Indares and Dunning, 2001; Fig. 5.1). In contrast, P–T data from the mid-P segment (HJ60b, this study) imply significantly larger T and lesser P variations compared to those in the high-P segment (244; Fig. 5.1) and metamorphic ages are more widely spread with data between *ca.* 1080 and 1000 Ma (sample HJ60b and others in the Canyon domain; ID–TIMS data; Dunning and Indares, 2010; LA–ICPMS data; this study).

Such a large difference in metamorphic evolution and P–T paths between the mid-P Canyon domain and high-P portion of the LBS, north of the Manicouagan Reservoir,

imply that they are separated by one or more extensional faults (*e.g.*, detachments labelled ?[1] and ?[2] on the cross-section; Fig. 5.1), presently masked by the Manicouagan Impact crater. This was also suggested by Indares and Moukhsil (2013). In terms of tectonic evolution, the *P–T* data from sample 244 in the high-*P* segment are consistent with exhumation from near the bottom of a double thickness crust up to mid-crustal level.

The *P–T* path predicted for the sillimanite-bearing sample HJ60b is the first ever determined for the mid-*P* segment of the central Grenville Province, and may be the first *P–T* path determined for mid-*P* Grenvillian rocks using modern phase equilibrium modelling methods. In this sample, the main population of Grenvillian-aged monazite varies in age between *ca.* 1080 and 1050 Ma (Table 5.1; Fig. 5.1), with a few analyses trailing down to 1020 Ma, as also suggested by ID–TIMS data from Dunning and Indares (2010). Within the context of the extensive anatexis in the granulite-facies host rocks, this age range likely represents distinct episodes of monazite growth linked to pulses of melt crystallization in rocks that remained under high-*T* conditions for a protracted period of time. Together, the style of the *P–T* path and the wide range of Grenvillian metamorphic ages imply an extended residence in hot mid-crust, consistent with an evolution at mid-crustal depth under an orogenic plateau (*e.g.*, Jamieson *et al.*, 2007, 2010).

Lastly, the late-Grenvillian BSE-bright monazite rims (*ca.* 1010–990 Ma), which are widespread in the mid-*P* samples, are attributed to fluid infiltration, possibly under greenschist-facies conditions, that also gave rise to the local retrogression observed in some samples. These fluids were temporally, and possibly also petrogenetically (?) linked to the intrusion of 990–980 Ma ultra-potassic dykes and felsic pegmatites in the Canyon domain, which in turn likely record a response of the hinterland to the orogenic collapse.

This late-Grenvillian age is similar to the age of the high-P granulite facies metamorphism in aluminous paragneisses at the adjacent rim of the Gagnon terrane (Fig. 5.1; see Indares *et al.,* 2008). Therefore, in a wider context, this event was also coeval with crustal shortening and high-grade metamorphism in the underlying Parautochthonous belt, and the late-stage propagation of the orogen to the northwest into its former foreland.

Table 5.1: Synthesis of main findings (see the legend below the table for the description of the abbreviations).

SAMPLE	244	333x	216 (a and c)	HJ60b	M1b
P-segment within the Hinterland	high-*P*	mid-*P*	mid-*P*	mid-*P*	mid-*P*
tectono-metamorphic domain within the Manicouagan area		Canyon domain	Canyon domain	Canyon domain	Canyon domain
unit within the domain	LBS (northern extension ?)	LBS; hydro. alter. zone	LBS; hydro. alter. zone	PLV	PLV
Main mineral assemblage (granulite-facies)	als + grt + bt + qtz + pl + Ksp + ru + liq	als + grt + bt + qtz + pl + Ksp + ru + liq	als + grt + bt + qtz + pl + Ksp + ru + liq	als + grt + bt + qtz + pl + Ksp + ru + liq	als + grt + bt + qtz + pl + Ksp + ru + liq
main alumino-silicate	kyanite	sillimanite	sillimanite	sillimanite	sillimanite
minor phases	ap	± ilm	ap ± graph	ilm, graph	n.d.
evidence for lower grade metamorphism (greenschist?)	none	none	chl with grt + sill pseudomorphs	chl with grt + sill pseudomorphs	n.d.
zircon texture	small relict igneous cores + wide metamorphic rims, 'soccer ball' grains	igneous grains, rare metamorphic rims	n.d.	relict igneous cores + metamorphic rims	relict igneous cores + metamorphic rims
protolith	sedimentary	felsic volcanic hydrothermally altered	n.d.	sedimentary	sedimentary
metamorphic peak *P–T*	14-16 kbar, 860-900 °C	n.d.	n.d.	~10 kbar, 850 °C	n.d.
P–T (path) evolution	steep prograde path + decompression (to 11 kbar) with minor cooling (to 870°C)	n.d.	n.d.	relatively flat prograde path + moderate decompression (to 8 kbar) & cooling (to 820°C)	n.d.

SAMPLE	244	333x	216 (a and c)	HJ60b	M1b
zircon core U–Pb ages*	*~1600 Ma & ~1400 Ma (disc. data)*	**~1240 Ma** *~1600 Ma (1 core)*	n.d.	**~1800 Ma–1500 Ma** *~2750 Ma & 2550 Ma*	**~1900 Ma–1500 Ma** *~2470 Ma*
zircon rim U–Pb ages*	**~1040 Ma (rims, mantles, + 'soccer ball' grains)**	**~1240 Ma** *~1000 Ma (1 metam. rim)*	n.d.	**~1300 Ma–1000 Ma** *~1040 Ma (3 metam. rims)*	**~1400 Ma–1200 Ma** *~1060 Ma (1 metam. rim)*
monazite core U–Pb ages*	**~1080–1020 Ma (cluster @1060 Ma)** *~1420 Ma (1 core)*	**~1070–1020 Ma**	**~1070–1020 Ma (cluster @1060 Ma)**	**~1080–1060 Ma** *~1440 & 1320 Ma*	n.d.
monazite rim U–Pb ages*	**~1080–1020 Ma (cluster @1060 Ma)** *~1000 Ma (1 rim)*	**~1020–980 Ma (bright-BSE rims)**	**~1000–960 Ma (bright-BSE rims)**	**~1060–990 Ma**	n.d.

als – aluminosilicate; grt – garnet; bt – biotite; qtz – quartz; pl – plagioclase; Ksp – K-feldspar; ru – rutile; liq – silicate melt; ap – apatite; ilm – ilmenite; graph – graphite; chl – chlorite; n.d. – not determined; disc. – discordant; metam. – metamorphic.

* U-Pb ages **in bold** represent the main population while *in italics* are ages found more rarely, in a few grains or portion of grain.
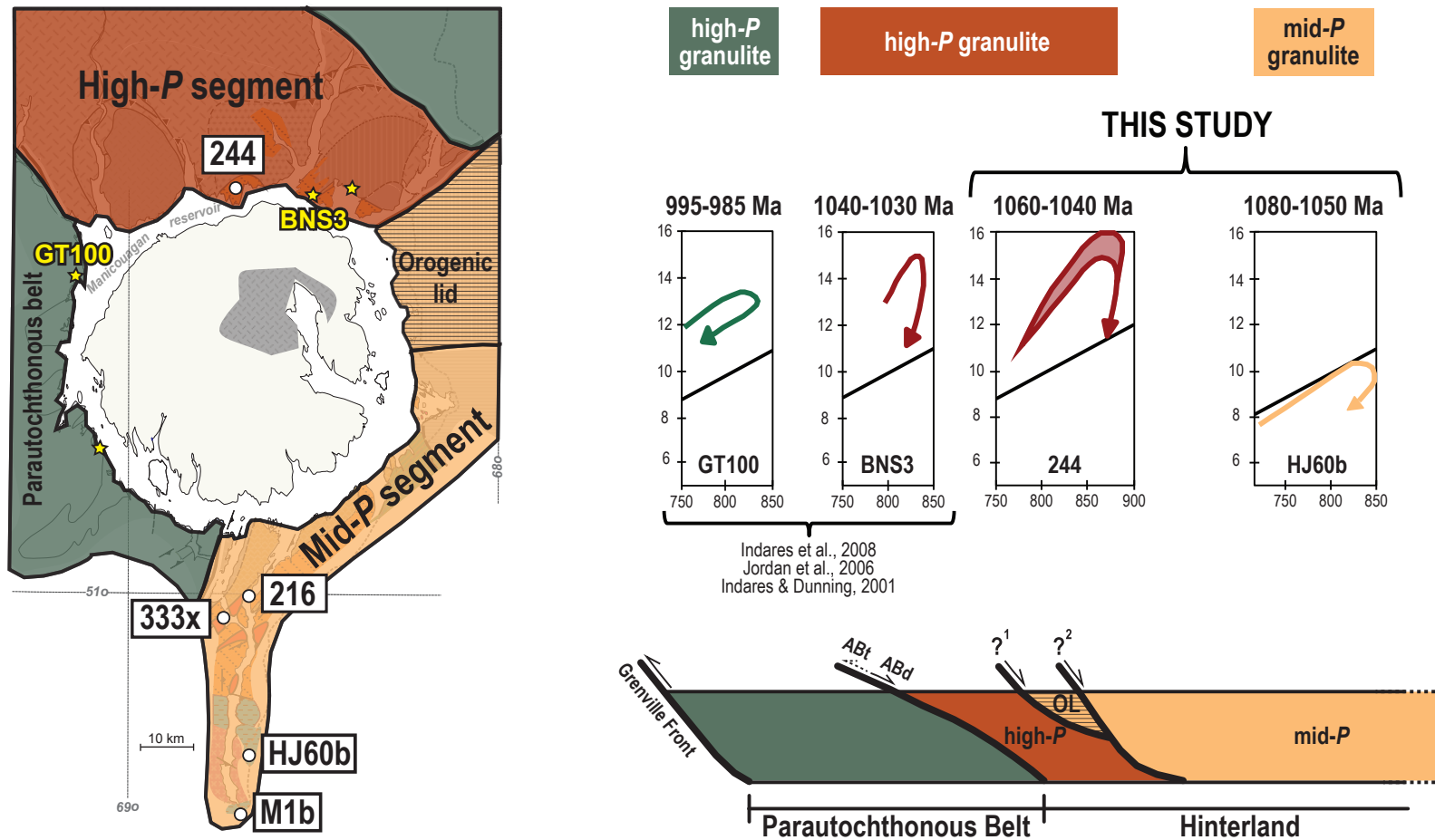
Figure 5.1: Synthesis. Simplified map of the Manicouagan area (modified after Dunning and Indares, 2010) highlighting the different *P*-segments, and a schematic N-S cross-section (inspired by Rivers, 2008). Metamorphic data (facies, ages and *P–T* paths) for each *P*-segment of interest are styled after those presented in this study and the three references cited on the figure itself. ABt – Allochthon Boundary thrust, which was re-worked as a normal-sense detachment (ABd – d for detachment); OL – Orogenic lid; ?[1] and ?[2] are possible extensional faults hidden underneath the Manicouagan Reservoir that separate the mid-*P* and high-*P* segments.

CHAPTER 6

6. COMPLETE BIBLIOGRAPHY

Aleinikoff, J. N., Schenck, W. S., Plank, M. O., Srogi, L. A., Fanning, C. M., Kamo, S. L. and Bosbyshell, H., 2006. Deciphering igneous and metamorphic events in high-grade rocks of the Wilmington Complex, Delaware: Morphology, cathodoluminescence and backscattered electron zoning, and SHRIMP U–Pb geochronology of zircon and monazite. *Geological Society of America Bulletin*, **118**: 39–64.

Beaumont, C., Nguyen, M. H., Jamieson, R. A. and Ellis, S., 2006. Crustal flow modes in large hot orogens. *In:* Law, R. D., Searle, M. P., and Godin, L. *(Eds).* Channel Flow, Ductile Extrusion and exhumation in Continental Collision Zones. *Geological Society, London*, Special Publications, **268**: 91–145.

Black, L. P., Williams, I. S. and Compston, W., 1986. Four zircon ages from one rock: the history of a 3930 Ma-old granulite from Mount Sones, Enderby Land, Antarctica. *Contribution to Mineralogy and Petrology,* **94**: 427–437.

Bonnet, A. and Corriveau, L., 2007. Alteration vectors to metamorphic hydrothermal systems in gneissic terranes. *In:* Goodfellow, W.D. *(Eds.).* Mineral Deposits of Canada: A Synthesis of Major Deposit-Types, District Metallogeny, the Evolution of Geological Provinces, and Exploration Methods. *Geological Association of Canada, Mineral Deposits Division, Special Publication,* **5**: 1035–1049.

Bonnet, A., Corriveau, L. and La Flèche, M. R., 2005. Chemical imprint of highly metamorphosed volcanic-hosted hydrothermal alterations in the Romaine Supracrustal Belt, eastern Grenville Province, Quebec. *Canadian Journal of Earth Sciences,* **42(10)**: 1783–1814.

Brown, M., 2010. Melting of the continental crust during orogenesis: the thermal, rheological, and compositional consequences of melt transport from lower to upper continental crust. *Canadian Journal of Earth Sciences*, **47**: 655–694.

Brown, M., 2007. Crustal melting and melt extraction, ascent and emplacement in orogens: mechanisms and consequences. *Journal of the Geological Society, London,* **164**: 709–730.

Brown, M., 2004. The mechanism of melt extraction from lower continental crust of orogens. *Transactions of the Royal Society of Edinburgh, Earth Sciences*, **95**: 35–48.

Brown, M., 2002. Retrograde processes in migmatites and granulites revisited. *Journal of Metamorphic Geology*, **20**: 24–40.

Cawood, P. A., Hawkesworth, C. J., Dhuime, B., 2012. Detrital zircon record and tectonic setting. *Geology*, **40**: 875–878.

Cherniak, D. J., 2010. Diffusion in Accessory Minerals: Zircon, Titanite, Apatite, Monazite and Xenotime. *Reviews in Mineralogy and Geochemistry*, **72**: 827–869.

Cherniak, D. J., Watson, E. B., Grove, M., Harrison, T. M., 2004. Pb diffusion in monazite: a combined RBS/SIMS study. *Geochimica et Cosmochimica Acta*, **68**: 829–840.

Coggon, R. and Holland, T. J. B., 2002. Mixing properties of phengitic micas and revised garnet-phengite thermobarometers. *Journal of Metamorphic Geology*, **20**: 683–696.

Connolly, J. A. D., 1990. Multivariable phase diagrams: an algorithm based on generalized thermodynamics. *American Journal of Science*, **290**: 666–718.

Connolly, J. A. D. and Kerrick, D. M., 1987. An algorithm and computer program for calculating composition phase diagrams. *CALPHAD*, **11**:1–55.

Corfu, F., 2013. A century of U-Pb geochronology: The long quest towards concordance. *GSA Bulletin*, **125 (1/2)**: 33–47.

Corfu, F., 2007. Multistage metamorphic evolution and nature of the amphibolite-granulite-facies transition in Lofoten-Vesterålen, Norway, revealed by U–Pb in accessory minerals. *Chemical Geology*, **214**: 108–128.

Corfu, F., Hanchar, J. M., Hoskin, P. W. O. and Kinny, P. D., 2003. Atlas of zircon textures. *In:* Hanchar, J. M., Hoskin, P. W. O. *(Eds.).* Zircon. *Reviews in Mineralogy and Geochemistry,* **53**: 469–500.

Corrigan, D and van Breemen, O., 1997. U–Pb age constraints for the lithotectonic evolution of the Grenville Province along the Mauricie transect, Quebec. *Canadian Journal of Earth Sciences*, **34**: 299–316.

Cox, R. A. and Indares, A., 1999a. Transformation of Fe-Ti gabbro to coronite, eclogite and amphibolite in the Baie du Nord segment, eastern Grenville Province. *Journal of Metamorphic Geology*, **17**: 537–555.

Cox, R. A. and Indares, A., 1999b. High pressure and temperature metamorphism of the mafic and ultramafic Lac Espadon suite, Manicouagan Imbricate Zone, eastern Grenville Province. *Canadian Mineralogist*, **37**: 335–357.

Cox, R. A., Dunning, G.R. and Indares, A., 1998. Petrology and U-Pb geochronology of mafic, high-pressure metamorphic coronites from the Tshenukutish domain, eastern Grenville Province. *Precambrian Research*, **90**: 59–83.

Cutts, K. A., Kinny, P. D., Strachan, R. A., Hand, M., Kelsey, D. E., Emery, M., Friend, C. R. L. and Leslie, A. G., 2010. Three metamorphic events recorded in a single garnet: Integrated phase modelling, *in situ* LA-ICPMS and SIMS geochronology from the Moine Supergroup, NW Scotland. *Journal of Metamorphic Geology*, **28**: 249–267.

de Capitani C. and Petrakakis K., 2010. The computation of equilibrium assemblage diagrams with Theriak/Domino software. *American Mineralogist,* **95**:1006–1016.

Dunning, G. and Indares, A., 2010. New insights on the 1.7-1.0 Ga crustal evolution of the central Grenville Province from the Manicouagan – Baie Comeau transect. *Precambrian Research*, **180**: 204–226.

Dunning, G. R., O'Brien, S. J., Colman-Sadd, S. P., Blackwood, R. F., Dickson, W. L., O'neill, P. P. and Krogh, T. E., 1990. Silurian orogeny in the Newfoundland Appalachians. *Journal of Geology*, **98**: 895–913.

Dunning, G. R., Barr, S. M., Giles, P. S., McGregor, D. C., Pe-Piper, G. and Piper, D. J. W., 2002. Chronology of Devonian to early Carboniferous rifting and igneous activity in southern Magdalen Basin based on U–Pb (zircon) dating. *Canadian Journal of Earth Sciences*, **39**: 1219–1237.

Feng, R., Machado, N. and Ludden, J., 1993. Lead geochronology of zircon by LaserProbe-inductively coupled plasma mass spectrometer (LP–ICPMS). *Geochimica et Cosmochimica Acta*, **57**: 3479–3486.

Fisher, C. M., McFarlane, C. R. M., Hanchar, J. M., Schmitz, M. D., Sylvester, P. J., Lam, R., Longerich, H. P., 2011. Sm–Nd isotope systematics by laser ablation-multicollector-inductively coupled plasma mass spectrometry: Methods and potential natural and synthetic reference materials. *Chemical Geology*, **284:** 1–20.

Florence, F. P. and Spear, F., 1991. Effects of diffusional modification of garnet growth zoning on P–T path calculations. *Contributions to Mineralogy and Petrology*, **107**: 487–500.

Foster, G., Gibson, H. D., Parrish, R., Horstwood, M., Fraser, J. and Tindle, A., 2002. Textural, chemical and isotopic insights into the nature and behavior of metamorphic monazite. *Chemical Geology*, **19**: 183–207.

Frei, D. and Gerdes, A., 2009. Precise and accurate in situ U–Pb dating of zircon with high sample throughput by automated LA-SF-ICP-MS. *Chemical geology*, **261**: 261–270.

Friend, C. R. and Kinny, P. D., 1995. New evidence for protolith ages of Lewisian granulites, northwest Scotland. *Geology*, **23**: 1027–1030.

Fryer, B. J, Jackson, S. E. and Longerich, H. P., 1993. The application of laser ablation microprobe-inductively coupled plasma mass spectrometer (LAM–ICPMS) to *in situ* (U)-Pb geochronology. *Chemical Geology*, **109**: 1–8.

Gehrels, G. E., Valencia, V. and Ruiz, J., 2008. Enhanced precision, accuracy, efficiency, and spatial resolution of U–Pb ages by laser ablation–multicollector–inductively

coupled plasma–mass spectrometry. *Geochemistry Geophysics Geosystems*, **9 (3)**, Q03017, DOI:10.1029/2007GC001805.

Gehrels, G., Rusmore, M., Woodsworth, G., Crawford, M., Andronicos, C., Hollister, L., Patchett, J., Ducea, M., Butler, R., Klepeis, K., Davidson, C., Friedman, R., Haggart, J., Mahoney, B., Crawford, W., Pearson, D. and Girardi, J., 2009. U-Th-Pb geochronology of the Coast Mountains batholith in north-coastal British Columbia: Constraints on age and tectonic evolution. Geological Society of America Bulletin, **121**: 1341–1361.

Gerdes, A. and Zeh, A., 2006. Combined U–Pb and Hf isotope LA-(MC-)ICP-MS analyses of detrital zircons: Comparison with SHRIMP and new constraints for the provenance and age of an Armorican metasediment in Central Germany. *Earth and Planetary Science Letters*, **249**: 47–61.

Gervais, F. and Hynes, A., 2012. Linking metamorphic textures to U–Pb monazite *in situ* geochronology to determine the age and nature of aluminosilicate-forming reactions in the Northern Monashee Mountains, British-Columbia. *Lithos*, **160–161**: 250–267.

Gibson, H. D. T, Carr, S. D., Hamilton, M. A. and Brown, R. L., 2004. Correlating yttrium zones and age domains in monazite with metamorphic reactions involving major pelitic phases: an integration of ID–TIMS and SHRIMP geochronology with Y-Th-U X-ray mapping. *Chemical Geology*, **211**: 237–260.

Gobeil, A., 1997a. Géologie de la région du Lac Grand Mesnil. Ministère des Ressources naturelles, Québec; RG 96–04, p. 10.

Gobeil, A., 1997b. Géologie de la région du Lac Lacoursière. Ministère des Ressources naturelles, Québec; RG 96–03, p. 14.

Godin, L., Grujic, D, Law, R. D. and Searle, M. P., 2006. Channel flow, ductile extrusion and exhumation in continental collision zones: an introduction. *In:* Law, R. D., Searle, M. P., and Godin, L. *(Eds).* Channel Flow, Ductile Extrusion and exhumation in Continental Collision Zones. *Geological Society, London*, Special Publications, **268**: 1–23.

Gower, C. F. and Krogh, T. E., 2002. A U–Pb geochronological review of the Proterozoic history of the eastern Grenville Province. *Canadian Journal of Earth Sciences,* **39**: 795–829.

Grujic, D., 2006. Channel flow and continental collision tectonics: an overview. *In:* Law, R. D., Searle, M. P., and Godin, L. *(Eds).* Channel Flow, Ductile Extrusion and exhumation in Continental Collision Zones. *Geological Society, London*, Special Publications, **268**: 25–37.

Gu, Y., 2003. Automated scanning electron microscopy based mineral liberation analysis. An introduction to JKMRC/FEI Mineral Liberation Analyser. *Journal of Minerals and Materials, Characterization and Engineering,* **2**: 33–41.

Guilmette, C., Indares, A. D. and Hébert, R., 2011. High-pressure anatectic paragneisses from the Namche Barwa, eastern Himalayan Syntaxis; textural evidence for partial melting, phase equilibria modelling and tectonic implications. *In:* Schulman, K., O'Brien, P., White, R., Brown, M., Lexa, Ondrej *(Eds.).* Granulite-facies metamorphism and the rheology of the lower crust, Granulites and Granulites 2009. *Lithos*, **124**: 66–81.

Hanchar, J. M. and Miller, C. F., 1993. Zircon zonation patterns as revealed by cathodoluminescence and backscattered electron images: Implications for interpretation of complex crustal histories. *Chemical Geology*, **110**: 1–13.

Hanchar, J. M. and Rudnick, R. L., 1995. Revealing hidden structures: the application of cathodoluminescence and back-scattered electron imaging to dating zircons from lower crustal xenoliths. *Lithos,* **36**: 289–303.

Harrison, T. M., Catlos, E. J., and Montel, J.-M., 2002. U–Th–Pb dating of phosphate minerals. *In:* Kohn, M. J., Rakovan, J., Hughes, J. M. *(Eds.).* Phosphates: geochemical, geobiological, and materials importance. *Reviews in Mineralogy and Geochemistry, Mineralogical Society of America,* **48 (14)**: 523–558.

Harte, B., Pattison, D. R. M. and Linklater, C. M., 1991. Field relations and petrography of partially melted pelitic and semi-pelitic rocks*. In:* Voll, G., Töpel, J., Pattison, D. R. M. and Seifert, F. *(Eds.).* Equilibrium and kinetics in contact metamorphism: The Ballachulish Igneous Complex and its thermal aureole. Springer Verlag: Heidelberg, 181–210.

Hartel, T. H. D. and Pattison, D. R. M., 1996. Genesis of the Kapuskasing (Ontario) migmatitic mafic granulites by dehydration melting of amphibolite: the importance of quartz to reaction progress. *Journal of Metamorphic Geology,* **14:** 591–611.

Hindemith, M.A., 2014. Petrography and geochemistry of hydrothermally altered volcanic rocks metamorphosed at granulite-facies conditions: and example from the Central Grenville Province. Msc Thesis, Earth Sciences Department, Memorial University of Newfoundland, St John's.

Hindemith, M. and Indares, A., 2013. The petrographic and geochemical study of hydrothermally altered metavolcanics, metamorphosed at granulite-facies conditions from the Canyon domain in the central Grenville Province of Quebec, Canada. GAC-MAC annual meeting Winnipeg, Abstract vol. 36, p. 113.

Holland, T. J. B. and Powell, R., 2003. Activity-composition relations for phases in petrological calculations: an asymmetric multicomponent formulation. *Contributions to Mineralogy and Petrology*, **145**: 492–501.

Holland, T. J. B. and Powell, R., 1998. An internally-consistent thermodynamic data set for phases of petrological interest. *Journal of Metamorphic Geology*, **16**: 309–343.

Holness, M. B. and Sawyer, E. W., 2008. On the pseudomorphing of melt-filled pores in migmatites. *Journal of Petrology*, **49 (7)**: 1343–1363.

Holness, M. B., Cesare, B. and Sawyer, E. W., 2011. Melted Rocks under the Microscope: Microstructures and Their Interpretation. *Elements*, **7 (4)**: 247–252.

Hynes, A., Indares, A., Rivers, T. and Gobeil, A., 2000. Lithoprobe line 55: integration of out-of-plane seismic results with surface structure, metamorphism, and geochronology, and the tectonic evolution of the eastern Grenville Province. *Canadian Journal of Earth Sciences*, **37**: 341–358.

Indares, A., 2003. Metamorphic textures and P–T evolution of high-P granulites from the Lelukuau terrane, NE Grenville Province. *Journal of Metamorphic Geology*, **21**: 35–48.

Indares, A. and Dunning, G., 2004. Crustal architecture above the high-pressure belt of the Grenville Province in the Manicouagan area: new structural, petrologic and U–Pb age constraints. *Precambrian Research*, **130**: 199–208.

Indares, A. and Dunning, G., 2001. Partial melting of high P–T metapelites from the Tshenukutish terrane (Grenville Province): petrography and U–Pb geochronology. *Journal of Petrology*, **42**: 1547–1565.

Indares, A. and Moukhsil, A., 2013. Geon 12 crustal extension in the central Grenville Province, implications for the orogenic architecture, and potential influence on the emplacement of anorthosites. *Canadian Journal of Earth Sciences*, **50**: 955–966.

Indares, A., Dunning, G. and Cox, R., 2000. Tectono-thermal evolution of deep crust in a Mesoproterozoic continental collision setting: the Manicouagan example. *Canadian Journal of Earth Sciences*, **37**: 325–340.

Indares, A., White, R. W. and Powell, R., 2008. Phase equilibria modelling of kyanite-bearing anatectic paragneisses from the central Grenville Province. *Journal of Metamorphic Geology*, **26**: 815–836.

Ireland, T. R. and Williams, I. S., 2003. Considerations in zircon geochronology by SIMS. *In:* Hanchar, J. M., Hoskin, P. W. O. *(Eds.).* Zircon. *Reviews in Mineralogy and Geochemistry,* **53**: 215–241.

Jamieson, R. A. and Beaumont, C., 2011. Coeval thrusting and extension during post-convergent ductile flow - implications for exhumation of high-grade metamorphic rocks. *Journal of Metamorphic Geology*, **29**: 33–51.

Jamieson, R. A., Beaumont, C., Nguyen, M. H. and Culshaw, N. G., 2007. Synconvergent ductile flow in variable-strength continental crust: Numerical models with application to the western Grenville orogen. *Tectonics*, **26**: 1–23.

Jamieson, R. A., Beaumont, C., Warren, C. J. and Nguyen, M. H., 2010. The Grenville Orogen explained? Applications and limitations of integrating numerical models

with geological and geophysical data. *In:* Lithoprobe - parameters, processes and the evolution of a continent (Lithoprobe Synthesis Volume II, *(Eds.)* Clowes, R M., and Skulski, T.). *Canadian Journal of Earth Sciences*, **47**: 517–539.

Johnson, T., Fischer, S. and White, R., 2013. Field and petrographic evidence for partial melting of TTG gneisses from the central region of the mainland Lewisian complex, NW Scotland. *Journal of the Geological Society*, **170**: 319–326.

Johnson, T., White, R. and Powell, R., 2008. Partial melting of metagreywacke: a calculated mineral equilibria study. Journal of Metamorphic Geology, **26**: 837 – 853.

Jones, R. R., Holdsworth, R. E., Hand, M. and Goscombe, B., 2006. Ductile extrusion in continental collision zones: ambiguities in the definition of channel flow and its identification in ancient orogens. *In:* Law, R. D., Searle, M. P., and Godin, L. *(Eds).* Channel Flow, Ductile Extrusion and exhumation in Continental Collision Zones. *Geological Society, London*, Special Publications, **268**: 201–219.

Jordan, S. L., Indares, A. and Dunning, G., 2006. Partial melting of metapelites in the Gagnon terrane below the high-pressure belt in the Manicouagan area (Grenville Province): pressure temperature (P–T) and U–Pb age constraints and implications. *Canadian Journal of Earth Sciences*, **38**: 1309–1329.

Kelly, N. M., Harley, S. L. and Möller, A., 2012. Complexity in the behavior and recrystallization of monazite during high-T metamorphism and fluid infiltration. *Chemical geology*, **322-323**: 192–208.

Kelsey, D. E., Clark, C. and Hand, M., 2008. Thermobarometric modelling of zircon and monazite growth in melt-bearing systems: examples using model metapelitic and metapsammitic granulites. *Journal of Metamorphic Geology*, **26**: 199–212.

Kelsey, D. E., Hand, M., Clark, C. and Wilson, C. J. L., 2007. On the application of *in situ* monazite chemical geochronology to constraining P-T-t histories in high-temperature (>850 °C) polymetamorphic granulites from Prydz Bay, East Antarctica. *Journal of the Geological Society*, **164**: 667–683.

Ketchum, J. W. F., Jackson, S. E., Culshaw, N. G. and Barr, S. M., 2001. Depositional and tectonic setting of the Paleoproterozoic Lower Aillik Group, Makkovik Province, Canada: evolution of a passive margin – foredeep sequence based on petrochemistry and U–Pb (ID-TIMS and LAM–ICP–MS) geochronology. *Precambrian Research*, **105**: 331–356.

Kingsbury, J. A., Miller, C. F., Wooden, J. L. and Harrison, T.M., 1993. Monazite paragenesis and U-Pb systematics in rocks of the eastern Mojave Desert, California, U.S.A.: implications for thermochronometry. *Chemical Geology*, **110**: 147–168.

Kohn, M. J. and Malloy, M. A., 2004. Formation of monazite via prograde metamorphic reactions among common silicates: Implications for age determinations. *Geochimica et Cosmochimica Acta*, **68**: 101–113.

Košler J. and Sylvester P., 2003. Present trends and the future of zircon in geochronology: laser ablation ICPMS. *In:* Hanchar, J. M., Hoskin, P. W. O. *(Eds.).* Zircon. *Reviews in Mineralogy and Geochemistry,* **53**: 243–275.

Krogh, T. E. 1982. Improved accuracy of U-Pb zircon ages by the creation of more concordant systems using an air abrasion technique. *Geochimica et Cosmochimica Acta*, **46**: 637–649.

Langone, A., Braga, R., Massonne, H. J. and Tiepolo, M., 2011. Preservation of old (prograde metamorphic) U–Th–Pb ages in unshielded monazite from the high-pressure paragneisses of the Variscan Ulten Zone (Italy). *Lithos*, **127**: 68–85.

Lasalle, S. and Indares, A., 2014. Anatectic and *P–T* record of aluminous gneisses from diverse protoliths and contrasting-pressure crustal belts in the central Grenville Province. *Journal of Metamorphic Geology*, *in press*, DOI: 10.1111/jmg.12083.

Lasalle, S., Dunning, G. and Indares, A., 2014. *In situ* laser ablation–ICPMS dating of monazite from aluminous gneisses: Insights on the tectono-metamorphic history of a granulite-facies domain in the central Grenville Province. *Canadian Journal of Earth Sciences, in press,* DOI:10.1139/cjes-2013-0170.

Lasalle, S., Fisher, C. M., Indares, A. and Dunning, G., 2013. Contrasting types of Grenvillian granulite-facies aluminous gneisses: Insights on protoliths and metamorphic events from zircon morphologies and ages. *Precambrian Research*, **228**: 117–130.

Ludwig, K. R., 2003. User's manual for Isoplot/Ex, Version 3.0. A geochronological toolkit for Microsoft Excel: Berkeley Geochronology Center Special Publication, **4**: 70 p.

McFarlane, C. R. M. and Harrison, T. M., 2006. Pb-diffusion in monazite: constraints from a high-*T* contact aureole setting. *Earth and Planetary Science Letters,* **250**: 376–384.

Mitchell, R., Indares, A. and Ryan, B., 2014. High to ultrahigh temperature contact metamorphism and dry partial melting of the Tasiuyak Paragneiss, Northern Labrador. *Journal of Metamorphic Geology, in press,* DOI:10.1111/jmg.12086.

Möller, A., O'Brien, P. J., Kennedy, A. and Kröner, A., 2002. Polyphase zircon in ultrahigh-temperature granulites (Rogaland, SW Norway): constraints for Pb diffusion in zircon. *Journal of Metamorphic Geology,* **20**: 727–740.

Montel, J.-M., Foret, S., Veschambre, M., Nicollet, C. and Provost, A., 1996. Electron microprobe dating of monazite. *Chemical Geology,* **131**: 37–53.

Moukhsil, A., Solgadi, F., Clark, T., Indares, A. and Blouin, S., 2013. Geology of the Daniel-Johnson Dam (Manic 5) area, Côte-Nord region (NTS 22K14, 22K15, 22K16, 22N03 and 22N02). Ministère des Ressources naturelles et de la Faune, RG-2013.

Moukhsil, A., Solgadi, F., Lacoste, P., Gagnon, M. and David, J., 2012. Géologie de la région du lac du Milieu (SNRC 22O03, 22O04, 22O06, 22J13 et 22J14). Ministère des Ressources naturelles et de la Faune, RG 2012–01.

Nadeau, L. and van Breemen, O., 1994. Do the 1.45–1.39 Ga Montauban group and the La Bostonnais complex constitute a Grenvillian accreted terrane? GAC–MAC, Program with Abstracts, 19, p. A81.

Nasdala, L., Hanchar, J. M., Kronz, A., and Whitehouse, M. J., 2005. Long-term stability of alpha particle damage in natural zircon. *Chemical Geology*, **220**: 83–103.

Owens, B.E., and Tomascak, P.B. 2002. Mesoproterozoic lamprophyres in the Labrieville Massif, Quebec: clues to the origin of alkalic anorthosites? Canadian Journal of Earth Sciences, **39(6):** 983–997. DOI:10.1139/e02-010.

Parrish, R. R., 1990. U–Pb dating of monazite and its application to geological problems. *Canadian Journal of Earth Sciences,* **27**: 1431–1450.

Parrish, R. R. and Noble, S. R., 2003. Zircon U-Th-Pb Geochronology by Isotope Dilution –Thermal Ionization Mass Spectrometry (ID-TIMS). *In:* Hanchar, J. M., Hoskin, P. W. O. *(Eds.).* Zircon. *Reviews in Mineralogy and Geochemistry,* **53**: 183–213.

Paton, C., Woodhead, J., Hellstrom, J., Hergt, J., Greig, A. and Maas, R., 2010. Improved laser ablation U–Pb zircon geochronology through robust downhole fractionation correction. *Geochemistry Geophysics Geosystems*, **11**: 1–36.

Pattison, D. R. M. and Begin, N. J., 1994a. Zoning patterns in orthopyroxene and garnet in granulites: implications for geothermometry. *Journal of Metamorphic Geology*, **12**: 387–410.

Pattison, D. R. M. and Bégin, N. J., 1994b. Hierarchy of closure temperatures in granulites and the importance of an intergranular exchange medium (melt?) in controlling maximum Fe-Mg exchange temperatures. *Mineralogical Magazine*, **58A**: 694–695.

Powell, R. and Holland, T. J. B., 1988. An internally consistent thermodynamic dataset with uncertainties and correlations: application, methods worked examples and a computer program. *Journal of Metamorphic Geology*, **6**: 173–204.

Powell, R., Holland, T. J. B. and Worley, B., 1998. Calculating phase diagrams involving solid solutions via non-linear equations, with examples using THERMOCALC. *Journal of Metamorphic Geology*, **16**: 577–588.

Powell, R., Guiraud, M. and White, R. W., 2005. Truth and beauty in metamorphic phase-equilibria: conjugate variables and phase diagrams. *The Canadian Mineralogist*, **43**: 21–33.

Pyle, J. M. and Spear, F. S., 2003. Four generations of accessory-phase growth in low-pressure migmatites from SW New Hampshire. *American Mineralogist*, **88**: 338–351.

Rivers, T., 2012. Upper-crustal orogenic lid and mid-crustal core complexes: signature of a collapsed orogenic plateau in the hinterland of the Grenville Province. *Canadian Journal of Earth Sciences,* **49**: 1–42.

Rivers, T. 2009. The Grenville Province as a large hot long-duration collisional orogen — insights from the spatial and thermal evolution of its orogenic fronts. In Ancient orogens and modern analogues. Edited by J.B. Murphy, J.D. Keppie, and A. Hynes. Geological Society (of London), Special Publication 327. pp. 405–444. doi:10.1144/SP327.17.

Rivers, T., 2008. Assembly and preservation of lower, mid, and upper orogenic crust in the Grenville Province-Implications for the evolution of large hot long-duration orogens. *Precambrian Research,* **167**: 237–259.

Rivers, T., 1997. Lithotectonic elements of the Grenville Province: review and tectonic implications. *Precambrian Research*, **86**: 117–154.

Rivers, T., Culshaw, N., Hynes, A., Indares, A., Jamieson, R. and Martignole, J., 2012. The Grenville Orogen - A post-LITHOPROBE perspective. Chapter 3 *In* Tectonic Styles in Canada: The LITHOPROBE Perspective. Edited by J.A. Percival, F.A. Cook, and R.M. Clowes. *Geological Association of Canada, Special Paper 49*, pp. 97–236.

Rivers, T., Martignole J., Gower, C. F. and Davidson, A., 1989. New tectonic divisions of the Grenville province, southeast Canadian Shield. *Tectonics*, **8**: 63–84.

Roberts, M. P. and Finger, F., 1997. Do U–Pb zircon ages from granulites reflect peak metamorphic conditions? *Geology*, **25**: 319–322.

Rosenberg, C. L. and Handy, M. R., 2005. Experimental deformation of partially melted granite revisited: implications for the continental crust. *Journal of metamorphic Geology*, **23**: 19–28.

Rubatto, D., 2002. Zircon trace element geochemistry: Partitioning with garnet and the link between U–Pb ages and metamorphism. *Chemical Geology,* **184**: 123–138.

Sawyer, E.W., 2001. Melt segregation in the continental crust: distribution and movement of melt in anatctic rocks. *Journal of Metamorphic Geology*, **19**: 291–309.

Sawyer, E.W., 1998. Criteria for the recognition of partial melting. *Physics, Chemistry and Earth* (A), **24**: 269–279.

Shaffer, M., 2009. Discrimination of hematite and magnetite and quantifying their associations using the JKTECH Mineral Liberation AnalyzerTM. In The 48th Annual Conference of Metallurgists, Laurentian University, Sudbury, Ontario 73.

Shaffer, M., Gu, Y., and Rohde, M., 2008. Practical Applications for the Silicon Drift Xray Detector in SEM-Platformed Image Analysis: The Bruker-MLA in Practice.

In SME Annual Meeting 2007 and CMS 109th National Western Conference 2007 The Power of Mining: Energy's Influence, Denver, CO, U.S.A., 25-28 February, 2007, 1(Preprint 07-029): 1-6.

Simonetti, A., Heaman, L. M., Chacko, T. and Banerjee, N. R., 2006. *In situ* petrographic thin-section U–Pb dating of zircon, monazite and titanite using laser ablation-MC-ICP-MS. *International Journal of Mass Spectrometry*, **253**: 87–97.

Slagstad, T., Hamilton, M.A., Jamieson, R.A., Culshaw, N.G., 2004. Timing and duration of melting in the mid orogenic crust: constraints from U-Pb (SHRIMP) data, Muskoka and Shawanaga domains, Grenville Province, Ontario. *Canadian Journal of Earth Sciences*, **41**: 1339–1365.

Sláma, J., Košler, J., Condon, D. J., Crowley, J. L., Gerdes, A., Hanchar, J. M., Horstwood, M. S. A., Morris, G. A., Nasdala, L., Norberg, N., Schaltegger, U., Schoene, B., Tubrett, M. N. and Whitehouse, M. J., 2008. Plešovice zircon – a new natural reference material for U–Pb and Hf isotopic microanalysis. *Chemical Geology*, **249**: 11–35.

Spear, F., 1991. On the interpretation of peak metamorphic temperatures in light of garnet diffusion during cooling. *Journal of Metamorphic Geology*, **9**: 379–388.

Spear, F. and Parrish, R., 1996. Petrology and cooling rates of the Valhalla Complex, British Columbia, Canada. *Journal of Petrology*, **37**: 733–765.

Spear, F. S. and Pyle, J. M., 2010 Theoretical modelling of monazite growth in a low-Ca metapelite. *Chemical Geology*, **273**: 111–119.

Spear, F. S. and Pyle, J. M., 2002. Apatite, monazite, and xenotine in metamorphic rocks. *In:* Kohn, M. J., Rakovan, J., Hughes, J. M. *(Eds.).* Phosphates: geochemical,

geobiological, and materials importance. *Reviews in Mineralogy and Geochemistry, Mineralogical Society of America*, **48**: 293–336.

Spear, F. S., Kohn, M. J. and Cheney, J. T., 1999. P–T paths from anatectic pelites. *Contributions to Mineralogy and Petrology*, **134**: 17–32.

Spear, F. S., Pyle, J. M., Wark, D. A., 2002. Electron Microprobe Analysis of REE in Apatite, Monazite and Xenotime: Protocols and Pitfalls *In:* Kohn, M. J., Rakovan, J., Hughes, J. M. *(Eds.).* Phosphates: geochemical, geobiological, and materials importance. *Reviews in Mineralogy and Geochemistry, Mineralogical Society of America*, **48**: 337–362.

Tichomirowa, M., 2003. Recrystallisation of zircons during granulite-facies metamorphism (Germany, Central Erzgebirge). *Journal of the Czech Geological Society*, **48**: 124.

Tohver, E., Teixeira, W., van der Pluijm, B., Geraldes, M. C., Bettencourt, J. S. and Rizzotto, G ., 2006. Restored transect across the exhumed Grenville orogen of Laurentia and Amazonia, with implications for crustal architecture. *Geology*, **34**: 669–672.

Tomascak, P. B., Krogstad, E. J., Walker, R. J., 1996. U–Pb monazite geochronology of granitic rocks from Maine: Implications for Late Paleozoic tectonics in the northern Appalachians, *Journal of Geology*, **104**: 185–195.

Valverde Cardenas, C., Indares, A. and Jenner, G., 2012 Mafic and ultrapotassic rocks from the Canyon domain (central Grenville Province): geochemistry and tectonic implications. *Canadian Journal of Earth Sciences*, **49(2)**: 412–433, DOI: 10.1139/e11-065.

van Gool, J. A. M., Rivers, T. and Calon, T., 2008. Grenville Front zone, Gagnon terrane, south-western Labrador: configuration of a midcrustal foreland fold-thrust belt. *Tectonics*, **27**: 1–35.

Vavra, G., Schmidt, R. and Gebauer, D., 1999. Internal morphology, habit and U–Th–Pb microanalysis of amphibolite to granulite-facies zircons: geochronology of the Ivrea zone (southern Alps). *Contributions to Mineralogy and Petrology*, **134**: 380–404.

Vavra, G., Gebauer, D., Schmid, R. and Compston, W., 1996. Multiple zircon growth and recrystallization during polyphase Late Carboniferous to Triassic metamorphism in granulites of the Ivrea Zone Southern Alps: an ion microprobe SHRIMP study. *Contributions to Mineralogy and Petrology*, **122**: 337–358.

Vernon, R. H. and Collins, W. J., 1988. Igneous microstructures in migmatites. *Geology,* **16**: 1126–1129.

WaveMetrics, Inc. IGOR Pro 6.3 manual, Lake Oswego, OR, www.wavemetrics.com.

White, R. W. and Powell, R., 2002. Melt loss and the preservation of granulite-facies mineral assemblages. *Journal of Metamorphic Geology*, **20**: 621–632.

White, R. W., Powell, R. and Clarke, G. L., 2002. The interpretation of reaction textures in Fe-rich metapelitic granulites of the Musgrave Block, central Australia: constraints from mineral equilibria calculations in the system K2O–FeO–MgO–Al2O3–SiO2–H2O–TiO2–Fe2O3. *Journal of Metamorphic Geology*, **20**: 621–632.

White, R. W., Powell, R. and Halpin, J. A., 2004. Spatially focused melt formation in aluminous metapelites from Broken Hill, Australia. *Journal of Metamorphic Geology*, **22**: 825–845.

White, R. W., Powell, R., and Holland, T. J. B., 2007. Progress relating to calculation of partial melting equilibria for metapelites. *Journal of Metamorphic Geology*, **25**: 511–527.

White, R. W., Powell, R., Holland, T. J. B. and Worley, B. A., 2000. The effect of TiO2 and Fe2O3 on metapelitic assemblages at greenschist and amphibolite facies conditions: mineral equilibria calculations in the system K2O–FeO–MgO–Al2O3–SiO2–H2O–TiO2–Fe2O3. *Journal of Metamorphic Geology*, **18**: 497–511.

Whitehouse, M. J. and Kamber, B. S., 2005. Assigning dates to thin gneissic veins in high-grade metamorphic terranes: A cautionary tale from Akilia, Southwest Greenland. Journal of Petrology, **46**: 291–318.

Whitehouse, M. J. and Kemp, A. I. S., 2010. On the difficulty of assigning crustal residence, magmatic protolith and metamorphic ages to Lewisian granulites: constraints from combined in situ U–Pb and Lu-Hf isotopes. *In:* Law, R. D., Butler, R. W. H., Holdsworth, R. E., Krabbendam, M., Strachan, R. A. *(Eds.).* Continental Tectonics and Mountain Building: The Legacy of Peach and Horne. *Geological Society of London Special Publication*, **335**: 81–101.

Wiedenbeck, M., Allé, P., Corfu, F., Griffin, W. L., Meier, M., Oberli, F., von Quadt, A., Roddick, J. C. and Spiegel, W., 1995. Three natural zircon standards for U-Th-Pb, Lu-Hf, trace element and REE analyses. *Geostandards Newsletter*, **19**: 11–23.

Wiedenbeck, M., Hanchar, J.M., Peck, W.H., Sylvester, P., Valley, J., Whitehouse, M., Kronz, A., Morishita, Y., Nasdala, L., Fiebig, J., Franchi, I., Girard, J-P., Greenwood, R.C., Hinton, R., Kita, N., Mason, P.R.D., Norman, M., Ogasawara, M., Piccoli, P.M., Rhede, D., Satoh, H., Schulz-Dobrick, B., Skar, O., Spicuzza, M.J., Terada, K., Tindle, A., Togashi, S., Vennemann, T., Xie, Q. and Zheng, Y-F., 2004. Further characterization of the 91500 zircon crystal. *Geostandards and Geoanalytical Research,* **28**: 91–139.

Whitney, D. L., and Evans, B. W., 2010. Abbreviations for names of rock-froming minerals. *American Mineralogist*, **95**: 185–187.

Williams, I., 2001. Response of detrital zircon and monazite, and their U–Pb isotopic systems, to regional metamorphism and host-rock partial melting, Cooma complex, southeastern Australia. *Australian Journal of Earth Sciences*, **48**: 557–580.

Williams, M. L., Jercinovic, M. J. and Hetherington, C. J., 2007. Microprobe monazite geochronology: Understanding geologic processes by integrating composition and chronology. *Annual Review Earth Planetary Sciences*, **35**: 137–175.

Williams, M. L., Jercinovic, M. J. and Terry, M. P., 1999. Age mapping and dating of monazite on the electron microprobe: Deconvoluting multistage tectonic histories. *Geology*, **27**: 1023–1026.

Yang, P., and Indares, A., 2005. Mineral zoning, phase relations, and *P–T* evolution of high-pressure granulites from the Lelukuau terrane, northeastern Grenville Province, Quebec. *The Canadian Mineralogist*, **43**: 442–462.